

22 March 2013 | \$10

# Science

AAAS

## EDITORIAL

- 1359** Two Revolutions in Learning  
*Susan R. Singer and William B. Bonvillian*

## NEWS OF THE WEEK

- 1364** A roundup of the week's top stories

## NEWS & ANALYSIS

- 1367** NFL Kicks Off Brain Injury Research Effort
- 1368** Austrian Academy of Sciences Faces Its Nazi History
- 1369** Drug Watchdog Ponders How to Open Clinical Trial Data Vault
- 1371** A Rescue Mission for Amphibians at the Brink of Extinction
- 1372** A More Modest Climate Agenda for Obama's Second Term
- 1373** Life Could Have Thrived on Mars, but Did It? Curiosity Still Has No Clue

## NEWS FOCUS

- 1374** Battle for the Barrel  
*>> Science Podcast*
- 1380** Suresh Leaves His Mark on NSF as He Heads to Carnegie Mellon

## LETTERS

- 1382** Libraries' Social Role in the Information Age  
*E. Herrera-Viedma and J. López-Gijón*
- China's Food Security Soiled by Contamination  
*Y. Liu et al.*
- Fostering Public Support for Vulture Protection  
*M. S. Dama*

- 1383** CORRECTIONS AND CLARIFICATIONS

## BOOKS ET AL.

- 1384** Henri Poincaré: A Scientific Biography  
*J. Gray, reviewed by P. Pesic*
- 1385** Taken for Grantedness  
*R. Ling, reviewed by J. B. Bayer*

## POLICY FORUM

- 1386** Drug Patents at the Supreme Court  
*C. S. Hemphill and B. Sampat*  
*>> Science Podcast*

## PERSPECTIVES

- 1388** Making a Point with Wnt Signals  
*J. D. Berndt and R. T. Moon*  
*>> Reports pp. 1436, 1441, and 1445*
- 1389** Robotic Walking in the Real World  
*M. L. Hunt*  
*>> Report p. 1408*
- 1390** Spatial Turn in Health Research  
*D. B. Richardson et al.*  
*>> Science Podcast*
- 1392** Dynamin Flexibility Drives Fission  
*R. W. Holz*  
*>> Report p. 1433*
- 1393** Probing an Extrasolar Planet  
*M. S. Marley*  
*>> Report p. 1398*
- 1395** Characterizing Giant Landslides  
*D. N. Petley*  
*>> Report p. 1416*
- 1396** A Transition in the Middle Ear  
*D. M. Fekete and D. M. Noden*  
*>> Report p. 1453*

**CONTENTS** continued >>



page 1374



page 1384



## COVER

Accumulation of algal biomass under thinning Arctic sea ice (image diameter ~25 meters). This photograph was taken on 17 September 2012 in the central Arctic basin at 85°30'47"N, 59°54'11"E, from the bridge of the research vessel *Polarstern*. Here, the central ice floe is surrounded by a green cloud of sub-ice diatoms. Current trends in sea-ice thinning may influence algal growth in this region. See page 1430.

*Photo: Stefan Hendricks, Alfred Wegener Institute, Expedition IceArc (ARK27-3)*

Explore our rich online offerings, including multimedia, news, *Science Careers*, and our two research journals—*Science Signaling* and *Science Translational Medicine*—at [www.sciencemag.org](http://www.sciencemag.org)

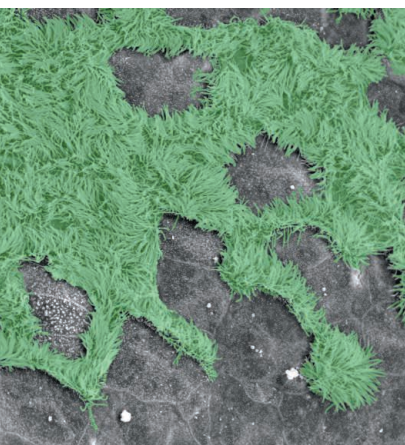
## DEPARTMENTS

- 1357** This Week in *Science*
- 1360** Editors' Choice
- 1362** *Science* Staff
- 1457** New Products
- 1458** *Science Careers*





pages 1389 & 1408



pages 1396 & 1453

## REPORTS

- 1398** Detection of Carbon Monoxide and Water Absorption Lines in an Exoplanet Atmosphere  
*Q. M. Konopacky et al.*  
A high-resolution spectrum of an exoplanet reveals molecular lines that provide clues about the planet's formation.  
>> *Perspective p. 1393*
- 1402** Suppression of Metal-Insulator Transition in VO<sub>2</sub> by Electric Field-Induced Oxygen Vacancy Formation  
*J. Jeong et al.*  
Electrochemistry plays a role in the ionic liquid gating of a strongly correlated oxide.
- 1405** Photonic Spin Hall Effect at Metasurfaces  
*X. Yin et al.*  
The polarization-dependent deflection of photons can be controlled with a designed metamaterial surface.
- 1408** A Terradynamics of Legged Locomotion on Granular Media  
*C. Li et al.*  
A model is developed to predict terrestrial animal locomotion on granular materials, where the terrain moves when stressed.  
>> *Perspective p. 1389; Science Podcast*
- 1412** DNA Gridiron Nanostructures Based on Four-Arm Junctions  
*D. Han et al.*  
Flexible DNA wireframe nanostructures have double-helical domains as edges and modified Holliday junctions as vertices.
- 1416** Simple Scaling of Catastrophic Landslide Dynamics  
*G. Ekström and C. P. Stark*  
Inverse modeling of seismic data reveals forces associated with catastrophic landslides.  
>> *Perspective p. 1395*
- 1419** Two Modes of Change in Southern Ocean Productivity Over the Past Million Years  
*S. L. Jaccard et al.*  
Subantarctic iron fertilization and Antarctic stratification explain the past 10 cycles' glacial-interglacial carbon dioxide variation.
- 1423** Emergence and Diversification of Fly Pigmentation Through Evolution of a Gene Regulatory Module  
*L. Arnoult et al.*  
Pigmentation spots on the wings of flies originate from changes at different levels of the underlying genetic hierarchy.
- 1426** Structural Reorganization of the Toll-Like Receptor 8 Dimer Induced by Agonistic Ligands  
*H. Tanji et al.*  
The crystal structure of unbound and ligand-bound Toll-like receptor 8 reveals ligand-induced conformational changes.
- 1430** Export of Algal Biomass from the Melting Arctic Sea Ice  
*A. Boetius et al.*  
As polar ice retreated in 2012, it left evidence of large algal deposits in its wake.
- 1433** Geometric Catalysis of Membrane Fission Driven by Flexible Dynamin Rings  
*A. V. Shnyrova et al.*  
Guanosine triphosphate hydrolysis limits polymerization of the membrane protein dynamin on lipid nanotubes into short, metastable collars.  
>> *Perspective p. 1392*
- 1436** RNA Helicase DDX3 Is a Regulatory Subunit of Casein Kinase 1 in Wnt-β-Catenin Signaling  
*C.-M. Cruciat et al.*  
A multifunctional protein is required for activation of casein kinase 1 in response to Wnt-β-catenin signaling.  
>> *Perspective p. 1388*
- 1441** Phosphorylation of Dishevelled by Protein Kinase RIPK4 Regulates Wnt Signaling  
*X. Huang et al.*  
The protein kinase RIPK4 is identified as a component of the Wnt signaling pathway.  
>> *Perspective p. 1388*
- 1445** A Localized Wnt Signal Orients Asymmetric Stem Cell Division in Vitro  
*S. J. Habib et al.*  
Stem cells orient their cell division apparatus to generate proximal and distal daughters relative to the Wnt source.  
>> *Perspective p. 1388*
- 1448** Type I Interferon Suppresses Type II Interferon-Triggered Human Anti-Mycobacterial Responses  
*R. M. B. Teles et al.*  
Disseminated *Mycobacterium leprae* infection is associated with blockade of the antimicrobial response by type I interferons.
- 1453** Dual Origin of the Epithelium of the Mammalian Middle Ear  
*H. Thompson and A. S. Tucker*  
When the endoderm fails, the neural crest does its best to pick up the slack.  
>> *Perspective p. 1396*

SCIENCE (ISSN 0036-8075) is published weekly on Friday, except the last week in December, by the American Association for the Advancement of Science, 1200 New York Avenue, NW, Washington, DC 20005. Periodicals Mail postage (publication No. 484460) paid at Washington, DC, and additional mailing offices. Copyright © 2013 by the American Association for the Advancement of Science. The title SCIENCE is a registered trademark of the AAAS. Domestic individual membership and subscription (51 issues): \$149 (\$74 allocated to subscription). Domestic institutional subscription (51 issues): \$990; Foreign postage extra: Mexico, Caribbean (surface mail) \$55; other countries (air assist delivery) \$85. First class, airmail, student, and emeritus rates on request. Canadian rates with GST available upon request, GST #1254 88122. Publications Mail Agreement Number 1069624. Printed in the U.S.A.

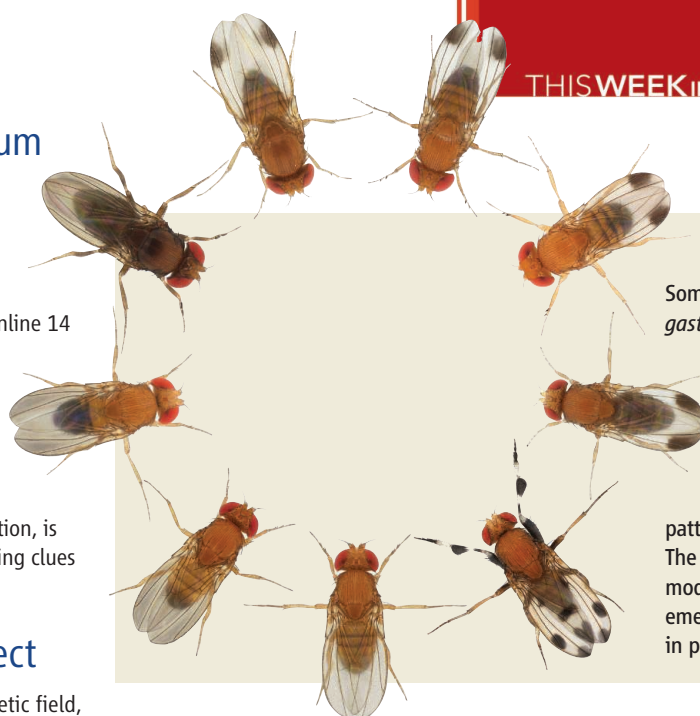
Change of address: Allow 4 weeks, giving old and new addresses and 8-digit account number. Postmaster: Send change of address to AAAS, P.O. Box 96178, Washington, DC 20090-6178. Single-copy sales: \$10.00 current issue, \$15.00 back issue prepaid includes surface postage; bulk rates on request. Authorization to photocopy material for internal or personal use under circumstances not falling within the fair use provisions of the Copyright Act is granted by AAAS to libraries and other users registered with the Copyright Clearance Center (CCC) Transactional Reporting Service, provided that \$30.00 per article is paid directly to CCC, 222 Rosewood Drive, Danvers, MA 01923. The identification code for Science is 0036-8075. Science is indexed in the Reader's Guide to Periodical Literature and in several specialized indexes.

CREDITS: (TOP) GALEN CLARK HAYNES, AARON M. JOHNSON, AND DANIEL E. KODITSCHKE; (BOTTOM) HANNAH THOMPSON AND ABIGAIL S. TUCKER

## High-Resolution Spectrum of an Exoplanet

Unlike most of the extrasolar planets we know about, the four planets around the star HR 8799 were detected directly.

**Konopacky et al.** (p. 1398, published online 14 March; see the Perspective by **Marley**) obtained a high-resolution spectrum of one of the planets that reveals both water and carbon monoxide but not methane in the planet's atmosphere. The atmospheric carbon-to-oxygen ratio, which traces the process of planet formation, is greater than that of the host star, providing clues to how the planets formed.



## << Seeing Spots

Some flies in the *Drosophila melanogaster* lineage exhibit wing spots, which vary among species. Examining the underlying genetics of spot determination, **Arnoult et al.** (p. 1423) provide evidence for a two-step scenario for the origin and diversification of patterning novelty in these fly wings. The findings suggest that the two-step model may generally apply to the emergence and diversification of traits in plants and animals.

## Photonic Spin Hall Effect

When charged carriers move in a magnetic field, they are deflected—an effect known as the Hall effect. Electrons possess charge and spin, a property related to magnetism. The symmetry of electromagnetism then allows for a spin Hall effect whereby the spin is deflected by an electric field. In optics, photons, too, have electric and magnetic components and should thus also exhibit a corresponding photonic spin Hall effect. Using designer metamaterial surfaces, **Yin et al.** (p. 1405) show that the spin-orbit coupling for photons can be amplified, giving rise to an observable photonic spin Hall effect.

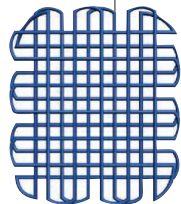
to understand these often catastrophic and costly natural hazards. **Ekström and Stark** (p. 1416; see the Perspective by **Petley**) analyzed global seismic network data using a method that identifies long-period events not recorded by traditional monitoring networks. The global seismic network was able to record landslide events and quantify dynamic properties—including duration, total mass, and direction of debris flow. The analysis located and quantified a series of seven previously undocumented massive landslides associated with the Siachen Glacier in the Himalayas.

for dynamin activity that takes into consideration all known aspects of dynamin function.

## Rewiring DNA Origami

Complex DNA nanostructures can be formed from a long scaffold strand of DNA by binding many shorter “staple”

strands. In these DNA origami structures, the path of the scaffold has been restricted by a double-crossover motif to form parallel helices. **Han et al.** (p. 1412) now describe a more flexible approach based on a “gridiron unit” in which four four-arm junctions link together to form a two-layer square frame. A variety of two- and three-dimensional structures were created, including highly curved structures, such as a sphere and a screw.



## Dissecting TLR8 Interactions

Toll-like receptors (TLRs) activate the innate immune system in response to invading pathogens. TLR7 and TLR8 recognize single-stranded RNA from viruses and also contribute to the pathogenesis of autoimmune diseases. **Tanji et al.** (p. 1426) now report the crystal structure of the unliganded TLR8 ectodomain and the TLR8 ectodomain bound to three different small-molecule agonists. Ligand binding to preformed TLR8 dimers induced conformational changes that brought the C-terminal domains closer together, presumably initiating downstream signaling.

## Interfering with Interferons

Infections with *Mycobacteria*, including *Mycobacterium leprae* or *M. tuberculosis*, vary substantially in their clinical presentation. For instance, in some cases of *M. leprae*, the infection is self-healing with very few lesions. In contrast, some people experience the disseminated form, where skin lesions abound and bacteria are abundant. In patients infected with *M. leprae*, **Teles et al.** (p. 1448, published online 28 February) found that the disseminated disease associates with a type I interferon gene signature, whereas the self-healing form associates with a type II interferon gene signature. In cultured cells, type I interferon and its downstream signaling cascade inhibited the antimicrobial response induced by type II interferons, providing a potential explanation for why robust disease rather than protection is seen in some cases of infection.

## Ear, Ear

Development of the middle ear has been the subject of competing hypotheses. **Thompson and Tucker** (p. 1453; see the Perspective by **Fekete and Noden**) used transgenic mice to follow the cell types that form the middle ear. During development of the middle ear, a balloon of endoderm expands that bursts, allowing entry of mesenchymal neural crest cells. As the mesenchyme withdraws, a cavity is formed, partly lined with remnants of the endodermal balloon. The mature middle ear in mouse is thus lined partly by endoderm, with its rich ciliation typical of mucosal epithelia, and in part by neural crest cells, which lack cilia.

## Bringing Down Landslides

Measuring landslide mechanics remotely, like seismic networks are used to quantify and locate earthquakes, would provide valuable information

## Making the Cut

Dynamin is the prototypical member of a large family of structurally related guanosine triphosphatases involved in membrane fission and fusion. A variety of models have been suggested to explain how dynamin works. **Shnyrova et al.** (p. 1433; see the Perspective by **Holz**) reconstituted dynamin-mediated membrane scission on lipid nanotubes and suggest a molecular model



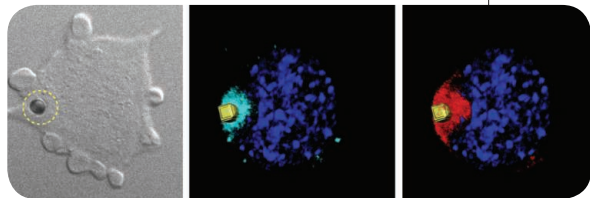
## Additional summaries

## Mind the Vacancies

Varying the carrier density of solid-state systems to manipulate their electrical properties usually involves chemical doping, which can lead to disorder. Recently, ionic liquids have been used to form an electronic double layer on the surface of a material, tuning its carrier density by the application of an electric field. **Jeong et al.** (p. 1402) used liquid gating on VO<sub>2</sub>, which undergoes a metal-insulator transition close to room temperature. The liquid gating suppressed the transition to lower and lower temperatures; however, the material remained in the metallic state, even when the gating fluid was washed off. It appears that, instead of a simple electrostatic effect, the properties of VO<sub>2</sub> are modulated by the introduction of oxygen vacancies, an electrochemical consequence of high electric fields. The results imply that careful interpretation of liquid gating experiments in condensed matter physics is needed.

## Three Tales of Wnt Signaling

The Wnt signaling pathway has important roles in regulating many biological processes during development and is also implicated in the behavior of some cancer cells (see the Perspective by **Berndt and Moon**). **Cruciat et al.** (p. 1436, pub-



lished online 14 February) describe the mechanism of action of a protein found in a screen for proteins that influence Wnt signaling. DDX3, a DEAD-box RNA helicase, is required for proper Wnt signaling in *Xenopus* and *Caenorhabditis elegans*. It appears to act not through its action as an RNA helicase or through adenosine triphosphate binding, but rather by interacting with the

protein kinase, casein kinase 1, and promoting its activation. **Huang et al.** (p. 1441, published online 31 January) investigated the function of receptor-interacting protein kinase 4 (RIPK4), the product of a gene whose mutation causes severe developmental defects in mice and humans. Overexpression of the protein in cultured human cells activated transcription of genes regulated by the Wnt signaling pathway, and loss of RIPK4 function inhibited Wnt signaling in *Xenopus* embryos. At the molecular level, RIPK4 interacted with the Wnt co-receptor LRP6 and the Wnt signaling adaptor protein DVL2 and promoted phosphorylation of DVL2. **Habib et al.** (p. 1445) used Wnt-immobilized beads to understand how external cues direct asymmetrical stem cell divisions. Spatially restricted Wnt signals oriented the plane of mitotic division and lead to pluripotency gene expression in the Wnt-proximal daughter cell while the more distal daughter cell acquired hallmarks of differentiation. Thus, asymmetric gene expression patterns can arise as a consequence of orientation by a short-range signal.

## Walking on Sand

Studies of objects moving through air or water have provided detailed models for designing objects with better flow dynamics. Examples include aircraft fins and wings, robots used as underwater probes, and even swimsuits to enhance swimmers' competitiveness. Much less is known about the mechanics of moving objects on or in materials that themselves have non-uniform dynamics. For example, when walking on a granular medium like sand, the moving leg and foot may penetrate to varying depths with small changes in material properties. **Li et al.** (p. 1408; see the Perspective by **Hunt**) study this system and develop a model for predicting the motion of legged bodies on granular media for a range of leg shapes and motion speeds. Factors that complicate the motion include leg shape and size and movement direction, as well as the size shape, and uniformity of the granular material.

## Working Together

The variability of atmospheric carbon dioxide concentrations over glacial cycles, which are central aspects of the climate cycle, was documented decades ago. However, it has been difficult to identify which mechanisms have driven CO<sub>2</sub> variability. Attention has focused on the Southern Ocean, because of its unique combination of hydrology and biology, although it has not been clear how the different behaviors of its Antarctic and Subantarctic zones might be reconciled with the observations of atmospheric CO<sub>2</sub> change. **Jaccard et al.** (p. 1419) present a record of productivity from the Atlantic Antarctic Zone that extends back in time far enough to cover the last 10 glacial cycles. The findings show how the combination of effects in the Antarctic and Subantarctic zones can explain most of the atmospheric CO<sub>2</sub> record over the past million years.

## Diatom Fall

2012 saw the greatest Arctic ice minimum ever recorded. This allowed unprecedented access for research vessels deep into the Arctic Ocean to make high-latitude observations of ice melt and associated phenomena. From the RV Polarstern between 84° to 89° North, **Boetius et al.** (p. 1430, published online 14 February; see the cover) observed large-scale algal aggregates of the diatom *Melosira arctica* hanging beneath multiyear and seasonal ice across a wide range of latitudes. The strands of algae were readily dislodged and formed aggregates on the seabed up to 4400 meters below, where the algae are consumed by large mobile invertebrates, such as sea cucumbers and brittle stars. Although Nansen observed sub-ice algae in the Arctic 100 years ago, the extent of this bloom phenomenon was unknown. The dynamics of such blooms must impinge on global carbon budgets, but how the dynamics will change as ice melt becomes more extensive remains unclear.



Susan R. Singer is Laurence McKinley Gould Professor of Biology at Carleton College, Northfield, MN, and chair of the NRC's Discipline-Based Education Research study. She served on the NRC's Board on Science Education. E-mail: [ssinger@carleton.edu](mailto:ssinger@carleton.edu).



William B. Bonvillian is director of the Massachusetts Institute of Technology's office in Washington, DC, and is on the adjunct faculty of the Science, Technology and International Affairs program, Georgetown University, Washington, DC. He served on the NRC's Board on Science Education. E-mail: [bonvill@mit.edu](mailto:bonvill@mit.edu).

## Two Revolutions in Learning

THE DAZZLING PROMISE OF AFFORDABLE, HIGH-QUALITY, GLOBALLY ACCESSIBLE ONLINE COURSES has renewed attention to learning and teaching. The opportunity to realize the full potential of so-called MOOCs (massively open online courses) may reside in a parallel, yet often unconnected, revolution in learning. Applying our understanding of undergraduate learning to online environments will build their educational value, while the scale and speed of data generation from MOOCs can accelerate research on learning. Approached iteratively, the outcomes can be transformative.

To improve the quality of education, U.S. universities are being called on to use a broader range of research-based practices to enhance student learning in the classroom.\* These practices need to be brought to scale online. A 2012 report released by the U.S. National Research Council (NRC) summarizes what we know about undergraduate learning in science and engineering.† Across all sciences, students struggle with fundamental concepts and underlying ideas, at both large and small spatial and temporal scales. Visual representations are crucial to conceptualizing and communicating science, but students often have difficulty interpreting the models, simulations, and graphs that are key to attaining a true understanding of science domains. And in problem solving, students too often focus on the superficial aspects of a problem, whereas experts know to focus on underlying principles. And yet, for example, research demonstrates that problem-solving skills can be developed through discussion-oriented learning environments where students collaborate, through the use of open-ended, real-world problems, and through tasks that provide students with prompts and guides. These findings must be translated into MOOCs.

In hybrid models—online plus face-to-face—learning can be accelerated, but there are many open questions. In some “flipped classrooms,” students view lectures online in advance of class, with class time reserved for engaging discussions. This strategy has drawn both praise and skepticism. Informing students about concepts and procedures before giving them practice in class undermines the type of learning needed for transferring and applying understanding; students who confront problems before the explanation are better able to use their knowledge in other contexts.‡ Thus, we still have much to learn about learning, both in brick-and-mortar classrooms and in blended or fully online environments. If meaningful learning analytics, informed by research on learning, are used to mine the mountains of online data that can be harvested from MOOCs, we can fill in many important gaps in our understanding. For example, how do students of different backgrounds and ages respond to different instructional strategies? How does learning develop over multiple courses and years, and how can students transfer understanding of cross-cutting concepts across courses? We need to tease apart which aspects of learning require face-to-face teaching, such as the development of expression, presentation, and advocacy skills. Which social features of give-and-take exchanges in the classroom are essential to build student involvement and commitment to learning? When is real “human scaffolding” required for discourse, argumentation, mentoring, and making conceptual leaps? How can online resources enhance the learning-by-doing aspects of research?

Online technology will not stand still; its interactive social and evaluation features will evolve, and the boundaries between online and face-to-face education will shift and affect the answers to such questions. Students will increasingly be learning in both physical and virtual spaces. It's the human-online symbiosis—the right blend of students, teachers, and teams with online capabilities, all informed by advances in learning science—that will be the enabler for a new generation of science learning. Let's not miss the opportunity to transform higher education by effectively integrating the online and learning science revolutions.

— Susan R. Singer and William B. Bonvillian



\*[www.whitehouse.gov/sites/default/files/microsites/ostp/pcast-engage-to-excel-final\\_2-25-12.pdf](http://www.whitehouse.gov/sites/default/files/microsites/ostp/pcast-engage-to-excel-final_2-25-12.pdf).

†[www.nap.edu/openbook.php?record\\_id=13362](http://www.nap.edu/openbook.php?record_id=13362). ‡D. L. Schwartz et al., *J. Educ. Psychol.* **103**, 759 (2011).



## POLICY

## Returning Home

There have been many discussions of the importance of “returnees,” expatriates who have gained their technical education in the United States and then return to their native country. Kenney *et al.* examine the supposition that such returnees have been responsible for pioneering new industries in China, Taiwan, and India, with a focus on the information and communications technology (ICT) industry. Although each country had its own history of development, returnees were important in the expansion of domestic industries, not at the start. For example, none of the founders of the pioneering ICT companies examined in China were educated or had worked in the United States. Rather, government support and interactions with multinational companies were crucial in providing fertile ground for domestic entrepreneurs in all three regions studied. Although this analysis is focused only on one type of industry, these insights could help policy-makers in thinking about the best way to nurture industry development. For example, it may be more important to first build an environment conducive to local entrepreneurs than to invest money in enticing émigrés to return home to a system that is not yet ready to build on their contributions. — BJ

*Res. Pol.* **42**, 391 (2013).



## CLIMATE SCIENCE

## The Effects of Land-Use Change

Land-use changes around the world are affecting local and regional climate, but the exact patterns of these changes remain poorly understood. Georgescu *et al.* modeled the hydroclimatic effects of the boom in sugarcane production within



south-central Brazil, where most of the sugarcane plantations are located and where further intensification is expected. In their model, conversion from other cropland or savannah to sugarcane leads to a cooling by around 1°C at the

peak of the growing season, because sugarcane reflects more incoming sunlight than does the former land cover. Warming by ~1°C is found after harvest. Rainfall changes were more difficult to predict, but the authors suggest that a net annual drop in the transfer of water from land to atmosphere could lead to reduced rainfall. Christidis *et al.* analyzed past observations

and model results to find out whether land-use changes across the world have had an effect on temperature extremes. Trees absorb more incoming sunlight than grassland; thus, replacing trees with grasslands tends to cool the climate. The authors find that this effect of land-use change can be detected in mean and extreme warm temperatures, although the effect is much smaller than the warming caused by other human influences on the climate. These two studies suggest that land-use changes must be included in projections of future climate change. — JFU

*Geophys. Res. Lett.* **10.1002/grl.50206**;  
**10.1002/grl.50159** (2013).

## CELL BIOLOGY

## Stressful Lipids

Lipid perturbations activate the endoplasmic reticulum (ER) unfolded protein response (UPR), and UPR activity modifies cellular and organismal responses to changes in dietary lipids. The physiological ramifications of the lipid-UPR axis affect diseases of aging such as diabetes, atherosclerosis, and cirrhosis, but its molecular basis has remained obscure. It is unclear if the sensors of the UPR respond to altered membrane lipid composition

because of its indirect effects on the protein-folding environment in the ER lumen or if direct sensing of lipids contributes to UPR activation. Working in mammalian tissue culture cells, Volmer *et al.* found that the mammalian UPR sensors PERK and IRE1 lacking their luminal stress-sensing domains selectively lost the ability to respond to unfolded protein stress, but retained sensitivity to changes in membrane lipids. This sensitivity to changes in lipid composition was reconstituted in vitro in liposomes with defined acyl-chain saturation, which suggests that a UPR transducer can directly sense and respond to its lipid environment. — SMH

*Proc. Natl. Acad. Sci. U.S.A.* **110**, 10.1073/pnas.1217611110 (2013).

## CHEMISTRY

## 3D Pathfinder

As laser technology grows ever more sophisticated, chemists continue to home in on a goal of precisely controlling reactivity through the use of light. Applied photochemistry, of course, is centuries old, and it has long been possible to vary outcomes by populating different excited states via different impinging wavelengths. In the

past several decades, however, the capability of fine-tuning phase in ultrashort laser pulses has helped to enable a degree of coherent control of the light-matter interaction. Nonetheless, steering molecules (or even atoms) through a maze of different quantum pathways in real time remains a major challenge, given the complexity of the energy landscape. Li *et al.* showcase a technique to map out this landscape in particularly fine detail, in the interest of facilitating coherent control. Termed optical three-dimensional (3D) Fourier transform spectroscopy, the method builds on previously developed 2D schemes, effectively resolving all the transition energies, dipole moments, and relaxation rates associated with the system Hamiltonian within the bandwidth of the excitation source. The authors applied the method to a sample of potassium vapor as a proof of principle. — JSY

*Nat. Commun.* **4**, 1390 (2013).

## BEHAVIOR

### People Like Us

Do I, a citizen of a country, want a legally resident immigrant to enjoy the rights of citizenship? There are, of course, many characteristics of an immigrant—such as country of origin, education or professional attainment, and language fluency—that might influence my answer. Hainmueller and Hangartner assess how citizens incorporate these factors into their votes for or against individual citizenship applications. They examined 2400 naturalization referendums held over a 30-year period in 40 Swiss municipalities; voters were supplied with detailed descriptions of each applicant before secret balloting. For otherwise comparable applicants, there was a large effect of country of origin (northern and western Europe favored over Turkey), a small effect of human capital status (skilled over unskilled), and no effect of proficiency in Swiss German. They went on to calculate that statistical discrimination (group membership) accounted for almost half of the country effect, with highly skilled or educated Turkish immigrants losing out by only 7 to 8 percentage points. Further analysis of temporal trends revealed that the remaining country of origin penalty could be linked to xenophobic attitudes evoked by feelings of out-group threat, or in other words, taste-based discrimination. — GJC

*Am. Pol. Sci. Rev.* **107**, 159 (2013).

## PHYSICS

### Optical Beam-Steering

Antenna arrays have long been used for communication and sensing purposes. In the microwave and radio wavelength regime of the electromagnetic spectrum, arrays of antennas in which the phase and amplitude input to each element is varied can provide tailored beam profiles with controlled directionality. Applications can be found across many fields, from target tracking and guidance to astronomy and weather observations. Carrying over the principles of phased-array antenna technology, DeRose *et al.* have developed an optical phased array based on metallic nanoemitters patterned on a complementary metal-oxide semiconductor (CMOS)-compatible substrate. With the input to each antenna element fed in using a coupled waveguide integrated with a phase shifter, they show that electrical control of the phase results in wide-angle beam-steering capability. Operating at near-infrared wavelength, the ability to manipulate an optical beam over a two-dimensional area should find use in compact high-speed communication over free space. — ISO

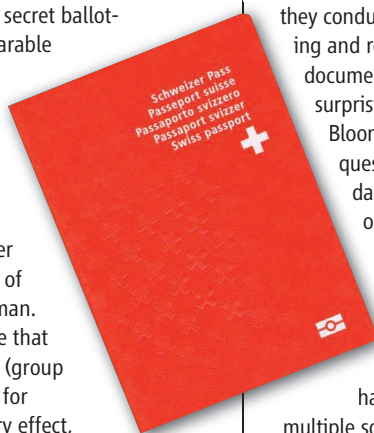
*Opt. Express* **21**, 5198 (2013).

## EDUCATION


### Testing at a Higher Level

The development of higher-order cognitive skills (HOCs) is central to recent education reform efforts, yet data indicate that few courses are able to successfully assess these skills. Lemons and Lemons performed qualitative analysis on interviews they conducted with biologists involved in writing and reviewing test questions in order to document their ideas relating to HOCs. Not surprisingly, most study participants used Bloom's taxonomy to logically analyze questions. However, 62% of categorical data relating to question design fell outside of Bloom's category and into categories labeled question difficulty, time required, student experience, and correct answers. Regrettably, some participants demonstrated an assumption that questions have one correct answer and not multiple solutions, possibly highlighting their discomfort with HOCs. Taken together, results suggest that, when asked to assess HOCs, participants did not use Bloom's taxonomy in a vacuum. Instead, they integrated their own assumptions and misconceptions regarding HOCs into the questions they wrote, suggesting that professional HOCs assessment training may be useful. — MM

*CBE Life Sci. Educ.* **12**, 47 (2013).



## AAAS Travels




### WILD INDONESIA

August 14-28, 2013

Discover the island of Flores and renowned Bali. See Komodo dragons (a monitor lizard of magnificent proportions!), coral reefs, the volcanic highlands of Flores, and the discovery site of the dwarf-humans *Homo floresiensis* that lived during the ice ages. The plants and animals of Indonesia mark a sharp transition between the Asian and Australian biogeographic realms. Enjoy a wealth of scenic, ecological, and cultural activities. \$3,790 + air.

**For a detailed brochure, please call (800) 252-4910**

All prices are per person twin share + air



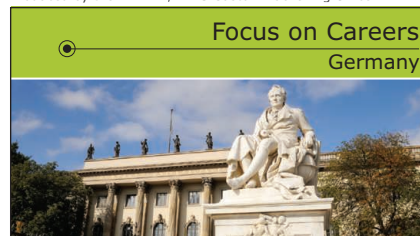
**BETCHART EXPEDITIONS Inc.**

17050 Montebello Rd, Cupertino, CA 95014

Email: [AAASInfo@betchartexpeditions.com](mailto:AAASInfo@betchartexpeditions.com)

[www.betchartexpeditions.com](http://www.betchartexpeditions.com)

Produced by the Science/AAAS Custom Publishing Office



## Focus on Careers Germany

### In the Global Competition For Smart Minds, Germany Grows Its Catch

#### In This Issue

Ever since the European Council's decision in 2000 to transform the European Union into "a competitive and dynamic knowledge-based economy," Germany's federal government has been pumping money into research and development through various mechanisms. With good long-term funding prospects and attractive salaries, Germany has become a major contender in the global competition among nations to draw in top talent.

See the full story on page 1459.

#### Upcoming Features

Cancer Research Careers:  
Academia vs. Industry—March 29

Biotech and Pharma:  
Forging Academic Collaborations—April 12

Regional Focus: Wales—April 26



1200 New York Avenue, NW  
Washington, DC 20005

Editorial: 202-326-6550, FAX 202-289-7562  
News: 202-326-6501, FAX 202-371-9227

Bateman House, 82-88 Hills Road

Cambridge, UK CB2 1LQ  
+44 (0) 1223 326500, FAX +44 (0) 1223 326501

**SUBSCRIPTION SERVICES** For change of address, missing issues, new orders and renewals, and payment questions: 866-434-AAAS (2227) or 202-326-6417, FAX 202-842-1065. Mailing addresses: AAAS, P.O. Box 96178, Washington, DC 20090-6178 or AAAS Member Services, 1200 New York Avenue, NW, Washington, DC 20005

**INSTITUTIONAL SITE LICENSES** please call 202-326-6755 for any questions or information

REPRINTS: Author Inquiries 800-635-7181

Commercial Inquiries 803-359-4578

PERMISSIONS 202-326-7074, FAX 202-682-0816

**MEMBER BENEFITS** AAAS Travels: Bethcart Expeditions 800-252-4910; Apple Store [www.store.apple.com/us/geoppstore/aaas](http://www.store.apple.com/us/geoppstore/aaas); NASA Federal, 1-888-NASA-FCU (1-888-627-2328) or [www.nasafcu.com](http://www.nasafcu.com); Cold Spring Harbor Laboratory Press Publications [www.cshlpress.com/affiliates/aaas.htm](http://www.cshlpress.com/affiliates/aaas.htm); GEICO Auto Insurance [www.geico.com/landingpage/go51.htm?logo=17624](http://www.geico.com/landingpage/go51.htm?logo=17624); Hertz 800-654-2200 CDP#343457; Office Depot <https://bsd.officedepot.com/portalLogin.do>; Seabury & Smith Life Insurance 800-424-9883; Subaru VIP Program 202-326-6417; VIP Moving Services [www.vipmymover.com/domestic/index.html](http://www.vipmymover.com/domestic/index.html); Other Benefits: AAAS Member Services 202-326-6417 or [www.aaasmember.org](http://www.aaasmember.org).

science\_editors@aaas.org (for general editorial queries)  
science\_letters@aaas.org (for queries about letters)  
science\_reviews@aaas.org (for returning manuscript reviews)  
science\_bookrevs@aaas.org (for book review queries)

Published by the American Association for the Advancement of Science (AAAS), *Science* serves its readers as a forum for the presentation and discussion of important issues related to the advancement of science, including the presentation of minority or conflicting points of view, rather than by publishing only material on which a consensus has been reached. Accordingly, all articles published in *Science*—including editorials, news and comment, and book reviews—are signed and reflect the individual views of the authors and not official points of view adopted by AAAS or the institutions with which the authors are affiliated.

AAAS was founded in 1848 and incorporated in 1874. Its mission is to advance science, engineering, and innovation throughout the world for the benefit of all people. The goals of the association are to: enhance communication among scientists, engineers, and the public; promote and defend the integrity of science and its use; strengthen support for the science and technology enterprise; provide a voice for science on societal issues; promote the responsible use of science in public policy; strengthen and diversify the science and technology workforce; foster education in science and technology for everyone; increase public engagement with science and technology; and advance international cooperation in science.

## INFORMATION FOR AUTHORS

See pages 716 and 717 of the 8 February 2013 issue or access [www.sciencemag.org/about/authors](http://www.sciencemag.org/about/authors)

## SENIOR EDITORIAL BOARD

A. Paul Alivisatos, Lawrence Berkeley Nat'l. Laboratory  
Cori Bargmann, The Rockefeller Univ.  
Ernst Fehr, Univ. of Zurich  
Erin O'Shea, Harvard Univ.  
Michael S. Turner, University of Chicago

## BOARD OF REVIEWING EDITORS

Adriano Aguzzi, Univ. Hospital Zürich  
Takuzo Aida, Univ. of Tokyo  
Lestlie Aiello, Wenner-Gren Foundation  
Sonia Altizer, Univ. of Georgia  
Sebastian Amigorena, Institut Curie  
Angelika Amon, MIT  
Karyne Anderson, Memorial Sloan-Kettering Cancer Center  
Siv G. E. Andersson, Uppsala Univ.  
Peter Andolfatto, Princeton Univ.  
Paola Ariotta, Max Planck Inst., Mainz  
John Auer, Harvard Univ.  
David Auschalom, Univ. of California Santa Barbara  
Ben Barres, Stanford Medical School  
Jordi Bascompte, Estación Biológica de Doñana, CSIC  
Facundo Batista, London Research Inst.  
Ray H. Baughman, Univ. of Texas, Dallas  
David Baum, Univ. of Wisconsin  
Mark Bear, Massachusetts Inst. of Technology  
Yasmine Belkaid, NIAID, NIH  
Philip Benfey, Duke Univ.  
Stephen J. Benkovic, Penn State Univ.  
Christophe Bernard, Aix-Marseille Univ.  
Gregory C. Berzosa, Stanford Univ.  
Gabriele Bergers, Univ. of California, San Francisco  
Peer Bork, EMBL  
Bernard Bourdon, Ecole Normale Supérieure de Lyon  
Chris Bowler, Ecole Normale Supérieure  
Ian Boyd, Univ. of St. Andrews  
Christian Büchel, Universitätsklinikum Hamburg-Eppendorf  
Joseph A. Burns, Cornell Univ.  
William P. Butz, Population Reference Bureau  
Gyorgy Buzsáki, New York Univ., School of Medicine  
Mats Carlsson, Univ. of Oslo  
Mildred Cho, Stanford Univ.  
David Clapham, Children's Hospital, Boston  
David Clary, Univ. of Oxford  
Jonathan D. Cohen, Princeton Univ.  
Robert Cook-Deegan, Duke Univ.  
James Collins, Boston Univ.  
Alan Cowman, Walter & Eliza Hall Inst.  
Robert H. Crabtree, Yale Univ.  
Wolfgang Gramer, Mediterranean Inst. of Biodiversity and Ecology  
Jeff L. Dangl, Univ. of North Carolina

Tom Daniel, Univ. of Washington  
Frans de Waal, Emory Univ.  
Stanislas Dehaene, Collège de France  
Robert Desimone, MIT  
Claude Desplan, New York Univ.  
Ap Dijksterhuis, Radboud Univ. of Nijmegen  
Dennis Discher, Univ. of Pennsylvania  
Gerald W. Dorn II, Washington Univ. School of Medicine  
Jennifer A. Doudna, Univ. of California, Berkeley  
Julian Downward, Cancer Research UK  
Bruce Dunn, Univ. of California, Los Angeles  
Christopher Dye, WHO  
David Ehrhard, Carnegie Inst. of Washington  
Tim Elston, Univ. of North Carolina at Chapel Hill  
Gerhard Ertl, Fritz-Haber-Institut, Berlin  
Barry Everitt, Univ. of Cambridge  
Paul G. Falkowski, Rutgers Univ.  
Ernst Fehr, Univ. of Zurich  
Tom Fenchel, Univ. of Copenhagen  
Michael Feuer, The George Washington Univ.  
Alain Fischer, INSERM  
Susan Flisak, Princeton Univ.  
Anne C. Ferguson-Smith, Univ. of Cambridge  
Peter Fratzl, Max Planck Inst.  
Elaine Fuchs, Rockefeller Univ.  
Wulfraim Gerstner, EPFL Lausanne  
Andrew Gewirth, Univ. of Illinois  
Karl-Heinz Glassner, TU Braunschweig  
Elizabeth Grove, Univ. of Chicago  
Kip Guy, St. Jude's Children's Research Hospital  
Taekjip Ha, Univ. of Illinois at Urbana-Champaign  
Christian Haass, Fred Hutchinson Cancer Research Center  
Steven Hahn, Fred Hutchinson Cancer Research Center  
Gregory J. Hannon, Cold Spring Harbor Lab.  
Martin Heimann, Max Planck Inst., Jena  
Yael Helariutta, Univ. of Finland  
Isaac Held, NOAA  
James A. Hendler, Rensselaer Polytechnic Inst.  
Janet G. Hering, Swiss Fed. Inst. of Aquatic Science & Technology  
Ray Hilborn, Univ. of Washington  
Michael E. Himmel, National Renewable Energy Lab.  
Kai-Uwe Hinrichs, Univ. of Bremen  
Kei Hirose, Tokyo Inst. of Technology  
David Hodell, Univ. of Cambridge  
David Hooper, UT Southwestern Medical Ctr at Dallas  
Jeffrey A. Hubbell, EPN Lausanne  
Thomas Hudson, Ontario Inst. for Cancer Research  
Ray Huey, Univ. of Washington  
Steven Jacobsen, Univ. of California, Los Angeles  
Kai Johnson, EPFL Lausanne  
Peter Jonas, Universität Freiburg  
Matt Kaebberlein, Univ. of Washington

William Kaelin Jr., Dana-Farber Cancer Inst.  
Daniel Kane, Harvard Univ.  
Daniel Kammen, Univ. of California, Berkeley  
Joel Kingsolver, Univ. of North Carolina at Chapel Hill  
Robert Kingston, Harvard Medical School  
Leonid Kolker, Harvard Medical School  
Alberto R. Kornblitt, Univ. of Buenos Aires  
Lionel Kruglyak, Princeton Univ.  
Thomas Langer, Univ. of Cologne  
Michelle A. Lazar, Univ. of Pennsylvania  
David Lazer, Harvard Univ.  
Virginia Lee, Univ. of Pennsylvania  
Otoline Leyser, Cambridge Univ.  
Marcia C. Linn, Univ. of California, Berkeley  
Jiangcui Liu, Michigan State Univ.  
Luis Liz-Marzan, CIC biomaGUNE  
Thomas Losos, Harvard Univ.  
Ke Lu, Chinese Acad. of Sciences  
Christian Lüscher, Univ. of Geneva  
Laura Machesky, CRUK Beatson Inst. for Cancer Research  
Anne Magurran, Univ. of St. Andrews  
Oscar Marin, USC & Univ. Miguel Hernández  
Charles Marshall, Univ. of California, Berkeley  
Chris Marshall, Inst. of Cancer Research  
Martin M. Matzuk, Baylor College of Medicine  
C. Robertson McClung, Dartmouth College  
Graham Medley, Univ. of Warwick  
Yasushi Miyashita, Univ. of Tokyo  
Richard Morris, Univ. of Edinburgh  
Edward Moser, Norwegian Univ. of Science and Technology  
Sean Munro, MRC Lab. of Molecular Biology  
Thomas Murray, Hastings Center  
Naoto Nagasawa, Univ. of Tokyo  
James Nelson, Stanford Univ. School of Med.  
Daniel Neumark, Univ. of California, Berkeley  
Stuart Newman, New York Medical College  
Timothy W. Nilsen, Case Western Reserve Univ.  
Pär Nordlund, Karolinska Inst.  
Helga Nowotny, European Research Advisory Board  
Luke O'Neill, Trinity College, Dublin  
Stuart Newman, New York Medical College  
N. Phuan Ong, Princeton Univ.  
Joe Orenstein, Univ. of California, Berkeley & Lawrence Berkeley National Lab.  
Harry Orr, Univ. of Minnesota  
Eduard Oswald, Univ. of Warwick  
Steve Palumbi, Stanford Univ.  
Jane Parker, Max Planck Inst. of Plant Breeding Research  
Donald R. Paul, Univ. of Texas at Austin  
P. David Pearson, Univ. of California, Berkeley  
John H. J. Petrini, Memorial Sloan-Kettering Cancer Center  
Simon Philippot, Univ. of Florida  
Joshua Plotkin, Univ. of Pennsylvania  
Philippe Poulin, CNRS

EXECUTIVE PUBLISHER **Alan I. Leshner**  
PUBLISHER **Beth Rosner**

**FULFILLMENT SYSTEMS AND OPERATIONS** ([membership@aaas.org](mailto:membership@aaas.org)); **CUSTOMER SERVICE SUPERVISOR** Pat Butler; **SPECIALISTS** LaToya Casteel, Michelle Oforidire, April Marshall; **MANAGER, DATA ENTRY** Mickie Napoleoni; **DATA ENTRY SPECIALISTS** JJ Regan, Jaimee Wise, Fiona Giblin

**BUSINESS OPERATIONS AND ADMINISTRATION** Director Deborah Rivera-Wienhold; **BUSINESS SYSTEMS AND FINANCIAL ANALYSIS** Director Randy Yi; **SYSTEMS ANALYST** Nicole Mehmedovich; **MANAGER, BUSINESS ANALYSIS** Eric Knott; **MANAGER, BUSINESS OPERATIONS** Jessica Tierney; **BUSINESS ANALYSTS** Cory Lipman, Celeste Troxler; **FINANCIAL ANALYST** Jeremy Clay; **RIGHTS AND PERMISSIONS: ADMINISTRATOR** Emilie David; **ASSOCIATE** Elizabeth Sandler; **MARKETING DIRECTOR** Ian King; **MARKETING MANAGERS** Alison Chandler, Julianne Wielga, Justin Sawyers; **MARKETING ASSOCIATES** Mary Ellen Crowley, Elizabeth Sattler, Rebecca Riffkin; **SENIOR MARKETING EXECUTIVE** Jennifer Reeves; **DIRECTOR, SITE LICENSING** Tom Ryan; **DIRECTOR, CORPORATE RELATIONS** Eileen Bernadette Moran; **SENIOR PUBLISHER RELATIONS SPECIALIST** Kiki Forsythe; **PUBLISHER RELATIONS MANAGER** Catherine Holland; **PUBLISHER RELATIONS, EASTERN REGION** Keith Layson; **PUBLISHER RELATIONS, WESTERN REGION** Ryan Rexroth; **CUSTOMER RELATIONS MANAGER** Iquo Edim; **CUSTOMER RELATIONS ANALYSTS** Simon Chong, Lana Guz; **MARKETING MANAGER** Christina Schlecht; **MARKETING ASSOCIATES** Paulina Curto, Mitchell Edmund; **ELECTRONIC MEDIA** Director Elizabeth Harman; **ASSISTANT MANAGER** Lisa Stanford; **PRODUCTION SPECIALISTS** Antoinette Hodal, Nichele Johnston, Lori Murphy, Kimberly Oster; **WEB AND NEW MEDIA: SENIOR PROJECT MANAGER** Trista Smith; **PROJECT LEADER** Luke Johnson; **COMPUTER SPECIALISTS** Walter Jones, Kai Zhang; **WEB DEVELOPER** Chris Coleman; **PROGRAM DIRECTOR, AAAS MEMBER CENTRAL** Peggy Mihelich

**DIRECTOR, GLOBAL COLLABORATION, CUSTOM PUBLICATIONS, ADVERTISING** Bill Moran

**EDITOR, CUSTOM PUBLISHING** Sean Sanders: 202-326-6430

**ASSISTANT EDITOR, CUSTOM PUBLISHING** Tianna Hicklin 202-326-6463

**ASSOCIATE DIRECTOR, COLLABORATION, CUSTOM PUBLICATIONS/CHINA/TAIWAN/KOREA/SINGAPORE** Ruolei Wu: +86-1367-101-5294

**PRODUCT** ([science\\_advertising@aaas.org](mailto:science_advertising@aaas.org)); **MIDWEST** Rick Bongiovanni: 330-405-7080, FAX 330-405-7081; **EAST COAST/E. CANADA** Laurie Faraday: 508-747-9395, FAX 617-507-8189; **WEST COAST/W. CANADA** Lynne Stickrod: 415-931-9782, FAX 415-520-6940; **UK EUROPE/ASIA** Roger Gonçalves: TEL/FAX +41 43 243 1358; **JAPAN, MAKIKO HARA**: +81 (0) 3 6802 4616, FAX +81 (0) 3 6802 4615; [ads@sciencemag.jp](mailto:ads@sciencemag.jp); **CHINA/TAIWAN** Ruolei Wu: +86 1367 1015 294 [rwu@aaas.org](mailto:rwu@aaas.org)

**WORLDWIDE ASSOCIATE DIRECTOR OF SCIENCE CAREERS** Tracy Holmes: +44 (0) 1223 326525, FAX +44 (0) 1223 326532

**CLASSIFIED** ([advertise@sciencemag.org](mailto:advertise@sciencemag.org)); **U.S./CANADA/SOUTH AMERICA** Tina Burks: 202-326-6577; **SALES ADMINISTRATOR** Marci Gallun; **EUROPE/ROW SALES** Lucy Nelson; **SALES ASSISTANT** Kelly Grace; **JAPAN** Yuri Kobayashi +81 (0)90-9110-1719; [careerads@sciencemag.jp](mailto:careerads@sciencemag.jp); **CHINA/TAIWAN** Ruolei Wu: +86 1367 1015 294 [rwu@aaas.org](mailto:rwu@aaas.org); **ADVERTISING SUPPORT MANAGER** Karen Foote: 202-326-6740; **ADVERTISING PRODUCTION OPERATIONS MANAGER** Deborah Tompkins; **SENIOR PRODUCTION SPECIALIST/GRAPHIC DESIGNER** Amy Hardcastle; **PRODUCTION SPECIALIST** Yuse Lajimimuh; **SENIOR TRAFFIC ASSOCIATE** Christine Hall; **SALES COORDINATOR** Shirley Young; **MARKETING MANAGER** Allison Pritchard; **MARKETING ASSOCIATE** Aimee Aponte

**AAAS BOARD OF DIRECTORS** RETIRING PRESIDENT, CHAIR William H. Press; PRESIDENT Phillip A. Sharp; PRESIDENT-ELECT Gerald R. Fink; TREASURER David Evans Shaw; CHIEF EXECUTIVE OFFICER Alan I. Leshner; BOARD BONNIE L. BASSLER, MAY R. BERENBAUM, CLAIRE M. FRASER, ELIZABETH LOFTUS, STEPHEN L. MAYO, RAYMOND ORBACH, SUE V. ROSSER, INDER M. VERMA



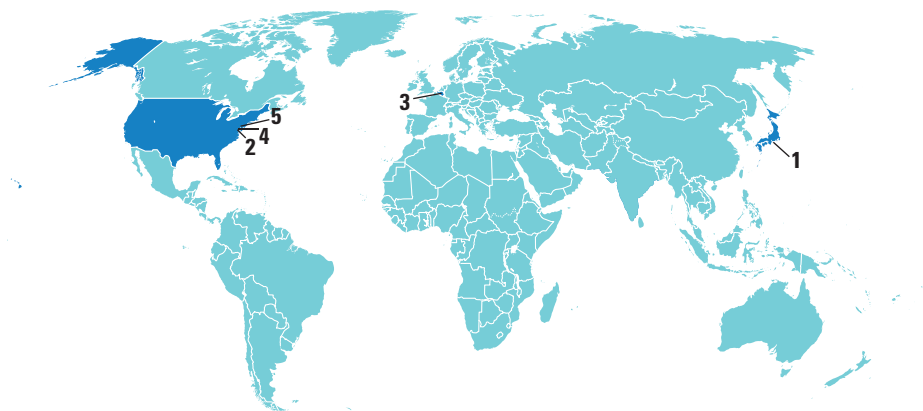
ADVANCING SCIENCE. SERVING SOCIETY

Colin Renfrew, Univ. of Cambridge  
Trevor Robbins, Univ. of Cambridge  
Jim Roberts, Fred Hutchinson Cancer Research Ctr.  
Barbara A. Romanowicz, Univ. of California, Berkeley  
Jens Rostup-Nielsen, Haldor Topsoe  
Mike Ryan, Univ. of Texas, Austin  
Shimon Sakaguchi, Kyoto Univ.  
Miguel Salmeron, Lawrence Berkeley National Lab  
Jürgen Sandkühner, Medical Univ. of Vienna  
Alexander Schier, Harvard Univ.  
Randy Seick, Univ. of Cincinnati  
Vladimir Shalagin, Penn State Univ.  
Joseph Silk, Institut d'Astrophysique de Paris  
Denis Simon, Arizona State Univ.  
Alison Smith, John Innes Centre  
Davor Solter, Inst. of Medical Biology, Singapore  
Peter Sorger, Harvard Medical School  
John Speakman, Univ. of Aberdeen  
Allan C. Spradling, Carnegie Institution of Washington  
Jonathan Sprent, Garvan Inst. of Medical Research  
Paula Stephan, Georgia State Univ. and National Bureau of Economic Research  
Elisbeth Stern, ETH Zürich  
V. S. Subrahmanian, Univ. of Maryland  
Ira Tabas, Columbia Univ.  
Yoshiko Takahashi, Kyoto University  
Shinichi Tamada, Cambridge Univ.  
John Thomas, Duke Univ.  
Herbert Virgin, Washington Univ.  
Bert Vogelstein, Johns Hopkins Univ.  
Cynthia Volkert, Univ. of Göttingen  
Bruce D. Walker, Harvard Medical School  
Douglas Wallace, Dalhousie Univ.  
Ian Walsley, Univ. of Oxford  
David A. Wardle, Swedish Univ. of Agric Sciences  
David Waxman, Fudan Univ.  
Jonathan Weissman, Univ. of California, San Francisco  
Kathy Willis, Oxford Univ.  
Ian A. Wilson, The Scripps Res. Inst.  
Timothy D. Wilson, Univ. of Virginia  
Rosemary Wyse, Johns Hopkins Univ.  
Jan Zaenen, Leiden Univ.  
Kenneth Zaret, Univ. of Penn. School of Medicine  
Jonathan Zehr, Univ. of California, Santa Cruz  
Maria Zuber, MIT

## BOOK REVIEW BOARD

John Aldrich, Duke Univ.  
David Bloom, Harvard Univ.  
Angela Creager, Princeton Univ.  
Richard Shweder, Univ. of Chicago  
Ed Wasserman, DuPont  
Lewis Wolpert, Univ. College London

## AROUND THE WORLD



Daini Atsumi Knoll, Japan 1

## Japanese Draw Methane From Sea Floor

In a world first, a Japanese group extracted natural gas from a deep-sea methane hydrate deposit. Methane hydrate, a mixture of ice and methane molecules, is found in permafrost and beneath the sea floor.

The Japan Oil, Gas and Metals National Corporation (JOGMEC) adapted oil-drilling technology and relied on *Chikyu*, Japan's deep-sea research drilling vessel, for the experimental probe at the Daini Atsumi Knoll, about 80 kilometers southeast of Atsumi Peninsula. Working in 1000-meter-deep water, the crew drilled through



*Chikyu* extracts methane hydrate.

330 meters of overlying sediment into a 60-meter-thick sandy layer containing the methane hydrate. Pumping water out of the sandy formation decreased pore pressure, allowing the gas to dissociate from the ice and flow through piping up to the ship.

JOGMEC estimates that an amount equivalent to 11 years' worth of Japan's current natural gas imports could be recovered from the test-site deposit. But environmentalists worry about leaks of methane, a greenhouse gas, and detrimental impacts on the marine environment.

JOGMEC started related R&D in 2001 and plans to continue technical development through 2018.

Washington, D.C. 2

## Yellow Light for Anthrax Vaccine Trial in Children

President Barack Obama's bioethics commission says that the U.S. government could consider testing the anthrax vaccine in children, if certain conditions are met.

Whether and how to test biodefense treatments in children is ethically challenging because such studies would expose kids to the risks of, say, a new vaccine, when they are unlikely to directly benefit. The Presidential Commission for the Study of Bioethical Issues investigated after another federal advisory board voted in favor of conducting an anthrax vaccine trial in children (*Science*, 4 November 2011, p. 577).

In a 146-page report this week, the bioethics commission says that an anthrax vaccine trial—as well as other tests of medical countermeasures in children—could “be considered” if data for young adults show that the risks are minimal for older children. The vaccine could be tested in the older group and then in progressively younger age groups. A study posing greater than minimal but still minor risk would require approval by a national ethics panel. <http://scim.ag/anthvac>

Brussels 3

## Proposed E.U. Pesticide Ban Fails to Win Support

The European Commission has failed to win over E.U. member states for restrictions on the use of neonicotinoids, widely used pesticides that have been linked to declining bee populations. The plan was scuttled in a 15 March vote that angered environmental activists.

Under the commission's January proposal, neonicotinoids would be banned



Activists urge bans on bee-killing pesticides.

from flowering crops such as corn, sunflowers, and rapeseed for 2 years starting this summer. The commission based the ban on growing evidence that neonicotinoids pose a threat to bee health, including three January reports from the European Food Safety that described the threat as an “acute risk.” Only 13 of the 27 member states supported the ban; five others, including Germany and the United Kingdom, whose votes carry more weight because of their size, abstained. The commission must now decide whether to revise the proposal or take the vote to an appeals committee.

The vote was hailed by neonicotinoid manufacturers Bayer CropScience and Syngenta, which dispute the evidence for environmental harm. “We are pleased that EU Member States did not support the European Commission's shamefully political proposal,” said Syngenta Chief Operating Officer John Atkin in a statement.

Bethesda, Maryland 4

## Hughes Gives \$22 Million To Bolster Teaching Training

The Howard Hughes Medical Institute this week gave \$22.5 million to expand a network of universities using an approach (UTeach) developed at the University of Texas to train math and science teachers.

The money goes to the Texas-based National Math and Science Initiative (NMSI), formed in 2007 to draw science and math majors into teaching. Students in the UTeach program, which began in 1997, graduate with both a science degree and a teaching certificate. That combination is designed to give them the content knowledge needed to inspire students and the pedagogical skills to be effective in the classroom.

Fueled by a \$125 million pledge from the ExxonMobil Foundation, NMSI has funded efforts at 34 universities that have agreed to replicate the UTeach model. Gaining support from HHMI, says NMSI Board of Directors Chair Tom Luce, “is a major achievement” for the initiative, which also promotes advanced placement courses in U.S. high schools.

CREDITS (TOP TO BOTTOM): ERIC VIDAL/REUTERS; THE YOMIURI SHIMBUN VIA AP IMAGES



NMSI will use the money to hold a competition to add 10 research-intensive universities to its network, which to date has trained 1150 teachers. <http://scim.ag/HHMltea>

Baltimore, Maryland 5

## Organ Recipient Contracts Rabies

A man from Maryland died in late February after being infected with rabies through a kidney transplant more than a year ago—a very unusual route of infection. The case was announced by the Maryland Department of Health and Mental Hygiene in Baltimore and the Centers for Disease Control and Prevention (CDC) in Atlanta on 15 March.

The victim received a kidney from a donor in Florida whose illness had not been identified as rabies when he died in September 2011. (Fewer than five human cases of rabies occur in the United States every year, and organ donors aren't routinely screened for the virus.) CDC says three other patients received organs from the same donor; they are now followed by medical teams and are receiving antirabies antibodies and a vaccine. In addition, close contacts of all four organ recipients are being traced because rabies can be transmitted through direct contact, although that is extremely rare.

## NEWSMAKERS

### Encryption Whizzes Win Turing Award

Two computer scientists from the Massachusetts Institute of Technology who pioneered advances in digital security have won the \$250,000 Turing Award—sometimes called



Goldwasser and Micali

the Nobel Prize for computer science—from the Association for Computing Machinery (ACM). **Shafi Goldwasser** and **Silvio Micali** will share the prize for work that became the bedrock of modern cryptography, which underlies various forms of security on the Internet. Micali and Goldwasser—who also holds a position at the Weizmann Institute of Science in Rehovot, Israel—developed



### Obama Touts Energy Research Plan at Argonne

President Barack Obama touted his proposed energy research funding plan, dubbed the Energy Security Trust, before a crowd of sequester-anxious, government-funded researchers at the Department of Energy's Argonne National Laboratory on 15 March. The plan proposes to funnel \$2 billion in revenues from the government's offshore oil leasing program into energy research and technology development over the next 10 years.

The plan drew bipartisan interest in Congress, but it has also drawn a skeptical reaction from senior Republicans on the U.S. House of Representative's Committee on Science, Space, and Technology. "The President's call today for \$2 billion in new spending for green energy programs is not the answer to the nation's energy challenges. And it adds billions more to the deficit," said Representative Lamar Smith (R-TX), the panel's chair, in a statement on 15 March. <http://scim.ag/ObamaArgonne>

the concept that the basis for encrypting information had to be computational. Their work enabled others to come up with ways to secure communications and transactions on the World Wide Web.

Micali and Goldwasser's contributions have affected pretty much everybody using the Internet. "The encryption schemes running in today's browsers meet their notions of security," ACM President Vint Cerf said in a statement announcing the prize. "The method of encrypting credit card numbers when shopping on the Internet also meets their test. We are indebted to these recipients for their innovative approaches to ensuring security in the digital age."

### Intel Top Prize to Algae Biofuel Study

To win Intel's Science Talent Search, you don't necessarily need a fancy lab; 17-year-old **Sara Volz**, of Colorado Springs, Colorado, simply turned the space under her loft bed into a lab bench. For her entry, Volz developed populations of algae cells that produce higher-than-normal levels of oil, which could potentially be used as a highly renewable and economically viable biofuel. Because growing and testing the algae

required a very specific regimen of exposure to light and darkness, Volz reworked her sleep schedule to sync up with her algae's light cycle—and her homegrown approach nabbed the top prize of \$100,000 at the 15th annual competition.



Kallenbach, Volz, and Bowman

The second place prize of \$75,000 went to **Jonah Kallenbach**, 17, of Ambler, Pennsylvania, for his bioinformatics study that predicted how proteins bind during drug therapy. And a third place prize of \$50,000 went to **Adam Bowman**, 17, of Brentwood, Tennessee, for designing and building a compact, inexpensive, low-energy pulsed plasma device that could make studies into plasma physics more feasible for researchers who lack the financial support of a premier lab. In total, about 1700 high school seniors applied to the contest, and 40 were selected as finalists.

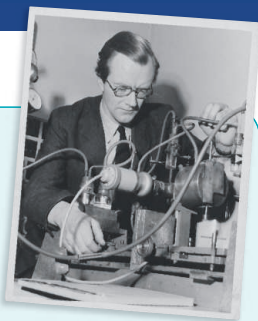
## Random Sample

## Digital Archive Marks DNA's Diamond Celebration

The discovery of DNA's structure signaled a biological revolution in which genetics moved to the forefront of the field. Now, in time for the 60th anniversary of the groundbreaking publication of that structure, the Wellcome Library in London has put together a Web site that tells the story behind this revolution.

"Codebreakers: Makers of Modern Genetics" makes available in digital form more than a million pages from letters, papers, personal notes, photographs, sketches, and essays related to James Watson and Francis Crick's 1953 *Nature* paper and the ensuing biological revolution during the 1950s and 1960s, including the eugenics movement.

Although Watson and Crick became household names, the Wellcome project drives home how others, including Rosalind Franklin and Maurice Wilkins (pictured), laid the groundwork for their discovery. Bringing together 20 smaller collections, the \$5.88 million project plans has digitized 650 related books and plans to add another 500,000 pages in the next few months. It includes letters that reveal the scientists "as humans rather than abstract figures," says Simon Chaplin, head of the Wellcome Library. Read their stories at <http://wellcomelibrary.org/using-the-library/subject-guides/genetics/makers-of-modern-genetics>.



spin and parity, a symmetry property. Measurements now show that the new particle has zero spin and positive parity, exactly what physicists' standard model of particles and forces predicts for the Higgs. "It sure does look like the standard model Higgs boson, you bet," says Sally Dawson, a theorist at Brookhaven National Laboratory in Upton, New York.

Physicists hope that the LHC will produce something beyond the standard model's cast of particles. Some theories predict that other Higgs bosons lurk over the energy horizon. That's why CERN officials now call the new particle "a Higgs boson" and not "the Higgs boson." Searching for other Higgses will take time: The LHC has shut down for repairs and won't take data again until 2015.

## &gt;&gt;NEWSMAKERS

## Soil Scientist Wins Tyler Prize



The fate of nematodes in Antarctica may not seem compelling. But in her studies of these and other soil creatures, **Diana Wall**, of Colorado State University, Fort Collins, has found

that climate change can fundamentally alter the ecology of soils, with a profound effect on how soil stores carbon. For her work, including 17 seasons studying the hardy nematodes of Antarctica's Dry Valleys, Wall has earned the 2013 Tyler Prize for Environmental Achievement. The award, which has previously recognized primatologist Jane Goodall and biologist Edward O. Wilson, comes with a \$200,000 cash prize and a gold medal.

Wall and her team of "worm herders" are still working in the Dry Valleys, studying how the nematode *Scottinema lindsayae*—the "Rocky Balboa of nematodes"—responds to wetter and warmer soil conditions. With so few species in this polar desert environment, she says, it's possible to study interactions at a species level and how population distributions alter with changing climate.

## Brain Prize Goes to Optogenetics

Originally a cell biologist, neuroscientist **Gero Miesenböck** says that his route to winning the world's largest brain research prize was "tortuous."

"It took me a while to find my niche," he says. He appears to have found it: On Monday, 11 March, the Grete Lundbeck European Brain Research Foundation announced that Miesenböck, along with five other researchers including **Ernst Bamberg**, **Peter Hegemann**, **Georg Nagel**, **Ed Boyden**, and **Karl Deisseroth**, will share €1 million for fundamental research into optogenetics, a technology that allows scientists to control the brain's activity by genetically engineering neurons to fire in response to light.



(*Science* named optogenetics an Insight of the Decade in 2010.) Since Miesenböck first demonstrated the proof-of-concept in fruit flies in 2002, hundreds of labs have begun to use the technique to manipulate brain activity in experimental animals, exploring the neurobiology underlying behaviors like decision-making as well as diseases such as Alzheimer's disease, epilepsy, schizophrenia, and addiction.

## FINDINGS

## Call a Higgs a Higgs

The "Higgs-like particle" that physicists discovered last summer has the right characteristics to be a genuine Higgs boson. So say experimenters working with the Large Hadron Collider (LHC) at the European particle physics laboratory, CERN, near Geneva, Switzerland.

A particle's characteristics include its



## Sobering Long-Term Results For Malaria Vaccine

There is more cautionary news for the world's only malaria vaccine that has reached phase III trials. The vaccine, called RTS,S, showed promising initial results, but recent data have injected caution, as the vaccine failed to protect young babies as much as hoped (*Science*, 16 November 2012, p. 871).

Now, data from a 4-year follow-up study of 223 children in Kenya who received the vaccine as part of an earlier phase II trial show that the vaccine's protection wanes over time, dropping to near zero after 4 years. Still, because African children have malaria so often, 65 cases of malaria were prevented for every 100 children vaccinated. The results, published in the 21 March issue of *The New England Journal of Medicine*, suggest that decisions about using the potentially expensive vaccine will be complex, says Philip Bejon of the University of Oxford in the United Kingdom, who helped lead the study. <http://scim.ag/malvacc>

## Science LIVE

Join us on Thursday, 28 March, at 3 p.m. EDT for a live chat on whether conservation strategies are working. <http://scim.ag/science-live>





NEUROSCIENCE

## NFL Kicks Off Brain Injury Research Effort

When a retired National Football League (NFL) player with signs of progressive cognitive decline came to see neuropsychologist Samuel Gandy at Mount Sinai School of Medicine in New York last year, it was clear from the athlete's history of multiple concussions that his brain had taken a beating. During the athlete's 10-year career, Gandy says, "routinely, by halftime, he didn't know what end of the field he was on."

Gandy and four other Mount Sinai brain specialists evaluated the former athlete, but they couldn't agree on a diagnosis. Three thought he had Alzheimer's disease, while the remaining two suspected chronic traumatic encephalopathy (CTE)—a neurodegenerative disease associated with concussions, also known as mild traumatic brain injury (mTBI). Ultimately, the medical team ruled out Alzheimer's with a newly approved PET imaging technique that detects the disease's characteristic clusters of amyloid protein in the brain. However, there's no way to identify CTE in the brain of a living person.

On 11 March, the NFL announced a major new research effort, the Head Health Initiative, aimed at changing that state of affairs. Along with General Electric, which develops MRI machines, and the sports gear company Under Armour, the league is investing \$60 million in a 4-year program on mTBI, focusing on improving diagnostic accuracy with better imaging tools. The move came a few days after scientists and physicians studying such brain injuries gathered just outside Washington, D.C., to discuss their latest results and plot a research strategy for the future of the rapidly growing field.

Underscoring the threat to the NFL's

future, the new initiative isn't the league's first gesture addressing the potential high mental cost that many of its players may face. Last year, in the wake of several suicides by football players diagnosed with CTE through autopsies, as well as a class action lawsuit filed by former athletes and their families, the NFL donated \$30 million to the U.S. National Institutes of Health (NIH) for research into sports-related head injuries. Although NIH has yet to approve proposals for using that money, roughly \$10 million will likely go toward CTE research and \$2 million toward sports-related brain and spinal cord injury, says Walter Koroshetz, deputy director of the National Institute of Neurological Disorders and Stroke and one of the participants in the new initiative.

Much of the damage that occurs when an NFL player gets violently hit can't be seen on a traditional CT or MRI scan, Koroshetz says. As a result, clinicians are left with often-murky behavioral and cognitive symptoms to judge whether an athlete can safely play again. At the TBI workshop, Martha Shenton of Harvard Medical School in Boston described a range of sophisticated new MRI techniques, such as diffusion tensor imaging, that can reveal the microscopic damage to axons and minute areas of bleeding, swelling, and brain lesions characteristic of mTBI. Shenton says her lab plans to apply for money from the new initiative—\$20 million of which will be awarded competitively to researchers with ideas for new ways to diagnose concussions or mTBI and gauge their prognosis. "We're chomping at the bit," she says.

Some of that money will also help researchers investigate how concussions lead

**Game daze.** NFL quarterback Robert Griffin III suffered a cut cheek and concussion after a hit to the head.

to long-lasting brain damage and whether certain people are more susceptible. In addition to changes in the brain's white and gray matter, mTBI and CTE are characterized by tangles of a protein called tau that build up inside nerve cells. (Something similar happens in Alzheimer's disease.) Because no method of imaging tau in vivo has been approved for clinical use, researchers and clinicians must wait until patients die to see if their brains have tau tangles. However, a new tau-binding compound developed by Siemens and visible in PET scans may soon enable tracking tau clusters in the living brain, Gandy says.

The biggest infusion of new cash will go to a \$40 million multicenter search for additional imaging biomarkers for concussion and CTE. Not all researchers are thrilled with the emphasis. "I have concerns that the majority of money is going toward diagnosis and not enough toward treatment," says Kim Heidenreich, a pharmacologist at the University of Colorado, Denver. Heidenreich is studying a drug used for asthma that, in mice, can reduce the initial swelling of the brain after trauma, preventing a cascade of neurochemical responses that can lead to cell death. So far, she hasn't been able to get funding from NIH to advance her research to human trials.

That's a common story, explained Andrew Maas, director of neurosurgery at the University of Antwerp, at the TBI conference. Despite decades of studies funded by NIH, which estimates that it spends roughly \$80 million per year overall on TBI research, no drug to treat or prevent damage from TBI has progressed past animal studies to clinical use.

The U.S. Department of Defense has already devoted between \$700 million and \$800 million to TBI research, amid signs that soldiers harmed by explosives in Iraq and other countries also suffer CTE (*Science*, 29 July 2011, p. 517). One thing is clear, says Col. Dallas Hack, a physician at the U.S. Army Medical Research and Materiel Command in Fort Detrick, Maryland, and one of those who will judge how to spend the newly pledged \$60 million: It will take "many times" the amount of money and time in the Head Health Initiative to address the issue. "Understanding and molding the brain's response to injury is the most complex scientific endeavor ever," he says. "We need as many people as possible working on this problem."

—EMILY UNDERWOOD

CREDIT: AP PHOTO/RICHARD LIPSKI

## SCIENCE COMMUNITY

# Austrian Academy of Sciences Faces Its Nazi History

**VIENNA**—After the end of World War II, the Austrian Academy of Sciences officially suspended members who had joined the Nazi Party—but it quickly reinstated nearly every one. That was true even when the member was implicated enough to be kept out of the university, and even, in one case, when the person had been an officer in the notorious SS.

This decision had lasting effects on the academy, according to an academy-sponsored poster exhibit and a hefty exhibit catalog released to coincide with the 75th anniversary of the “Anschluss,” the annexation of Austria to Germany in March 1938.

One effect is that some of these members were given the chance to write the official history in their favor or to suppress it. Indeed, the exhibit is the academy’s first extended examination of its actions during the Nazi period, and many decried the long delay during an 11 March symposium that opened the exhibit.

“It’s lamentably late,” said Gary B. Cohen, a historian at the University of Minnesota, Twin Cities, who served as a moderator and panelist at the symposium. But, he added, “in some senses it’s never too late. The issues need to be faced.”

The first opportunity to tell the history of the war period came as early as 1947, the 100-year anniversary of the academy. “It was a kind of whitewashing,” said historian Heidemarie Uhl of the Austrian Academy of Sciences. During the war, the Nazis had chosen historian Richard Meister—an academy member, but not a Nazi Party member—to write an anniversary history, which he finished after the war ended. In it, he declared that “the work of the academy was not infected by the Nazi period,” Uhl said. That assertion was in line with a growing cultural consensus, which still persists in some sectors of Austrian society, that Austria was a victim of Nazi Germany instead of a collaborator.

Research by historian Johannes Feichtinger, also of the academy, contradicts

Meister’s claim. Among other projects, the academy funded racial research on prisoners of war in Austrian camps. Scientists took measurements and photographs of people, including “North Africans,” “negroes,” and “Jews,” with the goal of gaining “insights into the racial composition of the peoples of western Europe,” according to historical documents. The academy also began publishing its own series on racial theory and human genetics that intended to determine the extent to which the character of an ethnic minority was biologically determined.

(Only one volume in the series was published.) And the academy’s Institute for Radium Research turned from basic

was elected secretary general, and in 1967 the academy awarded him the Bene Merito medal of honor of his service. “I can’t understand why they did this,” said the academy’s vice president, historian Arnold Suppan, who worked on the exhibit.

The first official history that attempted an honest accounting didn’t come until 1997, the academy’s 150th anniversary. Historian Herbert Matis, who also contributed to the exhibit, wrote a 67-page booklet that was the “first step” in coming to terms with the past, Uhl said.

Six years ago, with a grant from the City of Vienna, Uhl and Feichtinger began a follow-up to Matis’s research, focusing on the period immediately after the war. With the support of

the academy, they decided to pull together all the research into “a comprehensive overview” of the war and postwar period to coincide with the anniversary of the Anschluss, Feichtinger said. The result is a 274-page exhibit catalog, which will also be released in English.

The academy may have been particularly hostile to Jews and nonconformists even before the Nazis arrived, said historian Mitchell Ash of the University of Vienna at the symposium. After the Anschluss, only 9% of the regular members were forced out on “racial” or political grounds, while

nearly half of the university’s faculty members were dismissed. That means membership was “not entirely based on meritocratic, but also on folkish and anti-Semitic criteria,” even before the Nazi ideology took over, Ash said.

Symposium participants expressed hopes that the academy would continue to publicly address the history. An exhibit about one of the academy’s Jewish-run institutes is planned for next year. Knoll may be stripped posthumously of the Bene Merito medal, and one symposium speaker made a well-received suggestion that the academy reinstate a medal named after Jewish pharmacologist Hans Horst Meyer, which was discontinued by the Nazis.

—CHELSEA WALD



**Swastika armbands and seal.** At the time of this 1939 meeting of the Austrian Academy of Sciences, leaders were in the process of forcing out Jewish members and political objectors.

to applied research, as the Nazis were eager for nuclear power.

Later, in the 1950s, botanist Fritz Knoll edited two academy-sponsored volumes about famous Austrian scientists, doctors, and engineers. During the war, as the Nazi Party representative to the academy, he had overseen the dismissal of Jews from the academy’s institutes. In the volumes, he omitted researchers whose distinguished careers he had ended. One of them, zoologist Hans Przibram, died in the Theresienstadt concentration camp.

Research by Klaus Taschwer, a newspaper science editor who contributed to the exhibit, reveals that Knoll had an extensive career as a Nazi. But the academy ignored his Nazi activities after the war. In 1959 he





**Change of heart.** EMA, headquartered in London, embarked on a radically new transparency policy after a reprimand from the European Ombudsman.

hopes that the Food and Drug Administration (FDA), EMA's U.S. counterpart, will follow the European example. "We should focus on getting the EMA [rules] right first. But I'm also excited by the possibility to move further," she says.

Proponents of full access to clinical trial data say that independent researchers must be able to examine the risks and benefits of medicines and balance the industry's power to assess its own products in clinical studies. They find support in the Declaration of Helsinki, a set of ethical principles for clinical trials last revised in 2008, which states that "[a]uthors have a duty to make publicly available the results of their research on human subjects and are accountable for the completeness and accuracy of their reports."

The reality is different. Companies must share their data with regulatory agencies such

as EMA or FDA, but they aren't obliged to publish them in a journal—and some negative trials never see the light of day. (Moreover, there can be discrepancies between CSRs and published papers, say researchers from the Cochrane Collaboration, an international group of scientists carrying out medical reviews in a bid to provide unbiased, evidence-based clinical advice.)

In the United States, clinical trials must be registered on a federally funded Web site called ClinicalTrials.gov, and basic results must be posted within a year after completion. But this doesn't include full CSRs or patient-level data, and compliance has been low so far. Researchers seeking a grant of more than \$500,000 in a year from the U.S. National Institutes of Health are expected to share clinical data. "But there's no single place [to do so], no single format, no oversight, so it's a hit or miss," Dickersin says.

There is increasing pressure to change that, especially in Europe. In recent years, academics, nongovernmental organizations, and members of the European Parliament have slammed EMA, set up in 1995 to harmonize drug approval systems in the European Union, for lacking transparency.

## EUROPE

# Drug Watchdog Ponders How to Open Clinical Trial Data Vault

**BRUSSELS**—In the summer of 2007, Peter Gøtzsche, director of the Nordic Cochrane Centre in Copenhagen, sent the European Medicines Agency (EMA) a simple request: He wanted the London-based watchdog to give him detailed information about 15 placebo-controlled trials of two antiobesity drugs in its possession. Weight-loss drugs are controversial because of their side effects, and several had been pulled from the market; Gøtzsche wanted to see for himself what exactly the trials for the two EMA-approved drugs had shown.

Few could have predicted that Gøtzsche's demand would set in motion a process that will have far-reaching consequences for drug companies, researchers, and patients in Europe. EMA initially turned down the request, arguing that making the data public could hurt the commercial interests of the manufacturers—a decision that Gøtzsche appealed to the European Ombudsman. He obtained a resounding victory in 2010, when the ombudsman accused EMA of "maladministration" and urged it to release the studies. Gøtzsche finally received the reports in early 2011, and EMA pledged to become more transparent.

Now, the agency is making good on that promise in an unprecedented way. By January 2014, it plans to introduce a broad new policy of public access to clinical trial data that may include access to clinical study reports (CSRs), company-written documents often numbering thousands of pages with detailed information about study design, efficacy and safety analysis, as well as patient data listings.

Such sweeping glasnost doesn't appeal to the pharmaceutical industry, which is concerned that disclosing CSRs could open sensitive data to potential competitors. It also says that nonexperts sifting through mountains of data could cause health scares. Others, meanwhile, worry that without stringent safeguards, sensitive data about individual patients could end up in the wrong hands. EMA is discussing how to shape the new policy with academics, patient organizations, and drug companies; their final advice is due by the end of next month.

The debate is watched with great interest elsewhere in the world. Kay Dickersin, director of the Center for Clinical Trials at the Johns Hopkins Bloomberg School of Public Health in Baltimore, Maryland,



An international campaign called the All-Trials initiative is urging regulators and research organizations to publish full CSRs from all trials—past, present, and future—on all medical treatments now in use. Release of trial data has also become one of the most controversial issues in ongoing debates over the European Union's unloved 2001 clinical trials legislation (*Science*, 1 March, p. 1024).

After its slap on the wrist by the ombudsman, EMA stopped treating clinical trials data as secret by default. Between November 2010 and 2012, the agency released about 1.6 million pages of clinical data in response to requests. (Among the first to benefit was a Cochrane research group engaged in a high-profile battle to obtain clinical data on oseltamivir, a drug stockpiled by many countries to fight flu pandemics.) But this “reactive” approach is time-consuming both for requesters and for EMA, says Hans-Georg Eichler, senior medical officer at EMA; now, the agency will make it more systematic.

A few drug companies have climbed on the openness bandwagon. U.K. drug firm Glaxo-SmithKline has signed the All-Trials petition and promised to share its trial data, a decision that pro-access campaigners hail as historic. But many other companies are less enthusiastic. In January, for instance, U.S. drug company AbbVie sued EMA for divulging data on its rheumatoid arthritis medicine Humira to competitors, including Belgian firm UCB.

“The industry is absolutely open to releasing a lot more information,” says Richard Bergström, director-general of the European Federation of Pharmaceutical Industries and Associations (EFPIA) here. But its concerns about confidentiality are legitimate, Bergström says: Out of 457 requests for data EMA received between November 2010 and 2012, only 38 came from academics, whereas a majority came from drug companies, lawyers, and consultants.

Protecting sensitive patient information is another hotly debated issue. For example, patients taking part in a trial would not want their neighbors to find out if they suffered from depression or how much alcohol they drink, says Mike Clarke, director of the All-Ireland Hub for Trials Methodology

Research at Queen's University Belfast in the United Kingdom.

The crux of these debates is how much transparency is enough. At the most open end of the spectrum, all trial data could be downloaded from the Internet by anyone. That option appeals to Ilaria Passarani, a senior health policy officer at the European Consumers' Organisation here. Broad disclosure would allow the public to regain trust in regulators after recent European drug scandals, she says. Data would be anonymized so that it's difficult to trace back to



**Opening up.** Advocates say data for all clinical trials—such as this test of a drug against lung disease in healthy volunteers—should be publicly available.

individuals. Passarani concedes that there is a “remote” possibility that patients suffering from rare diseases might be identified, but her agency, usually hawkish on privacy, believes that the potential public health benefits outweigh any risk.

At the other end of the spectrum, data would be made available only to bona fide researchers—an option preferred by many in the pharmaceutical industry, which considers itself the data's owner. EFPIA's Bergström suggests that researchers who want access should explain their objective and sign a confidentiality agreement stating that they won't use the information for commercial purposes.

A dual system somewhere between these two options is probably the best idea, Clarke suggests. For instance, some data stripped of any identifying information could be posted on the Internet for all to see, while richer data sets would be made available to only legitimate researchers who provide a reasonable scientific plan—even if they are competitors of the drug-maker. As a researcher, “I want as much information as possible. For instance, if it's a young child, I may need his or her age in days,” Clarke says. Such detailed information, which could violate patient privacy, is less relevant to a broader audience.

There are other dilemmas as well. Scientist-only access would require a gatekeeper. Observers point out that EMA may not be sufficiently independent to judge the legitimacy of data requests, as a reanalysis may contradict its official assessment of a drug's risks and benefits. “There should be a mix of academics, nonacademics, and regulators [assessing data requests], and all decisions should be transparent, publicly logged, and accountable,” Clarke says.

Dickersin proposes a different option, in which clinical data could be checked out of a repository, with users providing their name and a short abstract about what they want to do with the data. “You need money for the repository to be indexed and curated, but no one should claim ownership” of the data, Dickersin says. ClinicalTrials.gov provides a model of good curation, Dickersin says, with a template that makes submitting useful data easy for companies and scientists.

Whichever option EMA settles on, the rest of the world will be watching. An FDA spokesperson tells *Science* in an e-mail that the agency is “following with interest” the changes in Europe, but remains cautious when asked if it may emulate EMA's move. “We operate under different legal requirements than the EMA and will continue to provide data as legally permitted,” the spokesperson writes.

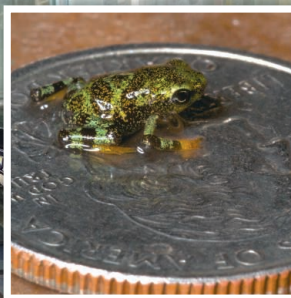
“I'm hopeful that we will have something [in Europe] that the world will want to copy,” Clarke says. “Good trials are so valuable, and we're not using their full value.”

—TANIA RABESANDRATANA

Tania Rabesandratana is a writer in Brussels.

CREDIT: ANTONIA REEVE/SCIENCE SOURCE





## CONSERVATION BIOLOGY

## A Rescue Mission for Amphibians At the Brink of Extinction

**GAMBOA, PANAMA**—Brian Gratwicke reaches into a terrarium with a gloved hand and gently nudges a tiny froglet onto a U.S. quarter. Smaller than George Washington's head, the 5-day-old *Limosa harlequin* frog, its slick skin sporting green and black chevrons, squats calmly as Gratwicke snaps photos. The little tyke is a celebrity. When Gratwicke, a conservation biologist at the Smithsonian Conservation Biology Institute in Washington, D.C., and his team first captured a few of the endangered toads in 2009, he says: "We couldn't keep them alive for even 2 days." The toads had been taken in jungle in central Panama thought to be free of chytrid fungus, which has been mowing down amphibians worldwide. But the captives had been infected in the wild and succumbed in Gamboa. The team found healthy individuals on subsequent forays.

"We came this close to losing the species," Gratwicke says, holding his thumb and index finger a hair's width apart.

Whether the story has a happy ending will depend largely on a facility set to open next month in this town established a century ago to house Panama Canal workers. The Smithsonian is at work on an amphibian research laboratory: seven refrigerated shipping containers, donated by Maersk Line, filled with glass terrariums, reptile UV lights, and souped-up environmental controls. The "rescue pods" will offer a sanctuary for colonies of embattled species now kept at nearby

Summit Botanical Gardens and at El Valle Amphibian Conservation Center.

Only a tiny fraction of the planet's approximately 7100 amphibian species would be candidates for such life support, notes David Wake, a biologist at University of California, Berkeley. "There is a feeling of helplessness in the community of amphibian biologists as we witness declines in one species after another," says Wake, who spent a sabbatical here 15 years ago. "At least these good people are trying to do something!"

As candidates line up for the amphibian ark, scientists have taken a step toward bringing one frog species back from extinction. Last week, at a TEDx symposium in Washington, D.C., sponsored by The Long Now Foundation, paleontologist Michael Archer of the University of New South Wales in Sydney, Australia, revealed that his

team has produced embryos from lab tissue of gastric brooding frogs—two species that went extinct in the 1980s. Discovered in Queensland, Australia, in 1972, the frogs were the only known creature able to transform one organ into another. After laying eggs, the females converted their stomach into a womb, swallowed the eggs, brooded tadpoles, and gave birth to froglets through the mouth. "When biologists saw this, they were agog," Archer says. Then, "just as everybody got excited, bang! It was extinct." Another gastric brooder species winked out in 1985 soon after discovery.



**Froggy chow.** Brian Gratwicke cradles zoo-reared crickets—food for hungry amphibians.

**Amphibian ark.** The Smithsonian is readying rescue pods for endangered amphibians in Panama, such as this *Limosa harlequin* frog (*inset*).

Archer has an abiding interest in species resurrection. In the late 1990s, he set out to revive the thylacine, an extinct hyenalike marsupial. While that effort has sputtered, his "Lazarus Project," launched 5 years ago to raise gastric brooders, is making headway. Archer's team recovered cell nuclei from frog tissue frozen in the 1970s and used somatic cell nuclear transfer to insert nuclei into eggs from the great barred frog. After "hundreds and hundreds" of failures—"It was much more difficult than we thought," Archer says—in 2011 they produced blastocysts with gastric brooder DNA, then last month hardier blastocysts that survived a few days. "We're trying to learn what is stopping development of blastocysts."

Gratwicke and his colleagues hope that staving off extinctions will make such heroics unnecessary. Chytrid has hammered about a quarter of Panama's 200 amphibian species. Most frogs at Summit come from Darién, the province nearest Colombia and the last neotropical bulwark against chytrid before the fungus's arrival there 3 years ago. Scientists have been dashing into Darién to rescue frogs from disease-free pockets and moving them to shelters, though lately another scourge—FARC rebels and drug traffickers—has made fieldwork perilous.

Here in Gamboa, containers are being fitted with air conditioners, water systems, and a backup generator. "We don't want to see the last of a species cooked in a metal box," Gratwicke says. The project's next phase includes a lab building for devising vaccines or probiotic treatments against chytrid and tinkering with breeding techniques for species like the La Loma tree frog that fare poorly in captivity. Visiting researchers are welcome. "This is a glimpse of the evolving role of zoos," says Smithsonian National Zoo Director Dennis Kelly, who visited the facility earlier this month. Smithsonian is working with Cheyenne Mountain Zoo, Houston Zoo, and Zoo New England on the project.

The hope is that the Gamboa ark will be a temporary limbo. First in line for a science-assisted comeback is the Panamanian golden frog. Locals believe that it brings good fortune to those who see it. That would be a miracle in the wild, where the toad was last spotted in 2008. But it's multiplying in captivity, and scientists are contemplating a reintroduction plan. Success may depend on a daunting prerequisite: bringing chytrid to heel.

—RICHARD STONE

CREDITS (TOP TO BOTTOM): BRIAN GRATWICKE (2); R. STONE/SCIENCE



**Prepared?** The White House science council says the nation needs to do more to prepare for disasters, such as last year's drought and Superstorm Sandy (left), that could come in a warmer world.

## CLIMATE POLICY

## A More Modest Climate Agenda for Obama's Second Term?

When it comes to tackling climate change, President Barack Obama once had grand ambitions, including forging a global deal on reducing greenhouse gas emissions and persuading Congress to enact legislation that would impose fees on U.S. carbon pollution. With those hopes dashed by political realities, however, the president's science advisers last week proposed some potentially more doable climate actions that Obama could take during his second term. But some climate scientists say that the proposals, while laudable, fall short of what's needed.

The 10-page report approved on 15 March by the President's Council of Advisors on Science and Technology (PCAST) outlines a range of steps that Obama could take, most without requiring new legislation, to address the causes and consequences of global warming. To curb U.S. emissions, for instance, PCAST says Obama should extend recently developed regulations that cover emissions from new power plants that burn fossil fuels to the much larger number of existing plants. It also suggests that the administration consider negotiating a regional pact on greenhouse gas emissions with the country's North American neighbors, Canada and Mexico. And it urges Obama to appoint a new national commission on "climate preparedness" that would recommend ways to improve the government's planning for droughts, floods, and other natural disasters that could be spurred by climate change.

The president has read a draft of the report, says PCAST member Daniel Schrag, a geochemist and an energy specialist at Harvard University, and "was broadly supportive, mostly, of what we were doing."

Conspicuously absent from PCAST's list, however, are the big climate agenda items from Obama's first term, including setting a price on carbon and negotiating a global pact. In large part, the omissions reflect PCAST's interest in focusing on things that Obama

"could push for and achieve," Schrag says. "A price on carbon would be great, but we don't expect it to happen politically" because of opposition in Congress.

That approach isn't sitting well with some researchers. "It is not PCAST's job to do Obama's political strategizing for him," says climate modeler Raymond Pierrehumbert of the University of Chicago in Illinois. "I believe that PCAST should have emphasized the importance of implementing a price on carbon." It is "one thing to be realistic about what legislation you can pass this year," adds geochemist Ken Caldeira of the Carnegie Institution for Science in Stanford, California. "It is another thing entirely not to be realistic about the scale of energy transition our nation must undertake if we are to make a substantial dent in climate risk."

Other critics note that the report is silent on whether the White House should approve the controversial Keystone XL oil pipeline from Canada, which opponents say would promote unwise energy development. Eighteen scientists, led by NASA climatologist James Hansen, urged the president earlier this year to stop the project, saying it runs counter to "national and planetary interests."

Instead of wading into such "largely political" issues, PCAST emphasized a topic that often gets short shrift in policy discussions, Schrag says: the need "to prepare the country for the impacts of climate change." The proposed preparedness commission, he says, could help lay the ground work for changing "federal policies on disaster relief and insurance ... [so] that financial capital, when invested following a disaster, is used not just to rebuild, but to rebuild better." Homes could be moved out of coastal areas that are likely to be flooded again by rising seas, for example, and farming areas could be better prepared for droughts. The United States has "too many programs that essentially provide economic incentives for people to live in harm's way," Schrag told PCAST at a briefing.

Efforts to adapt to climate change "will ultimately be overwhelmed," however, unless the government moves to curb, or mitigate, carbon emissions, PCAST notes. That's why the report also encourages Obama to support more drilling for natural gas, which produces fewer carbon emissions than oil or coal. And it urges the expansion of tax credits for developing renewable energy sources, such as wind and solar power.

Although the administration can take action independently on some of PCAST's ideas—such as regulating power plants or supporting expanded drilling—it will need cooperation from a sometimes hostile Congress for others, such as retooling the tax code. But energy expert Robert Socolow of Princeton University says PCAST's emphasis on "adaptation first and mitigation second" could help reframe public discussion about such policies. There is a large "overlap of climate threats and threats we already deal with," such as floods and droughts, he notes. Linking the two could "reduce resistance" to discussing climate policy, Socolow says, and reopen a "completely muffled" national conversation.

Obama could also leverage action at the state level during his second term, adds former Obama adviser Joseph Aldy, now at Harvard University. This year, the nation's first comprehensive emissions trading system began operating in California, while an existing nine-state pact in the Northeast, the Regional Greenhouse Gas Initiative, is mulling stricter limits for existing plants. If federal officials could link such systems piece by piece, Aldy says, it could open the door to the broader type of emissions trading system that Obama was unable to get through Congress during his first term. And that step, he says, could help Obama meet his first-term goal of cutting U.S. carbon emissions by 17% from 2005 levels by 2020—an aspiration rarely mentioned these days by the president or his advisers.

—ELI KINTISCH

CREDITS (LEFT TO RIGHT): STAN HONDA/AFP/GETTY IMAGES/NEWS.COM; JEFF TUTTLE/REUTERS/NEWS.COM



## PLANETARY SCIENCE

# Life Could Have Thrived on Mars, but Did It? Curiosity Still Has No Clue

With its first sample of martian rock, the Curiosity rover has achieved the primary objective of its \$2.5 billion mission. For the first time, Mars scientists have shown that, at least in one place and time on ancient Mars, life as we know it could have survived. Curiosity has shown that all the essential ingredients were there for a habitable environment: prolonged benign wetness, the essential building blocks of life, and an energy source.

As to ancient martian life itself—the focus of public interest since Curiosity's harrowing landing last August—the news has been another letdown. Curiosity's first drill sample produced a trace of organic compounds, but the whole issue of organic remains lingering from ancient martian life has been muddled by contamination inside Curiosity from organics intentionally brought from Earth. And team members announced this week that atmospheric methane—which any present-day life could be producing—has still not made a certain appearance.

Confirmation of a habitable environment came as a pleasant surprise to Curiosity scientists. They had sent the rover a few hundred meters from its landing site on the floor of Gale crater to investigate a geologically intriguing intersection of three different-looking terrains mapped from orbit. There had been no sign of lake sediments—an ideal target for Curiosity—or of the clay and sulfur minerals that signify minerals' interaction with water. Mainly, Curiosity's first destination was an opportunity to test out its armamentarium of analytical instruments on the first rock sample drilled out of the martian subsurface.

But at the drill site, Curiosity found everything life would have needed. Visual inspection showed fine-grained sediments that could well have been the bottom mud of a crater lake several billion years ago. The rover's chemistry and mineralogy (CheMin) x-ray instrument showed that the drilled rock is 20% to 30% clay, team members reported at a NASA press conference last week. That means rock was not just briefly wet but wet for many millennia if not millions of years.

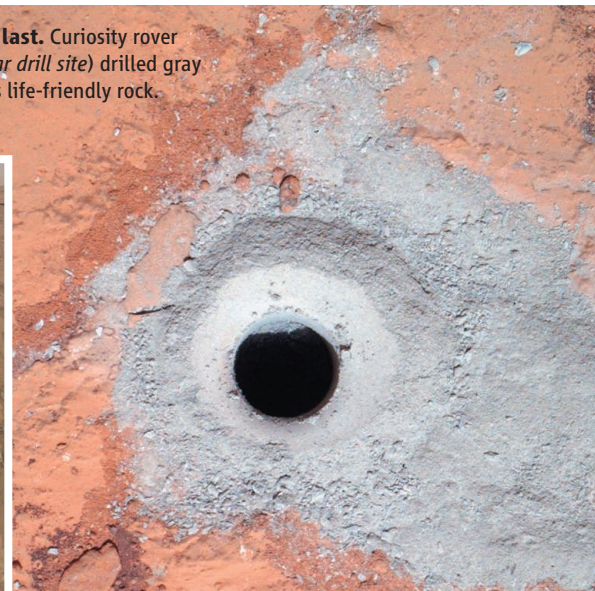
And the water that turned rock to clay would have been friendly to life. CheMin and the Sample Analysis at Mars (SAM) instrument package found no mineralogical or chemical signs of ancient environmental conditions inimical to life like those the Oppor-

tunity rover has encountered at Meridiani Planum. There, highly acidic brines had long ago rotted the rock.

SAM did find the essential ingredients in the recipe for life, including the elements carbon, hydrogen, oxygen, phosphorus, nitrogen, and sulfur. And just as importantly, those and other elements were combined in compounds that have a range of oxidation states. Living organisms can tap less oxidized compounds for energy rather than using sunlight for photosynthesis or eating organic matter. They just eat the tastiest bits of rock. "We have found a habitable environment so benign that if you were on the planet when water was around, you would have been able to drink it," said Curiosity project scientist John Grotzinger of the California Institute of Technology in Pasadena.



**Gray at last.** Curiosity rover (left, near drill site) drilled gray and thus life-friendly rock.



The drill analyses did disappoint in one respect: The search for traces of early life is as muddled as ever. Earlier SAM analyses of wind-blown martian dust in which a sample is progressively heated had produced chlorine-containing, single-carbon organic compounds like those produced in Viking lander experiments in the 1970s. Viking team members attributed those simple organics to contamination and still do. Now, Curiosity team members are saying that their dust-derived organics likely came from contamination as well.

At the Lunar and Planetary Science Conference (LPSC) this week at The Woodlands, Texas, Daniel Glavin of NASA's Goddard Space Flight Center (GSFC) in Greenbelt, Maryland, reported that an organic chemical

carried in SAM for a different kind of analysis for organics seems to have leaked into the sample cells of the heating analysis. The errant reagent's combustion and reaction with martian chlorine can explain the presence of all the chlorinated organic compounds produced by heating martian dust, he reported. So the drill sample was flushed with helium before heating to try to remove the contaminant, and in fact fewer types of the simple organics were produced and those in lesser amounts, SAM Principal Investigator Paul Mahaffy of GSFC said at last week's press conference. But more samples must be run to check the nature of the carbon before heating, he said.

The news on methane in the atmosphere of Mars was also a letdown. In a talk at LPSC, Christopher Webster of NASA's Jet Propulsion Laboratory in Pasadena—the lead scientist on the SAM instrument that measures atmospheric methane—reported

a somewhat lower upper limit based on a refinement of three measurements made by the end of last November. His best upper limit has dropped from 5 parts per billion by volume to 2.7 parts per billion. He is still reporting a measured value in the plus range—0.4 parts per billion, but given the uncertainties, "We have no definitive detection of methane," according to his abstract.

"We still have a lot to do," he said. The first high-sensitivity analysis that will be 10 to 50 times as sensitive as early runs has been delayed by the running of the drill sample analyses in the rest of SAM. But within a month or two, methane analyses should be pushed well down into the parts per trillion range.

—RICHARD A. KERR





# BATTLE FOR THE BARREL

**This year is shaping up to be decisive for “cellulosic” ethanol made from corn stalks and other agricultural waste, as oil companies and the ethanol industry clash over government mandates for the automotive fuel**

**DRIVE EAST FROM PORTLAND, OREGON, ON** Interstate 84 past the 189-meter-tall Multnomah Falls waterfall, past the scores of Day-Glo-garbed windsurfers slicing through the whitecaps on the Columbia River at the town Hood River, and into the brown high-plains desert, and eventually you see what looks like a green postage stamp in the distance. As you draw near you realize its true size. It’s an irrigated oasis of more than 10,000 hectares of poplar trees aligned in tidy rows. According to James Imbler, these trees are one of the keys to a revolution in transportation fuel that’s now on the cusp of becoming reality. The poplars are committed to be the feedstock for ZeaChem, the chemical company that Imbler heads, which plans to mow them down, chop them to bits, and convert the sugars in their tissues to ethanol to be blended with gasoline and pumped into your tank. ZeaChem officials say that their chemical plant is in the final stages of development and will begin commercial production later this year, eventually producing some 94.6 million liters a year of ethanol.

ZeaChem isn’t alone in ramping up production of cellulosic ethanol, which is made from nonedible plant biomass. In Decem-

ber 2012, a company called Beta Renewables commissioned a plant near Turin, Italy, that will convert rice straw and other agricultural materials into 75.7 million liters a year of ethanol. In June 2012, INEOS Bio finished building a plant in Vero Beach, Florida, that will convert landfill waste and yard waste into 30.3 million liters of ethanol a year. And a 37.9-million-liter-a-year plant opened in Shandong, China, last year as well. Articles in *The New York Times* and elsewhere have hailed these developments as the long-awaited commercialization of cellulosic ethanol. Company executives agree. “The technology is ready to deliver,” says Guido Ghisolfi, CEO of Beta Renewables in Italy.

Perhaps. Critics of cellulosic ethanol say that they’ve heard it all before. The U.S. government ordered refineries to blend 75.7 million liters of cellulosic ethanol into gasoline between 2010 and 2012, citing annual estimates that repeatedly concluded that the fuel would be available. But cellulosic ethanol producers failed to deliver. Oil companies have responded by deriding cellulosic ethanol as a “phantom fuel.”

Now, they’re calling for such mandates to be scrapped and are enlisting their friends in Congress to make it happen.

Ethanol producers of all stripes are girding for a fight. “It’s a battle for the barrel,” says Robert Dinneen, the president and CEO of the Renewable Fuels Association (RFA) in Washington, D.C., an industry association of ethanol producers. “It will be an epic fight,” he predicts, pitting the world’s largest oil and car companies against giant agricultural firms and Midwest farmers. The winner will likely determine not only the kind of car you drive in the future, but also perhaps the future of global fuel production. This conflict is creating a pressure-cooker environment for cellulosic ethanol producers. They need to deliver millions of liters

of their fuel this year to take some of the political heat off the industry. “It’s crunch time for cellulosic ethanol,” says Brooke Coleman, executive director of the Advanced Ethanol Council in Washington, D.C.

Ironically, things might be even worse for cellulosic ethanol-makers if they succeed. This year’s mandates call for 53 million liters of cellulosic ethanol to be blended into gasoline. If producers go beyond such mandates over the next few years and flood the market with their fuel, there may be nowhere for it to go, as refiners aren’t

## Online

**sciencemag.org**

Podcast interview  
with author  
Robert F. Service ([http://scim.ag/pod\\_6126](http://scim.ag/pod_6126)).

CREDIT: ANDREW BOURQUE/GREENWOOD RESOURCES INC.



**Future fuel.** Poplar trees near Boardman, Oregon, are slated to be the feedstock for ZeaChem's cellulosic ethanol plant.

required to blend any excess ethanol into their gasoline. Add to this the insecurity over how the ongoing budget battles in Congress will affect U.S. national energy policy and tax breaks that the ethanol industry enjoys, and 2013 is shaping up to be the make-or-break year for cellulosic ethanol. At the National Ethanol Conference (NEC) held in February in Las Vegas, Nevada, U.S. Agriculture Department Secretary Tom Vilsack warned his audience that the road ahead looks rough. "It's a very dicey time," Vilsack said.

### Higher standards

The ethanol industry seems as though it's been around forever. And in a way, it has. The fermentation of ethanol, more commonly known as alcohol, is one of humanity's oldest known technologies. Analysis of 9000-year-old clay jars recovered in China reveals that Neolithic people consumed alcohol. The use of the energy-rich molecule as a fuel dates back to the dawn of the automobile age: In 1908, the Ford Motor Company's Model T could be powered by ethanol. But eventually carmakers settled on a mixture of organic compounds even richer in energy that could be refined from oil pumped right out of the ground. Gasoline took over in America and has been king ever since.

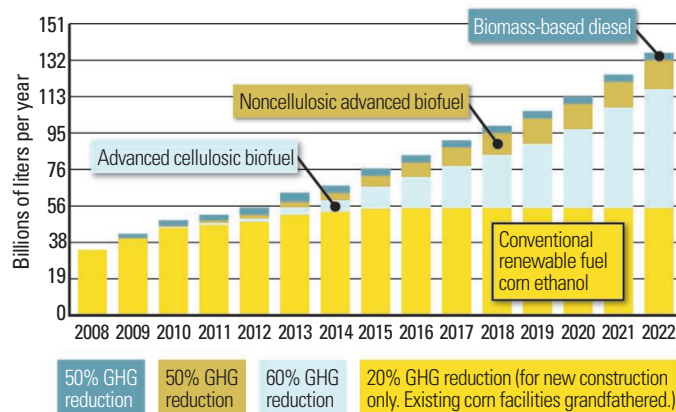
In 2005, Congress set out to change this picture. It passed the Renewable Fuel Standard (RFS) and updated it in 2007 with RFS2. The law guaranteed a market for renewable fuels by requiring blenders to incorporate increasing amounts of ethanol and other renewable fuels into gasoline, up to 136.3 billion liters in 2022 (see figure, above). By doing so, Congress hoped to reduce the country's rising dependence on imported oil, bolster rural economies that would produce the corn and other biomass that would serve as the fuel feedstock, and lower the amount of greenhouse gases pumped into the atmosphere each year.

Oil companies initially welcomed the move. The 1990 amendments to the U.S. Clean Air Act already required them to add high-octane fuel additives to help engines burn more cleanly. And in 2004, the industry began losing the use of its primary additive, MTBE, after

California and New York started a nationwide trend by banning MTBE after it was shown to be poisoning ground water. Refiners turned to ethanol instead.

RFS envisioned that, initially, the primary source of renewable fuel would come from ethanol fermented from the sugars in corn, a relatively mature technology. But growing corn requires relatively large amounts of water, fertilizer, and land. So Congress sought to cap corn's use. The amount of corn ethanol used was slated to rise from 30.3 billion liters in 2009 to a maximum of 56.8 billion liters a year by 2015. Last year, blenders added 50 billion liters of ethanol derived from corn and sugar. That meant that by 2022, the remaining 79.5 billion liters of growth in renewable fuel use had to come from "advanced" biofuels, primarily cellulosic ethanol, with relatively small amounts of biodiesel and biofuels derived from algae, among other sources. This surge in cellulosic ethanol production was originally planned to begin in 2010 with the first 378.5 million liters of the fuel, with year-by-year increases up to 60.6 billion liters a year in 2022. But the technology didn't mature fast enough. So the Environmental Protection Agency (EPA), which Congress empowered to change the RFS schedule, has had to dial back the mandates.

### Renewable Fuel Standard



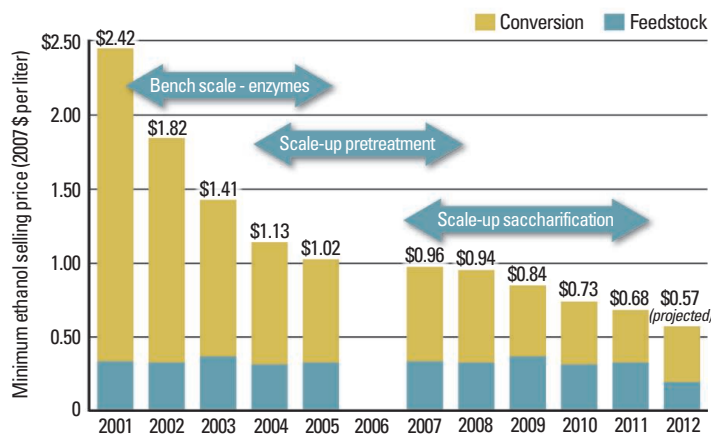
**Ramping up.** Current law requires fuelmakers to blend an increasing volume of renewable fuels into gasoline, lowering greenhouse-gas (GHG) emissions.

To absorb the rising ethanol production, initially the U.S. Department of Energy (DOE) and EPA permitted refiners to sell E5, consisting of 95% gasoline blended with 5% ethanol. By 2008, numerous states mandated E10, and in 2011 EPA certified—but did not require—the sale of E15 for cars built after 2001. Refiners also blend an ethanol-rich E85 for vehicles with specialized flexible-fuel engines.

But the new market for ethanol didn't immediately pave the way for cellulosic ethanol. Its development has been slow, because it's harder to make alcohol from nonagricultural biomass than from corn starch or sugar cane. That's because the leaves and stalks of plants have a more complex molecular structure made of a mixture of the biopolymers cellulose, hemicelluloses, and a woody material called lignin that prevents microbes from digesting plants as they grow. To make the sugars available for fermentation, cellulosic ethanol-makers must first grind the plant matter and separate out the lignin with acids and other chemical additives. They then need to add cocktails of different enzymes to break apart the different sugar chains, with each feedstock needing a slightly different cocktail. Finally, many cellulosic ethanol producers have had to engineer specialized microbes to convert the broader mixture of sugars in cellulosic material into ethanol. All these extra steps add to the cost.

For decades, that made cellulosic ethanol far more expensive than corn- and sugar-derived

### Cellulosic Ethanol: Historic State of Technology



**Steady drop.** The cost of cellulosic ethanol has declined steadily thanks to improvements in technology for converting agricultural wastes into fermentable sugars.

versions. As recently as 2001, researchers from the National Renewable Energy Laboratory (NREL) estimated that cellulosic ethanol cost more than \$2.38 a liter. That price fell as researchers and companies began coming up with better enzyme cocktails and better pretreatment methods. Now, a recent NREL analysis concludes that cellulosic ethanol can be produced for just 57 cents a liter, only modestly above the cost to produce corn ethanol. A 27-cent-per-liter tax credit awarded to companies that actually sell the fuel also stands to lower the cost of cellulosic ethanol that makes it to market. And cellulosic ethanol companies and enzyme producers insist they are doing even better. "Today we are at the point where cellulosic ethanol can be made at a cost similar to corn ethanol," says Poul Andersen, a vice president with Novozymes, the world's largest cellulosic ethanol enzyme producer based in Bagsværd, Denmark. Beta Renewables' Ghisolfi goes even further, saying his company can produce cellulosic ethanol for less than 40 cents a liter. That's well below today's price of gasoline. But because the price of gasoline depends primarily on the price of crude oil, if oil prices decline, so, too, will gas prices.

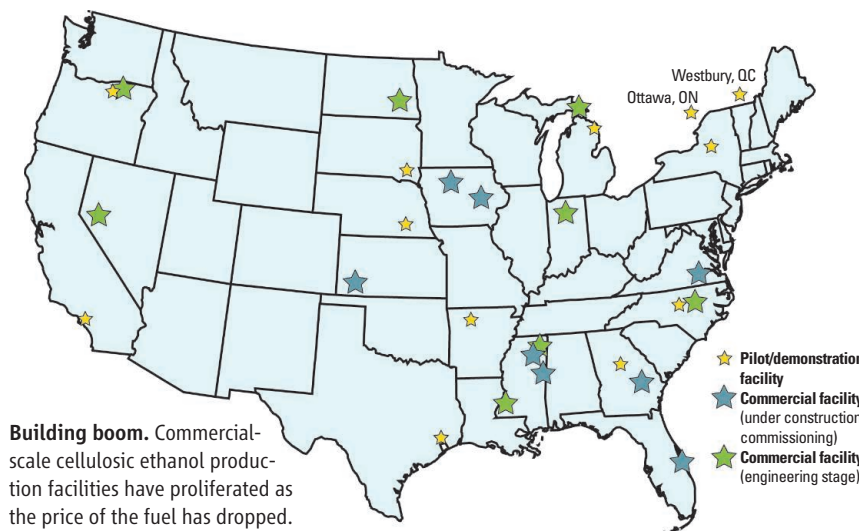
Ethanol industry leaders say that this price decline has sparked a construction boom. In 2012, the Advanced Ethanol Council, a group made up primarily of cellulosic ethanol producers, reported that eight commercial-scale cellulosic ethanol plants in the United States—such as the ZeaChem plant in Oregon—were either open, in their final commissioning stage, or under construction. Another eight commercial facilities are in the engineering stage. Outside U.S. borders, in addition to the projects in Italy and China, commercial plants are under development in Brazil, Spain, Germany, and Denmark. It will take a few years for all those plants to be built, Ghisolfi says. But change is coming. "Worldwide, there will be tens of millions of tons of cellulosic ethanol delivered regardless of the rules in the U.S.," Ghisolfi says.

### Phantom fuel

That all sounds well and good. But while the world waits, cellulosic ethanol critics in the petroleum industry complain that man-

dates for a so-far nonexistent fuel are driving up their costs. Those added costs come as a byproduct of the way EPA monitors compliance with the mandates. EPA does so by issuing renewable fuel credits, called Renewable Identification Numbers, or RINs. At the end of each year, refiners and blenders must show that they have at least one RIN for every 37.9 liters of gasoline they sell. They receive those RINs either by earning one for each gallon of renewable fuel they blend or by buying excess RINs from other companies that have more RINs than they need.

Over the past 3 years, EPA decided to keep the lowered mandates for cellulosic ethanol in order to maintain the incentive for cellulosic ethanol companies to continue commercial development. That meant that oil refiners and blenders had no way to earn those RINs and thus had to buy them to fulfill the mandates.



**Building boom.** Commercial-scale cellulosic ethanol production facilities have proliferated as the price of the fuel has dropped.

Oil companies objected that the requirement amounted to an added tax on their product and filed suit against EPA. In January, a federal appeals court for the District of Columbia agreed, at least in part. The court ruled that EPA can't require blenders to pay for credits for a product that is unavailable commercially. Nevertheless, the court continued to allow EPA to set mandates for how much renewable fuels, including cellulosic ethanol, should be blended each year. And the week after the court's decision, EPA proposed a new rule requiring refiners and blenders to blend 53 million liters of cellulosic ethanol in 2013, again citing internal market projections that the fuel would be available.

The decision drew an immediate backlash. "We are disturbed that EPA is mandating 14 million gallons [53 million liters] of cellulosic ethanol when zero gallons are available for compliance as of today," says

Charles Drevna, president of the American Fuel & Petrochemical Manufacturers in Washington, D.C. Louis Finkel, executive vice president of the Grocery Manufacturers Association, which is also in Washington and recently came out against RFS, notes that RFS was intended to help drive the development of technology for cellulosic ethanol and other advanced biofuels. But so far, it hasn't worked. "The technology has not come forward," Finkel says.

With no cellulosic fuel on the market, "it's just silly" to keep the blending mandates, says Marty Durbin, executive vice president of the American Petroleum Institute in Washington. Even worse, Durbin adds, the RFS mandate keeps rising even though U.S. gasoline sales have been declining for several years. Less gas means less ethanol needed for blending. "The pool is going down. The mandate is going up. That doesn't make sense," Durbin

says. "We're not against renewable fuels. We think the [RFS] program doesn't work."

That's not the only grenade being tossed by cellulosic ethanol critics. Durbin and others argue that rising ethanol mandates are putting the squeeze on food producers and consumers. "Ethanol drives up food costs," Finkel says, though he acknowledges that other factors play a role as well. Ethanol opponents have been

swinging even harder at E15. In January, the Coordinating Research Council released a study suggesting that increasing the ethanol content of gasoline from 10% to 15% can damage engines, including causing swelling to fuel system components, erratic fuel level indicators, and faulty check engine signals. Previous testing by the industry-backed group found E15 could damage engine valves. Citing such industry studies, last year AAA and a group of auto manufacturers also warned that E15 may damage car engines.

Putting horsepower behind their studies, ethanol's critics are now pushing for policy changes. In January, following EPA's decision to up its 2013 mandate for cellulosic ethanol up to 53 million liters, Drevna called on Congress to repeal the RFS. It didn't take long for members of Congress to take up the baton. In Congress, in February, Representative James Sensenbrenner (R-WI) intro-

CREDIT: ADVANCED ETHANOL COUNCIL



duced a bill to limit the increase in the RFS mandate for cellulosic ethanol to 5% per year or 3.79 million liters, whichever is greater—far below the rate of growth needed to reach RFS's mandate of 60.6 billion liters per year by 2022. Senators David Vitter (R–LA) and Roger Wicker (R–MS) introduced a separate bill to roll back the EPA approval of E15, saying the fuel needs more testing.

### Fighting back

Ethanol backers acknowledge that their opponents are landing blows. “We are getting hammered by the oil industry,” Coleman says. The ethanol industry is “under siege and fighting back,” Dinneen told the NEC audience, sounding like a general trying to rally his troops.

But Dinneen and other ethanol true-believers don't concede any of their critics'

2008 recession and rising fuel efficiency standards, for example, would have driven oil imports down to 48% without ethanol, and studies show that the ethanol mandate has driven corn prices up slightly. But Dinneen notes that according to the U.S. Department of Agriculture, food inflation has increased only 2.5% per year since 2005, when RFS was instituted, essentially unchanged compared with the long-term average. Crude oil prices over that same period, meanwhile, have risen 68%. And when it comes to growing corn, energy prices affect a wide variety of things, including the cost of fertilizer, transportation, and processing; the cost of



**Steel in the ground.** Construction crews put together the infrastructure for POET-DSM's 76-million-liter cellulosic ethanol plant in Emmetsburg, Iowa.

points. Instead, they charge that their opponents—led by oil companies—are stepping up their attacks because renewable fuels are eating away at their market share. “You're being tested in the courts. You're being tested in the halls of Congress,” Vilsack says. “Why now? I believe there is a reason: You are winning. And the folks on the other side are concerned.”

In response, proponents of the new fuel muster studies and figures of their own. Far from being a failure, says Geoff Cooper, RFA's vice president for research and analysis, RFS is the most successful energy legislation ever enacted. In just 8 years, he says, it has prompted the growth of an industry that now supplies 10% of all the transportation fuel in the country. It's directly created 70,000 jobs; increased household farm revenues by \$28.9 billion; helped lower oil imports from 60% of U.S. transportation fuel in 2006 to 41% last year; and, according to a recent analysis using a computer model developed by DOE researchers, cut greenhouse gas emissions by 33.4 million tons in 2012 alone, equivalent to removing 5.2 million cars and trucks from the road.

Those numbers come with caveats. The

ingredients makes up only 14% of food's final cost to consumers.

Not only is ethanol already lowering oil imports and helping farmers, but its impact is also expected to grow sharply over the next decade, Cooper says. For example, in the November 2012 issue of *Biofuels*, Gbadebo Oladosu, an environmental economist at Oak Ridge National Laboratory in Tennessee, and colleagues looked at the expected impact of RFS2 on the U.S. economy over the next decade. They conclude that adding renewable fuels will be responsible for a 3% decline in oil prices by 2015 and a 7% decline by 2022. That decline in energy costs is expected to boost the U.S. gross domestic product by 0.8%, or \$120 billion, over that same period. “It's a great American success story,” Cooper says.

As for industry complaints that cellulosic ethanol RINs amount to a tax, Dinneen notes that the credits have cost oil refiners and blenders just \$25 million over 3 years—less than one-fiftieth of 1% of their profits over the same period. Besides, ethanol proponents say, the \$4 billion to \$5 billion a year in permanent tax breaks that oil companies receive for things like oil drilling and profits

earned overseas have long tilted the market in the companies' favor.

In response to possible engine damage from E15, RFA and other groups note that studies suggesting engine damage were funded by oil and auto companies, and they point out several technical flaws in the studies themselves. Besides, Dinneen says, E15-burning vehicles in the United States have already driven more than 10 million kilometers—the most extensive testing of any fuel mixture in history.

Dinneen says proposed legislation to end incentives for cellulosic ethanol amounts to a bald attempt by oil industry backers to take down the competition and insists it won't work. Shane Karr, the vice president for federal government affairs at the Alliance of Automobile Manufacturers in Washington, D.C., says that he, too, believes it's “extremely unlikely” that any RFS repeal or reform will make it through while Barack Obama is president, unless it winds up being tucked into a large budget package or the like. Still, clearly the pressure is building. And cellulosic ethanol producers as well as makers of other “advanced” biofuels are feeling the need to get commercial production

rolling. “We need to get advanced biofuels into the market,” Vilsack says. “That will mute some of the criticism and erase some of the skepticism.”

### The road ahead

If Imbler, Ghisolfi, and other cellulosic ethanol company CEOs are right, the spigots are ready to be opened. But if they do, that could spell a very different sort of trouble. That’s because corn ethanol producers already supply enough fuel to fill the entire volume needed for E10 gasoline. Gas stations aren’t required to sell E15, and so far only a handful of them do. That means that unless cellulosic ethanol can be made cheaper than corn ethanol, there will be nowhere for the cellulosic ethanol to go, a situation industry insiders call the “blend wall.” “The blend wall is the big issue for 2013 and 2014,” says Wallace Tyner, an agricultural economist at Purdue University in West Lafayette, Indiana. “There’s no place for cellulose to go,” he adds.

The blend wall, it appears, has already arrived. This year RFS requires blenders to use 52.6 billion liters of ethanol, 2.65 billion liters more than the amount of ethanol needed for E10. That extra 2.65-billion-liter requirement is intended to encourage retailers to move to E15 and other higher ethanol blends. But so far, all it seems to be doing is driving up the cost of RINs. RIN prices have jumped from an average of 2 to 3 cents per RIN in January to 75 cents per RIN last month. The price spike, observers say, is forcing blenders to look to buy RIN credits when they run out of room for their renewable fuel.

But Dinneen and other RFS proponents call for patience and say that the market will handle the blend wall if given a chance. As cellulosic ethanol comes onto the market, the price of ethanol should drop. So refiners will be able to make more money by blending E15 instead of by buying costly RINs, Dinneen explains. “The marketplace will work if you don’t change the RFS,” Dinneen says. This year is critical, he says, because it is the first in which RFS mandates adding more ethanol than E10 fuel can absorb: “This is where the rubber meets the road, and the policy hits the marketplace.”

Even if cellulosic ethanol companies manage to avoid the blend wall over the next year, other obstacles are looming further out. To incorporate into gasoline the 60.6 billion liters of cellulosic ethanol that RFS calls for by 2022, refiners will need to up their blend mixture to 20% to 25% ethanol. “We’re nowhere close to doing that today,” says

Michael Pacheco, associate laboratory director of the National Renewable Energy Laboratory in Golden, Colorado.

To work with higher ethanol blends, carmakers will need to modify their engine designs. That’s doable. In fact, Brazil has required such designs for years to work with a wide variety of high-ethanol blends. As well, carmakers are already redesigning their engines in an effort to comply with higher U.S. mileage standards instituted last year. But carmakers say that they are wary of tailoring engines to work with ethanol for two key reasons. The first is low demand from consumers. Flexible-fuel cars that run on E85 have been meager sellers in the United States, because the fuel mixture is not universally available and there are few incentives for car buyers to make the switch. And unless demand rises for other novel designs, companies say they can’t make money. “If there is no market pull, we will stop building those cars,” says Stuart Johnson, a senior manager for Volkswagen Group of America in Herndon, Virginia.

The second problem for carmakers is that they need to be sure the fuel blends for the new engines will be widely available. “If we are going to build dedicated vehicles, we need a dedicated fuel supply,” says Coleman Jones, biofuel implementation manager with General Motors in Franklin, Michigan. Fuel refiners say it works both ways: If cars that run on high-ethanol blends aren’t widely available, there’s no reason to offer the fuels at all gas stations.

This has created a classic chicken-and-egg problem between the car companies that will build the cars only if they are sure there will be a fuel supply in place and the fuel refiners who will distribute the fuel only if they know they have cars on the road to use it. The problem is so acute, Pacheco says, that automakers are more comfortable with pushing more expensive electric car designs, because they know that they won’t face the fueling problem.

Pacheco, who in the early 2000s worked on DOE studies that inspired RFS, now

wishes that he and other analysts had pushed harder for Congress to make the use of biofuels mandatory. That would have solved the problem of demand from the get-go, he says. “I was naive to think that the industry would start to prepare for the change,” Pacheco says. “I really underestimated the lack of support from the auto industry. They have effectively dug in their heels.”

Cellulosic ethanol boosters say there’s still time to take action. For starters, Imbler argues, Congress could give all alternative energy producers a huge lift by making permanent the tax credits they’ve been renewing on an annual basis. This would give investors confidence that a single set of rules would be in place for the duration of their investment. Pacheco is pushing a different approach. He says that he and his NREL col-



**New kid.** In 2011, EPA began allowing gas stations to sell E15. So far, only a handful of stations in the United States offer it.

leagues are working to convene a meeting of representatives from oil companies, refiners, carmakers, and gas stations to begin to hammer out the transition to higher octane fuel blends. Finally, station owners such as Scott Zarembo, who sells E15 at all seven stations he owns in Kansas, says in making the transition to higher ethanol fuel blends, there’s no option other than to talk with concerned customers one-on-one every day. “Nothing is easy,” Zarembo says, “but I believe in it.”

The question is whether Zarembo and his fellow retailers can convince consumers quickly enough to buy the millions of liters of cellulosic ethanol headed their way. If not, an industry that is only now getting up to speed may soon resemble the piles of waste it’s trying to use to revolutionize the future of transportation.

—ROBERT F. SERVICE



## U.S. SCIENCE POLICY

# Suresh Leaves His Mark on NSF As He Heads to Carnegie Mellon

**Outgoing NSF director hopes his initiatives on interdisciplinary research, global partnerships, and entrepreneurship will be sustained**

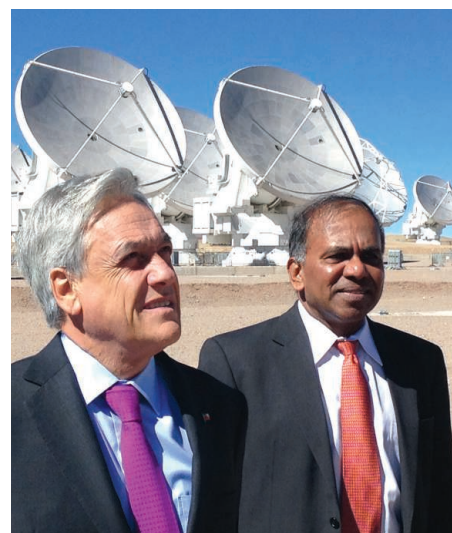
A \$10 billion budget would have been nice, Subra Suresh admits. But having to work with a smaller budget than Congress and the president had once promised the National Science Foundation may be Suresh's only real regret as he steps down today as NSF director.

The Indian-born, U.S.-trained mechanical engineer is leaving NSF less than half-

In tweaking how NSF does its business, Suresh hasn't neglected his outside game. He's preserved NSF's enviable reputation on Capitol Hill by assiduously courting influential legislators from both parties. He's been in step with White House priorities to the point that first lady Michelle Obama kicked off an initiative to help scientists balance work and family responsibilities. He worked with

Technology (MIT). In fact, some NSF staffers whose lives have been disrupted by Suresh's management changes breathed a collective sigh of relief when Suresh announced he was headed to Carnegie Mellon. But many other program officers say that they appreciate what Suresh has done in moving NSF in new directions. "I've been at NSF for 28 years, and this is the most fun I've ever had," says Richard Behnke, head of the geospace section within the geosciences directorate and co-chair of the internal working group that designed the INSPIRE (Integrated NSF Support Promoting Interdisciplinary Research and Education) grants program.

"Subra came in with a vision for the foundation, and he's effectively implemented it in a way that has been very collegial," says Dan Arvizu, chair of the National Science Board,



**Team leader.** Subra Suresh (left) celebrated his appointment last month as the ninth president of Carnegie Mellon University with outgoing CMU President Jared Cohon. Last week, he joined Chilean President Sebastián Piñera in dedicating ALMA, a \$1.5 billion millimeter array on the 5000-meter-high Chajnantor plateau in Chile's Atacama Desert (above).

way through his 6-year term to become president of Carnegie Mellon University. Still, in 29 months he's managed to put his stamp on the 62-year-old agency. He has launched initiatives designed to make scientists more entrepreneurial (Innovation Corps), to foster high-risk interdisciplinary research (INSPIRE), and to build stronger ties between U.S. researchers and colleagues in other countries (SAVI). He also reassigned several programs that had reported directly to him, notably international and polar activities, as part of a move to integrate the foundation's activities under a concept he calls OneNSF.

his counterparts around the world to create the Global Research Council (GRC), a voluntary forum of funding agencies from some 50 countries to discuss common concerns. And he's done it all on a budget that remained stuck at about \$7 billion during his tenure—and will shrink this year.

"I never felt I couldn't initiate an idea because of a flat budget or budget constraints," Suresh says. "A lot of things aren't limited by money; they are limited by ideas and energy."

Those qualities have never been in short supply for the 56-year-old former dean of engineering at the Massachusetts Institute of

NSF's presidentially appointed oversight body. "He's also raised the visibility of NSF around the world."

Speaking with *Science* during a 7 March interview in his 12th-floor office at NSF headquarters in Arlington, Virginia, Suresh said he relishes the opportunity to return to academia. Before he starts at Carnegie Mellon on 1 July, however, Suresh hopes to crank out a few more publications with his remaining graduate students at MIT. "You'd be surprised at how much can be accomplished in a week with no interruptions," he noted.

Here are excerpts from that interview.

—JEFFREY MERVIS

CREDITS (LEFT TO RIGHT): PHOTO COURTESY OF CARNEGIE MELLON UNIVERSITY; NSF

**On any regrets:**

NSF has been enormously successful over its 62 years. But the evolution of its organizational structures lags the evolution of science. ... I would have loved to have seen a \$10 billion budget. I would have really liked that. But regardless of what we have to spend, we cannot continue to carry out activities that started 30 or 40 years ago. It's difficult for any institution to end things that have already provided their full value, but having that ability is critical for an agency to be able to move ahead with new and exciting things.

**On the origins of INSPIRE:**

INSPIRE [*Science*, 18 November 2011, p. 883] came about because of a lot of conversations, internally and externally, to foster exciting, interdisciplinary work that usually falls through the cracks because of traditional ways of identifying new ideas.

This is not just a problem I noticed as an administrator. I also came to it as a scientist. I went from mechanical engineering to microbiology, so as someone in his late 40s, and a department head, I wondered, "How do I get my funding? How do I get my first experimental results?" So I know the issue from the customer's viewpoint.

It developed over several months from the time I arrived [in October 2010] to the release of the president's 2012 budget [in February 2012]. I proposed it to the administration and OMB [Office of Management and Budget], they embraced it and funded it, for the first year, for up to \$24 million. And it also grew out of conversations with the NSF community over the summer, when I was waiting for the Senate to take up my confirmation. ...

We put in \$12 million from the director's office, and program officers were asked to match it. They ended up contributing \$18 million, and every office participated. And last summer we made 40 awards.

**On the Career-Life Balance Initiative:**

Although 40% of all STEM [science, technology, engineering, and mathematics] Ph.D.s are women, they are only 26% of the STEM workforce. Given that they are one-third below their ability to contribute for a variety of factors, NSF had a chance to play a huge leadership role.

So for a very small amount of money—in contrast, we spend hundreds of millions of dollars on broadening diversity—we worked to adjust our policies and practices [*Science*, 30 September 2011, p. 1811]. Then I socialized it with members of Congress, and with the White House, which was quite taken by this idea. And that's

why I think for the first time we had an NSF event at the White House, and the first lady participated.

**On the Innovation Corps:**

We spend \$6 billion a year on basic research, and we don't want to deviate from that, because if we don't fund basic research, there aren't a lot of other opportunities for people to get funded.

But having said that, a lot of the projects that we fund don't go beyond a publication. That's not because the PIs [principal investigators] aren't capable of taking it further, but because some don't have the opportunity to do it at the institutions in which they work.

I thought NSF can exercise its status and its bully pulpit to create, on a national scale, a set of activities that otherwise would not be possible. And I've been enormously pleased—it's far surpassed my expectations [*Science*, 20 July 2012, p. 281].

In the first year we made 100 awards (to three-person teams); in the second year it grew to 300. There are now five national nodes—in the [San Francisco] Bay area, in the New York City area, in the Washington-Baltimore metropolitan area, as well as at the University of Michigan and Georgia Tech [the Georgia Institute of Technology].

**On GRC:**

A recent report from Battelle noted that, for the first time in history of science funding, the Asian nations together invested more in R&D than the U.S. did, a total of \$425 billion. (Global investment is \$1.5 trillion.) Given that level of investment from developing countries, there are a lot of questions. For example, how do we make sure all the basic elements of the scientific process—issues like peer review, research integrity, intellectual property rights, and so on—evolve as quickly as possible, so that we all benefit from it?

So we thought, since countries look up to NSF, rather than creating many bilateral collaborations, this allows us to work on a larger stage. For our first meeting [last spring] I invited the head of one funding agency from 48 countries, and 47 came. There was unanimous support for the GRC, and the second meeting will be in Berlin at the end of May.

Right now, there's not anybody to monitor these issues. It's not done by heads of state, or between the State Departments of each coun-

try. It's not individual scientists that can do it, and funding agencies are right in the middle of this. And at Berlin they will discuss a plan for future action on open access.

**On a new NSF report showing that the share of U.S. undergraduate STEM degrees awarded to blacks has remained flat for the past decade:**

It's a lot of complicated issues. A lot of students arrive at college wanting to go into STEM fields and, for a variety of reasons, they drop out in the freshman year. I don't know that there is a simple answer.

And it's not just an undergraduate issue. If taking high school STEM courses is not regarded as cool, you're not going to have a lot of people from any race wanting to go into these fields.

There is another statistic that is important. In Asia, the fraction of all college graduates that earn engineering degrees is 21%. In Europe it's 13%. In the United States it's 4.5%. And that has been slightly declining in the U.S.

How do we remain an innovation leader if only 4.5% of our graduates choose to go into engineering?

[Education Secretary] Arne Duncan has said how, in Singapore, it's so prestigious to be a high school science teacher. And the pay scale reflects that. And all of this contributes to how many STEM graduates we will have.

**On becoming a college president:**

Universities are places where you have an opportunity to continuously interact, educate, and learn from young people. And it's a very satisfying environment. I've always enjoyed university life. And being at a university that is a leader in research and education is an exciting prospect.

**Advice to the next NSF director:**

I hope that my successor has a better economic climate in which to work. But even in the tough climate I faced, NSF probably did as well as any agency could have done.

I very much enjoyed my interactions with my colleagues at other agencies and with members of Congress on both sides of the aisle. I spent a lot of time cultivating those relationships in Washington, and I would strongly suggest that my successor spend enough amount of time cultivating those same relationships with Congress.

*"I would have loved to have seen a \$10 billion budget. ... But regardless of what we have to spend, we cannot continue to carry out activities that started 30 or 40 years ago."*

—SUBRA SURESH



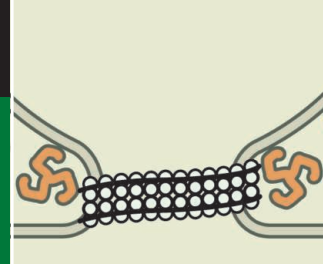
A dazzling sweep of accomplishments

1384



What controls cellular fission?

1392



LETTERS | BOOKS | POLICY FORUM | EDUCATION FORUM | PERSPECTIVES

## LETTERS

edited by Jennifer Sills

## Libraries' Social Role in the Information Age

RECENTLY, *THE NEW YORK TIMES* ASKED WHETHER WE STILL NEED LIBRARIES (1). THE ANSWER IS yes, but the role of libraries in our society is changing. Traditionally, the library's goal has been to store the information generated by society. People would visit libraries for the purpose of accessing this information with the help of a librarian. With the advent of the Internet, the Web has assumed the traditional role of libraries, and search engines (such as Google) have assumed the role of the librarians. However, we believe that there are new opportunities for the libraries in the current information and knowledge society.

In the 1980s, Ray Oldenburg theorized that people spend most of their time at home and at the workplace, and much of their remaining time in spaces dedicated to the social life of the community, such as coffee shops, bookstores, bars, and hair salons, which are central to the vitality of a democracy (2). Libraries can also serve as social spaces.

To transition into this new role, libraries should begin to focus on the users rather than the collection of information. Libraries should have social spaces of learning, thinking, and reading, where people can share their experiences and knowledge. People could go to the library to check out books, use the Internet, read a book or a newspaper, or watch a documentary; as well as to learn how to open a bank account or start a business; discuss the problems of their neighborhood or country; take classes in poetry, theater, or film; or learn good eating and health habits—all while having a drink with other users. In this paradigm, the library will belong to the community.

People are already demanding these new services from libraries. In many countries, including the United States, United Kingdom, and the Netherlands, the public is losing interest in traditional public libraries of information, but pilot experiences with the new format of libraries are emerging and succeeding (3).

In Spain, the local authorities of the city of Granada decided to close a public library located in the popular district of Zaidin. The council did not predict the residents' outcry, because it did not understand that the library played a central role as a social place for the community. Local residents, both young and old, struggled for a year to reopen the library, taking

their grievances to the streets, the media, social networks, and government authorities. They gained the support of prominent people in the Spanish cultural scene (such as the writer Antonio Muñoz Molina) as well as many of the residents of Granada. In January, they succeeded in reopening the library. Clearly, their library was more than a simple repository of information (4).

LibQUAL is a standard technique for assessing the quality of libraries according to users' satisfaction with

respect to three aspects: the physical space, the staff, and information control. In our quality assessment studies (5), we have observed that students are not concerned about the library's collection, but want development of the physical dimension of libraries and the creation of social spaces.

Libraries must adapt to stay relevant in today's society.

ENRIQUE HERRERA-VIEDMA<sup>1,3\*</sup> AND  
JAVIER LÓPEZ-GIJÓN<sup>2,3</sup>

<sup>1</sup>Department of Computer Sciences and Artificial Intelligence, University of Granada, Granada, Spain. <sup>2</sup>Department of Library Sciences, University of Granada, Granada, Spain.

<sup>3</sup>Secaba Laboratory, University of Granada, Granada, Spain.

\*To whom correspondence should be addressed. E-mail: viedma@decsai.ugr.es

## References

1. "Do we still need libraries?," *The New York Times* (27 December 2012); [www.nytimes.com/roomfordebate/2012/12/27/do-we-still-need-libraries](http://www.nytimes.com/roomfordebate/2012/12/27/do-we-still-need-libraries).
2. R. Oldenburg, *The Great Good Place: Cafes, Coffee Shops, Bookstores, Bars, Hair Salons, and Other Hangouts at the Heart of a Community* (Paragon House, New York, 1989).
3. International Federation of Library Associations (IFLA), Section on Library Buildings and Equipment, *Newsletter*, 1 (2012); [www.ifla.org/files/assets/library-buildings-and-equipment/newsletters/2012-1.pdf](http://www.ifla.org/files/assets/library-buildings-and-equipment/newsletters/2012-1.pdf).
4. La Biblioteca de las Palomas Renace ([http://nocierebibliotecadelzaidin.blogspot.com.es/2013\\_01\\_01\\_archive.html](http://nocierebibliotecadelzaidin.blogspot.com.es/2013_01_01_archive.html)).
5. E. Herrera-Viedma, "Asegurar la calidad de los servicios bibliotecarios," International Conference on University Libraries, National Autonomous University of Mexico, Mexico City, Federal District, Mexico, 7 to 9 November 2012 ([www.youtube.com/watch?feature=player\\_embedded&v=5eW99VNePmY](http://www.youtube.com/watch?feature=player_embedded&v=5eW99VNePmY)).

China's Food Security  
Soiled by Contamination

IN ADDITION TO THE RAPID REDUCTION OF arable land ("Losing arable land, China faces a stark choice: Adapt or go hungry," C. Larson, *News Focus*, 8 February, p. 644), soil contamination poses an often overlooked but no less critical threat to China's food security.

CREDIT: INMA VILLAR



**Community.** Local residents protest the closing of a library in Granada.

Approximately 8.3% of the country's 120 million hectares of arable land—about the size of South Korea—is contaminated by unbridled mining, trash dumping, and long-term use of pesticides (1, 2). Heavy metals such as cadmium and lead could enter the dining tables of households and restaurants through the rice, fruits, and vegetables grown in contaminated fields (3, 4). Health risks associated with soil contamination so far have been most severe in the industrialized parts of China (1, 4, 5).

Soil contamination could fundamentally undermine China's efforts for national food security. The country has long been pushing its food production: A required minimum amount of arable land was made part of the basic national policy (6), and research funds have poured in for more productive cultivars (7). However, all these efforts could be in vain if crops are from tainted fields. It is thus striking that soil contamination has received little attention from the public. Likewise, there has been little government effort to build necessary institutions, such as special laws and monitoring programs, targeting soil pollution.

China's Ministry of Environment and Ministry of Land and Resources conducted a national soil pollution survey from 2006 to 2010 (8), but the final report was never released. More recently, the Chinese State Council planned to comprehensively investigate its soil environment by 2015, monitor 60% of its arable lands on a regular basis, and endeavor to establish a national soil environmental protection system by 2020 (9).

Releasing information from these surveys will help to raise public awareness of soil contamination and facilitate research for pollution control.

YAO LIN LIU,<sup>1\*</sup> CHENG WEN,<sup>2</sup> XINGJIAN LIU<sup>3</sup>

<sup>1</sup>School of Resource and Environmental Sciences, Wuhan University, Wuhan, 430079, China. <sup>2</sup>School of Earth and Environment, University of Leeds, Leeds, LS2 9JT, UK. <sup>3</sup>Department of Geography, University of Cambridge, Cambridge, CB2 3EN, UK.

\*To whom correspondence should be addressed. E-mail: yaolin610@163.com

## References

1. Environmental Protection Report to the 11th National People's Congress of China (2011); [www.npc.gov.cn/npc/xinwen/2011-10/26/content\\_1678462.htm](http://www.npc.gov.cn/npc/xinwen/2011-10/26/content_1678462.htm) [in Chinese].

2. J. Liu, J. Diamond, *Nature* **435**, 1179 (2005).
3. P. N. Williams *et al.*, *Environ. Sci. Technol.* **43**, 3 (2009).
4. P. Zhuang *et al.*, *Sci. Total Environ.* **407**, 5 (2009).
5. X. Liao *et al.*, *Environ. Intl.* **31**, 6 (2005).
6. State Council of P. R. China, "National Land-Use Planning Outline (2006–2020)" (2008); [www.gov.cn/jrzq/2008-10/24/content\\_1129693.htm](http://www.gov.cn/jrzq/2008-10/24/content_1129693.htm) [in Chinese].
7. State Council of P. R. China, "National Plan for Development of the Crop Seed Industry (2012–2020)" (2012); [www.gov.cn/zwqk/2012-12/31/content\\_2302986.htm](http://www.gov.cn/zwqk/2012-12/31/content_2302986.htm) [in Chinese].
8. Ministry of Environmental Protection of P.R. China, "Special Program of National Soil Survey and Pollution Control" (2006); [http://sts.mep.gov.cn/trhjbjh/qgtrxd/200607/t20060725\\_91295.htm](http://sts.mep.gov.cn/trhjbjh/qgtrxd/200607/t20060725_91295.htm) [in Chinese].
9. State Council of P. R. China, "Plan of Soil Environmental Protection and Integrated Pollution Control No. 7" (2013); [www.gov.cn/zwqk/2013-01/28/content\\_2320888.htm](http://www.gov.cn/zwqk/2013-01/28/content_2320888.htm) [in Chinese].

## Fostering Public Support for Vulture Protection

THE PERSPECTIVE BY A. BALMFORD, "Pollution, politics, and vultures" (8 February, p. 653) reinforces the importance of collaborative efforts by the public and private sectors to protect vultures in the Indian subcontinent from the veterinary use of the painkiller drug diclofenac. The timely ban of diclofenac and its replacement with meloxicam was instrumental in saving vultures from extinction. Now we need to sustain and improve these efforts to return the vulture population to its previous numbers.

Although the ban of diclofenac was effective in reducing the number of contaminated cattle carcasses (1), two obstacles could hamper the efforts to completely replace its use with meloxicam. First, meloxicam is 4 to 5 times as expensive as diclofenac, and people are loath to accept new technologies and innovations, even if beneficial, when higher costs are required (2). Second, diclofenac for human use is still readily available for purchase, and the environmental effects of a decline in the vulture population may not be perceived as a serious problem by farmers (3, 4).

To encourage the use of meloxicam in lieu of diclofenac, I suggest taking the following steps: First, to avoid increase in the cost of treatment for livestock farmers, the majority of whom fall below the poverty line (5), the Indian government should subsidize the cost of meloxicam to make the price

commensurate with the price of diclofenac. Second, an awareness campaign should be put in place to educate veterinarians, pharmacists, and farmers about the negative effects of diclofenac and encourage them to use the alternative.

MADHUKAR SHIVAJIRAO DAMA

Institute of Wildlife Veterinary Research, KVAFSU, Kodagu, 571234, India. E-mail: madhukar262@gmail.com

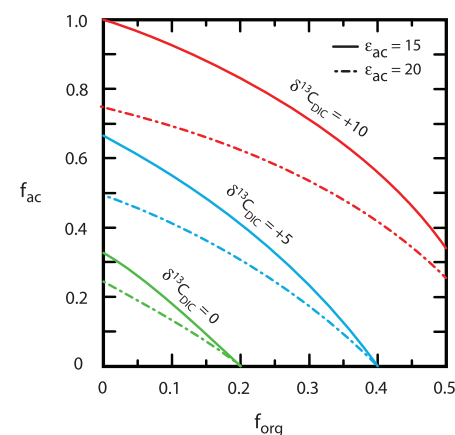
## References and Notes

1. R. Cuthbert *et al.*, *PLoS One* **6**, e19069 (2011).
2. K. Senthilkumar, P. S. Bindran, T. M. Thiagarajan, N. De Ridder, K. E. Giller, *Agricult. Syst.* **98**, 82 (2008).
3. M. Chong, *J. Risk Res.* **8**, 617 (2005).
4. C. Hall, *Geoforum* **39**, 204 (2008).
5. I. Z. Ansari, S. Akhtar, *Development* **2**, 443 (2012).
6. The measures expressed in this article solely represent the personal views of the author.

## CORRECTIONS AND CLARIFICATIONS

**News and Analysis:** "What it means for agencies to be under the sequester" by J. Mervis (1 March, p. 1020). The article incorrectly describes the impact of the sequester on the Manufacturing Extension Partnership (MEP) centers within the National Institute of Standards and Technology (NIST). An 8 February letter from NIST to Congress says "NIST would be forced to end work it is currently doing through the Manufacturing Extension Partnership (MEP) Center system." It does not address the potential impact on the staff of the centers.

**Research Articles:** "Authigenic carbonate and the history of the global carbon cycle" by D. P. Schrag *et al.* (1 February, p. 540). The published version of Fig. 2 was not in agreement with the equations in the text. The correct Fig. 2 is below. This error did not affect any conclusions in the paper. The HTML and PDF versions online have been corrected.



## Letters to the Editor

Letters (~300 words) discuss material published in *Science* in the past 3 months or matters of general interest. Letters are not acknowledged upon receipt. Whether published in full or in part, Letters are subject to editing for clarity and space. Letters submitted, published, or posted elsewhere, in print or online, will be disqualified. To submit a Letter, go to [www.submit2science.org](http://www.submit2science.org).



## HISTORY OF SCIENCE

## What Poincaré Knew

Peter Pesic

**H**enri Poincaré (1854–1912) was one of the most distinguished and influential scientists of his time, active in an astonishing variety of fields spanning pure mathematics, physics, astronomy, geodesy, telegraphy, and the philosophy of science. The centenary of his death is an appropriate occasion to look back at him, as Jeremy Gray (a historian of mathematics at the Open University and the University of Warwick) does in this biography.

Gray is a versatile and prolific writer, whose previous books include treatments of non-Euclidean geometry, the Hilbert problems, and (most recently) a wide-ranging treatment of mathematical modernism (*1–3*). Even so, Poincaré's vast and diverse scope of activities presents a formidable challenge, which Gray addresses with remarkable skill. His book is the first full-length attempt to deal with all the main aspects of Poincaré's work.

Gray's subtitle alerts us that this will be a scientific biography, a detailed account of Poincaré's work rather than of his life in a more private sense. Gray thus emphasizes "the mind which creates" rather than "the man who suffers," as T. S. Eliot phrased it. In so doing, Gray chooses to foreground the internal interplay of influences within science itself, rather than the external social influences that have been the main interest of many historians of science in recent decades. To be sure, Gray presents an overview of the historical situation in which Poincaré worked. We learn about Poincaré's involvement with political issues (such as the Dreyfus affair) and some details of his personal life and mannerisms that help fill out the sense of him as a human being. But the bulk of this hefty book unapologetically presents us with an account of Poincaré's multifarious works, mainly within the context of the various research fields in question.

Gray structures his book topically, rather than chronologically. He begins with Poincaré the essayist, whose lucid and trenchant writings became best-sellers and yet had

such depth and substance that the young Albert Einstein remembered being "breathless with excitement for weeks" as he read them. These accessible, popular works were the most visible signs of Poincaré as a public intellectual. Gray's skillful treatment of them gives a nice point of entry for general readers, who then are poised to read his overview of Poincaré's career. This includes Poincaré's practical activities in geodetic mapping and wireless telegraphy as well as his involvement in a few debacles (such as the discredited "N-rays," an elusive phenomenon that he endorsed for a time).

After devoting the first 200 pages to these eminently accessible topics, Gray then turns to more difficult and technical matters. He structures his account around certain pivotal episodes, such as the 1880 prize competition that crowned Poincaré's mathematical work or the problem of the celestial mechanics of three bodies, to which Poincaré contributed signally. Gray shows his mettle by the care and depth with which he has read a vast range

of technical writings by Poincaré and others. As he deals with this difficult material, Gray demonstrates a notable ability to give detailed and yet clear, succinct accounts, synthesizing and summarizing formidably technical issues.

Still, given the range of topics across mathematics and physics, many general readers will find the rest of the book quite challenging. Gray presents this technical material frankly, rather than avoiding its difficulties. He offers brief explanations to help the reader grab a foothold, along with useful appendices and a glossary. He always tries to keep the narrative going, rather than merely listing theorems. Although different readers may wish for more help at different points, what Gray manages to convey may be more remarkable than what remains obscure. In particular, his treatment of Poincaré's work in topology inspires the hope that these ideas are worth struggling to understand, especially the larger vista, the underlying project, behind the plethora of details.

Poincaré himself characteristically steered his abstract mathematics toward physical and practical issues. We learn from Gray that Poincaré's deepest concerns were for mathematical physics, that he valued intuition at least as much as rigor, and that he was always asking, whether in practical or theoretical matters, "How do you know that?" Indeed, the nature of knowledge was Poincaré's greatest concern in philosophy, which he brought also to his

work on physics. Gray gives an engrossing account of Poincaré's long involvement with many sides of physics, from the theory of electricity and magnetism (including very practical questions of telegraphy and transmission), through his independent approach to a relativistic theory, to his fascination, late in life, with the emergent quantum theory.

Despite his many brilliant interventions and mathematical virtuosity, Poincaré, Gray argues, made no great discovery in physics. Nonetheless, Gray emphasizes that for Poincaré "there is no valid or clear distinction to be made between mathematics and physics because the two are so intimately entangled." Gray shows us the full dazzling sweep of what Poincaré accomplished, including the work on dynamical systems and chaos that only came into its own in recent years. A tour de force, Gray's masterful treatment will long remain an invaluable

**Henri Poincaré:  
A Scientific Biography**

by **Jeremy Gray**

Princeton University Press,  
Princeton, NJ, 2013.  
608 pp. \$35, £24.95.  
ISBN 9780691152714.



Poincaré at 57.

The reviewer is at St. John's College, 1160 Camino de la Cruz Blanca, Santa Fe, NM 87505–4511, USA. E-mail: ppesic@mail.sjcsf.edu

CREDIT: FROM (4) COURTESY PRINCETON UNIVERSITY PRESS

able resource for all who want to understand Poincaré, so embedded within his times and yet so far ahead of them.

#### References

1. J. Gray, *Ideas of Space: Euclidean, Non-Euclidean, and Relativistic* (Oxford Univ. Press, Oxford, ed. 2, 1989).
2. J. Gray, *The Hilbert Challenge* (Oxford Univ. Press, Oxford, 2000).
3. J. Gray, *Plato's Ghost: The Modernist Transformation of Mathematics* (Princeton Univ. Press, Princeton, NJ, 2008).
4. H. Poincaré, *Oeuvres de Henri Poincaré* (vol. 11, Gauthier-Villars, Paris, 1954).

10.1126/science.1235655

## TECHNOLOGY AND SOCIETY

# The Lost Phone

Joseph B. Bayer

The mobile phone is missing from Rich Ling's *Taken for Grantedness: The Embedding of Mobile Communication into Society*. This is not to say the book is not about mobile communication. The mobile phone is missing because we are no longer aware of its presence. Mobile communication is now simply communication. To make this argument about the changing nature of our social structure, Ling (a sociologist at IT University of Copenhagen) advances a novel framework for understanding the transition from innovation to integration.

The book is Ling's third solo undertaking on the role of mobile communication in everyday life. In its predecessor, he illustrated the power of mobile communication technology to strengthen close ties among people (1). His current foray is bolder and more sprawling. The level of analysis verges on macrosociology, as he moves away from the academic microsociology that characterized much of his earlier work. Although he still uses interviews and focus-group data to map out phenomena, the scope of the work no longer centers on personal relationships. Rather, the concept of taken for grantedness presumes a societal scale.

Ling begins by arguing that three seemingly unrelated innovations—the clock, the car, and the cell phone—each represent what he terms social mediation technologies. These

tools “enable, but also set conditions for, the maintenance of our social sphere.” In framing the contrast with the more established developments of mechanical timekeeping and the automobile, the book aptly underscores the prominence of the mobile device. Ling does not claim these three innovations are the only social mediation technologies (for example, he also notes online calendar systems), but his case-study approach does elicit questions of theoretical purview. Ultimately, Ling sways between developing a theory of mobile communication as a distinct taken-for-granted technology and a wider theory on the nature of taken for grantedness across these particular social technologies.

An amalgam of perspectives—including recent theories on domestication and mobility and not-so-recent theories from a number of sociological greats (e.g., Emile Durkheim, Max Weber)—informs Ling's framework. This diverse collection of ideas works well overall, although it was surprising to find Pierre Bourdieu's highly germane concept of habitus absent from the discussion. For each social mediation technology, Ling divides the process of reaching taken for grantedness into the stages of diffusion, legitimation, social ecology, and reciprocal expectations. This format can be repetitive, but his sociological style of brief subsections and participant excerpts reads smoothly. It is clear that some of the interviews are a bit dated, and at times Ling relies on teen data while making generalizations across generations. However, these concerns do not detract from his core argument. The global approach serves to stress the effects of mobile communication on social structure more broadly.

The first three stages of the theory establish how these tools have rewired human communication and interaction. The crux of Ling's argument, though, is rooted in how this rewiring affects our reciprocal expectations as members of society. We now take it as a given that others abide by a standard system of time, drive a car in the suburbs, and carry a mobile phone. And as Ling reminds us, if we do not commit to these rules, we become a problem for others. Hence, the effects of reciprocal expectations expose an unconscious architecture of interactional rules—flowing through technological middlemen such as the mobile phone.



The book effectively documents the integration of these technologies into the fundamental structure of society, yet the author could have further developed the theoretical implications of this broader process. Ling demonstrates that interpersonal communication no longer equals meeting at a specific space and time; it is flexibly instinctive. In turn, one wonders whether it is the mobile phone that has become embedded or the underlying access to information in the present. His conclusion, however, is more a commentary on the state of social capital than a full realization of the concept of taken for grantedness. In general, Ling's emphasis appears to be on how we got here as opposed to where we are going. At the same time, the book raises important questions about voids that exist, or will exist, in our social ecology. What other social mediation technologies could alter the basic arrangement of communication and reach the state of taken for granted?

With *Taken for Grantedness*, Ling shows that the mobile phone is missing from our stream of consciousness—that is, until it is missing from our pockets. The book articulates how contemporary society depends on the seamless synthesis of mobile communication, timekeeping, and transportation. Thus, by demonstrating how ordinary mobile communication has become, Ling unveils how integral it is to the collective human psyche. Whereas many facets of new media are dynamic, the core elements of mobile communication, such as expectations of accessibility, are immobile. In a sense, the book represents a declaration of the permanence of mobile communication, as forecast by the author in 2004 (2). The mobile phone, once a harbinger of the changing world, is now lost in the ebb and flow of the quotidian.

#### References

1. R. Ling, *New Tech, New Ties: How Mobile Communication Is Reshaping Social Cohesion* (MIT Press, Cambridge, MA, 2008).
2. R. Ling, *The Mobile Connection: The Cell Phone's Impact on Society* (Morgan Kaufmann, San Francisco, 2004).

10.1126/science.1235516

**Taken for Grantedness**  
The Embedding of  
Mobile Communication  
into Society  
by Rich Ling  
MIT Press, Cambridge, MA,  
2012. 255 pp. \$34, £23.95.  
ISBN 9780262018135.

The reviewer is at the Department of Communication Studies, University of Michigan, 5370 North Quad, Ann Arbor, MI 48109-1285, USA. E-mail: joebayer@umich.edu



# Drug Patents at the Supreme Court

C. Scott Hemphill and Bhaven Sampat\*

U.S. pharmaceutical patent policy is poised for a major review by the U.S. Supreme Court. Later this month, the Court will hear a case, *Federal Trade Commission (FTC) v. Actavis, Inc.*, about a tactic alleged to be illegal by U.S. regulators, so-called “reverse payment” settlements of patent litigation. A maker of a branded drug pays a “generic” drug maker offering a competing, unbranded version of a drug, to abandon its challenge of the branded firm’s patent. This tactic has also received regulatory scrutiny in Europe (1, 2). The Court’s ruling promises to reset the innovation/access balance for drugs, whatever the result. We explain the stakes of the case, and how settlements of “secondary” patents affect that balance.

In 1984, the U.S. Congress enacted the Hatch-Waxman Act to balance incentives for drug innovation against robust consumer access. The act enables generics to challenge branded firm patents that they believe were erroneously issued (invalid) or impertinent (not infringed), under the theory that such patents ought not deprive consumers of low-priced generic drugs. Cheaper generic drugs have saved purchasers billions of dollars per year—an estimated \$1 trillion in the United States over the past decade, according to an industry-sponsored study—which makes such drugs a powerful way to keep down health-care costs (3).

Under rules created by the act, a generic must wait until patent expiration or assert that one or more branded patents are invalid or not infringed. That challenge is an act of patent infringement, which often prompts the brand to file a lawsuit to prevent the generic’s product launch. The outcome of that suit—including a settlement—determines when the generic firm can enter the market.

Since 1984, branded firms have substantially stepped up their patenting efforts, in an effort to postpone the loss of exclusivity. In the United States, patents per drug roughly doubled for the cohort of drugs approved between 2000 and 2002

compared with drugs approved between 1985 and 1987 (4). Multiple patents with overlapping terms result in a longer nominal term of protection. In Europe, the trend is similar (1).

## Secondary Patents

Part of this growth reflects a rise in secondary patents. These provide regulatory protection to ancillary aspects of drug innovation—such as particular drug formulations and compositions—beyond the core, traditional protection, a patent on a novel active ingredient. Secondary patents have become a focus of branded patenting and a major focus for generics’ efforts to enter the market before patent expiration. Such patents are viewed as less effective bars to generic entry, compared with active ingredient patents (5, 6). Secondary patents are thought to be less likely to meet legal standards of patent validity. Their prevalence, notwithstanding this, reflects the fact that the Patent and Trademark Office (PTO) generally provides only a limited review of patent applications, which is driven by resource constraints and incentives facing examiners. It is also easier for generic firms to avoid infringement by inventing around secondary patents, for example, by devising alternative formulations. For these reasons, generic firms’ challenges to these patents are likely to be on stronger footing, a point on which we provide empirical evidence below.

Previous work suggests that secondary patents, particularly late-expiring ones, are disproportionately targeted for preexpiration challenge by generic firms (7). Such challenges serve a potentially valuable role, subjecting a questionable patent to a second look after issuance. This is important given the relatively cursory review provided by the PTO. Aside from reducing prices sooner, the second look may have a salutary effect on innovation, channeling innovative efforts toward

Arguments for paying generic drug makers to abandon patent challenges may rest on dubious assumptions.

new chemical entities (which typically have “strong” active ingredient patents) and away from incremental improvements (which rely more on secondary patents). That channeling is valuable, provided that litigation tends to validate more deserving innovations.

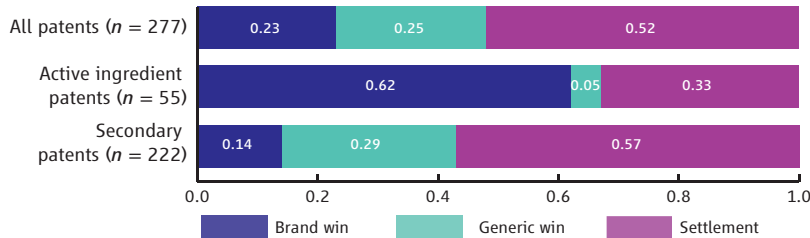
## Reverse Payment Settlements: Disrupting the Balance?

Beneficial effects of patent challenges can be lost by postchallenge settlements. Consider AndroGel, the drug at issue in the Supreme Court case. AndroGel is a testosterone replacement therapy manufactured by Solvay. In 2003, two drug makers—one of which was later bought by Actavis—sought to introduce generic versions of the drug. Although AndroGel is protected by a patent that expires in 2021, the generics challenged this patent as invalid, and not infringed by the proposed generic products (8). After the challenges, Solvay sued for patent infringement. In 2006, the parties settled. Under the settlement, generic AndroGel will not be available until 2015, compared with 2006 or 2007 if the patent had been found invalid or not infringed.

The FTC, which brought suit to prohibit the deal, alleges that Solvay made large payments to the generics, in violation of antitrust law, to induce them to abandon patent challenges and to delay entry for 9 years. The FTC argues that such deals, which are increasingly common (9), harm drug purchasers by prolonging the period of monopoly profits enjoyed by a branded firm. Such settlements have yielded >\$12 billion in estimated overcharges since 1993 (10).

Branded drug makers argue that a relaxed approach to reverse payment settlements is desirable because higher profits promote essential research and development (R&D) that lead to new drugs (11). In defense of

settlements, representatives of both branded and generic firms have pointed to outcomes of lawsuits that do not settle. Often, the branded firm wins (12, 13), which results in generic entry at patent expiration. In a case where the branded firm would probably win, it is argued, a settlement with



Outcomes for all drugs first eligible for patent challenge between 2000 and 2008.

Columbia Law School; Health Policy and Management, Columbia University, New York, NY 10032 USA.  
\*Corresponding author. bns3@columbia.edu

a late entry date may reflect the expectations of the parties (14). The more that settlements pertain to cases the branded firm will probably win, the less we ought to worry about reverse payment settlement as disrupting the second level of review provided by patent challenges and litigation (15).

### Settlement and Secondary Patents

These arguments are amenable to empirical analysis (16). Previous empirical work (10) collected public information about identified settlements with evidence of payment. For each drug in this data set, we collected information about which patents were litigated and settled. Each patent was coded, on the basis of whether at least one claim covered an active ingredient, by using the method outlined in (7). If not, the patent was coded secondary (17).

For the patents at issue in settled litigation, 89% were secondary patents (18). Far from offering generic entry earlier than under the presumed likely outcome, a brand win, reverse payment settlements usually limit early entry on patents that would otherwise result in a generic firm win. There is therefore serious concern that settlement unduly delays generic entry, harming consumers and potentially distorting R&D incentives.

This conclusion rests on the premise that active ingredient patents are more likely than secondary patents to be found valid and infringed. Some secondary patents are found valid and infringed, and some active ingredient patents are not (19). To evaluate this generalization, we collected information on completed patent litigation on all drugs that first became eligible for challenges between 2000 and 2008. The litigation covers 277 patents and 147 drugs. For each patent, we determined the outcome of litigation at the district/trial court level: brand win, generic win, or settlement, and coded the patent as described above.

Of the 48% of cases litigated to completion (not settlement), the branded firm nearly always wins a suit asserting an active ingredient patent (92%), but usually loses asserting secondary patents (32% wins) (see the chart). This is consistent with the generalization that active ingredient patents are indeed more likely to be found valid and infringed.

For 52% of cases, settlement is the result. Not all settlements in this data set involve reverse payments; we use these data only to assess win rates for different types of patents when litigated to completion. As win rates can be hard to interpret when there is an option to settle (20), we examined litigation in an era when settlements were less

common, before 2006 (21). For this subset ( $n = 25$ ), all patents were litigated to completion. The branded firm won every dispute involving active ingredient patents and lost nearly all secondary patent litigation (14% wins). These results are consistent with the full sample; generic challengers are likely to prevail on secondary patents if litigated to completion.

We have shown that reverse payment settlements disproportionately focus on secondary patents, and that, consistent with previous qualitative characterizations of these patents, secondary patent challenges are usually won by generics when litigated to completion. This challenges the argument that reverse payment settlements should be tolerated because they are on patents that brands are likely to win. Reverse payment settlements, focused on patents where the generic likely would have prevailed, interrupt the valuable patent-testing process when generic drug makers challenge patents before expiration. Such settlements are most disruptive in the very context, secondary patents, where this testing is most important.

If the FTC wins its case, we can expect fewer settlements with entry-delaying payments and a consequent increase in early consumer access to lower-priced generic drugs. Reverse payment settlements on secondary patents would be replaced by either procompetitive settlements or litigation, where we would expect a high degree of generic success. Some settlements with payments will survive, because the FTC's proposed rule allows drug makers to justify a payment by proving that it was made for unrelated services, not delay; defensible in light of the avoided litigation expense; or otherwise procompetitive.

If the Court endorses reverse payment settlements, we can expect delayed generic competition until the patent expires, even for drugs whose patent protection is weak. There might seem to be a benefit, with additional profits enjoyed by branded firms fueling new innovation. But this argument can be applied to any other conduct, even illegal, such as price-fixing, that raises branded profits.

Our results uncover a further critique, that this bonus accrues mainly to secondary, less important aspects of innovation. Thus, reverse payment settlement (if permitted by the court) can be expected to primarily benefit follow-on formulations and other forms of innovation covered by secondary patents. We doubt whether distortion in favor of secondary innovation is desirable, particularly given concerns about the slowdown in production of new chemical entities. At a minimum, it is this selective subsidy that settle-

ment advocates must explain and defend, not any subsidy to R&D generally.

### References and Notes

- European Commission, *Pharmaceutical Sector Inquiry Final Report* (EC, Brussels, 2009).
- J. Kanter, K. Thomas, *New York Times*, 1 February 2013, p. B1.
- IMS Health, *An Economic Analysis of Generic Drug Usage in the United States* (IMS Health, Falls Church, VA, ed. 4, 2012).
- C. S. Hemphill, B. N. Sampat, *J. Empirical Legal Stud.* **8**, 613 (2011).
- A. Gal, S. Nikhil, Predicting para IV: Generic companies have the upper hand in formulation patent cases (Bernstein Research, New York, 2007).
- C. Correa, Guidelines for the examination of pharmaceutical patents (Working Paper, WHO, Geneva, 2007).
- C. S. Hemphill, B. N. Sampat, *J. Health Econ.* **31**, 327 (2012).
- The contested patent does not cover the compound testosterone or the synthesis of artificial testosterone, the patent protection to which expired decades ago. The patent covers particular formulations of testosterone.
- FTC, Agreements filed with the FTC under the Medicare Prescription Drug, Improvement, and Modernization Act of 2003: Overview of agreements filed in fiscal year 2012—A report by the Bureau of Competition (FTC, Washington, DC, 2013).
- C. S. Hemphill, *Columbia Law Rev.* **109**, 629 (2009).
- W. J. Tausz, testimony before U.S. Senate Committee on the Judiciary, 17 January 2007.
- For example, settlement defenders point to a recent analysis (13), which suggests that branded firms win a majority of cases. This study does not distinguish between patent types.
- RBC Capital Markets, *Pharmaceuticals: Analyzing Litigation Success Rates* (RBC CM Research Publ., Toronto, 2010).
- B. Dickey, J. Orszag, L. Tyson, *Ann. Health Law* **19**, 367 (2010).
- The FTC rejects special dispensation for settlements in cases the branded firm is likely to win. In its view, a large payment secures less competition than the branded firm could expect by asserting the patent alone in litigation or settlement. Whether the branded firm would likely win or lose, a large payment disrupts the alignment of interest in early entry ordinarily shared by the generic firm and drug purchasers—the generic firm is compensated for accepting the delay, but purchasers are not.
- We evaluate defenses of reverse payment settlements that rely on assumptions about brand and generic win rates, also the implications of settlements on innovation incentives. Settlement advocates offer other defenses, including that a payment is sometimes necessary to induce a procompetitive settlement and thereby economize on litigation costs. Assessing these is beyond the scope of this paper.
- The method reflected a strict approach to active ingredient patents: A patent claim covering a particular enantiomer, polymorph, or salt did not qualify.
- This calculation omits three patents where the settlement was a variant on the standard reverse payment agreement (100% secondary) and five patents where the settlement occurred after a district court judgment (60%).
- A. Gal *et al.*, How watertight are composition-of-matter patents? Judge rules Baraclude's CoM patent is invalid (Bernstein Research, New York, 2013).
- G. Priest, B. Klein, *J. Legal Stud.* **13**, 1 (1984).
- In 2005, a U.S. appeals court decision, *FTC v. Schering-Plough Corp.*, signaled increased judicial tolerance for reverse-payment settlements.

**Acknowledgments:** A grant from the Public Health Law program of the Robert Wood Johnson Foundation supported this research. We thank K. Shadlen for comments.

### Supplementary Materials

[www.sciencemag.org/cgi/content/full/339/6126/1386/DC1](http://www.sciencemag.org/cgi/content/full/339/6126/1386/DC1)

10.1126/science.1235857



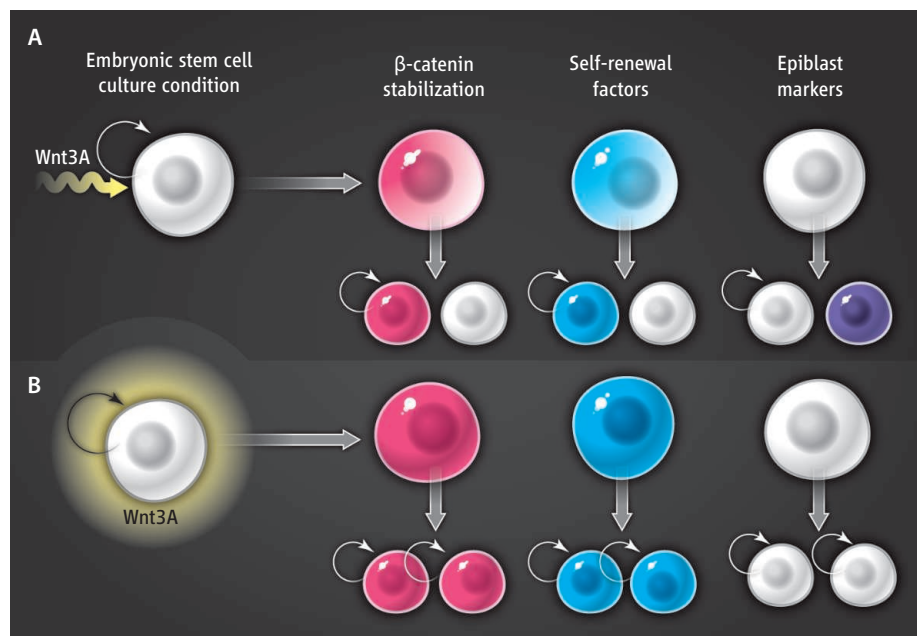
# Making a Point with Wnt Signals

J. D. Berndt<sup>1</sup> and R. T. Moon<sup>1,2</sup>

Embryonic stem cell division is influenced by the spatial orientation of the cells relative to the source of Wnt protein.

The Wnt family of secreted proteins is critical for cell fate specification during embryonic development and in adult stem cell niches. Wnts control diverse processes including body plan determination and tissue patterning, and aberrant Wnt signaling can lead to developmental abnormalities and disease, including cancer (1–3). It has long been suspected that Wnts act in a concentration-dependent manner. However, difficulty in purifying active recombinant Wnt proteins and the reduced activity displayed by Wnts expressed with epitope tags have hampered investigations into the role of localized Wnt signals. On page 1445 in this issue, Habib *et al.* (4) describe a technical advancement that allows cells to be exposed to a point source of Wnt. Such restricted Wnt activity induces polarization of embryonic stem (ES) cells and triggers asymmetric cell division, producing daughter cells with two distinct cell fates.

ES cells can differentiate into any cell type in the body. This pluripotent state is afforded by the repression of genes associated with cell fate determination. Wnt activates a cell signaling cascade (the canonical Wnt– $\beta$ -catenin pathway) that maintains pluripotency and self-renewal of mouse ES cells (5). Habib *et al.* observed that exposing an ES cell to Wnt3A molecules that are covalently attached to carboxylic acid–coated superparamagnetic beads enriched Wnt pathway components in the region of the cell nearest to the bead. These included the Wnt co-receptor, LRP6, and the intracellular proteins  $\beta$ -catenin and adenomatous polyposis coli (APC). After cell division, the daughter cell in contact with the Wnt3A bead had a greater amount of  $\beta$ -catenin protein (reflecting greater activation of Wnt signaling) than the distal daughter cell. Wnt3A beads were sufficient to orient the mitotic spindle in the parent stem cell and led to inheritance of the parent centriole by the daughter cell in contact with the bead. There was also asymmetric inheritance of proteins associated with pluripotency—such as the transcription regulatory proteins Rex1 and Nanog—whereas



**Orienting cell division.** (A) A point source of Wnt3A leads to the asymmetric inheritance of  $\beta$ -catenin, proteins associated with self-renewal and pluripotency, and markers of differentiation. (B) Bath application of Wnt3A promotes symmetric distribution of these factors and results in two daughter cells with equally pluripotent cell fates.

the daughter cell distal to the Wnt3A bead expressed markers of an epiblast cell, a more lineage-restricted fate (see the figure). Collectively, these findings indicate a role for Wnts in the self-renewal of ES cells and raise the question of additional signaling mechanisms downstream of Wnt receptor activation that control this process.

One key issue is the ability of localized Wnt3A to promote asymmetric division in other stem cells, including human ES cells. However, unlike in mouse ES cells, activating Wnt– $\beta$ -catenin signaling in human ES cells inhibits self-renewal and promotes differentiation (5, 6). This difference may reflect a closer resemblance of human ES cells to the mouse epiblast state, a slightly later developmental stage (7). Habib *et al.* show that the daughter cell distal to the Wnt3A bead adopted hallmarks of epiblast fate and had less  $\beta$ -catenin protein (reflecting less Wnt signaling). Genetic methods have been used to revert human ES cells to a more naïve state (7), thereby creating a tractable model for comparing localized Wnt activation in mouse and human ES cells. In addition to ES cells, other types of stem

cells may respond to localized Wnt activity. Induced pluripotent stem cells, intestinal stem cells of the colon crypt, and hair follicle stem cells also use Wnt– $\beta$ -catenin signaling to balance pluripotent and differentiated states (2, 3, 8). It will be interesting to assess whether Wnt3A beads can also induce asymmetric division in these cells.

What are the mechanisms by which localized Wnt3A stimulation leads to asymmetric inheritance of Wnt pathway components and pluripotency proteins? One possibility is that Wnt3A beads activate local signaling through Wnt receptor clustering. “Signalosomes” (or multiprotein complexes involved in transducing a signal) have been detected in cells treated with Wnt3A (9). Wnt pathway components, including LRP6, Dishevelled, Frizzled, and AP2-clathrin, are found in Wnt-mediated LRP6 signalosomes (9, 10). However, signalosome formation does not require LRP6 (11), unlike downstream  $\beta$ -catenin activation. This implies that additional signaling mechanisms exist. Studies on invertebrates support this hypothesis. In the worm *Caenorhabditis elegans*, mutations in Wnt pathway genes—e.g., *Wnt/mom-2*, *Frizzled/*

<sup>1</sup>Department of Pharmacology, Institute for Stem Cell and Regenerative Medicine, University of Washington School of Medicine, Seattle, WA 98109, USA. <sup>2</sup>The Howard Hughes Medical Institute, Seattle, WA 98109, USA. E-mail: rtmoon@uw.edu

*mom-5*, and *Dishevelled/dsh-2/mig-5*—lead to defects in mitotic spindle orientation and cell fate specification of blastomere and other cell types (11). Normally in these cells, the homolog of the transcription factor that binds to  $\beta$ -catenin, *TCF/pop-1*, is asymmetrically enriched in one daughter cell. However, mutations in *TCF/pop-1* itself disrupt cell fate determination but have no effect on orientation of the mitotic spindle, indicating that Wnts act through a transcription-independent mechanism for initial cell polarization (11). Habib *et al.* did not assess TCF-family members in mouse ES cells nor perform loss-of-function studies for  $\beta$ -catenin or TCF. Thus, it is unknown whether there is a transcriptional requirement for the ability of Wnt3A to polarize ES cells. There are notable differences in the biochemical details between the vertebrate Wnt– $\beta$ -catenin pathway and the *C. elegans* Wnt asymmetry pathway (12). It remains to be determined whether any aspects of this signaling are evolutionarily conserved.

Another possible mechanism of Wnt-dependent asymmetry involves the interaction between the canonical Wnt– $\beta$ -catenin signaling pathway and the Wnt–planar cell polarity (Wnt-PCP) signaling pathway,

which can polarize cells (13). Wnts that affect Wnt-PCP signaling, such as Wnt5A, can antagonize Wnt– $\beta$ -catenin signaling (14). Habib *et al.* found no effect of Wnt5A beads alone; however, when dividing ES cells were bathed in Wnt5A, the ability of Wnt3A beads to promote asymmetry was inhibited. As cells in vivo are often exposed to multiple different Wnts, it will be informative to characterize the behavior of ES cells exposed to multiple beads with different Wnts acting through the Wnt–PCP and Wnt– $\beta$ -catenin pathways. Alternatively, recapitulating Wnt3A-mediated asymmetry with microfluidic gradients (15) would make it possible to examine cell behavior in antiparallel or orthogonal concentration gradients of Wnts with opposing activities.

The study of Habib *et al.* is a modern response to questions posed by developmental biologists since the late 1800s and early 1900s regarding spatial asymmetries in informational molecules. Even after 30 years of study, molecular details of Wnt signaling are still being uncovered. Indeed, on page 1436 of this issue, Cruciat *et al.* (16) identify an RNA helicase (DDX) as part of the Wnt pathway, and on page 1441, Huang *et al.* (17) report that an enzyme (receptor

interacting protein kinase 4) interacts with a Wnt receptor to control signaling. As our understanding of Wnt signaling keeps expanding, and experimental approaches to dissect the details improve, manipulating the Wnt pathway as an effective treatment for disease may become a greater possibility.

## References

1. N. Perrimon, C. Pitsouli, B. Z. Shilo, *Cold Spring Harb. Perspect. Biol.* **4**, a005975 (2012).
2. J. Schuijers, H. Clevers, *EMBO J.* **31**, 2685 (2012).
3. E. Fuchs, T. Chen, *EMBO Rep.* **14**, 39 (2013).
4. S. J. Habib *et al.*, *Science* **339**, 1445 (2013).
5. D. ten Berge *et al.*, *Nat. Cell Biol.* **13**, 1070 (2011).
6. K. C. Davidson *et al.*, *Proc. Natl. Acad. Sci. U.S.A.* **109**, 4485 (2012).
7. J. Hanna *et al.*, *Proc. Natl. Acad. Sci. U.S.A.* **107**, 9222 (2010).
8. A. Marson *et al.*, *Cell Stem Cell* **3**, 132 (2008).
9. J. Bilić *et al.*, *Science* **316**, 1619 (2007).
10. I. Kim *et al.*, *J. Cell Biol.* **200**, 419 (2013).
11. T. D. Walston, J. Hardin, *Semin. Cell Dev. Biol.* **17**, 204 (2006).
12. B. M. Jackson, D. M. Eisenmann, *Cold Spring Harb. Perspect. Biol.* **4**, a007948 (2012).
13. R. S. Gray, I. Roszko, L. Solnica-Krezel, *Dev. Cell* **21**, 120 (2011).
14. M. A. Torres *et al.*, *J. Cell Biol.* **133**, 1123 (1996).
15. E. Cimetta *et al.*, *Lab Chip* **10**, 3277 (2010).
16. C. M. Cruciat *et al.*, *Science* **339**, 1436 (2013); 10.1126/science.1231499.
17. H.-D. Huang *et al.*, *Science* **339**, 1441 (2013); 10.1126/science.1232253.

10.1126/science.1236641

## APPLIED PHYSICS

# Robotic Walking in the Real World

Melany L. Hunt

Movement of robots over rough or unstable terrain is an outstanding challenge, especially for tasks such as remote planetary exploration, but animals manage such locomotion tasks every day. For example, in a natural environment, a lizard can traverse a sandy or pebbled surface in such a way that its limbs can push and move individual grains, which allow its limbs to penetrate beneath the surface of the loose layer. On page 1408 of this issue, Li *et al.* (1) present experiments and modeling of a biologically inspired, six-legged robotic device that was designed to move efficiently across a bed of dry, loose granular material. Based on the mechanics data, simulations were developed to identify designs that maximized walking speed.

The authors quantified the effect of the

limb intrusion by measuring the lift and drag forces on a simulated leg (a small rigid plate) as it entered and was extracted from loose surfaces at different orientations to the granular surface. In the current experiments, flat beds of glass beads or poppy seeds were used. These measured forces were used to model the stresses, given the assumption that the stress was linearly dependent on depth within the layer and independent of the speed of intrusion.

The authors then used the stress relations to compute the forces, the overall movement, and the forward speed versus time of their robot. These simulations were then compared with experimental measurements for a range of stride frequencies and differing leg shapes. From their simulation methodology, the authors note that the design of the robotic legs can be optimized for speed—in this case, a maximum speed of 72 cm/s for a forward C-shaped leg at a stride frequency of 5 Hz.

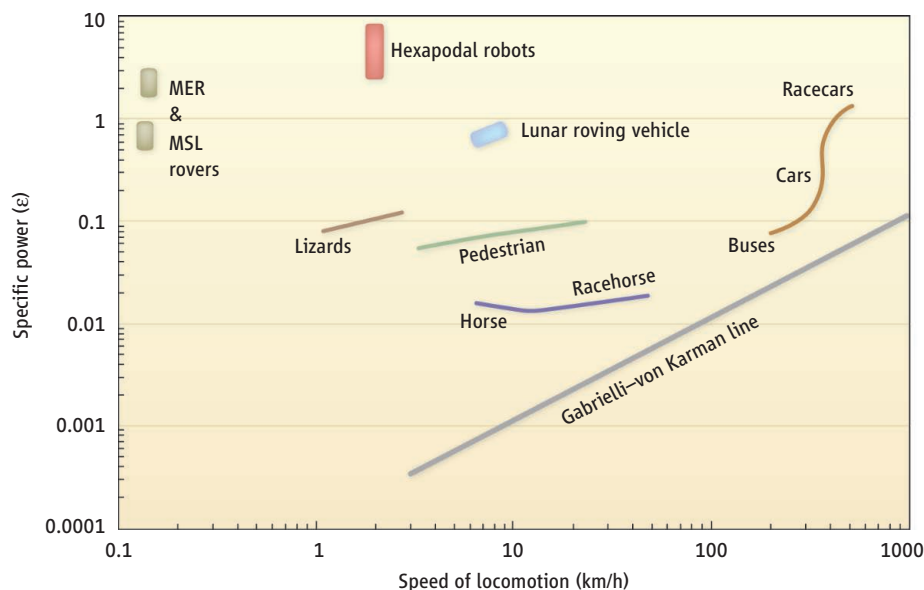
Studies of the mechanical stresses on plates moving through loose materials were used to simulate and optimize robot locomotion over soft ground.

This field of research is often described as terramechanics, the study of vehicle performance relative to its terrain (1–3). Terramechanics includes the locomotion of small robots (1, 4) and lizards (5), as well as the transport of off-road vehicles (2, 3), tractors, military tanks, the Lunar Roving Vehicle (LRV) used in Apollo missions in the early 1970s (6), and martian rovers, including the Mars Exploration Rovers (MER) launched in 2003 (7) and the Mars Science Laboratory (MSL) that landed in August 2012 (8). The work by Li *et al.* used the term “terradyamics” to emphasize the potential movement of the deformable terrain.

In terramechanics or terradyamics, the vehicle locomotion depends critically on the transmission of forces between the deformable terrain and the wheels, tracks, or legs of the vehicle. As illustrated by Li *et al.*, the mathematical relations for the forces are often unknown and depend on the local state of the granular material, the properties of the

Division of Engineering and Applied Science, California Institute of Technology, Pasadena, CA 91125, USA. E-mail: hunt@caltech.edu





grains, and the deformation rate (or speed of the intrusion) of the material. This study and others have demonstrated that the vehicle performance in terms of energy efficiency and speed depends critically on the terrain properties (2–4, 9). The terrain conditions may also prohibit vehicle motion, as was the case with the MER rover Spirit that ended its 6-year, 7.7-km journey across a rich variety of martian topography when it breached a thin surface crust and became embedded in underlying loose soil (10).

Early developments in terramechanics are often credited to the work by Bekker (2). His 1960 text on off-road locomotion began with a figure showing the vehicle power per weight as a function of locomotion speed. Similar information based on the dimensionless specific power,  $\epsilon$ , is shown in the figure. As was done in the original figure by Bekker, the figure here includes the Gabrielli–von Karman line, which was first presented in 1950 as an empirical fit of the best performance (lowest  $\epsilon$ ) for a range of vehicles (air, water, and ground) and speeds (10). Unlike the original Gabrielli–von Karman plot, Bekker's figure included animals and off-road vehicles to emphasize that vehicles and creatures traversing sands and soils have lower performance than when operating on hard, flat surfaces.

The figure includes data for pedestrians, horses, cars, and buses from Gabrielli and von Karman (11) and updated by Yong *et al.* (12); in addition, the figure presents measurements of the specific mechanical power of a walking lizard (5); the measured specific power for hexapod robots on a flat frictional and rough surfaces (4); and the specific power of the LRV and the MER

and MSL rovers based on electrical power, loads, and speeds (6–8). Overall, the performance of our machines does not match that of the walking animals. Hence, a better understanding of the underlying terrain such as that provided by the study by Li *et al.* may improve the performance of roving and walking robots.

**Getting over the ground.** The figure compares the dimensionless specific power  $\epsilon$ , the vehicle power normalized by a product of the gross weight and the speed, with locomotion speed. The Gabrielli–von Karman line is an empirical fit of best performance data. Walking machines are still outperformed by animals, but the analysis by Li *et al.* may help in efforts to improve robot locomotion.

## References

1. C. Li, T. Zhang, D. I. Goldman, *Science* **339**, 1408 (2013).
2. M. G. Bekker, *Off-the-Road Locomotion: Research and Development in Terramechanics* (University of Michigan Press, Ann Arbor, 1960).
3. J. Y. Wong, *Theory of Ground Vehicles* (Wiley, New York, ed. 3, 2001).
4. U. Saranli, M. Buehler, D. E. Koditschek, *Int. J. Robot. Res.* **20**, 616 (2001).
5. C. T. Farley, T. C. Ko, *J. Exp. Biol.* **200**, 2177 (1997).
6. S. F. Morea, The Lunar Roving Vehicle—Historical Perspective, Proc. 2nd Conference on Lunar Bases and Space Activities, NASA Conference Publications 3166, 1 619–632 (1988).
7. J. A. Crisp *et al.*, *J. Geophys. Res.* **108**, 8061 (2003).
8. J. P. Grotzinger *et al.*, *Space Sci. Rev.* **170**, 5 (2012).
9. C. Li, P. B. Umbanhowar, H. Komsuoglu, D. E. Koditschek, D. I. Goldman, *Proc. Natl. Acad. Sci. U.S.A.* **106**, 3029 (2009).
10. R. E. Arvidson *et al.*, *J. Geophys. Res.* **115**, E00F03 (2010).
11. G. Gabrielli, T. von Karman, *Mech. Eng.* **72**, 775 (1950).
12. J. Yong, R. Smith, L. Hatano, S. Hillmans, *Ingenia* **22**, 46 (2005).

10.1126/science.1235276

## MEDICINE

# Spatial Turn in Health Research

Douglas B. Richardson,<sup>1</sup> Nora D. Volkow,<sup>2</sup> Mei-Po Kwan,<sup>3</sup> Robert M. Kaplan,<sup>4</sup> Michael F. Goodchild,<sup>5</sup> Robert T. Croyle<sup>6</sup>

Developments in geographic science and technology can increase our understanding of disease prevalence, etiology, transmission, and treatment.

**S**patial analysis using maps to associate geographic information with disease can be traced as far back as the 17th century. Today, recent developments and the widespread diffusion of geospatial data acquisition technologies are enabling creation of highly accurate spatial (and temporal) data relevant to health research. This

has the potential to increase our understanding of the prevalence, etiology, transmission, and treatment of many diseases.

New approaches in geography and related fields, capitalizing on advances in technologies such as geographic information systems (GIS), the Global Positioning System (GPS), satellite remote sensing, and computer cartography, are often referred to collectively as geographic information science (1, 2). GPS and related systems make it possible to integrate highly accurate geographic location and time with virtually any observation. GIS provides the means to store, share, analyze, and visualize real-time and archived spatial data. It also permits the integration of multiple layers of interdisciplinary spatial data, such as health, environmental, genomic, social, or demo-

<sup>1</sup>Association of American Geographers (AAG), 1710 16th Street, NW, Washington, DC 20009, USA. <sup>2</sup>National Institute on Drug Abuse, National Institutes of Health, Bethesda, MD 20852, USA. <sup>3</sup>Department of Geography and Geographic Information Science, University of Illinois at Urbana–Champaign, Urbana, IL 61801, USA. <sup>4</sup>Office of Behavioral and Social Sciences Research, National Institutes of Health, Bethesda, MD 20892, USA. <sup>5</sup>Department of Geography, University of California, Santa Barbara, CA 93106, USA. <sup>6</sup>Division of Cancer Control and Population Sciences, National Cancer Institute, Rockville, MD 20852, USA. E-mail: drichardson@aag.org

graphic data, for interactive spatial analysis and modeling.

Spatial and spatiotemporal statistical methods (3), such as multilevel analysis, spatial data mining, and agent-based modeling, provide ways of relating health and disease to specific genetic, epigenetic, and environmental factors (4). The density, accuracy, and specificity of current geospatial data also facilitate sophisticated spatial and spatiotemporal analysis and the modeling of complex spatial health processes at the level of the individual rather than the aggregate (5, 6) (see the figure). Research based on data-intensive real-time GPS/GIS methods with miniaturized “wearable” environmental and biomedical monitors is generating advances in exposure assessment, as well as in mobility and obesity studies (7). In addition to individual interventions, this research can lead to outcomes such as the design of healthier environments, which enhance access to parks and quality foods, and better treatment programs for a wide range of health conditions, from asthma to diabetes.

GIS visualization and analytical tools also enable researchers to identify spatial patterns and to model specific processes of disease diffusion or contagion, such as of pandemic influenza viruses, or evolving genetic strains of hepatitis or tuberculosis.

Researchers have integrated patient demographics, daily activities, and HIV viral concentrations to map and model changing spatial patterns of HIV infections and their relationships to health care treatment programs (8), or to social risk factors (9). Researchers have also used GIS data, spatial statistics, and interactive mapping to identify HIV concentration hotspots near the Mexico–U.S. border (10). This kind of GIS-based analysis enables proactive and timely delivery of tailored prevention and treatment strategies, such as HIV testing, antiretroviral therapy intervention, and education to the affected communities.

Geospatial data on health and social environments have also been used to provide information about health disparities. Using GIS-based ethnic density measures and spatial data on mothers’ residential locations, a recent study of infant health inequalities among Bangladeshi immigrant women in New York City found that their infants were most vulnerable to poor health outcomes, such as low birth weight, when living either in very isolated settings or in areas of the highest ethnic density (11).

With real-time interactive GPS/GIS functionality (12) now increasingly embedded in cell phones and low-cost navigation and other mobile devices, individual citizens also are contributing to the flow of health-

related geospatial data. These activities are variously referred to as participatory GIS, crowdsourcing, or volunteered geographic information (13). Despite unresolved issues of privacy and quality assurance, the ability to access georeferenced data from millions of people could be transformative.

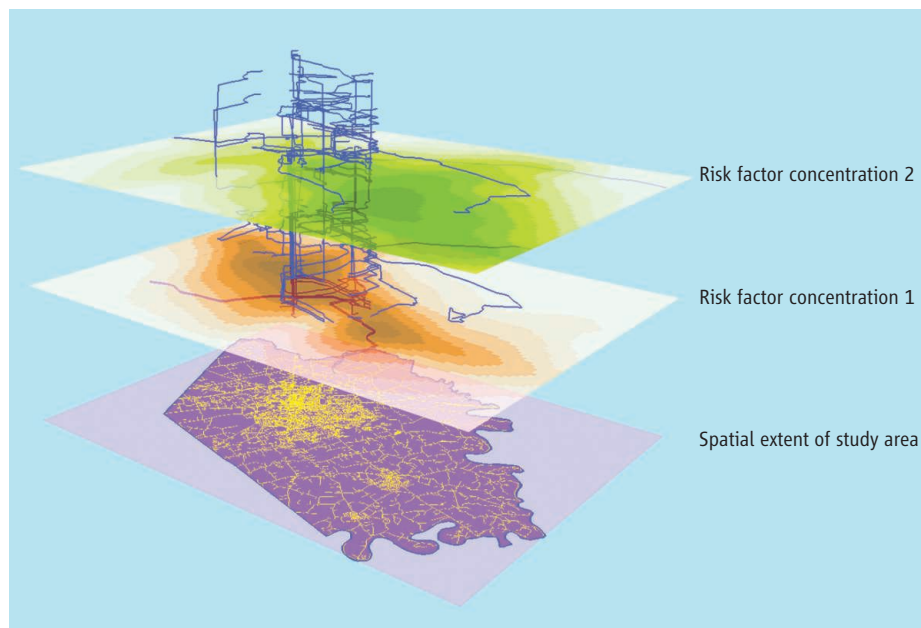
For example, by analyzing data from 15 million mobile-phone subscribers, Wesolowski *et al.* (14) could examine the complex interactions between human and animal movements and the spread of malaria in Kenya. From Japan to California, volunteers with GPS-enabled real-time air-quality monitoring systems are assessing exposures to air pollution and radiation at spatial resolution levels and data densities not previously feasible (15).

Better institutional and educational models for successfully integrating the spatial dimension into health research and practice are needed to achieve the full benefits of these new capabilities in a timely manner (16, 17). There is also an urgent need for the creation of distributed, interoperable spatial data infrastructures to integrate health research data across and within disparate health research programs. In addition to fostering standards and scientific access, such large-scale spatial data infrastructures are themselves powerful new resources for generating and testing hypotheses, detecting spatial patterns, and responding to health threats.

Ongoing collaborations between the NIH and the Association of American Geographers are addressing key technical and institutional challenges (e.g., standards, interoperability, common terminology, data confidentiality) to facilitate the generation, coordination, and use of the rapidly growing body of geospatial health data (18). Research agendas that systematically incorporate spatial data and analysis into global health research hold extraordinary potential for creating new discovery pathways in science (19).

#### References and Notes

1. M. F. Goodchild, *J. Spat. Inf. Sci.* **1**, 3 (2010).
2. D. Richardson, in *Geographic Information Science and Technology Body of Knowledge*, D. DiBiase *et al.*, Eds. (Association of American Geographers, Washington, DC, 2006), pp. vii–x.
3. N. A. C. Cressie, C. K. Winkle, *Statistics for Spatio-Temporal Data* (Wiley, New York, 2011).
4. R. Feil, M. F. Fraga, *Nat. Rev. Genet.* **13**, 97 (2011).
5. M.-P. Kwan, *Soc. Sci. Med.* **69**, 1311 (2009).
6. M.-P. Kwan, *Ann. Assoc. Am. Geogr.* **102**, 958 (2012).
7. S. N. Zenk *et al.*, *Health Place* **17**, 1150 (2011).
8. M. K. Smith, K. A. Powers, K. E. Muessig, W. C. Miller, M. S. Cohen, *PLoS Med.* **9**, e1001260 (2012).
9. M. Das *et al.*, *PLoS ONE* **5**, e11068 (2010).
10. K. Brouwer *et al.*, *Ann. Assoc. Am. Geogr.* **102**, 1190 (2012).



**Exposure assessment with GPS/GIS data of individuals.** Life paths of individuals collected with GPS/GIS methods can provide more accurate assessment of exposures to environmental or social risk factors when integrated with detailed GIS data about the spatial and temporal variations of these risk factors (20). Life paths of individuals are shown as trajectories that unfold along the vertical axis, which represents time; the bottom horizontal plane represents the spatial extent and transportation network of the study area. The green and orange horizontal planes illustrate the spatial distribution of risk factor concentrations (e.g., traffic-related air pollution, carcinogenic substances, liquor stores) for two time points.



11. S. McLafferty, M. Widener, R. Chakrabarti, S. Grady, *Ann. Assoc. Am. Geogr.* **102**, 893 (2012).
12. T. Mauney, A. Kong, D. Richardson, Interactive automated mapping system. U.S. Patent 5,214,757 (1993).
13. P. Mooney, P. Corcoran, B. Ciepluch, *J. Ambient. Intell. Human. Comput.* 10.1007/s12652-012-0149-4. (2012).
14. A. Wesolowski *et al.*, *Science* **338**, 267 (2012).
15. T. B. Fang, Y. Lu, *Ann. GIS* **18**, 279 (2012).
16. J. D. Mayer, *Soc. Sci. Med.* **50**, 937 (2000).
17. C. Scott, P. F. Robbins, A. C. Comrie, *Ann. Assoc. Am.*

*Geogr.* **102**, 977 (2012).

18. Y. F. Thomas, D. Richardson, I. Cheung, Eds., *Geography and Drug Addiction* (Springer, Berlin, 2008).
19. L. W. Pickle, M. Szczur, D. R. Lewis, D. G. Stinchcomb, *Int. J. Health Geogr.* **5**, 51 (2006).
20. M. P. Kwan, *Ann. GIS* **18**, 245 (2012).

**Acknowledgments:** Supported in part by the National Cancer Institute of the National Institutes of Health (R13CA162823), the National Science Foundation (BCS-

1244691), and the National Science Foundation of China (41228001). The content is solely the responsibility of the authors and does not necessarily represent the official views of the National Institutes of Health, the National Science Foundation, or the National Science Foundation of China. We thank J. McKendry, W. Compton, B. Deeds, D. Berrigan, Z. Tatalovich, and J. Wertman for contributions to AAG-NIH collaborative efforts.

10.1126/science.1232257

## CELL BIOLOGY

# Dynamin Flexibility Drives Fission

Ronald W. Holz

A study of short dynamin assemblies provides clues to the mechanism of cellular fission.

An unresolved issue in cell biology concerns the mechanisms by which lipid bilayers remodel in fission and fusion reactions in vesicular trafficking pathways. An important step in understanding comes from the report by Shnyrova *et al.* on page 1433 of this issue (1), which investigates the mechanism by which the dynamin guanosine triphosphatase (GTPase) catalyzes fission when bound to lipid tubes in vitro.

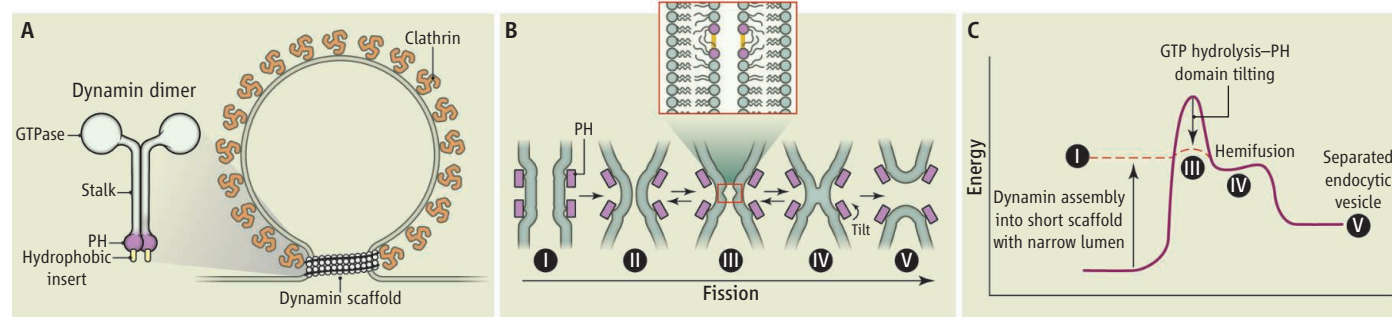
Dynamin has an established role as a master controller of fission during endocytosis. It forms a helical ring around the necks of budding endocytic vesicles (see the figure, panel A), triggering increased GTP hydrolysis and membrane remodeling lead-

min dimers with 12 to 13 dimers per turn. Interactions between neighboring rungs stimulate a large increase in GTPase activity, which is required for fission and causes scaffold disassembly.

Various structural changes in dynamin assemblies have been suggested to explain how GTP hydrolysis stimulates fission (3, 4). However, the micrometer-long dynamin scaffolds used in these studies could lead to cooperative interactions that may not occur in the much shorter assemblies at the fission neck during endocytosis (see the figure, panel A). To overcome this problem, Shnyrova *et al.* measured the conductance of the aqueous lumen of dynamin scaffolds

3.8 nm (see the figure, panel B), comparable to the thickness of the hydrophobic core of the bilayers (4 nm). This estimate is consistent with previous work and indicates that in the absence of GTP, the energy arising from dynamin assembly on the nanotube stabilizes the highly stressed lipids but cannot overcome the hydration barrier to fission (5).

The conductance measurements also revealed that the minimal dynamin scaffold that supports fission had a length of 20 nm. Because the pitch of the dynamin helix is ~12 nm, fission requires only two or three dynamin rungs. This length is sufficient to permit interaction of adjacent rungs to stimulate GTPase activity.



ing to fission. Although its function in situ is regulated through interaction with numerous proteins, dynamin alone is sufficient to catalyze fission in vitro. Dimeric dynamin (panel A, inset) binds through its pleckstrin homology (PH) domains to the phospholipid PIP<sub>2</sub> (phosphatidylinositol 4,5-bisphosphate) in lipid membranes (2) and reshapes bilayers into narrow tubes. Dynamin also has a strong affinity for preformed, highly curved PIP<sub>2</sub>-containing membranes, permitting assembly of spiral bands of dyna-

min dimers with 12 to 13 dimers per turn. Interactions between neighboring rungs stimulate a large increase in GTPase activity, which is required for fission and causes scaffold disassembly.

The measurements revealed the intermediates before fission with high precision and millisecond time resolution and allowed detection of the very shortest of dynamin assemblies. When no GTP was present, dynamin caused stepwise decreases in conductance without fission, whereas when GTP was present, dynamin caused a fluctuating conductance that ultimately led to fission. From the conductance changes upon addition of dynamin, the authors infer a luminal diameter of the squeezed nanotube of

**Catalytic function of dynamin in fission.** (A) Emerging clathrin-coated vesicle with a two-rung dynamin scaffold. The GTPase domains from adjacent rungs interact to greatly increase GTP hydrolysis, which is required for fission. (Inset) Dynamin dimer. (B) Sequence of events leading to fission [from fig. S10 in (1)]. Dynamin assembly constricts lipid neck (I). GTP hydrolysis causes flexibility in the short scaffold, resulting in tilting of the inserted PH domain (II–IV) as the combined scaffold-lipid system finds its lowest energy as a hemifusion stalk (IV). Fission spontaneously occurs from the hemifusion intermediate (V). (C) Energy landscape of the lipid tube during catalysis of fission by dynamin (1). Roman numerals refer to intermediates; the dashed line indicates the new energy landscape during GTPase hydrolysis.

Pharmacology Department, University of Michigan Medical School, Ann Arbor, MI 48109, USA. E-mail: holz@umich.edu

Ten percent of fission events were preceded by brief excursions to zero conductance, indicating reversible closing of the already narrow tube. The rapid fluctuations reflect the catalytic function of dynamin to reduce the kinetic barrier between the open and closed tube (see the figure, panel C). These fluctuations are much too rapid for disassembly of the dynamin scaffold (6). Because the closed state is nonconducting and reversible, the authors suggest that the flickering reflects transitions between a highly constricted but conducting neck and a metastable hemifission stalk (see the figure, panel B) (5, 7). Full fission occurs when the hemifission intermediate separates into unconnected bilayers.

How does dynamin catalyze the transition of the luminal hydrated polar head groups to a hemifission stalk? Shnyrova *et al.* found a clue when they studied a dynamin construct with a mutation in the hydrophobic membrane-inserting variable loop 1 of the PH domain. The mutant behaves similarly to the wild type, forming narrow nanotubes and short, dynamic scaffolds in the presence of GTP. However, in con-

trast to wild-type protein, the mutant did not support fission of nanotubes containing low PIP<sub>2</sub> concentrations. Insertion into and deformation of the outer monolayer leaflet is thus likely to be a central feature of the catalytic pathway.

The critical fission intermediate is neither purely lipidic nor purely proteinaceous but a combination of the two. Modeling indicates that if the assembled dynamin scaffold becomes sufficiently flexible to allow tilting of the inserted PH domains, the combined scaffold-lipid system relaxes to its lowest energy and thereby reduces the energy barrier to a hemifission stalk. This concept contradicts previous notions that GTPase activity applies force to further squeeze the lipid tube. Increased scaffold flexibility could result from hydrolysis-dependent conformational changes (8) occurring stochastically among the ~12 activated GTPases along a single scaffold rung. It is also favored by continuous GTPase activity, which prevents long assemblies. The importance of scaffold flexibility for membrane fission requires experimental verification.

Flickering also occurs not only in fission but also during fusion between the narrow conducting neck of the initial fusion pore and a zero conductance state (9). The similar geometries of the fusion pore and the fission neck suggest similar catalytic principles. In fact, dynamin may also play a role in secretion. It can stabilize the initial fusion pore (10) and could conceivably lower the transition barrier to a hemifusion state.

#### References and Notes

1. A. V. Shnyrova *et al.*, *Science* **339**, 1433 (2013).
2. S. M. Sweitzer, J. E. Hinshaw, *Cell* **93**, 1021 (1998).
3. S. M. Ferguson, P. De Camilli, *Nat. Rev. Mol. Cell Biol.* **13**, 75 (2012).
4. S. Morlot *et al.*, *Cell* **151**, 619 (2012).
5. P. I. Kuzmin, J. Zimmerberg, Y. A. Chizmadzhev, F. S. Cohen, *Proc. Natl. Acad. Sci. U.S.A.* **98**, 7235 (2001).
6. R. Ramachandran, S. L. Schmid, *EMBO J.* **27**, 27 (2008).
7. Y. Kozlovsky, L. V. Chernomordik, M. M. Kozlov, *Biophys. J.* **83**, 2634 (2002).
8. J. S. Chappie *et al.*, *Cell* **147**, 209 (2011).
9. A. Albillos *et al.*, *Nature* **389**, 509 (1997).
10. A. Anantharam *et al.*, *Mol. Biol. Cell* **22**, 1907 (2011).

**Acknowledgments:** Supported by NIH grant R21-NS073686. I thank M. A. Bittner and A. Ngatchou-Weiss for helpful discussions.

10.1126/science.1236005

## PLANETARY SCIENCE

# Probing an Extrasolar Planet

Mark S. Marley

With about 3000 known and candidate planets, and the pace of discovery increasing, the era of exoplanets is well into its golden age. Discoveries by the Kepler mission and numerous ground-based surveys have spawned statistical surveys of bulk planet occurrence rates, masses, and sizes, and provide insight into planet formation processes. However, the gold standard for exoplanet characterization—spectra of light that has interacted with a planet's atmosphere—remains elusive. Reliable spectra have been obtained for only a handful of planets, either at low spectral resolution or over narrow wavelength ranges. More numerous broadband photometric observations seldom uniquely identify specific atmospheric constituents, and such data are usually open to multiple interpretations. On page 1398 of this issue, Konopacky *et al.* (1) report the highest-quality spectrum yet obtained for any extra-

solar planet, providing firm constraints on the atmospheric composition of the directly imaged young gas giant planet HR 8799c.

Although the atmospheres of the giant planets in our solar system are predominantly composed of hydrogen and helium, they are enriched relative to the Sun in elements heavier than helium. The atmosphere of Jupiter, which was directly sampled by the Galileo entry probe, is enhanced in carbon, nitrogen, and sulfur by about a factor of 3 over solar abundance (2). Less massive Saturn is enhanced in carbon by a factor of 7 (3), and there are hints from measurements of transiting planets that such enhancements of heavy elements are also typical for extrasolar giant planets (4). The two most popular giant planet formation mechanisms—core accretion and gravitational instability—make different predictions for atmospheric elemental abundances. The enhancements of specific elements thus provide a fingerprint of the planet formation process.

The particular molecule within which an atom, such as carbon, is found depends

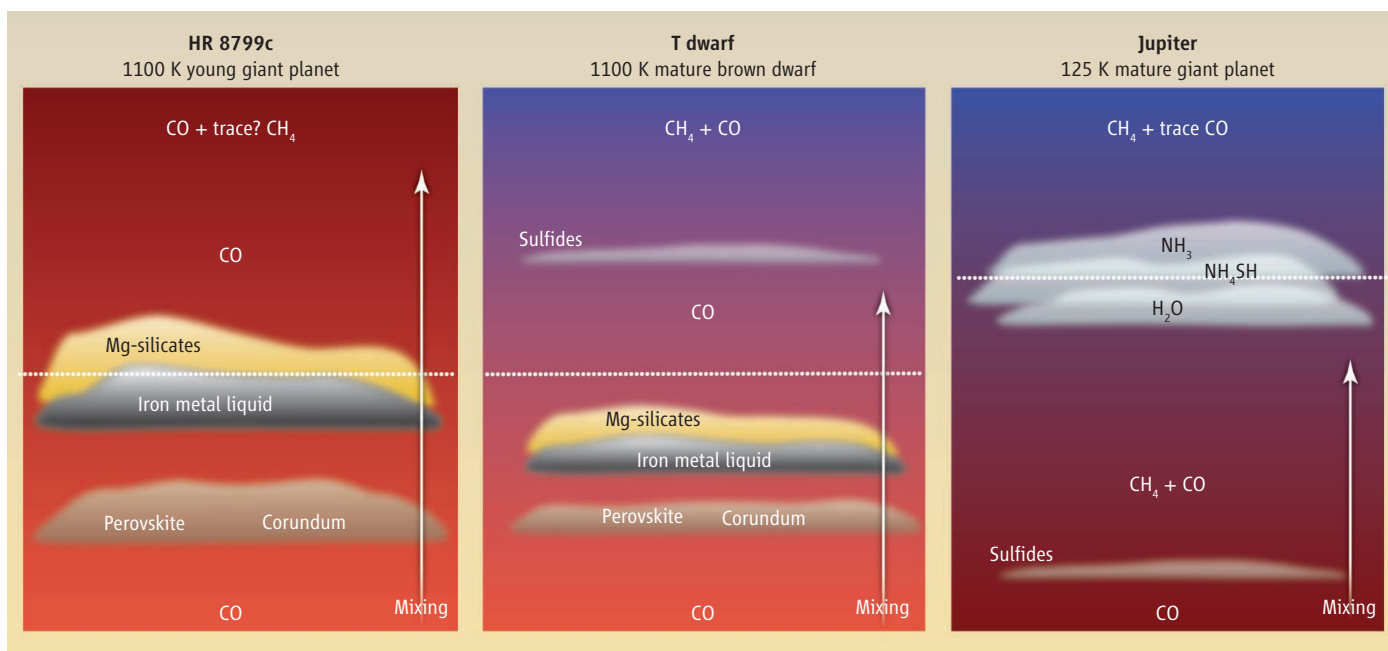
High-resolution spectroscopic observations of the atmosphere of an exoplanet provide constraints on its origin.

on the local temperature and pressure conditions. Equilibrium chemistry predicts that carbon in the atmosphere of Jupiter or a warm extrasolar planet should be found as CH<sub>4</sub>. It has long been known, however, that atmospheric mixing (5) delivers carbon as excess CO from Jupiter's deeper and warmer layers to the observable atmosphere. Similar disequilibrium excesses of CO and N<sub>2</sub>—resilient molecules found at high-temperature, high-pressure conditions—are also known in the atmospheres of brown dwarfs (6).

Spectroscopy, by measuring the abundance of molecules, thus helps to reveal both ancient planetary origins and modern atmospheric dynamics. But high-quality spectral observations for extrasolar planets have so far been sparse. The best available data have been for the transiting hot Jupiters HD 209458b and HD 189773b, for which a few atomic species and molecules have been reported (7–9). However, photochemical processes and planetary winds seem to dominate these highly irradiated atmo-

Space Sciences Division, NASA Ames Research Center, Moffett Field, CA 94035, USA. E-mail: mark.s.marley@nasa.gov





**Atmospheric mixing.** Conceptual views of the atmospheres of HR 8799c, a more massive brown dwarf, and the colder Jupiter. The composition of major cloud layers and the principal C-bearing molecules are noted; CO serves as a tracer of atmospheric mixing. Dotted lines denote approximate depth of the visible atmosphere. Vigorous vertical updrafts likely contribute to both the observed thicker cloud layers and the apparent overabundance of CO in the warm exoplanet atmosphere.

spheres, making the retrieval of atmospheric composition for these planets difficult and at times controversial. Because transiting planets in small orbits are the least difficult to characterize, questions of atmospheric composition and mixing and of planetary origin are unlikely to be systematically addressed solely by the known transiting planets.

Directly imaged planets, in contrast, are detected much farther from their primary stars, typically at a distance of tens of astronomical units with today's technology. Because they appear as distinct points of light, their spectra can be individually obtained, without need of a differential measurement to pull a spectral line out of an overwhelmingly bright stellar spectrum. The best-studied directly imaged planets are the four young gas giants orbiting the nearby A star HR 8799 (10, 11). These planets have masses in the range of 5 to 10 Jupiters. But data for these objects have been limited mostly to broadband photometry and low-resolution spectra (12, 13). Konopacky *et al.* used adaptive optics and an integral field spectrograph on the Keck II telescope, which records a near-infrared spectrum at each pixel, to obtain a high-quality spectrum

of planet c, the brightest of the four. The spectrum is the best ever obtained for any exoplanet and rivals that typically acquired on solar system planets not long ago.

The spectrum of HR 8799c reveals individual spectral features of both H<sub>2</sub>O and CO. Methane, which was expected at the atmospheric temperatures inferred for this planet, is not seen despite a strong spectral feature lying in this bandpass. With both H<sub>2</sub>O and CO detected, Konopacky *et al.* are able to estimate the bulk atmospheric carbon-to-oxygen ratio and find that it differs from that of the primary star, which leads them to speculate that the planet was most likely formed by core accretion rather than gas instability. This interpretation is still somewhat uncertain, but similar direct measurements for many such directly imaged planets will shed light on the planet formation process.

Furthermore, the lack of detectable CH<sub>4</sub> implies that vertical mixing must strongly affect the atmosphere of the young exoplanet by delivering CO to observable layers and removing methane (see the figure). There are also indications that iron and silicate cloud layers, which were widely expected to have dissipated by such temperatures, are nonetheless present in the planet's atmosphere. Strong vertical mixing may thus both thicken and preserve the clouds (13) and alter the expected carbon chemistry (12).

These new observations herald the era of characterization of the atmospheres of directly imaged extrasolar planets. The Gemini Planet Imager destined for the Gemini telescope (14) and the SPHERE

coronagraph headed to Europe's Very Large Telescope (15) will obtain spectra for dozens of young giant planets on a variety of orbits encircling stars of varying ages, compositions, and spectral types. NASA is currently studying space-based coronagraphs that will be capable of imaging and characterizing older, colder, and more solar system-like giant planets in reflected light. By measuring atmospheric abundances for a diversity of planets other than those roasting in the overpowering light of their primary stars, it will be possible to constrain atmospheric composition, vertical mixing, cloud dynamics, and, most important, formation mechanisms for entire classes of extrasolar planets.

## References

1. Q. M. Konopacky, T. S. Barman, B. A. Macintosh, C. Marois, *Science* **339**, 1398 (2013); 10.1126/science.1232003.
2. M. H. Wong, P. R. Mahaffy, S. K. Atreya, H. B. Niemann, T. C. Owen, *Icarus* **171**, 153 (2004).
3. F. M. Flasar *et al.*, *Science* **307**, 1247 (2005).
4. N. Miller, J. J. Fortney, *Astrophys. J.* **736**, L29 (2011).
5. S. S. Barshay, J. S. Lewis, *Icarus* **33**, 593 (1978).
6. D. C. Stephens *et al.*, *Astrophys. J.* **702**, 154 (2009).
7. S. Redfield, M. Endl, W. D. Cochran, L. Koesterke, *Astrophys. J.* **673**, L87 (2008).
8. M. R. Swain *et al.*, *Astrophys. J.* **704**, 1616 (2009).
9. C. J. Grillmair *et al.*, *Nature* **456**, 767 (2008).
10. C. Marois *et al.*, *Science* **322**, 1348 (2008).
11. C. Marois, B. Zuckerman, Q. M. Konopacky, B. Macintosh, T. Barman, *Nature* **468**, 1080 (2010).
12. T. S. Barman, B. Macintosh, Q. M. Konopacky, C. Marois, *Astrophys. J.* **733**, 65 (2011).
13. T. Currie *et al.*, *Astrophys. J.* **729**, 128 (2011).
14. B. Macintosh *et al.*, *Proc. SPIE* **7015**, 701518 (2008).
15. J.-L. Beuzit *et al.*, *Proc. SPIE* **7014**, 701418 (2008).

10.1126/science.1235078

CREDIT: ADAPTED FROM KATHARINA LODDERS/WASHINGTON UNIVERSITY IN ST. LOUIS

## GEOPHYSICS

# Characterizing Giant Landslides

David N. Petley

In the late 19th century, the director of the Geological Survey of Switzerland, Albert Heim, described the massive landslide that in 1881 buried the Swiss town of Elm, with the loss of 115 people (1). Heim proposed that this landslide represented a hitherto unknown type of very large, fast mass movement. The deposits from such landslides—now generally called rock avalanches—have been found in all high mountain areas around the world. On page 1416 of this issue, Ekström and Stark (2) introduce a technique for the detection and characterization of rock avalanches that uses the global seismic monitoring network.

Rock avalanches typically start when a large block of rock becomes detached from a near-vertical cliff face. The detached mass descends to the base of the slope through rapid sliding or freefall. It then transitions into a cohesionless avalanche of rock debris that moves very rapidly (often faster than 50 m/s) downslope. Rock avalanches can travel over very long distances and are extremely destructive. The 2002 Kolka rock avalanche in Russia traveled 19 km and claimed 125 lives before it was stopped by a valley constriction (3). Furthermore, large rock avalanches often block river valleys, leading to the formation of large lakes that can cause devastating debris flows and floods when the dam breaks.

Since Heim's work, the deposits of more than 300 rock avalanches have been documented (4). The mapped rock avalanches are likely to be a small proportion of the total number of events in global mountain chains. However, cataloging of very large terrestrial landslides has relied on manual identification of landslide deposits, which is time-consuming and unsystematic.

In recent years, examination of records from seismic stations close to large landslide events has suggested that these

events generate distinctive seismic signals (5–7). Can the global seismic network be used to detect the occurrence of rock avalanches in real time?

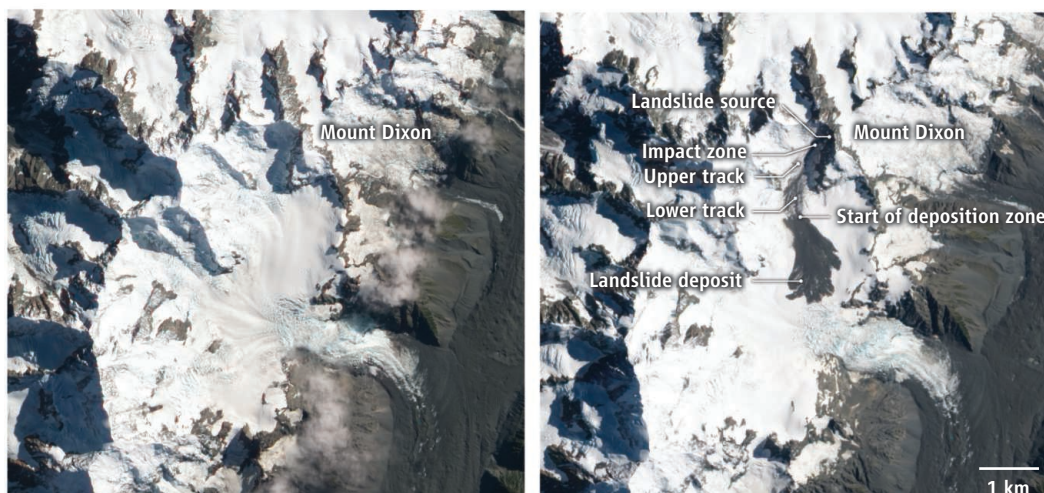
Ekström and Stark introduce a technique that shows that this is indeed viable. Using a dataset of 29 known very large landslides, they have developed an event-detection algorithm that can highlight rock avalanche events worldwide. The technique detects hitherto unreported landslides (e.g., in remote areas of Alaska) and enables rapid reevaluation of reported events—for example, showing that a reported flood event in Nepal was caused by a large rock avalanche (see the figure).

The technique currently overdetects large, fast landslides by an order of magnitude, requiring considerable work, for example, with satellite imagery to filter out the false-positive events. Nevertheless, it opens the way to a true global catalog of rock avalanches that will advance understanding of the dynamics of high mountain areas. It may also enable the real-time detection of large, valley-blocking landslides, providing a warning system for vulnerable communities downstream.

Analysis of global seismic data helps to catalog rock avalanches and understand how they form.

However, the technique's potential extends well beyond the spatiotemporal mapping of very large, fast landslides. Many controlling characteristics of rock avalanches remain unclear. In particular, the travel distances of very large landslides are often larger than classical mechanics would suggest (8), leading to the suggestion that some additional factor operates in these systems that does not operate in smaller mass movements (9). However, there remains considerable controversy about how this long travel distance can be achieved (8).

The great challenge in determining the mechanisms of rock avalanches lies in measuring and reproducing their dynamics. Rock avalanches are unpredictable and short-lived, making it difficult to capture data during such events. Furthermore, the high levels of energy involved means that the instruments usually used to collect landslide data would be destroyed. Considerable work has been undertaken to analyze rock avalanche deposits (10). However, they typically cover large areas to depths of up to 100 m, requiring large and expensive drilling and geophysical explorations. In addition, the deposits tend to capture processes that occur



**Complex dynamics.** Satellite images taken on 13 March 2012 (left) and 5 February 2013 (right) illustrate the scale and complexity of the Mount Dixon landslide in Aoraki/Mount Cook National Park, New Zealand on 21 January 2013. The landslide fell ~500 m from the near-vertical source before fragmenting into a rock avalanche in the impact zone. Video footage taken by a climber suggests that the initial motion was a very rapid rock avalanche, which left almost no deposit while traveling over the glacier. In the lower track, some deposition is seen. At the end of the lower track, the landslide transitioned into a sliding phase and started to deposit, eventually stopping after ~3 km. Until now, interpreting these distinct phases of motion could only be undertaken through analysis of the deposits. The techniques introduced by Ekström and Stark allow direct analysis of the mechanisms.

Department of Geography, Durham University, Durham DH1 3LE, UK. E-mail: d.n.petley@durham.ac.uk



at low velocities, not during the rapid phase of movement (see the figure). Knowledge of these landslides therefore lags behind that of most other geological hazards.

Through analysis of several seismic records from their rock avalanche data set, Ekström and Stark have generated an instrumental data set that records the nature of motion during these events. At this stage the analysis is fairly simple, relying on a set of basic assumptions about the nature of the landslide motion. There is little doubt that these types of analyses will become more mature. However, even the initial study provides important insights.

First, Ekström and Stark have analyzed a large rock avalanche on the flanks of the Siachen Glacier in northern Pakistan in September 2010. Such a landslide would normally be analyzed with satellite imagery. In this case the morphol-

ogy of the deposit would suggest that the event occurred in one or two stages. However, the seismic data analysis shows that it occurred as seven large landslides over 4 days, explaining why the debris traveled a relatively short distance for a rock avalanche event of this volume.

Second, the quantitative measurements extracted from the seismic data for the landslides provide key insights into the mechanisms controlling their motion at different phases of the event. In the case of rock avalanches traveling across glaciers, there is a prolonged phase in which the rate of energy dissipation is so low that no measurable seismic signal is generated. This suggests that—as other recent studies have also found (*11*)—multiphase flows or passage over low-friction surfaces such as ice or smooth bedrock may be important factors in the generation of long-runout landslides.

More than a century after the pioneering work of Heim, it is now possible to start to elucidate the dynamics of these large and fast landslide systems. With high mountain areas being increasingly used by humans, this is an important step.

#### References

1. A. Heim, *Gesell. Zeitschr.* **34**, 74 (1882).
2. G. Ekström, C. P. Stark, *Science* **339**, 1416 (2013).
3. C. Huggel *et al.*, *Nat. Hazard Earth Sys.* **5**, 173 (2005).
4. O. Korup *et al.*, *Earth Planet. Sci. Lett.* **261**, 578 (2007).
5. F. Dammeier, J. R. Moore, F. Haslinger, S. Loew, *J. Geophys. Res.* **116**, F04024 (2011).
6. Z. Feng, *Nat. Hazard Earth Sys.* **11**, 1559 (2011).
7. H. Kao *et al.*, *Landslides* **9**, 557 (2012).
8. F. Legros, *Eng. Geol.* **63**, 301 (2002).
9. T. Davies, M. McSaveney, in *Landslides*, J. Clague, D. Stead, Eds. (Cambridge Univ. Press, Cambridge, UK, 2012), chap. 5.
10. G. B. Crosta, J. J. Clague, *Geomorphol* **103**, 1 (2009).
11. D. Schneider, C. Huggel, W. Haeberli, R. Kaitna, *Earth Surf. Process. Landf.* **36**, 1948 (2011).

10.1126/science.1236165

## DEVELOPMENTAL BIOLOGY

# A Transition in the Middle Ear

Donna M. Fekete<sup>1</sup> and Drew M. Noden<sup>2</sup>

As a mammalian embryo develops, tubular tissues expand rapidly, often displacing resident mesenchymal cells, forming progressively enlarged areas such as the thoracic and abdominal cavities. Mechanistic explanations for such growth usually focus on cell proliferation and shape changes, or layering within the expanding tissue. On page 1453 of this issue, Thompson and Tucker (*1*) reveal that formation of the mammalian middle ear cavity is much more dynamic than thought, involving a programmed rupture of the epithelium and its replacement by a completely different cell type. In identifying two distinct origins of the cells that line the middle ear cavity, the authors overturn a long-held tenet of human embryology in suggesting that the process may be unique to mammals, perhaps in association with the evolution of the three middle ear sound-conducting bones.

The middle ear cavity forms in two phases (2, 3). Bilateral outgrowths of the oral cavity (the first pharyngeal pouches) extend into the future middle ear region. The pouches

become surrounded with mesenchyme composed primarily of neural crest cells, which migrate from the neural groove and arise by a process of epithelial-to-mesenchymal transformation. During a second expansion, the three small bones (ossicles) of the middle ear, and the muscles and blood vessels associated with them, fully incorporate into the middle ear cavity. Aeration of the cavity allows the ossicles to freely move. The embryological connection between the middle ear and oral cavities is retained in the adult as the auditory tube.

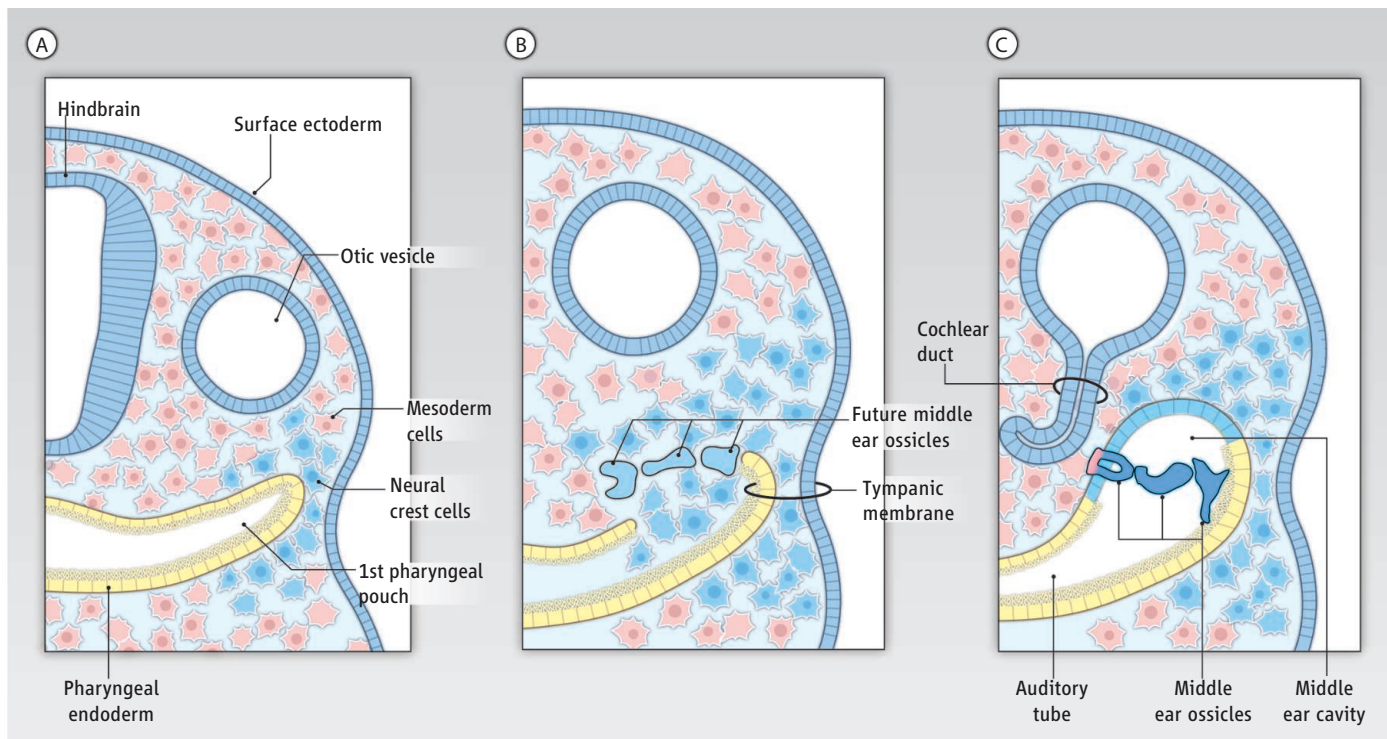
This classical view of the embryological origin of the mammalian middle ear was deduced from static histological images and lineage tracing studies, primarily in birds. However, a 1959 report (*4*) that examined the mastoid sinuses of human fetuses and infants observed that the sinuses become lined with endothelial-like cells that differentiate in situ. Cells lining the auditory tube are columnar and ciliated, a feature common to many embryonic endodermal cells. By contrast, the middle ear epithelial cells are flat and lack cilia. It was argued that these epithelial cells likely share the same mesodermal origin as those lining the sinuses, and must therefore go through a mesenchymal-to-epithelial transition. A rupture of the auditory tube would allow epithelia to

A new view of mammalian middle ear development may prompt reconsideration of its evolution.

directly contact mesenchymal populations and facilitate their merger into a contiguous epithelial sheet. However, this model never gained widespread acceptance.

Thompson and Tucker resurrect the 1959 model using modern cell fate-mapping techniques in the mouse to illustrate just such a dual origin of the middle ear epithelium, and define an unexpected alternative embryological origin for the nonciliated epithelial cells. They show that the upper (dorsal) half of the middle ear cavity is lined with epithelial cells arising from mesenchymal cells of neural crest origin, whereas the lower half and the auditory tube is lined with ciliated endodermal cells. At the tissue level, the cavitation of the middle ear is accompanied by negligible cell death and takes place in two successive steps rather similar to what was described in 1959 (*4*). The first pharyngeal pouch encroaches into the future middle ear region. Its roof then ruptures, and the exposed cavity fills with mesenchymal cells (see the figure). This temporary breach in the endoderm was also observed in the rat (*5*). The mesenchymal cells then retreat dorsally, reestablishing a cavity in the middle ear. During this process, which occurs postnatally in the mouse, mesenchymal neural crest cells transition into an epithelial phenotype and close the

<sup>1</sup>Department of Biological Sciences and Purdue University Center for Cancer Research, Purdue University, West Lafayette, IN 47907, USA. <sup>2</sup>Department of Biomedical Sciences, College of Veterinary Medicine, Cornell University, Ithaca, NY 14853, USA. E-mail: dfekete@purdue.edu; dmn2@cornell.edu



**Middle ear development.** (A) Cells that contribute to the mammalian middle ear (schematic of mouse shown) include loose mesenchymal cells from the neural crest and mesoderm and endodermal cells lining the pharyngeal cavity. As the otic vesicle invaginates from the surface ectoderm (not shown), the first pharyngeal pouch pushes toward the body wall. (B) The tympanic membrane develops as a merger of endoderm, neural crest, and ectoderm cells. Neural crest cells coalesce to form precursors of the middle ear ossicles, followed by a rupture of the endoderm along the upper surface of the pharyngeal pouch. (C) Neural crest mesenchymal cells transform into epithelial cells that fuse with endoderm to repair the lining of the cavity. The middle ear then fills with air through the auditory tube, its connection with the pharynx.

roof of the cavity, but fail to become ciliated. It is unclear whether mesenchymal cells first epithelialize by attaching directly to the ragged edge of the endodermal sheet, or instead epithelialize as small patches that must subsequently be stitched together. The latter process seems advantageous, given a need to also line and aerate the convoluted mastoid sinuses. By the time the process is completed, there is only modest intermingling between the bone fide oral endoderm and the crest-derived epithelia. The same sharpness of boundary is a characteristic of crest-mesoderm interfaces between cartilages and bones elsewhere in the head.

Perhaps the 1959 model faded because the standard textbook model of endodermal expansion, sans accounts of the rupture, was

based on the early stages of middle ear formation in mammals, from which the final outcome was extrapolated without examination of critical intermediate stages. Also, middle ear cavitation in birds apparently does not require a breach in the endoderm (6), and lineage tracing of the neural crest populations in avian embryos failed to note any crest contribution to the middle ear ectoderm (7, 8). It will be interesting to examine sites where ossicles directly abut other tissues. The stapes, which is homologous to the columella of birds and reptiles (9, 10), fuses with mesodermal chondroblasts that form its footplate (11), whereas the malleus contacts the endoderm-derived inner tympanic epithelium. The question is whether these ossicles become encased through primary cavity expansion or the secondary remodeling process that Thompson and Tucker document.

Mesenchymal-to-epithelial transitions occur frequently during embryogenesis, with examples found during somitogenesis and vasculogenesis. Yet, the cellular and molecular mechanisms are not fully characterized, particularly for the neural crest. This includes not only the process of middle ear cavitation, but also the mesenchymal-to-epithelial transitions that give rise to the posterior corneal epithelium (12). These revelations should prompt a reexamination of processes underlying the embryonic expansion of other structures, especially the body cavities, for potential contributions by mesenchymal lineages. The realization that epi-

thelial and mesenchymal lineages are naturally transformable during development further raises possibilities of using mesenchymal stem cells to repair or replace a broader range of tissues.

Motile cilia in the middle ear clear mucus and pathogens out of the cavity and into the throat. When this system breaks down, an infection can arise. This vital role of cilia argues for a thorough description of their distribution and embryological origins in humans. And knowledge of neural crest contributions not only to the ossicles, but also to the middle ear lining, could offer new insights into the causes of congenital anomalies leading to conductive hearing loss.

## References

1. H. Thompson, A. S. Tucker, *Science* **339**, 1453 (2013).
2. M. Mallo, *Dev. Biol.* **231**, 410 (2001).
3. S. C. Chapman, *Front. Biosci.* **16**, 1675 (2011).
4. A. Schwarzbart, *J. Laryngol. Otol.* **73**, 45 (1959).
5. W. F. Marovitz, E. S. Porubsky, *Ann. Otol. Rhinol. Laryngol.* **80**, 384 (1971).
6. T. F. Jaskoll, P. F. A. Maderson, *Anat. Rec.* **190**, 177 (1978).
7. C. S. Le Lièvre, *J. Embryol. Exp. Morphol.* **47**, 17 (1978).
8. D. M. Noden, *Dev. Biol.* **96**, 144 (1983).
9. D. M. Noden, in *Chimeras in Developmental Biology*, N. Le Douarin, A. McLaren, Eds. (Academic Press, London, 1984).
10. U. J. Sienknecht, *Hear. Res.* 10.1016/j.heares.2013.01.019 (2013).
11. H. Thompson, A. Ohazama, P. T. Sharpe, A. S. Tucker, *Dev. Dyn.* **241**, 1396 (2012).
12. M. C. Johnston, D. M. Noden, R. D. Hazelton, J. L. Coulombre, A. J. Coulombre, *Exp. Eye Res.* **29**, 27 (1979).

10.1126/science.1236645



# Detection of Carbon Monoxide and Water Absorption Lines in an Exoplanet Atmosphere

Quinn M. Konopacky,<sup>1,3\*</sup> Travis S. Barman,<sup>2</sup> Bruce A. Macintosh,<sup>3</sup> Christian Marois<sup>4</sup>

Determining the atmospheric structure and chemical composition of an exoplanet remains a formidable goal. Fortunately, advancements in the study of exoplanets and their atmospheres have come in the form of direct imaging—spatially resolving the planet from its parent star—which enables high-resolution spectroscopy of self-luminous planets in jovian-like orbits. Here, we present a spectrum with numerous, well-resolved molecular lines from both water and carbon monoxide from a massive planet orbiting less than 40 astronomical units from the star HR 8799. These data reveal the planet's chemical composition, atmospheric structure, and surface gravity, confirming that it is indeed a young planet. The spectral lines suggest an atmospheric carbon-to-oxygen ratio that is greater than that of the host star, providing hints about the planet's formation.

HR 8799 is a young [ $\sim 30$  million years (My)] (1) early type (A5 to F0) star  $\sim 130$  light years from the Sun. Near-infrared direct imaging with adaptive optics revealed four planets around this star (2, 3). A number of studies have broadly characterized these planets, showing that all four have masses between 5 and 10 times that of Jupiter ( $M_{\text{Jup}}$ ), effective temperatures between 900 and 1200 K (still hot from the gravitational energy released during their formation), and near-infrared colors that are redder than initially expected for their mass and temperature ranges. The red colors are best explained by the presence of iron and silicate atmospheric clouds. These clouds are normally located below the photosphere in old field brown dwarfs with temperatures less than 1400 K, but they are believed to persist at cooler temperatures in young planets where surface gravities are much lower (4–6). Low surface gravity may also contribute to extreme deviations from equilibrium concentrations of CO and CH<sub>4</sub>, potentially explaining the lack of strong CH<sub>4</sub> absorption (7) previously anticipated in young planets. The formation mechanism of the HR 8799 planets—and all exoplanets—remains uncertain, with both global disk instabilities (8) and bottom-up core accretion (9, 10) being proposed. One possible way to differentiate between these is through planetary composition. Planets that form through disk instabilities will track the bulk abundance of the original star-forming material, whereas core-accretion planets may be enhanced or depleted in some elements.

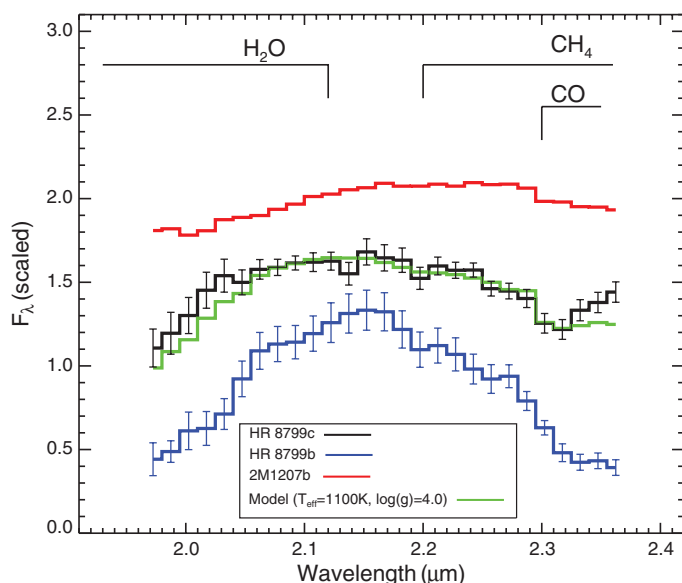
Further inferences on the chemical composition and surface gravity of the HR 8799 planets, and exoplanets in general, have thus far been limited by poor spectral resolution (typically  $\lambda/\Delta\lambda \sim 10$  to 100;  $\lambda$ , wavelength). Here, we present a moderate-resolution ( $\lambda/\Delta\lambda \sim 4000$ ) spectrum of the planet HR 8799c. We obtained our observations of HR 8799c in 2010 and 2011 with the Keck II 10-m telescope, using the integral field spectrograph OSIRIS (OH-Suppressing Infrared Integral Field Spectrograph) (11) in conjunction

with the facility adaptive optics system (12). These observations were obtained in the K band (1.965 to 2.381  $\mu\text{m}$ ) at the finest spatial sampling provided by OSIRIS (0.02" per spaxel). A total of 5.5 hours of observations were obtained, consisting of 33 exposures, each 600 s long. We processed the raw data through sky and dark subtraction, bad pixel removal, and telluric calibration from an A0 stellar standard, and we then transformed these data into data cubes (13). Each data cube has  $\sim 1600$  spectral channels with a 0.32"-by-1.28" field of view at a nominal spectral resolution ( $\lambda/\Delta\lambda$ )  $\sim 4000$  per spatial location.

Scattered starlight in the form of an interference pattern of speckles makes identification of the planet challenging. We used speckle modeling and subtraction (14) for spectral extraction. A key insight is that the residual speckle noise has a characteristic spectral signature: generally broad (500 Å) features passing through the planetary spectrum. This produces highly correlated noise in a low-resolution spectrum over the full band pass, but does not affect the detectability of individual narrow spectral lines. We extracted the spectra from each of the 33 data cubes and combined them into a single spectrum with an average signal-to-noise ratio per channel of  $\sim 30$  (15).

Only a handful of objects with mass and age similar to HR 8799c are known, and broad K-band spectra are available for only a few of these, all with resolutions substantially lower

**Fig. 1.** Low-resolution ( $\lambda/\Delta\lambda \sim 50$ ) binned K-band spectrum for HR 8799c compared with the spectra of HR 8799b and 2M1207b. Binning the data bypasses issues related to the different resolutions and sampling among the three data sets while allowing us to compare broad molecular absorption bands (note that the residual speckle noise is correlated between the individual spectral channels, though this does not affect the analysis here). Each spectrum shows expected broad H<sub>2</sub>O absorption at  $\lambda < 2.15$   $\mu\text{m}$  that appears strongest in HR 8799b.



Whereas CH<sub>4</sub> and CO absorption probably contribute to the downward slope redward of  $\sim 2.15$   $\mu\text{m}$  for HR 8799b (14, 40), their absorption is substantially weaker than is typical for an object near 1100 K. The spectrum of 2M1207b, however, has no discernible contribution from CH<sub>4</sub> and is likely shaped primarily by clouds, H<sub>2</sub>O, and CO opacity (7). The best-fitting model spectrum for HR 8799c, with a temperature of 1100 K and a surface gravity of  $100 \text{ m s}^{-2}$  [ $\log(g) = 4.0$ , cgs units], is shown in green. The best-fitting temperatures and gravities for HR 8799b and 2M1207b are  $\sim 750$  to 1100 K and  $\log(g) \sim 3.5$  to 4.5 (17) and  $\sim 1000$  K and  $\log(g) \sim 4.0$  (7), respectively.  $F_{\lambda}$ , flux in units of wavelength.

<sup>1</sup>Dunlap Institute for Astronomy and Astrophysics, University of Toronto, 50 St. George Street, Toronto, ON M5S 3H4, Canada. <sup>2</sup>Lowell Observatory, 1400 West Mars Hill Road, Flagstaff, AZ 86001, USA. <sup>3</sup>Lawrence Livermore National Laboratory (LLNL), 7000 East Avenue, Livermore, CA 94550, USA. <sup>4</sup>National Research Council of Canada, Dominion Astrophysical Observatory, 5071 West Saanich Road, Victoria, BC V9E 2E7, Canada.

\*Corresponding author. E-mail: konopacky@di.utoronto.ca

than 4000. We compared the extracted spectrum of HR 8799c to the spectrum of a  $\sim 5 M_{\text{Jup}}$  brown dwarf, 2MASS J12073346-3932539b (2M1207b) (16), and the spectrum of the planet HR 8799b (14), all three binned to the same resolution (Fig. 1). HR 8799c falls between 2M1207b and HR 8799b in appearance and, like 2M1207b, has an obvious CO bandhead at  $\sim 2.29 \mu\text{m}$ . The spectral morphology and colors of HR 8799b and 2M1207b also imply the presence of dust clouds in their atmospheres (14, 17, 18). The rough morphological similarity between HR 8799c and these objects implies that HR 8799c also has a cloudy atmosphere. The inference of atmospheric clouds is consistent with results from studies based on the photometry of HR 8799c (2, 17–21), which find that thick dust clouds are necessary to explain its spectral energy distribution.

With the speckles mostly removed, the long-exposure (5.5 hours) data are sufficient to examine the spectrum at the nominal resolution of OSIRIS (Fig. 2). Numerous spectral lines are immediately obvious, particularly those corresponding to strong CO (2,0) and (3,1) band heads at 2.29 and  $2.32 \mu\text{m}$ . The remaining absorption lines are expected to be due to  $\text{H}_2\text{O}$ .

To further verify that the features are, in fact, molecular lines and not residual noise, the spectrum was low-pass filtered. Filtering effectively removes any residual speckle artifacts in the spectrum, as well as the planet's continuum, leaving behind only the absorption lines (Fig. 3) (15). Because the scattered light has roughly the spectrum of HR 8799A, a nearly featureless A-type star, modulated at  $500 \text{ \AA}$  scales by the speckle process, all remaining narrow spectral lines are from the planet. Although many CO and  $\text{H}_2\text{O}$  lines are visible, we did not identify any  $\text{CH}_4$  lines. We cross-correlated the low-pass-filtered planetary spectrum with spectral templates of pure  $\text{H}_2\text{O}$ ,

CO, and  $\text{CH}_4$ . Given the incompleteness of methane molecular line data, we used three popular, yet fairly distinct  $\text{CH}_4$  lists as templates (22–25) (Fig. 3). The cross-correlation confirms that all lines detected in the low-pass-filtered observations are attributable to CO and  $\text{H}_2\text{O}$ .

Two quantities that greatly influence a planet's atmosphere are effective temperature and gravity. The effective temperature of HR 8799c is likely between 900 and 1300 K based on its observed bolometric luminosity ( $L$ ) [ $-4.8 < \log(L/L_\odot) < -4.6$ , where  $L_\odot$  is the luminosity of the Sun] (2) and the range of radii predicted by formation and evolution models (1 to 1.5 Jupiter radii). Dynamical stability requirements of the planetary system require all four planets to be less than  $10 M_{\text{Jup}}$  (2, 26). This mass limit, combined with the above radius range, implies a surface gravity below  $250 \text{ m s}^{-2}$ . Furthermore, the planetary system's youth ( $\sim 30 \text{ My}$ ) (1, 27) and cooling tracks for giant planets indicate a surface gravity between  $\sim 30$  and  $\sim 250 \text{ m s}^{-2}$ .

The upper limit we set on rotation ( $v \sin i$ ; where  $v$  is velocity and  $i$  is inclination of the rotation axis) for HR 8799c is  $\sim 40 \text{ km s}^{-1}$ , which is roughly equal to the resolution of our data, indicating that the cumulative effect of broadening by gravity and rotation is modest. We compared the grid of model spectra from (14), convolved to the nominal OSIRIS resolution ( $\sim 5 \text{ \AA}$ ) and low-pass filtered in the same manner as the observed spectrum, to the drop in flux across the CO (2,0) bandhead, a feature known to be sensitive to gravity (15). Surface gravities of  $\sim 100 \text{ m s}^{-2}$  or less, consistent with the range based on the system's youth and dynamical stability, provide the best match.

We further refined the effective temperature using the K-band spectrum and the surface gravity limit ( $< 100 \text{ m s}^{-2}$ ). The K-band spectrum has

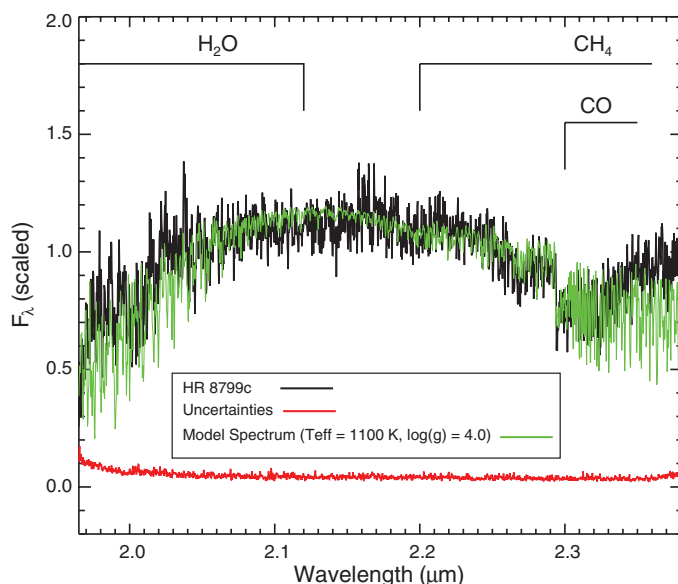
uniformly characterized systematics and uncertainties and contains key features: the overall shape and the CO bandhead depth. Fitting the binned, low-resolution spectrum with a subset of the model grid with  $\log(g) = 3.5$  to 4.0 [centimeter-gram-second (cgs) units;  $g$ , surface gravity] results in effective temperature ( $T_{\text{eff}} = 1100 \pm 100 \text{ K}$ ) (15). The best-matching model (Figs. 1 and 2) produces a cross-correlation peak that exceeds the correlations described above (Fig. 3). The model that best matches our K-band spectrum also compares well to the available photometry, including recent photometry (18), with  $\chi^2$  values equal to or smaller than previously published fits (2, 17–21). Previous results have converged on this temperature and gravity range by fitting photometric observations with broad wavelength coverage (17). For the remainder of the analysis,  $T_{\text{eff}} = 1100 \pm 100 \text{ K}$  and  $\log(g) = 3.5$  to 4.0 (cgs units) are adopted as the most plausible values. The implied mass and age ranges for these values are  $\sim 3$  to  $7 M_{\text{Jup}}$  and  $\sim 3$  to 30 My (hot start models) (28).

Our data require the mixing ratio of  $\text{CH}_4$  to be less than  $\sim 10^{-5}$  (assuming the methane templates are accurate for the strongest lines) (25). At  $T_{\text{eff}} \sim 1100 \text{ K}$ , such a low  $\text{CH}_4$  mixing ratio indicates that vertical mixing has quenched the CO and  $\text{CH}_4$  mole fractions at depths corresponding to their maximum and minimum values, respectively. Though many details concerning vertical mixing of CO and its effect on chemical equilibrium are poorly understood, it is well known that reestablishing equilibrium CO/ $\text{CH}_4$  after CO has been mixed into a normally  $\text{CH}_4$ -rich photosphere can take  $10^5$  to  $10^9$  years (29). Therefore, even modest vertical mixing will quench the CO and  $\text{CH}_4$  (and  $\text{H}_2\text{O}$ ) in the atmosphere where the chemical time scales exceed the mixing time scales (30). Deep quenching requires short mixing time scales ( $t_{\text{mix}} \sim H_p^2/K_{zz}$ , where  $H_p$  is the pressure scale height and  $K_{zz}$  is the eddy diffusion coefficient), which justify the use of a large  $K_{zz} = 10^8 \text{ cm}^2 \text{ s}^{-1}$  in our models.

Of course, the final quenched mixing ratios of CO,  $\text{CH}_4$ , and  $\text{H}_2\text{O}$  all depend on the bulk atmospheric elemental abundances that, so far, have been assumed to be equal to that of the Sun (31, 32). The planetary atmospheric abundances may differ from those of the host star, depending on how the planet formed, adding additional importance to chemical composition.

Under gravitational instability (GI), planets are the product of disk instabilities that gravitationally collapse, and though there are several important stages of the collapse, the planet interior and atmosphere are formed simultaneously with a stellar composition (ultimately, that of the molecular cloud from which the system formed). Deviations from a stellar composition are possible through postformation capture of solid material; however, if the HR 8799 planets are massive ( $> 3 M_{\text{Jup}}$ ), the time scale for substantial planetesimal capture is too short (especially at their current separations) to allow for compositions

**Fig. 2.** K-band spectrum of HR 8799c (black) at the full resolution of OSIRIS ( $\lambda/\Delta\lambda \sim 4000$ ). Both lines and continuum are shown, and the spectral features most relevant to objects of this mass are highlighted. For clarity, uncertainties are shown separately in red. The best-fitting model spectrum is shown in green. A clear drop from CO is detected, along with features typical of the CO bandhead at  $\lambda > 2.29 \mu\text{m}$ . The slight increase in the spectrum at the red end is attributed to residual speckle effects after the attenuation algorithm. Again, broad features from  $\text{CH}_4$  are not easily detected. Spectral data are provided in database S1 (15).





very different from stellar (33). If the HR8799 planets formed by GI, the spectrum of HR8799c should indicate a stellar composition and, in particular, a stellar C/O ratio (assumed to be equal to that of the Sun for HR8799) (34).

Under core accretion (CA), planets form in a multistep process involving the initial formation of a core (on the order of 10 Earth-masses of heavy elements) followed by runaway accretion, primarily of gas supplied by the disk. When the disk is no longer able to supply a substantial amount of material, the newly formed planet is isolated from what remains of the disk. The final atmospheric composition of a planet formed by CA depends on its location within the disk and the contribution of solids during the runaway accretion phase. A variety of compositions are possible (including stellar C/O with sufficient solid accretion), but a nonstellar composition is highly likely for massive giant planets.

Within the disk that formed the HR8799 planets, there are three important boundaries: the H<sub>2</sub>O [~10 astronomical units (AU)], CO<sub>2</sub> (~90 AU), and CO (~600 AU) frost lines. The planets currently orbit their star between 15 and 70 AU; therefore, are all located between the H<sub>2</sub>O and CO<sub>2</sub> lines where the gas-phase C and O abundances in the disk would have been reduced through the formation of ice and carbon and silicate grains (with CO and CO<sub>2</sub> remaining in the gas phase). Therefore, in the CA scenario, planetary atmospheres acquired through gas-only accretion will have substellar C and O abundances but superstellar C/O ratios, because water ice is more abundant than carbon-bearing grains. A simple model of ice formation suggests that the disk gas-phase C/O ratio ~0.9 (35). Increasing the fraction of the atmosphere acquired by solid accretion can lead to superstellar values of both C and O, with the C abundance rising more slowly than that of O, and an overall decrease in C/O (35). Between the CO<sub>2</sub> and CO ice-lines, the abundances follow a similar pattern.

To explore the consequences of nonstellar C and O abundances, we made a grid of planetary atmosphere models following that of Barman *et al.* (14) but using the C and O values predicted by (35) for different ratios of solid to gas accretion, with C/O ranging from 0.45 to 1 (tables S1 and S2). Again, we assumed that the C and O abundances of HR 8799A are solar (15, 32, 34). We found the best fit from this grid of model atmosphere spectra by minimizing  $\chi^2$  (Fig. 4). Though a comprehensive range of C and O values, independent of any disk-chemistry model, has not been explored, the results from these fits suggest that the C/O ratio is certainly less than 1 and not substellar, but is probably larger than the solar/stellar ratio with substellar C and O.

Although it is fairly straightforward to rule out the extrema of C/O ratios, understanding the uncertainty in our C/O measurement is less so. In addition to noise in the data, the uncertainties in temperature and surface gravity also contribute

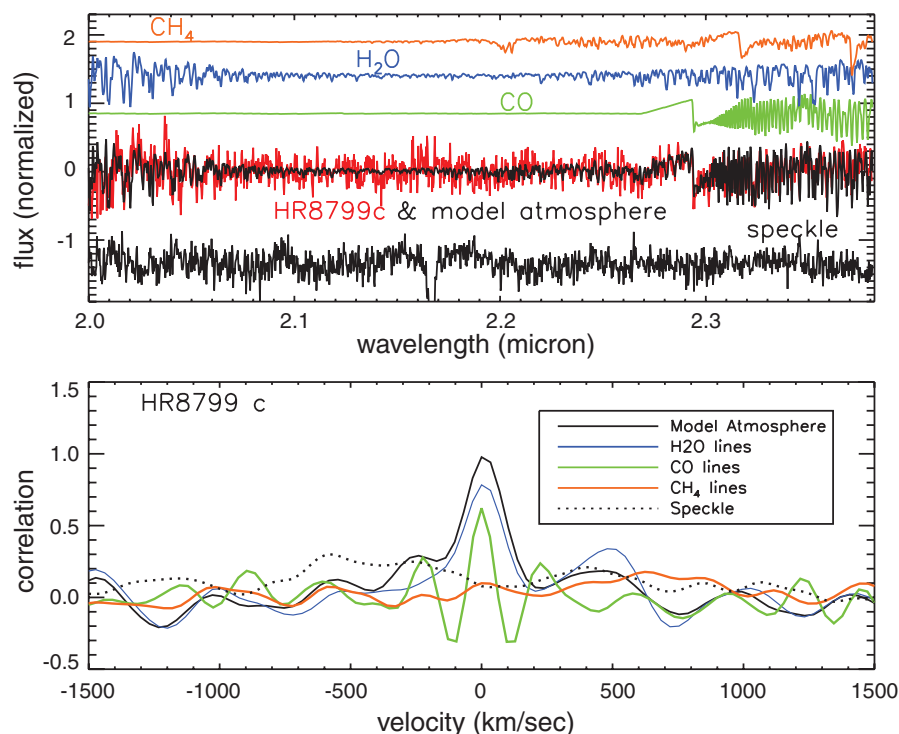


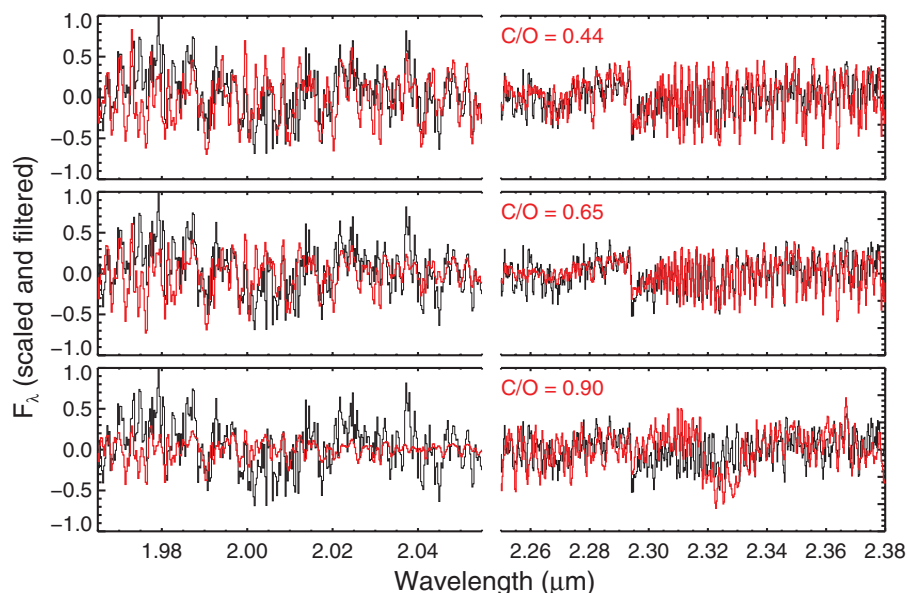
**Fig. 3.** (Top) Pure H<sub>2</sub>O (blue), CO (green), and CH<sub>4</sub> (orange) synthetic spectra demonstrate the predicted location of absorption lines (14). The filtered spectrum of HR 8799c is shown in red. A filtered model atmosphere spectrum of mostly H<sub>2</sub>O and CO is overplotted in black. Also shown is a spectrum of a bright speckle (black trace at bottom), scaled such that the variance is equal to the variance in a featureless region of HR 8799c. (Bottom) Cross-correlation functions for the spectrum of HR 8799c and the synthetic spectra shown in the top panel (solid curves), along with a baseline cross-correlation between the planet spectrum and a bright speckle (dotted curve). The cross-correlation with the H<sub>2</sub>O-only template covered the entire observed wavelength range. Correlations with the CO and CH<sub>4</sub> templates were performed only over wavelength regions with strong lines (CH<sub>4</sub>:  $\lambda > 2.18 \mu\text{m}$ ; CO:  $\lambda > 2.29 \mu\text{m}$ ). Large cross-correlation peaks are found for the pure CO and H<sub>2</sub>O templates, as expected. The CO-only template produces two smaller symmetric peaks at  $\pm 207 \text{ km s}^{-1}$ ; this velocity corresponds to the near-equal line spacing of the CO lines across the (2,0) bandhead starting at  $2.29 \mu\text{m}$ . Similar near-equal line spacing occurs for other CO bandheads [that is, the (3,1) bandhead at  $2.32 \mu\text{m}$ ], resulting in the ringing behavior seen in the cross-correlation. No peaks in the correlations were found with any of the three CH<sub>4</sub> templates or the speckle spectrum (this is true for any subset of the observed wavelength range used in this work). Cross-correlation is not required to detect molecular lines in our spectrum; however, this exercise aids in quantifying the relative detections (or nondetection, in the case of CH<sub>4</sub>) when lines from individual molecules overlap.

to measurement errors in C and O, as line depths are sensitive to both of these bulk parameters. To marginalize over the temperature and gravity uncertainties, we expanded the grid of atmosphere models (with abundances given in table S1) to include temperatures of 1000 to 1200 K and  $\log(g)$  of 3.5 to 4.0. We then performed a Monte Carlo simulation by resampling the spectral data from Gaussian distributions with widths determined by the (uncorrelated) uncertainties for all wavelength channels. We fit each resampled spectrum using the model grid and recorded the best-fit abundances. The resulting estimate (and uncertainty) for the C/O ratio is  $0.65^{+0.10}_{-0.05}$ , which is marginally greater than the assumed stellar ratio (~0.55).

Measuring abundances is complicated, and model atmospheres have not been thoroughly tested for systematic under- or overestimation of

C/O ratios in substellar objects. However, given the dominance of H<sub>2</sub>O, CO, and CH<sub>4</sub> opacities in their atmospheres, large variations in C/O should be easier to discern in brown dwarfs and giant planets than in stars (36). Planet migration and chemical evolution within the disk can muddy conclusions based on composition (37), as can core dredging, which may be important in planets more massive than Jupiter (38). With these caveats in mind, the above analysis rules out a planetary atmosphere for HR8799c that formed by gas-only accretion during a CA process at its current location (C/O > 0.9) and marginally excludes an atmosphere that formed from extreme amounts of solid accretion (C/O < 0.6). Between these extreme predictions, the picture is more complicated, but the enhanced C/O ratio and the depleted C and O levels tend to favor a history in which the planet formed via CA. In this case,

**Fig. 4.** Comparison of synthetic spectra (red) with different carbon and oxygen abundances to the low-pass-filtered spectrum of HR8799c (black). The central wavelength range is omitted due to the lack of strong absorption features. Under the assumption that HR 8799c formed near its current location (i.e., little to no migration), the best-matching carbon and oxygen abundances from the model grid are 8.33 and 8.51, respectively ( $\sim 0.06$  and  $0.13$  below the solar values, using the traditional astronomical log base-10 abundance scale in which the hydrogen abundance is 12.0), corresponding to a C/O ratio  $\sim 0.65$  (middle panel). If HR 8799c somehow formed beyond 100 AU and migrated to its current location, the best-matching C and O abundances are both sub-stellar: 8.29 and 8.45, respectively, with C/O  $\sim 0.7$  (not depicted). In either case, large C/O ( $\sim 0.9$ , bottom panel) results in a substantial increase in  $\text{CH}_4$  and a decrease in  $\text{H}_2\text{O}$  in the spectrum, whereas for small C/O ( $\sim 0.44$ , top panel), CO and  $\text{H}_2\text{O}$  increase. Thus, both cases increase or decrease the prominent molecular lines identified in the K-band spectrum by factors that are easily excluded by the data (for instance, the large  $\text{CH}_4$  absorption feature at  $2.32\ \mu\text{m}$  for C/O  $\sim 0.9$ ). Note that the exclusion of the high and low C/O values is independent of  $K_{\text{zz}}$  because the adopted value ( $10^8$ ) always quenches the CO and  $\text{CH}_4$  mole fractions at their maximum and minimum values, respectively. Raising  $K_{\text{zz}}$  would have no effect, and lowering  $K_{\text{zz}}$  would only increase  $\text{CH}_4$ . All abundance values for C and O in the model grid are given in tables S1 and S2.



after an initial solid core formed, the planet atmosphere accreted from material that was partially, but not completely depleted of solid planetesimals. However, given the uncertainties in parameters such as the stellar abundances (15), we cannot totally exclude a GI formation scenario for this system. Our work shows the power of high-resolution spectra, which allow molecular species to be seen directly through their individual absorption lines rather than inferred from overall spectral shapes that are more sensitive to model parameters.

## References and Notes

- B. Zuckerman, J. H. Rhee, I. Song, M. S. Bessell, *Astrophys. J.* **732**, 61 (2011).
- C. Marois *et al.*, *Science* **322**, 1348 (2008).
- C. Marois, B. Zuckerman, Q. M. Konopacky, B. Macintosh, T. Barman, *Nature* **468**, 1080 (2010).
- S. A. Metchev, L. A. Hillenbrand, *Astrophys. J.* **651**, 1166 (2006).
- D. Saumon, M. S. Marley, *Astrophys. J.* **689**, 1327 (2008).
- D. C. Stephens *et al.*, *Astrophys. J.* **702**, 154 (2009).
- T. S. Barman, B. Macintosh, Q. M. Konopacky, C. Marois, *Astrophys. J.* **735**, L39 (2011).
- A. P. Boss, *Science* **276**, 1836 (1997).
- J. B. Pollack *et al.*, *Icarus* **124**, 62 (1996).
- R. R. Rafikov, *Astrophys. J.* **727**, 86 (2011).
- J. Larkin *et al.*, *New Astron. Rev.* **50**, 362 (2006).
- P. L. Wizinowich *et al.*, *Proc. SPIE* **6272**, 627209 (2006).
- A. Krabbe *et al.*, *Proc. SPIE* **5492**, 1403 (2004).
- T. S. Barman, B. Macintosh, Q. M. Konopacky, C. Marois, *Astrophys. J.* **733**, 65 (2011).
- See the supplementary materials on Science Online for more information.
- J. Patience, R. R. King, R. J. de Rosa, C. Marois, *Astron. Astrophys.* **517**, A76 (2010).
- M. S. Marley *et al.*, *Astrophys. J.* **754**, 135 (2012).
- A. J. Skemer *et al.*, *Astrophys. J.* **753**, 14 (2012).
- T. Currie *et al.*, *Astrophys. J.* **729**, 128 (2011).
- N. Madhusudhan, A. Burrows, T. Currie, *Astrophys. J.* **737**, 34 (2011).
- R. Galicher, C. Marois, B. Macintosh, T. Barman, Q. Konopacky, *Astrophys. J.* **739**, L41 (2011).
- L. S. Rothman, F. J. Martin-Torres, J.-M. Flaud, *J. Quant. Spec. Rad. Trans.* **109**, 881 (2008).
- C. Wenger, J. P. Champion, *J. Quant. Spec. Rad. Trans.* **59**, 471 (1998).
- R. Warmbier *et al.*, *Astron. Astrophys.* **495**, 655 (2009).
- A. Borysov, J. P. Champion, U. G. Jørgensen, C. Wenger, *Mol. Phys.* **100**, 3585 (2002).
- J. J. Sudol, N. Haghighipour, *Astrophys. J.* **755**, 38 (2012).
- E. K. Baines *et al.*, *Astrophys. J.* **761**, 57 (2012).
- I. Baraffe, G. Chabrier, T. S. Barman, F. Allard, P. H. Hauschildt, *Astron. Astrophys.* **402**, 701 (2003).
- B. Fegley Jr., K. Lodders, *Astrophys. J.* **472**, L37 (1996).
- M. D. Smith, *Icarus* **132**, 176 (1998).
- M. Asplund, N. Grevesse, A. J. Sauval, in *Cosmic Abundances as Records of Stellar Evolution and Nucleosynthesis*, T. G. Barnes III, F. N. Bash, Eds. (Astronomical Society of the Pacific, San Francisco, 2005), p. 25.
- The spectrum of HR 8799, a classic Lambda Bootes star, shows substantial depletion of some elements. However, its peculiar abundances have been attributed to its extremely shallow photosphere and reaccretion of gas depleted in refractory elements—possibly associated with planet formation (39)—so we assume here that the planets formed from solar-abundance material.
- R. Helled, R. Bodenheimer, *Icarus* **207**, 503 (2010).
- K. Sadakane, *Publ. Astron. Soc. Jpn.* **58**, 1023 (2006).
- K. I. Öberg, R. Murray-Clay, E. A. Bergin, *Astrophys. J.* **743**, L16 (2011).
- J. J. Fortney, *Astrophys. J.* **747**, L27 (2012).
- K. Lodders, *Astrophys. J.* **611**, 587 (2004).
- H. F. Wilson, B. Militzer, *Phys. Rev. Lett.* **108**, 111101 (2012).
- R. O. Gray, C. J. Corbally, *Astron. J.* **124**, 989 (2002).
- B. P. Bowler, M. C. Liu, T. J. Dupuy, M. C. Cushing, *Astrophys. J.* **723**, 850 (2010).

**Acknowledgments:** We thank A. Conrad, S. Dahm, J. Lyke, H. Tran, H. Hershey, J. McIlroy, J. Rivera, and the entire Keck staff for maximizing our observing efficiency; J. Larkin and S. Wright for their assistance with OSIRIS data reduction; and R. Murray-Clay and K. Öberg for assistance with abundance values. Portions of this work were performed under the auspices of the U.S. Department of Energy by LLNL under contract no. DE-AC52-07NA27344. Support for this work was provided by NASA Origins of the Solar System grants to LLNL and Lowell Observatory and from the Keck Principal Investigator Data Analysis Fund, managed by NExSci on behalf of NASA. Support was also provided by the NASA High-End Computing Program through the NASA Advanced Supercomputing Division at Ames Research Center. Q.M.K. is a Dunlap Fellow at the Dunlap Institute for Astronomy and Astrophysics, University of Toronto. The Dunlap Institute is funded through an endowment established by the David Dunlap family and the University of Toronto. The W. M. Keck Observatory is operated as a scientific partnership among the California Institute of Technology, the University of California, and NASA. The Keck Observatory was made possible by the generous financial support of the W. M. Keck Foundation. We also wish to recognize the very important cultural role and reverence that the summit of Mauna Kea has always had within the indigenous Hawaiian community. We are most fortunate to have the opportunity to conduct observations from this mountain. All authors contributed equally to this work.

## Supplementary Materials

www.sciencemag.org/cgi/content/full/science.1232003/DC1  
Materials and Methods  
Figs. S1 to S4  
Tables S1 and S2  
References (41–44)  
Database S1

25 October 2012; accepted 19 February 2013  
Published online 14 March 2013;  
10.1126/science.1232003



# Suppression of Metal-Insulator Transition in VO<sub>2</sub> by Electric Field–Induced Oxygen Vacancy Formation

Jaewoo Jeong,<sup>1,2</sup> Nagaphani Aetukuri,<sup>1,3</sup> Tanja Graf,<sup>1</sup> Thomas D. Schladt,<sup>1</sup> Mahesh G. Samant,<sup>1</sup> Stuart S. P. Parkin<sup>1\*</sup>

Electrolyte gating with ionic liquids is a powerful tool for inducing novel conducting phases in correlated insulators. An archetypal correlated material is vanadium dioxide (VO<sub>2</sub>), which is insulating only at temperatures below a characteristic phase transition temperature. We show that electrolyte gating of epitaxial thin films of VO<sub>2</sub> suppresses the metal-to-insulator transition and stabilizes the metallic phase to temperatures below 5 kelvin, even after the ionic liquid is completely removed. We found that electrolyte gating of VO<sub>2</sub> leads not to electrostatically induced carriers but instead to the electric field–induced creation of oxygen vacancies, with consequent migration of oxygen from the oxide film into the ionic liquid. This mechanism should be taken into account in the interpretation of ionic liquid gating experiments.

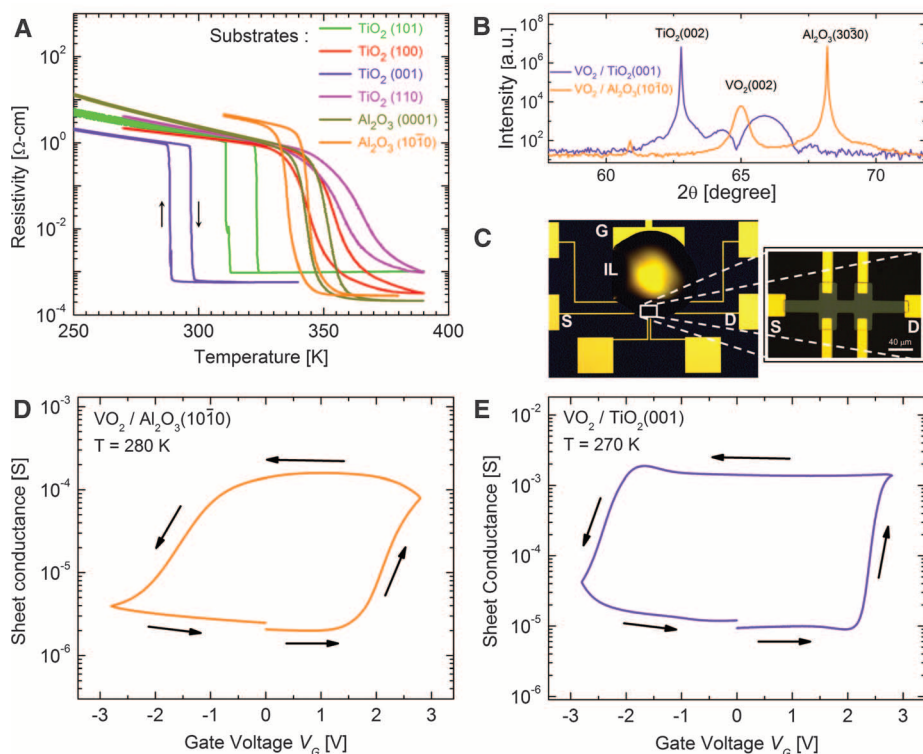
The electric field–induced metallization of correlated insulators is a powerful means of creating novel electronic phases, but the process requires high electric fields often beyond those achievable by conventional dielectric gates (1–3). Such fields can be achieved at interfaces with the use of Schottky junctions (4) or polar materials (5, 6), or at surfaces with the use of ionic liquids (ILs) (7) as the gate dielectric in field-effect transistor devices (8–10). The latter method allows for tunable electric fields without restriction on the channel material or its crystal orientation. One of the most interesting and widely studied correlated materials is the insulator VO<sub>2</sub> (11, 12), which exhibits a metal-to-insulator phase transition (MIT) as the temperature is reduced below ~340 K in bulk material (13). Recently, electrolyte gating (EG) was shown to substantially alter the properties of thin films of VO<sub>2</sub>; in particular, the metallization of the insulating state was achieved and attributed to the introduction of small numbers of carriers that are electrostatically induced by the gating process (14). This would be consistent with the destabilization of a Mott insulating state in VO<sub>2</sub> that depends critically on electronic band half-filling, which has been a long-standing goal in condensed matter physics (15). We find that an entirely different mechanism accounts for the EG suppression of the MIT to low temperatures in epitaxial thin films of VO<sub>2</sub> that we have prepared on TiO<sub>2</sub> and Al<sub>2</sub>O<sub>3</sub> single-crystal substrates.

Figure 1A shows resistivity-temperature curves for VO<sub>2</sub> films grown by pulsed laser deposition on various facets of TiO<sub>2</sub> and Al<sub>2</sub>O<sub>3</sub> single crystals in an O<sub>2</sub> pressure ( $P_{O_2}$ ) of 10<sup>–2</sup> torr during deposition (16). The MIT temperature ( $T_{MIT}$ ) varied as a result of different strains in the VO<sub>2</sub>

films (17). Henceforth, we focus on films grown on TiO<sub>2</sub>(001) and Al<sub>2</sub>O<sub>3</sub>(10 $\bar{1}$ 0), which have a large difference in  $T_{MIT}$  but have the same crystallographic orientation. For these films, high-resolution x-ray diffraction (Fig. 1B) indicated excellent epitaxial growth with the *c* axis out of the plane. The film on TiO<sub>2</sub>(001) is 10 nm thick, is strained along the *c* axis by –1.2% (18, 19),

and has a  $T_{MIT}$  of ~290 K. By contrast, the film on Al<sub>2</sub>O<sub>3</sub>(10 $\bar{1}$ 0) is 20 nm thick, is completely relaxed (18, 19), and has a  $T_{MIT}$  of ~340 K.

Devices for EG studies were fabricated from 10-nm VO<sub>2</sub>/TiO<sub>2</sub>(001) and 20-nm VO<sub>2</sub>/Al<sub>2</sub>O<sub>3</sub>(10 $\bar{1}$ 0) films (Fig. 1C), unless otherwise noted, using standard optical lithographic techniques. The electrical contacts to the channel included source and drain contacts as well as four side contacts that were used for four-wire resistance and Hall measurements. A ~100-nl droplet of the IL 1-hexyl-3-methylimidazolium bis(trifluoromethylsulfonyl)imide (HMIM-TFSI) covered the channel and lateral gate electrode. The gate voltage  $V_G$  was swept at 5 mV/s and a source drain voltage  $V_{SD}$  = 0.1 V was used, except where noted. Hysteresis in the sheet conductance centered about  $V_G$  = 0 V was observed for both substrates (Fig. 1, D and E). By sweeping  $V_G$ , the device could be reversibly switched between low- and high-conductance states. Once switched to the high-conductance state, the device was stable at  $V_G$  = 0 V and maintained its conductance for many days, even when the IL was washed off the device with isopropyl alcohol (fig. S1). We used x-ray photoelectron spectroscopy (XPS) to verify that the IL was completely removed; no spectroscopic signature of the IL was found (fig. S2). This suggests that the gating effect was not electrostatic in



**Fig. 1.** Temperature- and gate voltage–dependent conductivity of epitaxial VO<sub>2</sub> thin films. (A) Resistivity-temperature curves for VO<sub>2</sub> films grown on various orientations of TiO<sub>2</sub> and Al<sub>2</sub>O<sub>3</sub> single-crystal substrates. (B) High-resolution Cu K $\alpha$   $\theta$ -2 $\theta$  x-ray diffraction pattern of VO<sub>2</sub> films deposited on Al<sub>2</sub>O<sub>3</sub>(10 $\bar{1}$ 0) and TiO<sub>2</sub>(001), respectively, showing highly oriented films with the *c* axis out of plane. (C) Optical image of a typical device showing a droplet of the ionic liquid (IL) HMIM-TFSI. The electrical contacts can be seen in the magnified image of the channel (right). S, source contact; D, drain contact; G, gate electrode. (D and E) Sheet conductance versus  $V_G$  for devices fabricated from VO<sub>2</sub> films prepared on Al<sub>2</sub>O<sub>3</sub>(10 $\bar{1}$ 0) (D) and TiO<sub>2</sub>(001) (E).

<sup>1</sup>IBM Almaden Research Center, San Jose, CA 95120, USA. <sup>2</sup>Materials Department, University of California, Santa Barbara, CA 93106, USA. <sup>3</sup>Department of Materials Science and Engineering, Stanford University, Stanford, CA 94305, USA.

\*Corresponding author. E-mail: stuart.parkin@us.ibm.com

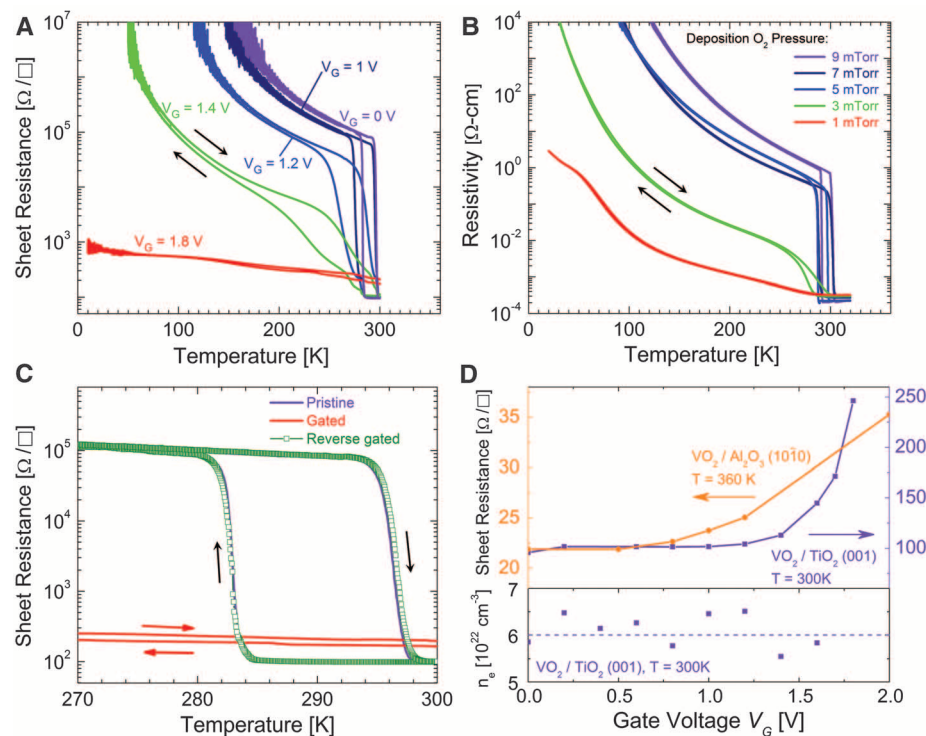
origin. Moreover, the fact that films on both types of substrates showed similar behavior rules out any appreciable influence of the substrate—for example, the role of strain. The electric field-induced metallic phase, reflected in the source-drain current  $I_{SD}$ , was stable over extended periods

of time in the presence of the IL at  $V_G = 0$  V (fig. S3A) and also for modest  $V_G$ , but the insulating phase could be nearly recovered by applying reverse gate voltages similar in value to those needed to induce the metallic phase (Fig. 1, D and E). The insulating phase could also be recovered by

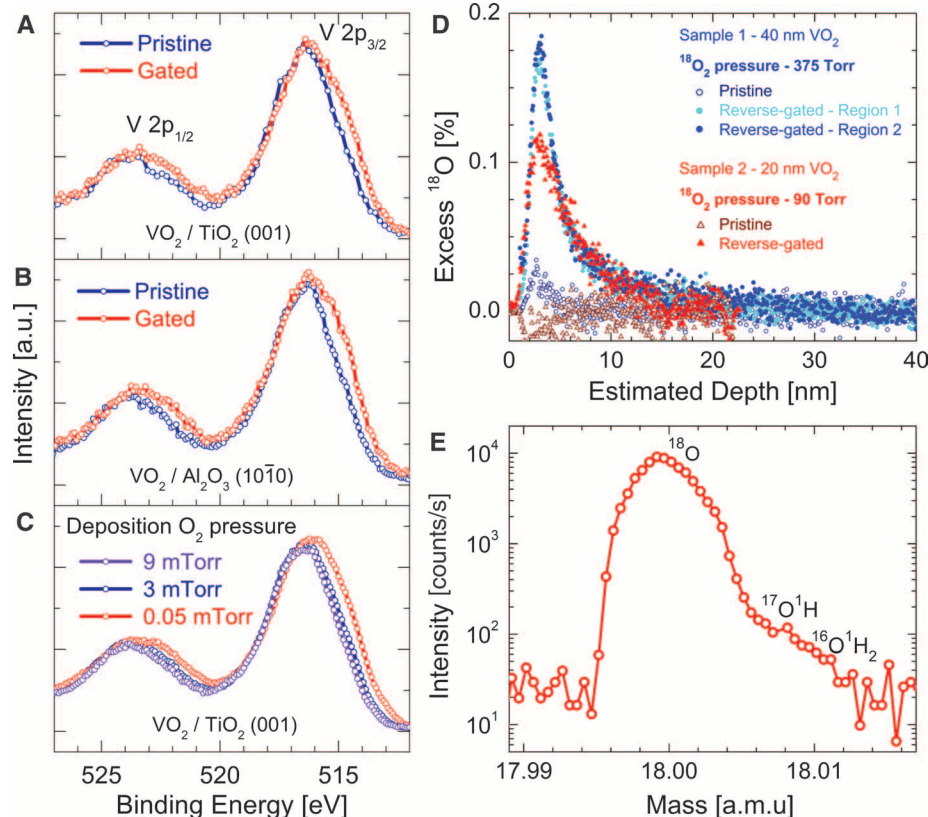
annealing in oxygen at modest temperatures ( $\sim 200^\circ\text{C}$ ; fig. S4).

Figure 2A shows the temperature dependence of the channel sheet resistance  $R_s$  of  $\text{VO}_2/\text{TiO}_2(001)$  devices for several positive values of  $V_G$ . A progressive suppression of the MIT as the gate bias

**Fig. 2.** Suppression of the MIT in  $\text{VO}_2$  films. (A) Sheet resistance  $R_s$  versus temperature  $T$  for various gate voltages varying from 0 to 1.8 V for  $\text{VO}_2/\text{TiO}_2(001)$ . (B) Resistivity of  $\text{VO}_2$  versus temperature as a function of  $P_{\text{O}_2}$  used for film deposition on  $\text{TiO}_2(001)$ . (C)  $R_s$  versus  $T$  for the same device as in (A) in its pristine state, at  $V_G = 1.8$  V (gated) and at  $V_G = -0.8$  V (reverse gated), showing complete recovery of the MIT in the latter case.  $V_G$  was applied at 300 K for measurements in (A) and (C) while the films were in their metallic state. (D) Sheet resistance for EG devices formed from  $\text{VO}_2/\text{TiO}_2(001)$  and  $\text{VO}_2/\text{Al}_2\text{O}_3(10\bar{1}0)$ , and electron carrier density  $n_e$  from Hall measurements for an EG device fabricated from  $\text{VO}_2/\text{TiO}_2(001)$ , versus  $V_G$ . The dashed line is a guide to the eye.



**Fig. 3.** XPS and SIMS measurements. (A and B) V 2p core-level spectra for pristine and gated  $\text{VO}_2/\text{TiO}_2(001)$  (A) and  $\text{VO}_2/\text{Al}_2\text{O}_3(10\bar{1}0)$  (B);  $V_G = 1.8$  V in both cases. (C) Comparison of data in (A) and (B) with spectra for  $\text{VO}_2$  films deposited under reduced  $P_{\text{O}_2}$  on  $\text{TiO}_2(001)$ . (D) Excess  $^{18}\text{O}$  concentration above the natural abundance ( $\sim 0.2$  atomic %) versus depth for two EG devices fabricated from 40- and 20-nm  $\text{VO}_2$  on  $\text{Al}_2\text{O}_3(10\bar{1}0)$  determined by SIMS. The devices were gated to the metallic state in vacuum and reverse-gated to recover the insulating state in  $^{18}\text{O}_2$ . Data are compared to pristine channels on the same wafer that were not gated but were subjected to the same dosage of  $^{18}\text{O}_2$ . Measurements on two different areas of sample 1 are very similar. (E) Scan at a mass resolution of 4000 (atomic mass units divided by full width at half maximum) showing clear separation of  $^{18}\text{O}$ ,  $^{16}\text{O}^1\text{H}_2$ , and  $^{17}\text{O}^1\text{H}$ .





was increased is observed until the MIT is suppressed to below 5 K at  $V_G \sim 1.8$  V. This gating effect is compared in Fig. 2B with the effect of changing the oxygen content of  $\text{VO}_2$  by depositing  $\text{VO}_2/\text{TiO}_2(001)$  in reduced  $P_{\text{O}_2}$  at  $400^\circ\text{C}$ . The  $T_{\text{MIT}}$  is systematically reduced and the MIT is suppressed as  $P_{\text{O}_2}$  is lowered. The transport data in Fig. 2, A and B, are notably similar. In both cases, the onset temperature for the MIT is decreased and the magnitude of the resistivity change drops. The similarity in these data suggests that the EG effect could also be due to the electric field–induced formation of oxygen vacancies, thereby leading to a reduced MIT.

As discussed above, the  $\text{VO}_2$  devices can be reversibly switched between insulating and metallic phases. The temperature dependence of the resistivity for the same device in Fig. 2A in its pristine (i.e., ungated) state is nearly identical after being reversibly gated (Fig. 2C).

The sheet resistance in the metallic phase just above the MIT is plotted versus  $V_G$  in Fig. 2D for the devices used in Fig. 2A, and for devices on  $\text{Al}_2\text{O}_3$  substrates in fig. S5. For  $\text{VO}_2$  devices on both substrates,  $R_S$  increases considerably as  $V_G$  is increased. If the gating effect were electrostatic, the electron carrier density  $n_e$  should increase for positive  $V_G$ ; thus, one would anticipate a decrease rather than an increase in  $R_S$ . Moreover, Hall resistivity measurements for  $\text{VO}_2/\text{TiO}_2$  show no evidence for any increase in  $n_e$  (Fig. 2D, bottom); rather,  $n_e$  is independent of  $V_G$  and its measured value is  $\sim 6 \times 10^{22} \text{ cm}^{-3}$ , similar to bulk  $\text{VO}_2$  (20).

To confirm the possibility of oxygen vacancy creation during EG that was suggested by our transport data, we carried out three independent experimental studies. First, we used XPS to measure changes in the oxidation state of vanadium in gated  $\text{VO}_2$  films. Devices with much larger channel areas ( $\sim 900$  by  $300 \mu\text{m}$ ) than those used above were fabricated to accommodate the x-ray (Al  $K\alpha$ ) beam size (diameter  $\sim 150 \mu\text{m}$ ). Transport data for these devices were similar to those shown in Fig. 2 for similar  $V_G$ . In Fig. 3, A and B, the V 2p core-level spectra obtained within the channel for pristine devices are com-

pared with the spectra for the same devices gated to completely suppress the MIT to low temperatures. The results for devices fabricated on  $\text{Al}_2\text{O}_3(10\bar{1}0)$  and  $\text{TiO}_2(001)$  are similar. The position of the V 2p<sub>3/2</sub> core-level peak in the pristine sample is  $\sim 516.3$  eV, close to the well-established value of  $\sim 516.1$  eV for  $\text{V}^{4+}$  in  $\text{VO}_2$ . In the gated sample (for which the IL was removed), the V 2p<sub>3/2</sub> core-level peak broadens and is shifted toward lower binding energy by  $\sim 0.2$  eV. (Note that the peak is observed to be at  $\sim 515.8$  eV for  $\text{V}^{3+}$  in  $\text{V}_2\text{O}_3$ .) These observations indicate a reduction in the oxidation state of V from  $\text{V}^{4+}$  toward  $\text{V}^{3+}$  (21). Similarly, in situ measured films prepared at different values of  $P_{\text{O}_2}$  (Fig. 3C) have V 2p peaks that shift systematically to lower binding energies and broaden monotonically as  $P_{\text{O}_2}$  is reduced. Thus, the V oxidation state continuously evolves toward  $\text{V}^{3+}$ , concomitant with a suppression of the MIT (as shown in Fig. 2B).

The changes in the oxidation state of V observed by XPS strongly indicate the formation of oxygen vacancies. In the absence of electric fields, the formation energies of oxygen vacancies in rutile oxides are known to be very high (22). However, we hypothesize that the electric fields created at the electric double layer (EDL) at the IL-oxide interface are sufficiently high (23) to drive oxygen out of the  $\text{VO}_2$  surface into the IL, and that once the oxygen vacancies are created, these vacancies are stable in the absence of the EDL at  $V_G = 0$ . This explains the nonvolatility of the gating (Fig. 1, D and E). To test this hypothesis, we carried out gating in a high-vacuum chamber in which we could introduce  $^{18}\text{O}_2$ . First, an EG device with a large channel area ( $900$  by  $300 \mu\text{m}$ ) was gated in high vacuum ( $V_G = 3$  V) to suppress the MIT to low temperatures. After gating for long times ( $\sim 10$  to  $20$  min), the channel conductance was found to be nearly saturated and remained unchanged when  $V_G$  was reduced to zero (16). Once a stable channel current was obtained,  $^{18}\text{O}_2$  was introduced into the chamber at  $V_G = 0$  V. Then a reverse gate voltage of  $-1.5$  V was applied until the insulating state was recovered; this took several hours. This proce-

dures was repeated three and four times, respectively, for two experimental devices termed sample 1 and sample 2. Samples 1 and 2 were fabricated from  $40\text{-nm}$  and  $20\text{-nm}$   $\text{VO}_2/\text{Al}_2\text{O}_3(10\bar{1}0)$ , respectively. Depth profile secondary ion mass spectrometry (SIMS) was then performed on these devices after the IL was removed. A comparison was made to pristine regions on the same sample that were otherwise subjected to identical procedures concurrently. In the latter case, no excess  $^{18}\text{O}$  above its natural isotopic abundance in oxygen (0.2 atomic percent) was measured. However, a notable increase in the concentration of  $^{18}\text{O}$  to nearly twice the natural abundance was found at the surfaces of both devices in the gated channels, with a higher value in sample 1, the device that was gated in higher pressures of  $^{18}\text{O}_2$  (Fig. 3D). The excess  $^{18}\text{O}$  was seen to depths of nearly  $20$  nm from the oxide surface, with similar depth profiles for the two samples. The incorporation of  $^{18}\text{O}$  within the  $\text{VO}_2$  channels during reverse gating supports our hypothesis that gating creates oxygen vacancies within the channel.

Given the large area of the channel, the most likely migration path for the oxygen that must be released to create the vacancies during gating is into the IL. Then one might speculate that saturation of the IL with oxygen would prevent such migration. Figure 4A indeed shows that there is no change in the source-drain current even when a large  $V_G$  is applied in the presence of  $\text{O}_2$  (at  $150$  torr) to a  $100$  by  $20 \mu\text{m}$  device of  $\text{VO}_2/\text{Al}_2\text{O}_3(10\bar{1}0)$ . After  $200$  s,  $\text{O}_2$  was pumped out from the chamber and, concomitantly,  $I_{\text{SD}}$  gradually increased. When oxygen was reintroduced into the chamber while maintaining  $V_G = 3$  V,  $I_{\text{SD}}$  began to decrease. We found a clear correlation between the source-drain current and the amount of oxygen in the chamber. A detailed dependence of the sheet conductance on  $V_G$  and  $P_{\text{O}_2}$  is shown in Fig. 4B. Appreciable gating effects were found only at low values of  $P_{\text{O}_2}$  (for  $V_G > \sim 1.5$  V).

Our experiments show that modest gate voltages result in the electric field–induced migration of oxygen into and out of the IL even though the energy required to create an oxygen vacancy in  $\text{VO}_2$  in zero electric field is high. This phenomenon is likely to be common to many experiments using high electric fields, especially those using IL gating; many of these experimental results have been interpreted by the electrostatic creation of carriers. Our results suggest that the electric field–induced migration of species into and out of electrolyte-gated materials is an exciting avenue for the creation of novel, non-equilibrium phases of matter.

#### References and Notes

1. C. H. Ahn et al., *Rev. Mod. Phys.* **78**, 1185 (2006).
2. A. Cavalleri et al., *Phys. Rev. Lett.* **95**, 067405 (2005).
3. H. Takagi, H. Y. Hwang, *Science* **327**, 1601 (2010).
4. J. Robertson, *J. Vac. Sci. Technol. B* **18**, 1785 (2000).
5. A. Ohtomo, H. Y. Hwang, *Nature* **427**, 423 (2004).
6. P. Moetakef et al., *Appl. Phys. Lett.* **99**, 232116 (2011).
7. M. Galiński, A. Lewandowski, I. Stępnik, *Electrochim. Acta* **51**, 5567 (2006).
8. K. Ueno et al., *Nat. Mater.* **7**, 855 (2008).

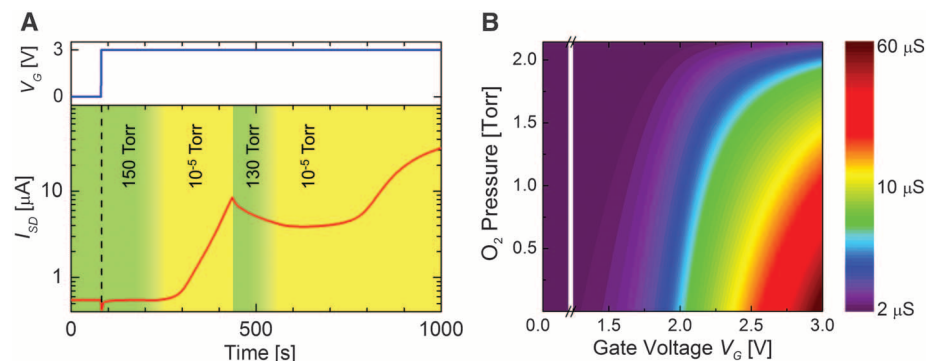


**Fig. 4.** Electrolyte gating of a device fabricated from  $\text{VO}_2/\text{Al}_2\text{O}_3(10\bar{1}0)$  in the presence of oxygen at  $300$  K. **(A)** Source-drain current at  $V_G = 3$  V versus time as  $P_{\text{O}_2}$  was varied from an initial pressure of  $150$  torr, gradually reduced to  $10^{-5}$  torr, abruptly increased to  $130$  torr, and then gradually reduced to  $10^{-5}$  torr (indicated schematically by color). **(B)** Sheet conductance (color scale) as a function of  $V_G$  and  $P_{\text{O}_2}$ .

9. J. T. Ye *et al.*, *Nat. Mater.* **9**, 125 (2010).
10. Y. Lee *et al.*, *Phys. Rev. Lett.* **106**, 136809 (2011).
11. M. M. Qazilbash *et al.*, *Science* **318**, 1750 (2007).
12. M. Liu *et al.*, *Nature* **487**, 345 (2012).
13. F. J. Morin, *Phys. Rev. Lett.* **3**, 34 (1959).
14. M. Nakano *et al.*, *Nature* **487**, 459 (2012).
15. M. Imada, A. Fujimori, Y. Tokura, *Rev. Mod. Phys.* **70**, 1039 (1998).
16. See supplementary materials on Science Online.
17. J. Cao *et al.*, *Nat. Nanotechnol.* **4**, 732 (2009).
18. N. F. Mott, *Metal Insulator Transitions* (Taylor & Francis, New York, ed. 2, 1990).
19. R. Restori, D. Schwarzenbach, J. R. Schneider, *Acta Crystallogr. B* **43**, 251 (1987).
20. W. H. Rosevear, W. Paul, *Phys. Rev. B* **7**, 2109 (1973).
21. G. Silversmit, D. Depla, H. Poelman, G. B. Marin, R. De Gryse, *J. Electron Spectrosc. Relat. Phenom.* **135**, 167 (2004).
22. A. Janotti *et al.*, *Phys. Rev. B* **81**, 085212 (2010).
23. R. Kötz, M. Carlen, *Electrochim. Acta* **45**, 2483 (2000).

**Acknowledgments:** We thank V. Deline, A. Kellogg, T. Topuria, and P. Rice for sample characterization, B. Hughes for help with device fabrication, and K. Martens and A. Pushp for useful discussions. Supported by the Graduate School "Material Science in Mainz" [Deutsche Forschungsgemeinschaft (DFG) GSC 266] (T.G.), the Multidisciplinary University Research Initiative program of

the Army Research Office (grant W911-NF-09-1-0398) (J.J.), a Feodor Lynen Research Fellowship from the Alexander von Humboldt Foundation (T.D.S.), and a stipend from DFG (GR4000/1-1) (T.G.).

#### Supplementary Materials

[www.sciencemag.org/cgi/content/full/339/6126/1402/DC1](http://www.sciencemag.org/cgi/content/full/339/6126/1402/DC1)

Materials and Methods

Supplementary Text

Figs. S1 to S8

Table S1

References (24–31)

20 September 2012; accepted 24 January 2013

10.1126/science.1230512

# Photonic Spin Hall Effect at Metasurfaces

Xiaobo Yin,<sup>1,2</sup> Ziliang Ye,<sup>1</sup> Junsuk Rho,<sup>1</sup> Yuan Wang,<sup>1</sup> Xiang Zhang<sup>1,2\*</sup>

The spin Hall effect (SHE) of light is very weak because of the extremely small photon momentum and spin-orbit interaction. Here, we report a strong photonic SHE resulting in a measured large splitting of polarized light at metasurfaces. The rapidly varying phase discontinuities along a metasurface, breaking the axial symmetry of the system, enable the direct observation of large transverse motion of circularly polarized light, even at normal incidence. The strong spin-orbit interaction deviates the polarized light from the trajectory prescribed by the ordinary Fermat principle. Such a strong and broadband photonic SHE may provide a route for exploiting the spin and orbit angular momentum of light for information processing and communication.

The relativistic spin-orbit coupling of electrons results in intrinsic spin precessions and, therefore, spin polarization-dependent transverse currents, leading to the observation of the spin Hall effect (SHE) and the emerging field of spintronics (1–3). The coupling between an electron's spin degree of freedom and its orbital motion is similar to the coupling of the transverse electric and magnetic components of a propagating electromagnetic field (4). To conserve total angular momentum, an inhomogeneity of material's index of refraction can cause momentum transfer between the orbital and the spin angular momentum of light along its propagation trajectory, resulting in transverse splitting in polarizations. Such a photonic spin Hall effect (PSHE) was recently proposed theoretically to describe the spin-orbit interaction, the geometric phase, and the precession of polarization in weakly inhomogeneous media, as well as the interfaces between homogeneous media (5, 6).

However, the experimental observation of the SHE of light is challenging, because the amount of momentum that a photon carries and the spin-orbit interaction between the photon and its medium are exceedingly small. The exploration of such a weak process relies on the accumulation of the effect through many multiple reflections (7) or ultrasensitive quantum weak measurements with pre- and postselections of spin states (8, 9). Moreover, the present theory of PSHE assumes

the conservation of total angular momentum over the entire beam (5–9), which may not hold, especially when tailored wavelength-scale photonic structures are introduced. In this work, we demonstrate experimentally the strong interactions between the spin and the orbital angular momentum of light in a thin metasurface—a two-dimensional (2D) electromagnetic nanostructure with designed in-plane phase retardation at the wavelength scale. In such an optically thin material, the resonance-induced anomalous "skew scattering" of light

destroys the axial symmetry of the system that enables us to observe a giant PSHE, even at the normal incidence. In contrast, for interfaces between two homogeneous media, the spin-orbit coupling does not exist at normal incidence (5–9).

Metamaterial made of subwavelength composites has electromagnetic responses that largely originate from the designed structures rather than the constituent materials, leading to extraordinary properties including negative index of refraction (10, 11), superlens (12), and optical invisibilities (13, 14). As 2D metamaterials, metasurfaces have shown intriguing abilities in manifesting electromagnetic waves (15, 16). Recently, anomalous reflection and refraction at a metasurface has been reported (17, 18), and a variety of applications, such as flat lenses, have been explored (19–22). However, the general approach toward metasurfaces neglects the spin degree of freedom of light, which can be substantial in these materials. We show here that the rapidly varying in-plane phase retardation that is dependent on position along the metasurface introduces strong spin-orbit interactions, departing the light trajectory (S) from what is depicted by Fermat principles,  $S = S_{\text{Fermat}} + S_{\text{SO}}$  (where  $S_{\text{SO}}$

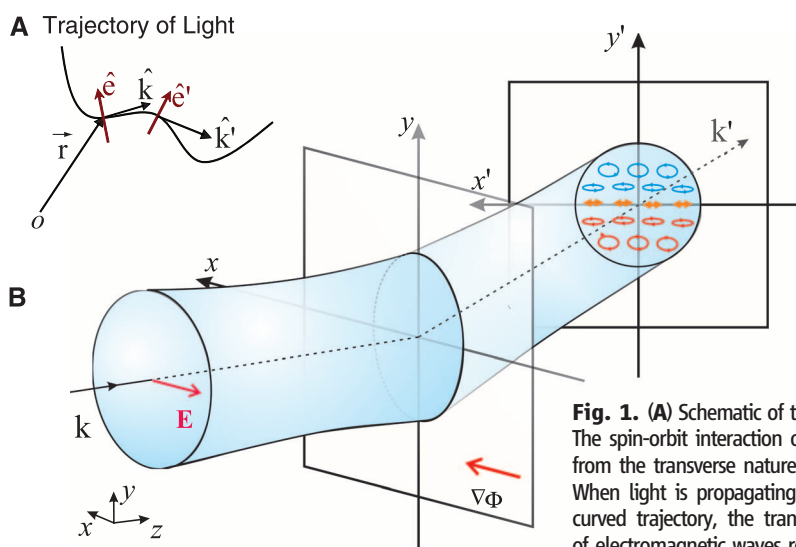


**Fig. 1.** (A) Schematic of the PSHE. The spin-orbit interaction originates from the transversality of electromagnetic waves. When light is propagating along a curved trajectory, the transversality of electromagnetic waves requires a rotation in polarization. (B) Transverse polarization splitting induced by a metasurface with a strong gradient of phase retardation along the  $x$  direction. The rapid phase retardation refracts light in a skewing direction and results in the PSHE. The strong spin-orbit interaction within the optically thin material leads to the accumulation of circular components of the beam in the transverse directions ( $y'$  directions) of the beam, even when the incident angle is normal to the surface.

<sup>1</sup>National Science Foundation Nanoscale Science and Engineering Center, 3112 Etchervy Hall, University of California at Berkeley, Berkeley, CA 94720, USA. <sup>2</sup>Materials Sciences Division, Lawrence Berkeley National Laboratory (LBNL), 1 Cyclotron Road, Berkeley, CA 94720, USA.

\*Corresponding author. E-mail: [xiang@berkeley.edu](mailto:xiang@berkeley.edu)



is a correction to the light trajectory raised from the metasurface-induced spin-orbit interaction).

The PSHE or the spin-orbit interaction arises from the noncolinear momentum and velocity (the change of trajectory) of light. When light is propagating along a curved trajectory (Fig. 1A), the time-varying momentum along the light path must introduce a geometric polarization rotation to maintain the polarization transverse to its new propagation direction (23),  $\hat{e} = -\mathbf{k}(\hat{e} \cdot \hat{\mathbf{k}})/k^2$ . Here,  $\hat{e}$  and  $\mathbf{k}$  are the polarization vector and the wave vector, respectively,  $\hat{\mathbf{k}}$  is the change of the propagation direction, and  $k$  is the amplitude of the wave vector. The rotation of the polarization depends on the helicity of light and may be considered as circular birefringence with a pure geometric origin (23–25). As the back-action from geometric polarization rotations, the spin-orbit interaction also changes the propagation path of light, as we will show in later sections, resulting in a helicity-dependent transverse displacement for light; i.e., photonic SHE.

For an ordinary interface between two homogeneous media, when a Gaussian beam impinges onto the interface at normal incidence, the axial symmetry normal to the surface eliminates the spin-orbit coupling, and the total angular momentum of the entire beam is conserved. However, by designing a metasurface with a rapid gradient of phase discontinuity  $\nabla\Phi$  along the interface in the  $x$  direction (Fig. 1B), we introduce a strong spin-orbit coupling when the light is refracted off the interface. The rapid, wavelength-scale phase retardation can be incorporated in the optical path by suitable design of the interface (17, 18, 26). Such a position-dependent phase discontinuity removes the axial symmetry of the interface and, therefore, allows us to observe the PSHE, even at the normal incident angle. Figure 1B schematically depicts the PSHE for the light beam that is refracted off a metasurface with rapid in-plane phase retardation. The momentum conservation at the metasurface now must take into account that the position-dependent phase retardation and the induced effective circular birefringence are determined by the gradient of the in-plane phase change or the curvature of the ray trajectory,  $(\hat{\mathbf{k}} \times \mathbf{k})/k^2$  (7), where  $\hat{\mathbf{k}}$  depends on the rapid phase change. For a linearly polarized incidence, light of opposite helicities will be accumulated at the opposite edges of an anomalously refracted beam in the transverse direction (Fig. 1B). The faster the in-plane phase changes, the stronger the effect becomes. Because both the local phase response and its gradient are tailored through metamaterial design, the optical spin-orbit interaction from the metasurface is strong, broadband, and widely tunable.

To experimentally observe the strong PSHE at the metasurfaces, we used a polarization-resolved detection setup (Fig. 2), which allows precise measurement of Stokes parameters of the refracted beam, providing the spin-state information of the light in the far field. A supercontinuum light source is used for broadband measurement, and

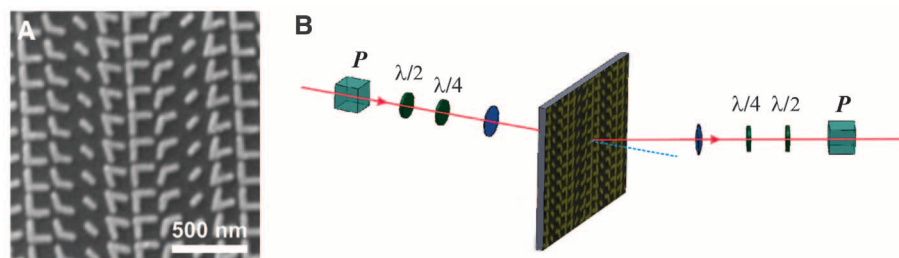


**Fig. 2.** (A) Scanning electron microscope image of a metasurface with a rapid phase gradient in the horizontal ( $x$ ) direction. The period of the constituent V-shaped antenna is 180 nm. Eight antennas with different lengths, orientations, and spanning angles were chosen for a linear phase retardation, ranging from 0 to  $2\pi$  with  $\pi/4$  intervals. Scale bar, 500 nm. (B) Light from a broadband source was focused onto the sample with a lens (focal length  $f = 50$  mm). The polarization can be adjusted in both the  $x$  and  $y$  directions with a half-wave plate. The regularly and anomalously refracted far-field transmission through the metasurface was collected using a lens ( $f = 50$  mm) and imaged on an InGaAs camera. The polarization state of the transmission is resolved by using an achromatic quarter-wave plate ( $\lambda/4$ ), a half-wave plate ( $\lambda/2$ ), and a polarizer with a high extinction ratio.  $P$ , polarizer.

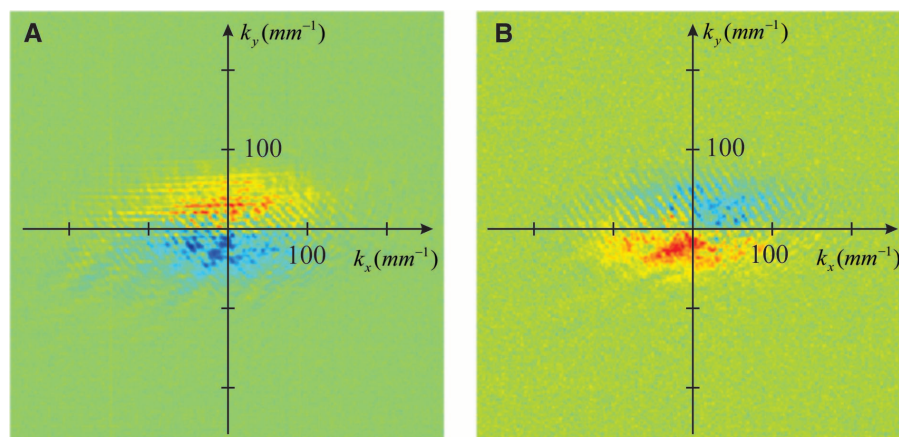


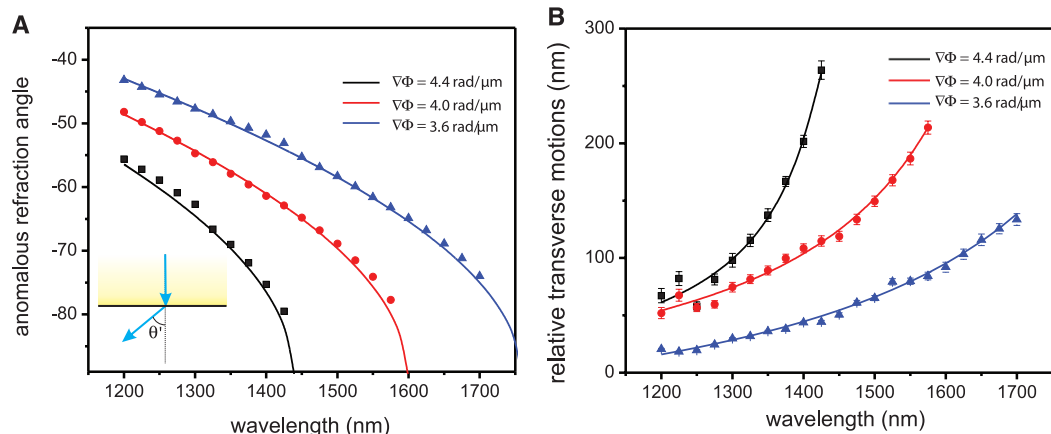
**Fig. 3.** (A) Observation of a giant SHE: the helicity of the anomalously refracted beam. The incidence is from the silicon side onto the metasurface and is polarized along the  $x$  direction along the phase gradient. The incidence angle is at surface normal. Red and blue represent the right and left circular polarizations, respectively. (B) Helicity of the refracted beam with incidence polarized along the  $y$  direction.

the beam is focused onto the sample with a spot size of  $\sim 50$   $\mu\text{m}$ . Our metasurfaces consist of V-shaped gold antennas. By changing the length and orientation of the arms of the V-shaped structures, the subwavelength antennas at resonance introduce tunable phase retardations between the incident and the forward-propagating fields. For linear phase retardation along the  $x$  direction, we chose eight antennas with optimized geometry parameters. We measured samples with different phase gradients; a scanning electron microscope image of the antenna array with a phase gradient of 4.4  $\text{rad}/\mu\text{m}$  is shown in Fig. 2A as one example. We used a lens of 50-mm focal length to collect the anomalously refracted far-field transmission through the metasurface, and we imaged this transmission on an InGaAs camera. The polarization of the incidence is linear and can be adjusted in either the  $x$  or  $y$  directions with a half-wave plate. The polarization states of the anomalously and the regularly refracted beams are resolved at the far field using an achromatic quarter-wave plate, a half-wave plate, and a po-

larizer with an extinction ratio greater than  $10^5$  for all wavelengths of interest.

Because the polarization state of light is unambiguously determined by the Stokes vector  $\hat{\mathbf{S}}$  on a unit Poincaré sphere, the evolution of the polarization due to spin-orbit interaction is well described by the precession of the Stokes vector on a Poincaré sphere. The helicity or the handedness of light is given by the circular Stokes  $S_z$  parameter (circular polarization)  $S_z = \frac{I_{\sigma^+} - I_{\sigma^-}}{I_{\sigma^+} + I_{\sigma^-}}$ , where  $I_{\sigma^+}$  and  $I_{\sigma^-}$  are the intensities of the anomalous refraction with circular polarization basis, which were imaged successively using the camera. The coordinates of the image represent the in-plane wave vectors of the refracted beams. The right circular  $\sigma^+$  and left circular  $\sigma^-$  polarizations are discriminated by setting appropriately the angle of the wave plates and polarization analyzer. Using the polarization-resolved detection, we calculated the circular Stokes parameter of the anomalously refracted beam from measurements for each pixel; this is shown in Fig. 3A for  $x$ -polarized incidence. The in-plane wave vector dependence

**Fig. 4. (A)** Wavelength dependence of the refraction angles when excitation is normally incident onto the metasurface. The measurement was conducted for three samples with different phase gradients of 3.6, 4.0, and 4.4 rad/ $\mu\text{m}$ . The measured refraction angles agree well with the theoretical predictions (solid curves). The angles are the same for both the left and right circularly polarized light. (Inset) Schematic depiction of the light trajectory for the anomalous refraction for the surface normal incidence. **(B)** Transverse motion (data points with error bars) between anomalously refracted light beams with right and left circular polarizations, showing a PSHE effect over a broad range of wavelengths. Solid curves are a guide for the eyes. The measurement was performed for three metasurfaces with different phase gradients. The



of the circular Stokes parameters shows a maximal value of  $\sim 0.1$  located at  $\pm\pi/2$ , and the sign of  $S_z$  is reversed between  $+\pi/2$  and  $-\pi/2$ , showing a transverse motion of the polarization. Whereas the incident angle is kept at zero throughout the experiment, the phase gradient along the interface removes the axial symmetry of the optical system and enables the direct observation of the PSHE for the anomalously refracted beams with different circularly polarized light. Figure 3B shows the PSHE effect for y-polarized incidence: The helicity of the refracted beam is clearly inverted due to the  $90^\circ$  phase rotation of the incidence. As the transverse spin current is solely determined by the longitudinal components of electromagnetic fields, such a distinct PSHE can only be observed in the anomalously refracted beam. As a control experiment, the spin-orbit coupling vanishes for the regularly transmitted beam, which exits the metasurface in the direction of the surface normal.

The photonic spin-orbit interaction in a curved light path not only manifests a helicity-dependent circular birefringence but also influences the trajectory of light. This effect resembles the Imbert-Fedorov shifts in the case of total internal reflections (27) and the recently observed optical Magnus effect at the near field (28, 29). When considering spin-orbit coupling, the ordinary Fermat principle based on ray optics is not sufficient in predicting the light trajectory; therefore, a helicity-dependent transverse motion of light emerges from the additional geometric phases due to spin-orbit interaction. For the incident light with a pure spin state (circularly polarized), a transverse motion of the beam's center of mass is thus expected.

Such a transverse motion occurs in real space and can be directly measured. Replacing the polarization optics shown in Fig. 2B with a variable liquid-crystal phase retarder, we measured the spin-dependent motion of photons (the relative displacement between the anomalously refracted  $I_{\sigma^+}$  and  $I_{\sigma^-}$ ) by an InGaAs quadrant detector with polarized incident beam periodically modulated in either left- ( $\sigma^+$ ) or right-handed ( $\sigma^-$ ) polarization states. Throughout the experiment, the incidence

angle was kept at normal incidence to the sample. The tailored in-plane phase gradient induces anomalous transmission at different refracting angles determined by the gradient. Figure 4A shows the refraction angle at different incident wavelengths for multiple samples with different phase gradients. The anomalous refraction angle approaches  $90^\circ$  when the incident wavelength approaches eight times the period of the V-shaped antennas. In Fig. 4B, the transverse motions of the beams are shown at the normal incident for wavelengths over hundreds of nanometers in bandwidth. The feedback from the polarization clearly deviates the trajectory from that given by the ordinary Fermat Principle. The strong spin-orbit interactions induced by the resonant V-shaped antenna array enable the observation of the transverse displacement, which increases rapidly as the anomalous refraction angle approaches  $90^\circ$ . Current PSHE theory assumes the conserved momentum solely over the Gaussian wave packet. However, the rapid phase gradient along the metasurface supplies additional momentum, making such a theoretical treatment incomplete. A new apparatus for analytical analysis should be developed to account for such a rapid phase gradient along the surface. By considering the energy transport at the interface, however, the polarization-dependent transverse motion of light can be analyzed by integrating the Poynting vectors (including the evanescent fields) over the half-space of the exiting medium (see the supplementary materials).

The strong photonic SHE at a metasurface with a designed phase discontinuity over the wavelength scale enables the observation of transverse motions of circularly polarized light. The anomalous skew scattering of light simultaneously breaks the rotational symmetry in the polarization space and the axial symmetry along its trajectory, giving rise to a broadband PSHE, even at the normal incidence. The generation and manipulation of strong spin-orbit interaction of light with tailored nanomaterials provide a new degree of freedom in information transfer between spin and orbital angular momentum of photons.

incidence was kept at surface normal but was periodically modulated between the left and right circular polarizations. Any transverse motion of the weight center of the beam was detected by a position-sensitive detector.

## References and Notes

1. E. Hirsch, *Phys. Rev. Lett.* **83**, 1834 (1999).
2. S. A. Wolf *et al.*, *Science* **294**, 1488 (2001).
3. T. Jungwirth, J. Wunderlich, K. Olejnik, *Nat. Mater.* **11**, 382 (2012).
4. B. A. Bernevig, X. W. Yu, S. C. Zhang, *Phys. Rev. Lett.* **95**, 076602 (2005).
5. M. Onoda, S. Murakami, N. Nagaosa, *Phys. Rev. Lett.* **93**, 083901 (2004).
6. K. Y. Bliokh, Y. P. Bliokh, *Phys. Rev. Lett.* **96**, 073903 (2006).
7. K. Bliokh, A. Niv, V. Kleiner, E. Hasman, *Nat. Photonics* **2**, 748 (2008).
8. O. Hosten, P. Kwiat, *Science* **319**, 787 (2008).
9. Y. Gorodetski *et al.*, *Phys. Rev. Lett.* **109**, 013901 (2012).
10. J. B. Pendry, *Phys. Rev. Lett.* **85**, 3966 (2000).
11. R. A. Shelby, D. R. Smith, S. Schultz, *Science* **292**, 77 (2001).
12. N. Fang, H. Lee, C. Sun, X. Zhang, *Science* **308**, 534 (2005).
13. J. B. Pendry, D. Schurig, D. R. Smith, *Science* **312**, 1780 (2006).
14. J. Valentine, J. Li, T. Zentgraf, G. Bartal, X. Zhang, *Nat. Mater.* **8**, 568 (2009).
15. F. Falcone *et al.*, *Phys. Rev. Lett.* **93**, 197401 (2004).
16. S. L. Sun *et al.*, *Nat. Mater.* **11**, 426 (2012).
17. N. Yu *et al.*, *Science* **334**, 333 (2011).
18. X. Ni, N. K. Emani, A. V. Kildishev, A. Boltasseva, V. M. Shalae, *Science* **335**, 427 (2012).
19. Y. Zhao, A. Alù, *Phys. Rev. B* **84**, 205428 (2011).
20. P. Genevet *et al.*, *Appl. Phys. Lett.* **100**, 013101 (2012).
21. F. Aieta *et al.*, *Nano Lett.* **12**, 4932 (2012).
22. M. A. Kats *et al.*, *Proc. Natl. Acad. Sci. U.S.A.* **109**, 12364 (2012).
23. V. S. Liberman, B. Y. Zel'dovich, *Phys. Rev. E* **49**, 2389 (1994).
24. R. Y. Chiao, Y. S. Wu, *Phys. Rev. Lett.* **57**, 933 (1986).
25. M. V. Berry, *Nature* **326**, 277 (1987).
26. D. R. Smith, J. J. Mock, A. F. Starr, D. Schurig, *Phys. Rev. E* **71**, 036609 (2005).
27. O. Costa de Beauregard, C. Imbert, Y. Levy, *Phys. Rev. D* **15**, 3553 (1977).
28. K. Y. Bliokh, Y. Gorodetski, V. Kleiner, E. Hasman, *Phys. Rev. Lett.* **101**, 030404 (2008).
29. Y. Gorodetski, A. Niv, V. Kleiner, E. Hasman, *Phys. Rev. Lett.* **101**, 043903 (2008).

**Acknowledgments:** This research is supported by the U.S. Department of Energy, Office of Basic Energy Sciences under contract no. DE-AC02-05CH11231 through the Materials Sciences Division of LBNL. J.R. acknowledges a fellowship from the Samsung Scholarship Foundation, Republic of Korea. We thank S. Dhuey and S. Cabrini of the Molecular Foundry at LBNL for their help on electron beam lithography over large areas.

## Supplementary Materials

www.sciencemag.org/cgi/content/full/339/6126/1405/DC1  
Supplementary Text  
Fig. S1  
References (30, 31)

19 October 2012; accepted 9 January 2013  
10.1126/science.1231758



# A Terradynamics of Legged Locomotion on Granular Media

Chen Li,<sup>1,2</sup> Tingnan Zhang,<sup>1</sup> Daniel I. Goldman<sup>1\*</sup>

The theories of aero- and hydrodynamics predict animal movement and device design in air and water through the computation of lift, drag, and thrust forces. Although models of terrestrial legged locomotion have focused on interactions with solid ground, many animals move on substrates that flow in response to intrusion. However, locomotor-ground interaction models on such flowable ground are often unavailable. We developed a force model for arbitrarily-shaped legs and bodies moving freely in granular media, and used this “terradynamics” to predict a small legged robot’s locomotion on granular media using various leg shapes and stride frequencies. Our study reveals a complex but generic dependence of stresses in granular media on intruder depth, orientation, and movement direction and gives insight into the effects of leg morphology and kinematics on movement.

The locomotion of animals (1) and devices (2–4) emerges from the effective interaction of bodies and/or appendages with an environment. For flying in air and swimming in water, there is a history of theoretical predictive models (3–5) to describe the complex interactions between the locomotor and the surrounding fluids, based on the fundamental equations for fluid flow, the Navier-Stokes equations. These models have not only allowed understanding of the movement of a variety of aerial and aquatic organisms (5) [such as bacteria and spermatazoa (6), insects (7), birds (8), and fish and whales (9)] and their functional morphology, evolution, and ecology (9, 10), but also advanced the engineering design of aircraft (3), marine vehicles (4), and flying (11) and swimming (12) robots. For running and walking on ground, studies using solid ground such as running tracks and treadmills have inspired general models (13, 14); building on these models, researchers have begun to apply dynamical systems theory (15). In these studies, the leg-ground interaction was often approximated as a point contact on a rigid, flat, and nonslip ground (13–15).

Many small legged animals (16–19) [and increasingly robots (20–23)] face the challenges of moving on natural substrates such as sand (16, 17, 21), gravel (16, 20), rubble (20), soil (20, 22), mud (17, 20), snow (18, 20), grass (20, 22), and leaf litter (19, 20, 22), which, unlike solid ground, can flow during movement when a yield stress is exceeded. The complexity of the interactions with such “flowable ground” may rival or even exceed that during movement in fluids. For example, recent studies of legged animals (16) and robots (21) moving on granular media [collections of particles (24)] such as sand and gravel (Fig. 1, A and B) have demonstrated that at an instant of time during a step, each element of a leg moves through the substrate at a specific depth, orientation, and movement direction, all of which can change over time (16, 21). Furthermore, the

leg interacts with a material that can display both solid-like and fluid-like features (24) (Fig. 1, C and D). Compared to the theories of aero- and hydrodynamics, predictive models are less well developed for calculating forces and predicting legged locomotion on such flowable ground (16, 21).

Research in the field of terramechanics (2) has advanced the mobility of off-road vehicles on flowable ground such as sand and soil. These models were developed for large wheeled and tracked vehicles, which sink only slightly into the substrate (2, 25). Thus, in terramechanical models, interaction with the ground is approximated as the indentation of a horizontal, flat, rectangular plate (2, 25). It was a breakdown of this flat-plate approximation, however, that led to overpredicted speeds for small vehicles such as the Mars rovers, whose small wheels have substantially curved ground contact interfaces

(25). Because leg-ground interaction on flowable substrates is a more diverse, complex, and dynamic process (16, 21) than the flat-plate indentation, terramechanics is not expected to apply to legged locomotors on flowable ground (2).

Granular materials such as sand and gravel (24), home to a variety of small desert animals (16, 17, 26), have proved to be a promising model substrate for studying legged locomotion on flowable ground (16, 21). Despite their diversity in particle size, shape, density, friction, polydispersity, and compaction (24), dry granular media are relatively simple as compared to media such as soil and mud, because granular particles interact purely through dissipative, repulsive contact forces and have no cohesion (24). In addition, the penetration resistance of granular media can be repeatedly controlled using laboratory apparatus such as an air-fluidized bed (16, 21, 26).

To begin to create a “terradynamics” that allows the prediction of legged locomotion on a flowable ground, we hypothesized that the net forces on a leg (or a body) moving in a granular medium in the vertical plane could be approximated by the linear superposition of resistive forces on infinitesimal leg (or body) elements. Our hypothesis was inspired by our recent success in applying the methods of resistive force theory (6) to predict the forces and movement during the limbless locomotion of a lizard swimming in sand (26) and in describing the drag (26, 27) and lift (27) on simple objects moving in granular media at fixed depths. In these studies, the linear superposition was valid for intruders moving in granular media in the horizontal plane at low enough speeds [for example,  $\leq 0.5$  m/s for

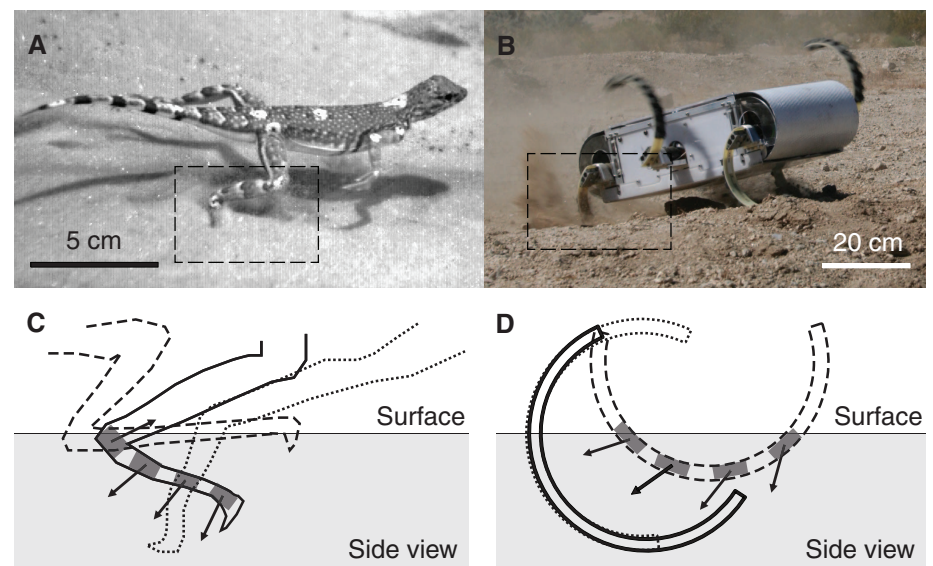


**Fig. 1.** Examples of legged locomotion on flowable ground. (A) A zebra-tailed lizard running on sand (16). (B) A biologically inspired RHex robot (22) walking on dirt [Photo credit: Galen Clark Haynes, Aaron M. Johnson, and Daniel E. Koditschek, University of Pennsylvania]. Dashed boxes in (A) and (B) indicate the regions of leg-ground interaction shown in (C) and (D). Schematic of leg-ground interaction for (C) a hind foot of a zebra-tailed lizard (16) and (D) a c-leg of a RHex robot (21) during a step on granular media. Dashed, solid, and dotted tracings are leg positions at early, mid-, and late stance. Bars and arrows indicate local orientations and movement directions of leg elements. The gray area is the granular substrate.

<sup>1</sup>School of Physics, Georgia Institute of Technology, Atlanta, GA 30332, USA. <sup>2</sup>Department of Integrative Biology, University of California, Berkeley, CA 94720, USA.

\*Corresponding author. E-mail: daniel.goldman@physics.gatech.edu

0.3-mm glass particles (26)], where intrusion forces are dominated by particle friction (insensitive to speed) and non-inertial (26). However, it was unclear whether linear superposition could apply to legs (or bodies) of complex morphology and kinematics moving in the vertical plane.

To measure resistive forces for leg elements, we moved a thin rigid plate (of area  $A$ ) in granular media in the vertical plane at 1 cm/s and measured lift  $f_z$  and drag  $f_x$  on the plate (in the continuously yielding regime). We determined vertical and horizontal stresses  $\sigma_{z,x} = f_{z,x}/A$  as a function of the plate's depth  $|z|$  below the surface, angle of attack  $\beta$ , and angle of intrusion  $\gamma$  (Fig. 2A and movie S1) (28). To test the generality of our resistive force model, we used three dry granular media of various particle size, shape, density, and friction, prepared into flat, naturally occurring, loosely and closely packed states (16, 21, 26) (supplementary text section 2, fig. S3, and table S1). Slightly polydispersed near-spherical glass particles 0.3 and 3 mm in diameter [covering the particle size range of natural dry sand ( $\sim 0.1$  to  $\sim 1$  mm) (29)] and rounded, slightly kidney-shaped poppy seeds (0.7 mm in diameter) allowed us to probe general principles for naturally occurring granular media of high sphericity and roundness [such as Ottawa sand (30)]. We discuss at the end of the paper possible effects of particle nonsphericity and angularity also found in many natural sands (30).

In all media tested, we observed that for all attack angles  $\beta$  and intrusion angles  $\gamma$ ,  $\sigma_{z,x}$  were nearly proportional to depth  $|z|$  when the plate

was fully submerged and far from the bottom of the container (Fig. 2B and movie S1). This is because friction-dominated forces are proportional to the hydrostatic-like pressure in granular media. Therefore, we modeled the hydrostatic-like stresses as

$$\sigma_{z,x}(|z|, \beta, \gamma) = \begin{cases} \alpha_{z,x}(\beta, \gamma)|z| & \text{if } z < 0 \\ 0 & \text{if } z > 0 \end{cases} \quad (1)$$

where  $\alpha_{z,x}$  are vertical and horizontal stresses per unit depth (slopes of dashed fit lines in Fig. 2B). We found that in all media tested,  $\alpha_{z,x}$  depended sensitively on both attack angle  $\beta$  and intrusion angle  $\gamma$  (Fig. 2, C and D, fig. S4, and additional data table S5).  $\alpha_z$  (or  $\alpha_x$ ) was opposing the plate's vertical (or horizontal) velocity for most but, counterintuitively, not all  $\beta$  and  $\gamma$  (exceptions are indicated by the shaded regions). For almost all attack angles  $\beta$ ,  $\alpha_{z,x}$  had larger magnitudes ( $|\alpha_{z,x}|$ ) for intrusion angle  $\gamma \geq 0$  than for  $\gamma \leq 0$ ; i.e., it was harder to push the plate into granular media than to extract it. For all intrusion angles  $\gamma$  except  $\gamma = \pm\pi/2$ ,  $|\alpha_{z,x}|$  were asymmetric to attack angles  $\beta = 0$  and  $\beta = \pm\pi/2$ ; i.e., only when the plate moved vertically were stress magnitudes the same for vertically or horizontally mirrored orientations (e.g.,  $\beta = \pm\pi/6$ ). These asymmetries are a result of gravity breaking symmetry in the vertical plane and differ from the case in the horizontal plane (26). Our resistive force measurements are an advance from previous force models based on the flat-plate approximation used in many teramechanical models (2, 25), which capture only

the dependence of stresses on intruder depth, but not on its orientation or movement direction (supplementary text section 1 and fig. S1). Despite their different magnitudes and subtle differences in shape, the overall profiles of stresses (per unit depth)  $\alpha_{z,x}(\beta, \gamma)$  were similar for all media tested. Furthermore, these stress profiles could be approximated (to the first order) by a simple scaling of generic stress profiles (supplementary text section 3, figs. S6 and S7, and tables S2 and S3).

We next tested our hypothesis that forces on a complex intruder moving in granular media in the vertical plane could be approximated by the linear superposition of forces on all intruder elements. We measured the net lift  $F_z$  and thrust  $F_x$  on thin rigid model legs rotating about a fixed axle [simulating a tethered body (7, 11)] through granular media in the vertical plane at  $\sim 1$  cm/s (Fig. 3 and movie S2) (28). We then compared them to predictions from the resistive force model by the integration of stresses over the legs (movie S3)

$$\begin{aligned} F_{z,x} &= \int_S \sigma_{z,x}(|z|_s, \beta_s, \gamma_s) dA_s \\ &= \int_S \alpha_{z,x}(\beta_s, \gamma_s) |z|_s dA_s \end{aligned} \quad (2)$$

where  $S$  is the leading surface of the leg;  $dA_s$ ,  $|z|_s$ ,  $\beta_s$ , and  $\gamma_s$  are the area, depth below the surface, angle of attack, and angle of intrusion of infinitesimal leg elements; and  $\alpha_{z,x}(\beta_s, \gamma_s)$  are element stresses per unit depth (interpolated from data in Fig. 2, C and D). To test the robustness of our force model, we used three model legs of different geometries [with the same maximal leg length  $2R$

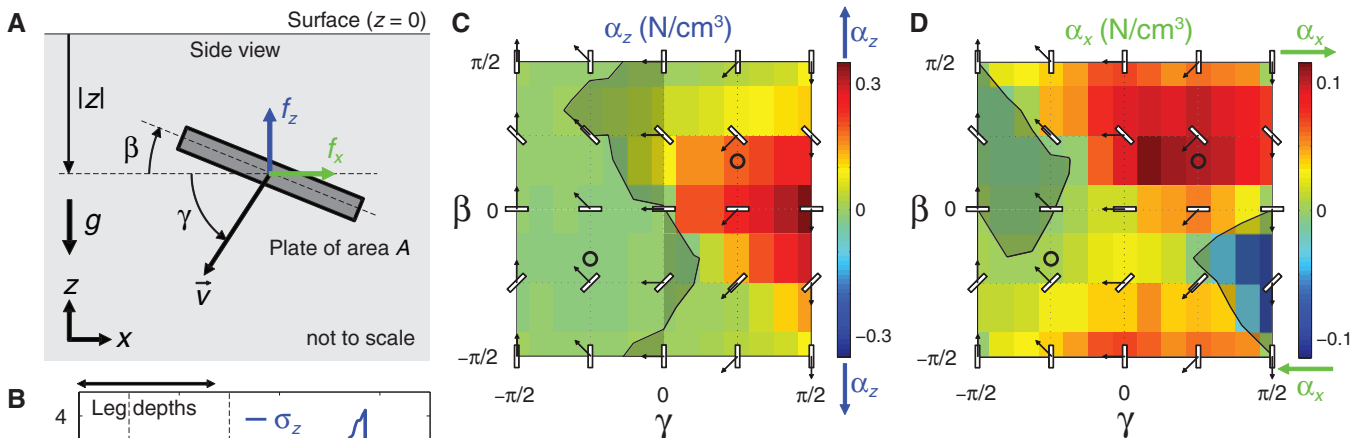


**Fig. 2.** Measurement of resistive forces in granular media in the vertical plane using a plate element (28). (A) Lift  $f_z$  (blue arrow) and drag  $f_x$  (green arrow) on a thin rigid plate of area  $A$  moving in granular media (gray area) in the vertical plane at speed  $v = 1$  cm/s were measured as a function of the plate's depth  $|z|$  below the surface, angle of attack  $\beta$ , and angle of intrusion  $\gamma$ . The granular media were fluidized (and then compacted when a closely packed state was prepared) using an air-fluidized bed (26) before each intrusion ( $\gamma \geq 0$ ) and extraction ( $\gamma \leq 0$ ).  $g$  is gravitational acceleration. (B) Vertical (blue curve) and horizontal (green curve) stresses  $\sigma_{z,x} = f_{z,x}/A$  versus  $|z|$  for representative intrusion and extraction using  $(\beta, \gamma) = (\pm\pi/6, \pi/4)$  (movie S1). Blue and green dashed lines are linear fits with zero intercept over intermediate depths at which the plate was fully submerged and far from the bottom of the container. Horizontal arrows on top indicate the range of leg depths in Figs. 3 and 4. (C) Vertical and (D) horizontal stresses per unit depth  $\alpha_{z,x}$  [slopes of dashed fit lines in (B)] versus  $\beta$  and  $\gamma$ . Plate schematics with arrows denote representative orientations and movement directions. Black curves indicate where  $\alpha_{z,x} = 0$ . The shaded areas indicate where  $\alpha_z$  (or  $\alpha_x$ ) is not opposing the plate's vertical (or horizontal) velocity. Circles indicate  $\alpha_{z,x}$  from data shown in (B). Arrows above and below the color bars indicate directions of  $\alpha_{z,x}$  for positive and negative values.

and movement directions. Black curves indicate where  $\alpha_{z,x} = 0$ . The shaded areas indicate where  $\alpha_z$  (or  $\alpha_x$ ) is not opposing the plate's vertical (or horizontal) velocity. Circles indicate  $\alpha_{z,x}$  from data shown in (B). Arrows above and below the color bars indicate directions of  $\alpha_{z,x}$  for positive and negative values.



(28): a RHex robot's c-leg (21, 22), a flat leg, and a reversed c-leg (Fig. 3, A to C). In model calculations, each leg was divided into 30 elements.

In all media tested (Fig. 3, D to F, and fig. S5), we observed that for all three legs, the measured net lift and thrust  $F_{z,x}$  as a function of leg angle  $\theta$  (solid curves) were asymmetric to the vertical downward direction ( $\theta = 0$ ), and were larger during intrusion ( $\theta \leq 0$ ) than during extraction ( $\theta \geq 0$ ). Peak  $F_{z,x}$  were largest on the c-leg and smallest on the reversed c-leg. The reversed c-leg experienced significant negative lift (suction force,  $F_z < 0$ ) during extraction. For all media tested, our resistive force model predicted  $F_{z,x}$  versus  $\theta$  for all three legs (dashed curves), capturing both the magnitudes and asymmetric profiles. The relative errors of peak forces between data and model predictions were within 10% for the c-leg in four media tested, and within 33% for all three legs in all media tested. The accuracy of our resistive force model was significantly better than that of previous force models in which stresses depended only on depth (Fig. 3, D to F, insets; supplementary text section 1 and fig. S2). Furthermore, our resistive force model revealed that the c-leg generated the largest forces, because its morphology allowed leg elements to not only reach deeper depths but also access larger stress regions in Fig. 2, C and D (particularly for elements at large depths).

Our discovery of the insensitivity of the stress profiles to particle properties (fig. S4) has practical benefits: For granular media of near-monodispersed, near-spherical, rounded particles, as an alternative to measuring  $\alpha_{z,x}$  for all attack angles  $\beta$  and intrusion angles  $\gamma$  in the laboratory, one can simply perform a single measurement [of  $\alpha_z(0, \pi/2)$ ], using a horizontal plate penetrating vertically downward] to infer all  $\alpha_{z,x}(\beta, \gamma)$  by a scaling routine (supplementary text section 3 and fig. S9) and predict forces (with a small loss in accuracy for the c-leg and the flat leg, but a larger loss in accuracy for the reversed c-leg, fig. S8).

We tested the ability of our resistive force model to predict legged locomotion. We chose to study the locomotor performance (speed) of a small RHex-like robot (22) (Fig. 4A, top, and movie S4) moving on granular media (28). The robot's six legs rotated nearly entirely in the vertical plane during locomotion, and its small size ensured that leg intrusion speeds were low enough for particle inertia to be negligible. We chose poppy seeds as the test granular medium, because the grains were both small enough to be prepared in our fluidized bed track (21) and large enough to not jam the robot's motor and gear trains. The robot's legs had a similar friction coefficient with poppy seeds to that of the model legs and were sufficiently rigid so that they experienced negligible bending during movement. (28).

Unlike the sand-swimming lizard, which moves within granular media quasistatically (thrust and drag are always roughly balanced) (26), legged locomotion on the surface of granular media is dynamic (forces are not always instantaneously balanced). As a result, the resistive force theory

(which solves for speed by balancing forces) (6, 26) cannot be directly applied. Thus, to use our resistive force model to calculate robot speed, we developed a three-dimensional multi-body dynamic simulation of the robot (Fig. 4A, bottom) (28). The simulated robot had the same body and leg morphology and used the same alternating tripod gait as the actual robot and had its motion constrained in the vertical plane. We divided each body plate and leg into 30 elements. The velocity  $\vec{v}$  and angular velocity  $\vec{\omega}$  of the simulated robot's body were calculated by

$$\begin{cases} \vec{v}(t+dt) = \vec{v}(t) + \frac{\vec{F}}{m} dt \\ \vec{\omega}(t+dt) = \vec{\omega}(t) + \frac{\vec{N}}{I} dt \end{cases} \quad (3)$$

where  $\vec{F}$  and  $\vec{N}$  are the sum of net forces and torques on all the six legs and the body exerted by the granular medium, calculated from our resistive force model by the integration of stresses over each leg and the body using Eq. 2;  $m$  and  $I$  are the robot's mass and moment of inertia; and  $t$  and  $dt$  are time and time step. To test the robustness of our resistive force model and simulation, we used legs of seven geometries with different curvatures  $1/r$  (given maximal leg length  $2R$ ) (Fig. 4C, inset) and varied stride frequency  $f$  to up to 5 Hz (28).

We observed similar robot kinematics (Fig. 4A) and forward speed  $v_x$  versus time  $t$  (Fig. 4B) in both the experiment (movie S5) and simulation (movie S6). The robot moved faster and penetrated its legs less deeply during stance using c-legs (Fig. 4A, left; Fig. 4B, red) than using reversed c-legs (Fig. 4A, right; Fig. 4B, blue). Average forward speed  $\bar{v}_x$  increased with stride frequency  $f$  for legs of all curvatures  $1/r$  and was lower at any  $f$  using legs of negative curvatures than using legs of positive curvatures (Fig. 4, C and D). The agreement between experiment and simulation in  $\bar{v}_x(f, 1/r)$  was remarkable: Errors were within 20% for 90% of the  $f$  and  $1/r$  tested and within 35% for all the  $f$  and  $1/r$  tested. Simulation using our scaling routine also achieved reasonable accuracy (supplementary text section 5 and fig. S13). This was an improvement over simulation using previous force models in which stresses depended only on depth (fig. S13). Our resistive force model and simulation revealed that the robot moved faster using c-legs than using reversed c-legs, because whereas the c-legs penetrated less deeply, their elements accessed larger stress regions in Fig. 2, C and D, resulting in larger leg lift (fig. S14) and smaller body drag. Our model and simulation also allowed the prediction of ground reaction forces on granular media (Fig. 4A, red arrows, and fig. S13), which

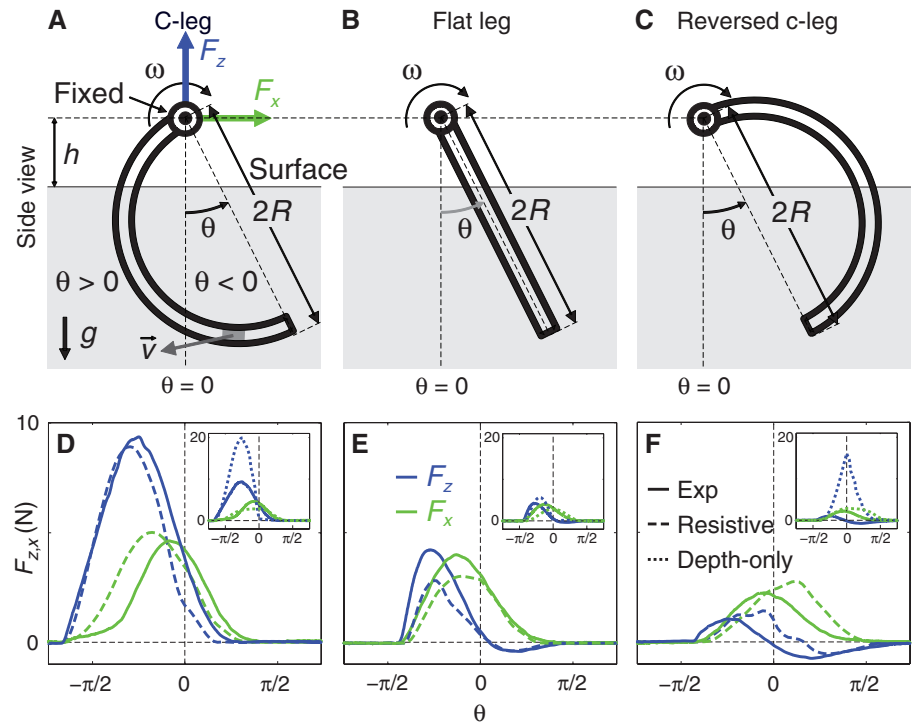


**Fig. 3.** The resistive force model predicts forces on intruders of complex morphology and kinematics moving in granular media (28). Three thin rigid model legs of different geometries, (A) a c-leg, (B) a flat leg, and (C) a reversed c-leg, were rotated about a fixed axle at a hip height  $h$  through granular media (gray area) in the vertical plane at an angular velocity  $\omega$ , generating leg speeds of  $v \sim 1$  cm/s, and net lift  $F_z$  (blue) and thrust  $F_x$  (green) were measured as a function of leg angle  $\theta$  (movie S2). All three legs had identical maximal length  $2R$  from the axle.  $g$  is gravitational acceleration. (D to F)  $F_{z,x}$  versus  $\theta$  on the three legs measured in the experiment (solid curves) and predicted by the resistive force model (dashed curves) using Eq. 2 (movie S3). Insets:  $F_{z,x}$  versus  $\theta$  from experiment (solid curves) versus predicted (dotted curves) using Eq. 2 and previous force models in which stresses depended only on depth (supplementary text section 1 and fig. S2).

would be difficult to measure otherwise. Furthermore, our model and simulation predicted that using arc-like legs (given maximal leg length  $2R'$ ) of an optimal curvature of  $1/r = 0.86/R'$ , the robot would achieve maximal speed of  $\bar{v}_x = 72$  cm/s ( $\approx 5$  body length/s) at 5 Hz. Our approach affords significant reduction in the computational time needed to model movement on granular media. For example, relative to our multiparticle discrete element method (DEM) simulation of movement on granular media (23, 27), our simulation using the resistive force model can achieve a factor of  $10^6$  in speed-up (e.g., 10 s versus 30 days using DEM to simulate 1 s of locomotion on a granular bed of  $5 \times 10^6$  poppy seeds).

We close with a brief discussion of the limitations of our model. We tested the predictive power of our scaling routine (supplementary text section 3 and fig. S9) for two highly polydispersed, nonspherical, highly angular natural sands (supplementary text section 4, figs. S10 to S12, and table S4). We found that the model accuracy for natural sands was slightly worse than found in the glass spheres and poppy seeds (for example, 35% versus 20% error in peak  $F_z$  for a rotating c-leg). As was the case for the near-spherical granular media tested, the functional forms of

forces on the c-leg and the flat leg were still well captured by our scaling routine. Furthermore, the overestimation was not affected by reducing the polydispersity of the natural sand. This suggests that the nonsphericity and angularity of natural sand particles (30) may be the cause of this overestimation, which may require additional model fitting parameters and scaling factors. Our model is intended for dry sand [ $\sim 0.1$  to  $\sim 1$  mm in particle diameter (29)] and may not work for dry cohesive powder ( $\leq \sim 0.01$  mm) (31). We do not expect our model to work if the particle size approaches a characteristic length of the locomotor (for example,  $\sim 1$ -cm particles for our robot of  $\sim 1$ -cm foot size), so that the continuum assumption breaks down and particles effectively become “boulders.” We also do not expect our model to capture wet, cohesive flowable media such as soil and mud.

We have developed a new approach to predicting legged locomotion on granular media. This terradynamics relies on new resistive force measurements and linear superposition (6, 26, 27). The general profiles of these resistive force measurements are insensitive (other than magnitudes) to a variety of granular media composed of slightly polydispersed, approximately spherical, rounded particles. Our terradynamics may not be limited

to legged locomotion, because the integration of stresses should in principle work for devices of other morphology and kinematics, such as wheels, tracks, and earth movers moving on granular media (2, 25). For the particle types tested here, an important addition to our model would be to capture three-dimensional effects (16) and spatial and temporal variation in compaction (21) and slopes (17), and test its validity in the high-speed “inertial fluid” regime (when leg intrusion speed is  $\geq 1$  m/s, at which particle inertia dominates forces) (23). Our resistive force model also provides opportunities to test and develop new physics theories of dense granular flow (32). Finally, we envision that, in concert with aero- and hydrodynamics (3–12), a general terradynamics of complex ground will not only advance understanding of how animals move (1) at present (5–10, 13–19, 26) and in the past (17, 33), but also facilitate the development of robots with locomotor capabilities approaching those of organisms (11, 12, 20–23).

## References and Notes

1. M. H. Dickinson *et al.*, *Science* **288**, 100 (2000).
2. M. G. Bekker, *Off-the-Road Locomotion, Research and Development in Terramechanics* (Univ. of Michigan Press, Ann Arbor, MI, 1960).
3. B. Etkin, *Dynamics of Atmospheric Flight* (Wiley, New York, 1972).
4. J. N. Newman, *Marine Hydrodynamics* (MIT Press, Cambridge, MA, 1977).
5. S. Vogel, *Life in Moving Fluids: The Physical Biology of Flow* (Princeton Univ. Press, Princeton, NJ, 1996).
6. E. Lauga, T. R. Powers, *Rep. Prog. Phys.* **72**, 096601 (2009).
7. Z. J. Wang, *Annu. Rev. Fluid Mech.* **37**, 183 (2005).
8. C. J. Pennycuik, *Avian Biol.* **5**, 1 (1975).
9. G. V. Lauder, J. C. Nauen, E. G. Drucker, *Integr. Comp. Biol.* **42**, 1009 (2002).
10. R. Dudley, *The Biomechanics of Insect Flight: Form, Function, Evolution* (Princeton Univ. Press, Princeton, NJ, 2002).
11. R. S. Fearing *et al.*, *IEEE Int. Conf. Rob. Auto.* **2000**, 1509 (2000).
12. G. V. Lauder, E. J. Anderson, J. Tangorra, P. G. A. Madden, *J. Exp. Biol.* **210**, 2767 (2007).
13. R. Blickhan, *J. Biomech.* **22**, 1217 (1989).
14. G. A. Cavagna, H. Thys, A. Zamboni, *J. Physiol.* **262**, 639 (1976).
15. P. Holmes, R. J. Full, D. E. Koditschek, J. Guckenheimer, *SIAM Rev.* **48**, 207 (2006).
16. C. Li, S. T. Hsieh, D. I. Goldman, *J. Exp. Biol.* **215**, 3293 (2012).
17. L. R. Brand, *J. Paleontol.* **70**, 1004 (1996).
18. S. G. Fanc, R. G. White, *J. Wildl. Manage.* **49**, 987 (1985).
19. L. J. Vitt, S. S. Sartorius, T. C. S. Avila-Pires, M. C. Espósito, *Copeia* **2001**, 401 (2001).
20. M. Raibert, K. Blankespoor, G. Nelson, R. Playter, and the BigDog Team; BigDog, the rough-terrain quadruped robot. *Inter. Fed. Auto. Cont.* **2008**, 10822 (2008).
21. C. Li, P. B. Umbanhowar, H. Komsuoglu, D. E. Koditschek, D. I. Goldman, *Proc. Natl. Acad. Sci. U.S.A.* **106**, 3029 (2009).
22. A. M. Johnson, M. T. Hale, G. C. Haynes, D. E. Koditschek, *2011 IEEE Saf. Sec. Res. Rob.* **2011**, 134 (2011).
23. T. Zhang *et al.*, *Int. J. Robotics. Res.* **32**, 10.1177/0278364913481690 (2013).
24. R. M. Nedderman, *Statics and Kinematics of Granular Materials* (Cambridge Univ. Press, New York, 1992).
25. G. Meirion-Griffith, M. Spenko, *IEEE Aerospace Conf.* **2010**, 1 (2010).
26. R. D. Maladen, Y. Ding, C. Li, D. I. Goldman, *Science* **325**, 314 (2009).
27. Y. Ding, N. Gravish, D. I. Goldman, *Phys. Rev. Lett.* **106**, 028001 (2011).

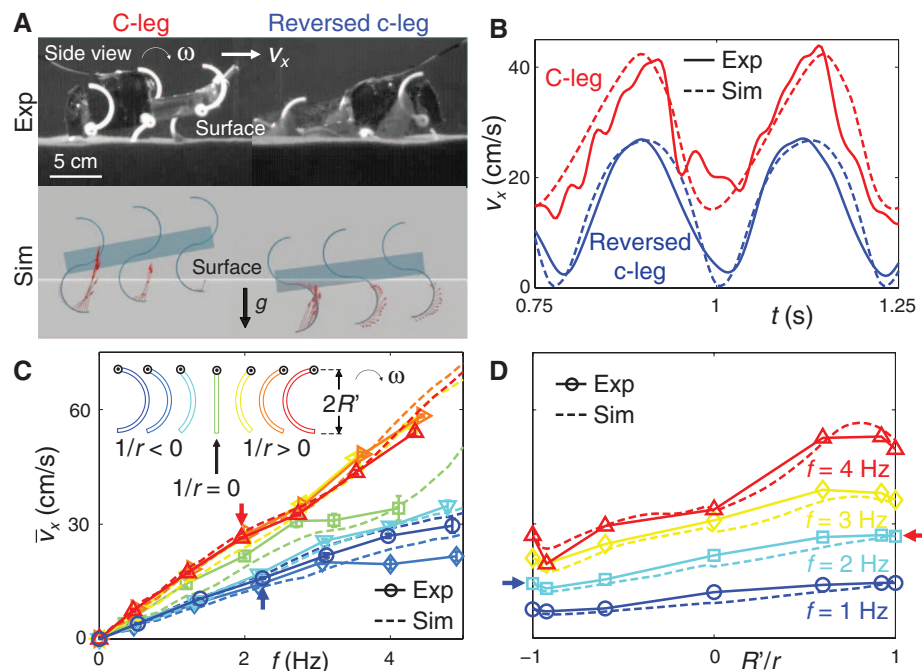


**Fig. 4.** A multibody dynamic simulation using the resistive force model predicts legged locomotion on granular media (28). **(A)** Side views of a small RHex-like robot (movie S4) at mid-stance during locomotion on granular media, using c-legs (left) and reversed c-legs (right) in the experiment (top, movie S5) and simulation (bottom, movie S6). Arrows in the simulation indicate element forces on one tripod of legs.  $g$  is gravitational acceleration. **(B)** Forward speed  $v_x$  versus time  $t$  from two representative runs using c-legs (red, stride frequency  $f = 2.0$  Hz, curvature  $1/r = 1/R'$ ) and reversed c-legs (blue,  $f = 2.2$  Hz,  $1/r = -1/R'$ ). **(C)** Average forward speed  $\bar{v}_x$  versus  $f$  using legs of seven curvatures  $1/r$  transitioning from reversed c-legs to c-legs (inset), where  $r$  is the radius of curvature,  $2R'$  is the maximal length of the robot legs, and the minus sign denotes reversed legs. **(D)**  $\bar{v}_x$  versus  $1/r$  at  $f = 1, 2, 3$ , and 4 Hz. In **(B)** to **(D)**, solid and dashed curves indicate the experiment and simulation, respectively. Error bars in **(C)** denote  $\pm 1$  SD ( $\ll 1$  cm/s in the simulation). Experimental data in **(D)** are interpolated from those in **(C)** (hence no error bars). Red and blue arrows in **(C)** and **(D)** indicate averages from data shown in **(B)**.



28. Materials and methods are available as supplementary materials on *Science* Online.
29. R. A. Bagnold, *The Physics of Blown Sand and Desert Dunes* (Dover Publications, Mineola, NY, 2005).
30. G. Cho, J. Dodds, J. C. Santamarina, *J. Geotech. Geoenviron. Eng.* **132**, 591 (2006).
31. B. Chaudhuri, A. Mehrotra, F. J. Muzzio, M. S. Tomassone, *Powder Technol.* **165**, 105 (2006).
32. K. Kamrin, G. Koval, *Phys. Rev. Lett.* **108**, 178301 (2012).
33. J. A. Clack, *Gaining Ground: The Origin and Evolution of Tetrapods* (Indiana Univ. Press, Bloomington, IN, 2012).

**Acknowledgments:** We thank Y. Ding, P. Umbanhowar, N. Gravish, G. Meirion-Griffith, S. Sharpe, H. Komsuoglu, D. Koditschek, and R. Full for discussions; J. Shen for

assistance with robot modification; P. Masarati for multibody dynamic simulator support; S. Sharpe for measuring the angle of repose of 3-mm glass spheres and assistance with photography; P. Umbanhowar and H. Marvi for natural sand collection; and all the members of the Complex Rheology And Biomechanics Lab at Georgia Tech for general assistance. This work was supported by the Burroughs Wellcome Fund, the Army Research Laboratory Micro Autonomous Systems and Technology Collaborative Technology Alliance, the Army Research Office, and the NSF Physics of Living Systems program. C.L. was partially supported by a Miller Research Fellowship from the Miller Institute for Basic Research in Science of the University of California, Berkeley. The authors declare that they have no competing interests. C.L. designed the study, performed resistive force measurements,

and performed robot experiments; C.L. and T.Z. performed model calculations; T.Z. performed robot simulation; D.I.G. oversaw the study; and C.L. and D.I.G. wrote the paper.

#### Supplementary Materials

[www.sciencemag.org/cgi/content/full/339/6126/1408/DC1](http://www.sciencemag.org/cgi/content/full/339/6126/1408/DC1)  
Materials and Methods  
Supplementary Text  
Figs. S1 to S14  
Tables S1 to S4  
References (34–38)  
Movies S1 to S6  
Additional Data Table S5

22 August 2012; accepted 15 January 2013  
10.1126/science.1229163

# DNA Gridiron Nanostructures Based on Four-Arm Junctions

Dongran Han,<sup>1,2\*</sup> Suchetan Pal,<sup>1,2</sup> Yang Yang,<sup>1,2</sup> Shuoxing Jiang,<sup>1,2</sup> Jeanette Nangreave,<sup>1,2</sup> Yan Liu,<sup>1,2\*</sup> Hao Yan<sup>1,2\*</sup>

Engineering wireframe architectures and scaffolds of increasing complexity is one of the important challenges in nanotechnology. We present a design strategy to create gridiron-like DNA structures. A series of four-arm junctions are used as vertices within a network of double-helical DNA fragments. Deliberate distortion of the junctions from their most relaxed conformations ensures that a scaffold strand can traverse through individual vertices in multiple directions. DNA gridirons were assembled, ranging from two-dimensional arrays with reconfigurability to multilayer and three-dimensional structures and curved objects.

Self-assembling nucleic acid molecules have shown merit as versatile materials for organizing and constructing complex nanoscale structures (1). In 2006, Rothemund described a method to generate complex DNA origami nanostructures with addressable surface features. In this method, a long scaffold strand, most often the 7429-nucleotide (nt) circular genome of the M13mp18 bacteriophage, is organized and folded by interactions with a large number of short, synthetic, staple strands (2). The path of the scaffold strand in this approach has been restricted to discrete domains of parallel lines because it is based on the double crossover unit motif to link adjacent helices (3–5). We present a design strategy that uses an unusual set of immobile Holliday junction analogs (four-arm junctions) as the basic structural unit of DNA origami nanostructures and as joints to construct a variety of two-dimensional (2D) and 3D gridiron structures, in which the scaffold strand and corresponding double helices are not restricted to a 1D parallel, raster-fill pattern. By programming the connection between individual joints with DNA segments of variable lengths, we constructed complex wireframe geometries.

Although intuitively one could imagine threading a single-stranded scaffold through a number

of four-arm junction units in both horizontal and vertical directions to create gridiron like patterns, the structural properties of traditional Holliday junction (6–8) impose certain challenges that require unconventional rearrangement of the junction unit conformation, as revealed by the design principles described below. We compared a gridiron unit to a double crossover motif (9) (Fig. 1A), and the DNA strands are abstracted to display only their polarity with the arrows pointing from 5' to 3'. In the gridiron unit, four four-arm junctions are linked together to form a two-layer square frame in which the helices on opposite sides lie in the same plane. An antiparallel arrangement between opposite sides of the square frame permits a single, central strand to traverse each of the helices.

Each of the four junctions is depicted in its relaxed conformation (Fig. 1B) such that the helices form a right-handed twist with a 60° torsion angle. Deviation from a relaxed conformation is required of each junction to form the gridiron unit cell. First, the red strands in the horizontally oriented helices (both top and bottom images) can be linked together to produce continuous strands without reversing the 5'-to-3' polarity (Fig. 1, B and C). Next, the vertically oriented helices need to be rotated in the plane about the junction points (Fig. 1C) to allow the formation of continuous 5'-to-3' connections between upper and lower junctions (Fig. 1, D and E).

Connecting a number of gridiron units leads to the formation of a variety of 2D lattices (Fig. 1, F and G). The red lines represent the DNA strands

that are expected to retain an unperturbed helical structure with continuous base stacking. Meanwhile, the short strands (in gray) form the crossovers between helical domains and function as staples. A long scaffold strand is created by connecting the termini of the red strands with short single-stranded DNA (ssDNA) loops. In the most basic design, the scaffold begins at one corner, fills the first layer, changes direction at the opposite corner, and then fills the second layer to produce a structure in which the helices within the two layers are oriented perpendicularly with respect to each other. Lastly, the scaffold returns to its initial position to form a closed loop (Fig. 1G).

The cavity size of gridiron structures can be tailored by altering the number of base pairs between the adjacent junction points. An 11-by-11 gridiron structure (11 vertical helices by 11 horizontal helices) with 21 base pairs (bp) between junctions in both directions uses 5301 of 7249 nt of the M13mp18 ssDNA scaffold strand and contains 120 staple strands (42 nt each). The remaining 1948 nt of the scaffold form a single-stranded loop at one corner that is visible in atomic force microscope (AFM, Fig. 2, A and B) and transmission electron microscope (TEM) images (Fig. 2, C and D). Gridiron structures with 63-by-63-bp cavities (Fig. 2, E and F) were assembled to demonstrate the programmability of the design strategy.

To test whether the ssDNA scaffold is required to force the junction to rotate and form the intended gridiron structures, we designed and successfully constructed a scaffold-free 11-by-11 gridiron structure (figs. S13 and S14). We also found that scaffolded and scaffold-free gridiron elements can be combined within a single structure (figs. S13 and S15). Further, a scaffold-free gridiron unit was examined by native gel electrophoresis to verify its formation when the component strands were mixed in equal stoichiometric ratios (fig. S33). Although the schematic diagram in Fig. 1D depicts 90° angles between the helices in the upper and lower layers, the angles are not fixed because the junctions are flexible. The experimental results reveal the formation of rhomboid rather than square structures; the junctions most likely behave cooperatively in order to maintain optimized base-stacking interactions and the lowest overall free energy. The single-stranded

<sup>1</sup>The Biodesign Institute, Arizona State University, Tempe, AZ 85287, USA. <sup>2</sup>Department of Chemistry and Biochemistry, Arizona State University, Tempe, AZ 85287, USA.

\*Corresponding author. E-mail: hao.yan@asu (H.Y.); yan\_liu@asu.edu (Y.L.); dongran.han@asu.edu (D.H.)

scaffold loop in one corner serves as an intrinsic marker to determine the angles adopted by the gridiron, and the angles display a bimodal distribution with nearly equal amplitudes, centered at  $76^\circ \pm 7^\circ$  (SD) and  $103^\circ \pm 7^\circ$  (for additional details regarding image analysis, see fig. S7). A closer examination of the AFM images further reveals the existence of two alternative conformations that the structural can adopt (figs. S6 and S8 and discussion in supplementary text).

The flexibility of the joints makes it possible to control or reconfigure the conformation of the gridiron structure by exerting external forces on selected corners of a gridiron. A modified version of a 15-by-15 gridiron structure with 21-bp cavities has about one quadrant of the gridiron unfolded and forms a randomly coiled 836-nt single-stranded loop between two “arms” of tweezers (Fig. 2G). The ssDNA loop is long enough to allow the structure to adopt a relaxed conformation. The observed distribution of the inner angle ( $\theta$ ) of the

tweezers (measured from 309 individual structures) is broad and centered at  $80^\circ$  to  $90^\circ$ .

We could contract and extend the ssDNA loop by introducing secondary or tertiary structures that generate enough force to control the angle (the design details are described in the supplementary materials). Sets of staple strands were designed to either contract the ssDNA loop and fix an acute angle (a narrow distribution centered at  $41^\circ \pm 7^\circ$ ) via the formation of a two-helix bundle (Fig. 2H) or to extend the loop to secure a right (Fig. 2I) or obtuse angle (Fig. 2J) via the formation of a three-helix bundle of specific length. The design with the right angle shows a narrow and symmetrical distribution centered at  $94^\circ \pm 10^\circ$ , and the design with the obtuse angle has a broader angle distribution centered at  $102^\circ$  and exhibits an asymmetry that is more heavily weighted toward smaller angles.

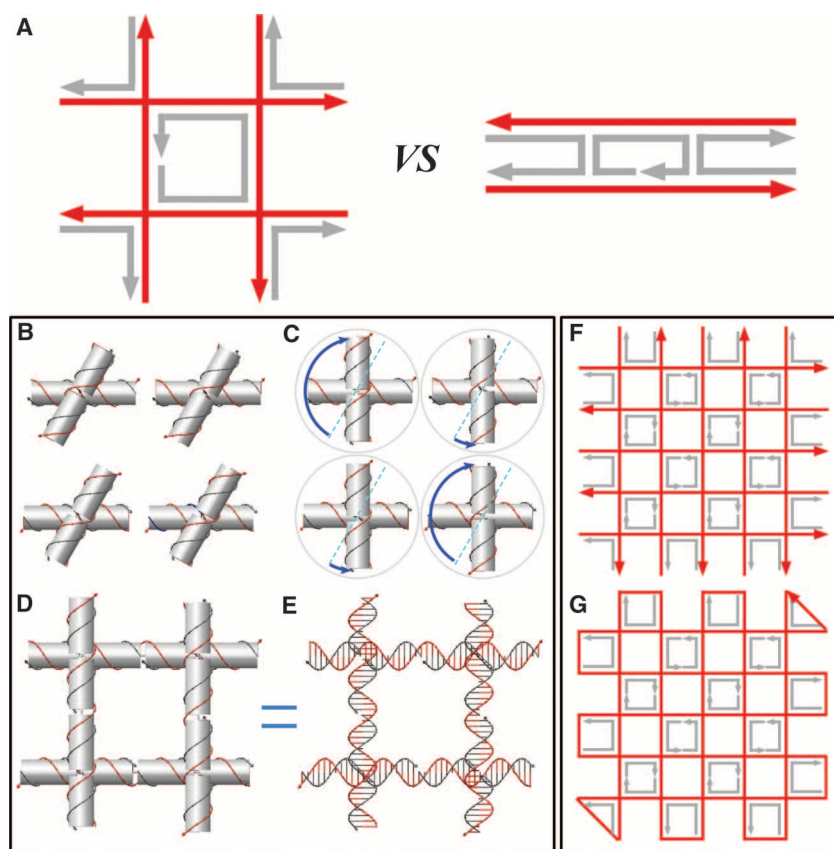
We extended the gridiron design into the third dimension by three different strategies. The first

involves stacking multiple layers of 2D gridiron lattices at selected connection points (Fig. 3, A and B). The second relies on intertwining several gridiron planes in  $x$ - $y$ - $z$  directions (Fig. 3C). The third method has its basis in distorting a single layer of DNA gridiron into 3D structures by controlling their curvatures (Fig. 4). By using the first strategy, we constructed a three-layer hexagonal (Fig. 3D), a four-layer rectangular gridiron (Fig. 3E), and a three-layer parallelogram (fig. S58) structure. For all multilayer gridiron structures, the scaffold strand raster fills each layer, with an offset in the angle formed between the helices of adjacent layers. The three-layer hexagonal and four-layer rectangular structures maintained  $60^\circ$  and  $90^\circ$  offsets between layers, respectively.

Varying the location and distance between connection points will yield differently patterned multilayer structures. In contrast to the angle flexibility present in the quasi-2D structures, the addition of a third layer fixes the angles at junction points. The only exception to this is for connections through the center of the same unit motif, as shown by the green dashed line (Fig. 3A). In a 3D model of an eight-by-eight-by-eight three-layer hexagonal gridiron structure (Fig. 3D), neighboring junctions in the top and bottom layers are 52 bp apart, and neighboring junctions in the middle layer (alternating connections to the top and bottom layers) are 26 bp apart. Because  $X = Y = L$  (Fig. 3B), each junction should adopt a  $60^\circ$  torsion angle. A four-layer rectangular gridiron structure (Fig. 3E) can be broken down into two six-by-five double-layer gridirons (with 52-bp cavities) stacked on top of one another with a 26-bp offset in the connections between the first and third, and second and fourth, layers.

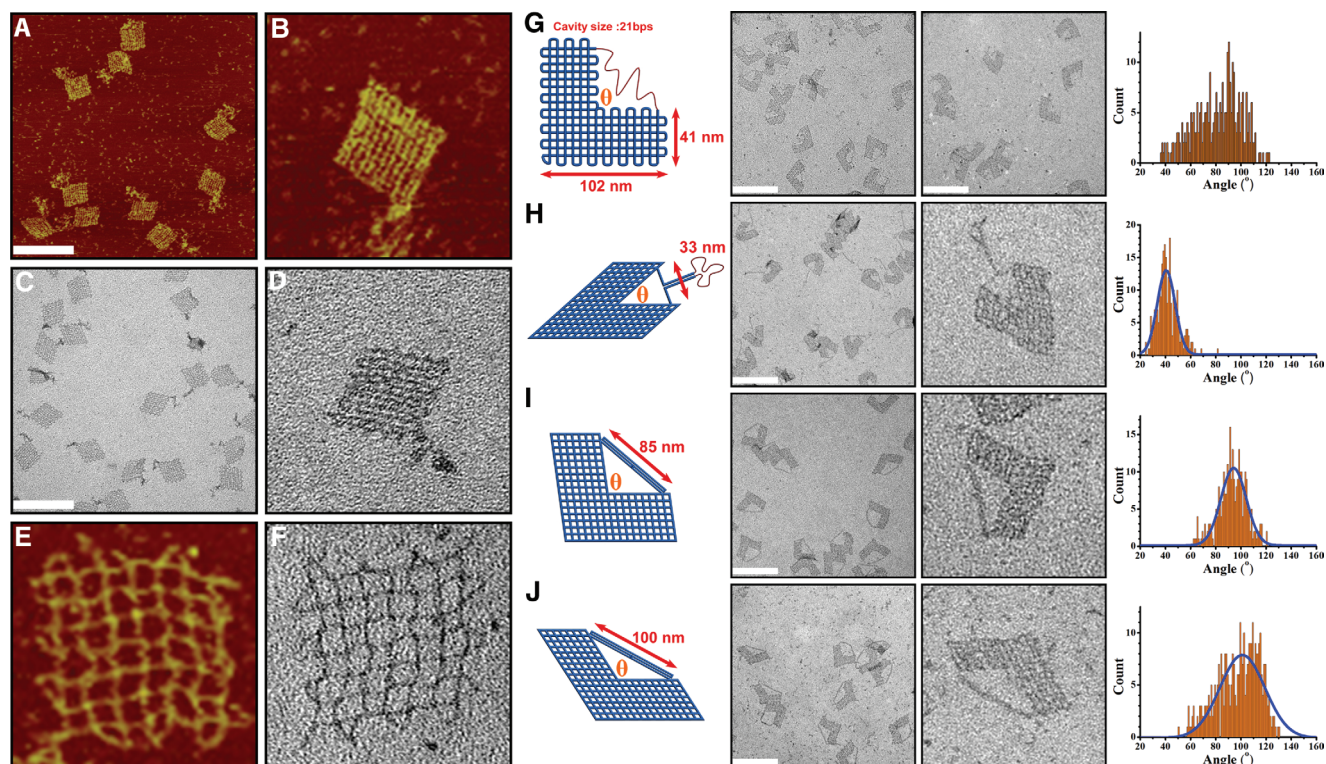
The relations of the lattice planes in gridiron structures are not restricted to stacked multilayer structures. The 3D gridiron structures can also be assembled by integrating gridiron lattices with scaffold-free elements (see supplementary materials for description of various design possibilities). Figure 3F presents such a design in which a nine-by-nine gridiron plane (shown in blue) is intertwined with an eight-by-eight scaffold-free gridiron plane (shown in yellow). The complex, interwoven topology of this particular structure required combining scaffolded and scaffold-free components (see supplementary materials for additional details).

Gridiron designs can allow assembly of even more complex structures by inducing a desired curvature in the basic structural unit described in Fig. 1. Maintaining the distance between junctions in one direction while simultaneously shrinking or extending the distance in the other direction (by varying the number of base pairs) creates an isosceles trapezoid unit. The lengths of the parallel sides of the trapezoidal units can be progressively changed between layers and combined to generate curved gridiron structures such as an S-shaped structure (Fig. 4A). One layer is composed of nine concentric, evenly spaced curved helices, and the second layer contains 13 linear,



**Fig. 1.** (A) (Left) Geometry and strand polarity of a single gridiron unit formed from four four-arm junctions. (Right) Geometry and polarity of a double-crossover molecule motif used in conventional DNA origami structures. For both structures, the ssDNAs depicted in red are components of DNA double helices that serve as the scaffold strands. The ssDNA depicted in gray represents staple strands. (B) Models of four four-arm junction molecules in their relaxed conformation. The orientation of the upper two junctions differs from that of the lower two by a  $180^\circ$  in-plane rotation. Thus, the polarities of the continuous red strands in the upper and lower layers of the horizontally oriented helices are antiparallel to one another. (C) Models illustrating the deviation from a relaxed conformation required of the four individual junctions to form a gridiron unit. The blue arrows indicate that the top helix of the junctions in the upper-left and lower-right corners must be rotated  $\sim 150^\circ$  clockwise, whereas in the upper-right and lower-left junctions they must be rotated  $\sim 30^\circ$  counterclockwise. (D and E) Helical models illustrating a complete gridiron unit. (F and G) Schematics illustrating a typical scaffold-folding path for a 2D DNA gridiron pattern.

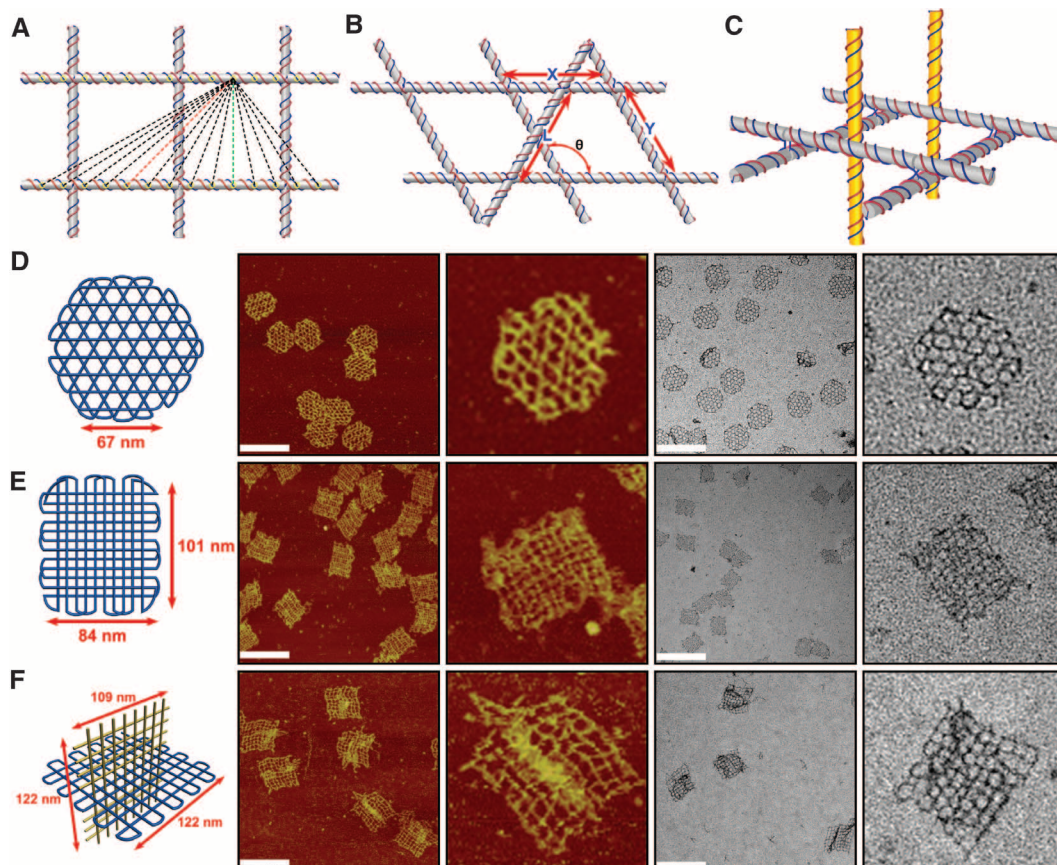




**Fig. 2.** (A to D) Images for a 2D gridiron structures with 21-bp cavities with AFM [(A) and (B)] and TEM images [(C) and (D)]. (E and F) Images for a 2D gridiron with 63-bp cavities with AFM (E) and TEM images (F). (G to J) Schematic

images (left), TEM images (middle), and histogram analysis (right) of the angle distributions for angle control. All scale bars indicate 200 nm, and all zoom-in images (images without scale bars) are 200 by 200 nm.

**Fig. 3.** Multilayer gridiron design strategies. (A and B) Strategy 1 is stacked layers. (A) A portion of a double-layer gridiron lattice with 52-bp cavity size. The yellow circles designate the permissible connection points to a third layer. The dashed lines correspond to possible connection points to form additional layers. (B) Given the double-layer gridiron lattice ( $X$  and  $Y$  lengths) and the distance between crossover points in the third layer, the angle  $\theta$  can be calculated as  $180^\circ - \cos^{-1}[(X^2 + Y^2 - L^2)/2XY]$ . (C) Strategy 2 is intertwining gridiron planes. (D to F) Schematic (left), AFM (middle), and TEM (right) images of (D) a three-layer hexagonal gridiron design,  $\theta = 120^\circ$ ; (E) a four-layer gridiron design,  $\theta$  is not controlled because the dashed green line in (A) represents a connection strategy that cannot fix the angle; and (F) a 3D gridiron assembled by using strategy 2. All scale bars indicate 200 nm, and all zoom-in images (images without scale bars) are 200 by 200 nm.





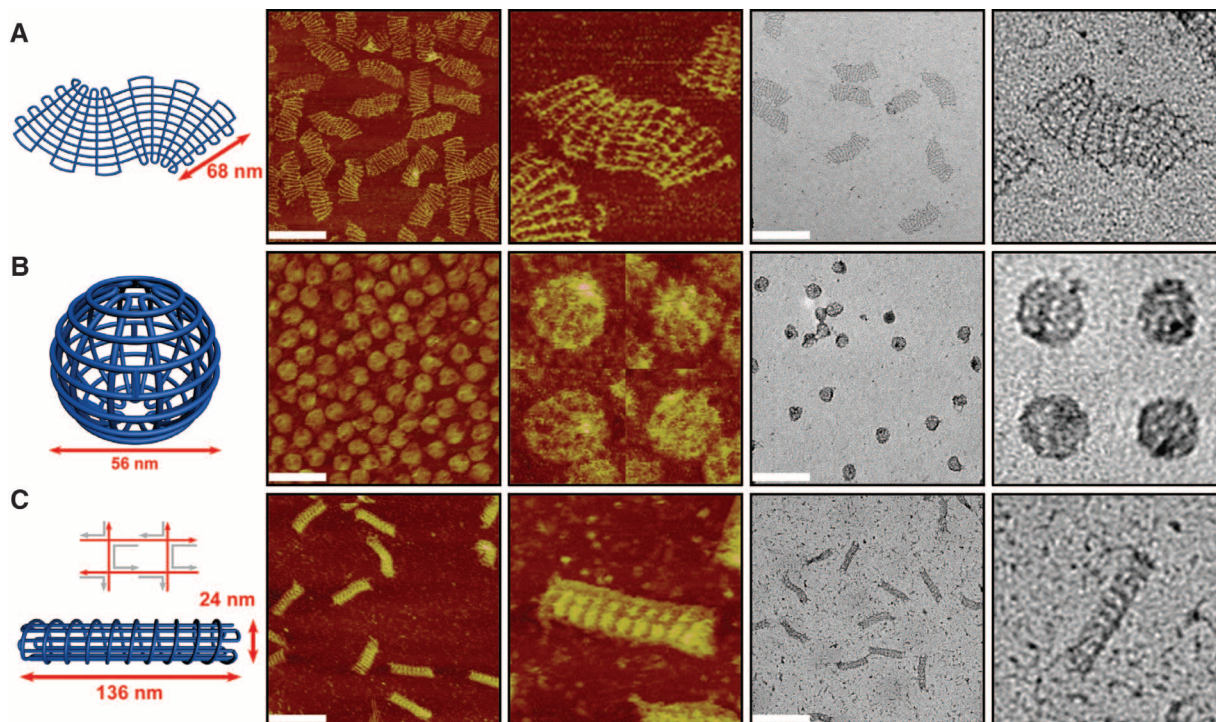


**Fig. 4.** Schematics (left), AFM (middle), and TEM images (right) of (A) an S-shaped structure, (B) a sphere, and (C) a screw. All scale bars indicate 200 nm, and all zoom-in images (images without scale bars) are 200 by 200 nm. In (B)

and (C), the diameter and the width, respectively, appear to be larger in the AFM images compared with the TEM images. This difference is probably a result of flattening of the 3D objects into two-layer structures and AFM tip convolution.

nonparallel helices. The relation between adjacent linear helices (the angles formed by their theoretical intersection) between adjacent linear helices was varied. Some 3D gridiron structures that contain curvature were also achieved, such as the sphere shown in Fig. 4B. The helices in concentric ring and radial spoke layers are stretched in the center and shrunk at the edges, forming a latitudinal and longitudinal framework, respectively. This is realized by progressively adjusting the distance between junctions in latitudinal directions. Additional modifications to the basic structural motif can be used to produce other complex structures. In the screw structure (Fig. 4C), the polarity of the DNA strands in the square unit motif differs from what is illustrated in Fig. 1B (where adjacent scaffold helices have an antiparallel polarity in one direction and the same polarity in the other direction). The scaffold strand is arranged in an antiparallel configuration to form a wireframe cylinder structure (11 helices are arranged axially) and subsequently wraps around the cylinder (analogous to a left-handed screw) until the two ends meet. The distance between adjacent axial helices is 21 bp, the interthread distance is 42 bp, and the AFM and TEM images display the expected left-handed conformation.

The design principles of creating gridiron units allow scaffold strands to travel in multiple directions, which represent an important departure from certain aspects of the previous DNA origami methods. Traditional Holliday junctions do not naturally adopt conformations that would

allow them to be connected in such a way, and it was unexpected to find that these motifs could (within a larger network of crossovers) endure a 150° rotation of one of the arms while simultaneously maintaining their integrity. Indeed, the flexible and dynamic behavior of these motifs may have excluded these types of junction conformations for consideration in scaffolded structures. Yield analysis from agarose gel and TEM images shows that the structures, even without purification, form with reasonably high yield (from ~36% for the gridiron tweezers to ~85% for the gridiron screw, estimated from agarose gels; from ~51% for the gridiron sphere to ~89% for the four-layer gridiron, estimated from TEM images; see supplementary materials for yield analysis). The ability to engineer DNA gridirons that are analogous to vector-based objects, where a series of points with defined positions in 3D space are connected by lines, is an important milestone in the development of synthetic nucleic acid structures. In particular, this opens up new opportunities to implement the design of complex wireframe structures (see discussion in supplementary materials) that are amenable to dynamic controls. A future challenge in DNA origami is to achieve true folding, starting from a 2D sheet (miura ori), rather than the 1D M13 scaffolds commonly used in traditional DNA origami construction. The loose 2D networks and freely rotating hinges between different planes of DNA gridirons provide the design features necessary to implement Miura ori type of origami.

## References and Notes

1. N. C. Seeman, *Annu. Rev. Biochem.* **79**, 65 (2010).
2. P. W. K. Rothemund, *Nature* **440**, 297 (2006).
3. S. M. Douglas *et al.*, *Nature* **459**, 414 (2009).
4. H. Dietz, S. M. Douglas, W. M. Shih, *Science* **325**, 725 (2009).
5. D. Han *et al.*, *Science* **332**, 342 (2011).
6. C. Mao, W. Sun, N. C. Seeman, *J. Am. Chem. Soc.* **121**, 5437 (1999).
7. S. M. Miick, R. S. Fee, D. P. Millar, W. J. Chazin, *Proc. Natl. Acad. Sci. U.S.A.* **94**, 9080 (1997).
8. S. A. McKinney, A. C. Déclais, D. M. J. Lilley, T. Ha, *Nat. Struct. Biol.* **10**, 93 (2002).
9. T. J. Fu, N. C. Seeman, *Biochemistry* **32**, 3211 (1993).

**Acknowledgments:** We thank N. Seeman and R. Sha from New York University for helpful discussions. This work is supported by NSF grant 1104373, Office of Naval Research grant N000140911118, Army Research Office grant W911NF-11-1-0137 to H.Y. and Y.L. and Army Research Office Multidisciplinary University Research Initiative award W911NF-12-1-0420 and National Science Foundation of China grant 21028005 to H.Y. H.Y. and Y.L. are part of the Center for Bio-Inspired Solar Fuel Production, an Energy Frontier Research Center funded by the U.S. Department of Energy, Office of Science, Office of Basic Energy Sciences under award no. DE-SC0001016. H.Y. is supported by the Presidential Strategic Initiative Fund from Arizona State University. The DNA sequences for the nanostructures and additional data described in this work can be found in the online supplementary materials.

## Supplementary Materials

www.sciencemag.org/cgi/content/full/339/6126/1412/DC1  
Materials and Methods  
Supplementary Text  
Figs. S1 to S96  
Tables S1 to S17

1 November 2012; accepted 31 December 2012  
10.1126/science.1232252



# Simple Scaling of Catastrophic Landslide Dynamics

Göran Ekström\* and Colin P. Stark

Catastrophic landslides involve the acceleration and deceleration of millions of tons of rock and debris in response to the forces of gravity and dissipation. Their unpredictability and frequent location in remote areas have made observations of their dynamics rare. Through real-time detection and inverse modeling of teleseismic data, we show that landslide dynamics are primarily determined by the length scale of the source mass. When combined with geometric constraints from satellite imagery, the seismically determined landslide force histories yield estimates of landslide duration, momenta, potential energy loss, mass, and runout trajectory. Measurements of these dynamical properties for 29 teleseismogenic landslides are consistent with a simple acceleration model in which height drop and rupture depth scale with the length of the failing slope.

Seismic radiation from landslides is broadband and complex (1). Short-period waves result from the myriad momentum exchanges taking place within the granular mass and along its sliding boundary. They are distributed in time and low in amplitude compared with the impulsive radiation associated with the sudden stress drop in tectonic earthquakes. Long-period waves radiated by landslides are simpler: They are generated by the broad cycle of unloading and re-loading of the solid Earth (2–4) induced by the bulk acceleration and deceleration of the landslide mass. The corresponding momentum exchange is complicated by entrainment and deposition (5–7) during motion and by topographic undulations along the slide path (8). Characteristic unloading-reloading times in large landslides are several tens of seconds, making them efficient sources of seismic waves at periods of that order (9).

Traditional earthquake monitoring conducted by national and international agencies is designed for detection of impulsive short-period seismic waves and for location of associated tectonic earthquakes and explosions. Landslide detections are rare. A complementary method based on near-real-time data from the Global Seismographic Network (GSN) allows for the detection of seis-

mic events through continuous back-projection of the long-period wavefield (10–12). This event-detection algorithm detects >90% of magnitude  $M \geq 5.0$  shallow earthquakes reported by other agencies and identifies about 10 events each month that are not in other seismicity catalogs. Some of these unassociated events have been correlated with large-scale glacier calving (13, 14) and volcanic unrest (15). Here, we identify and investigate another subset of these events associated with catastrophic (large and fast) landslides.

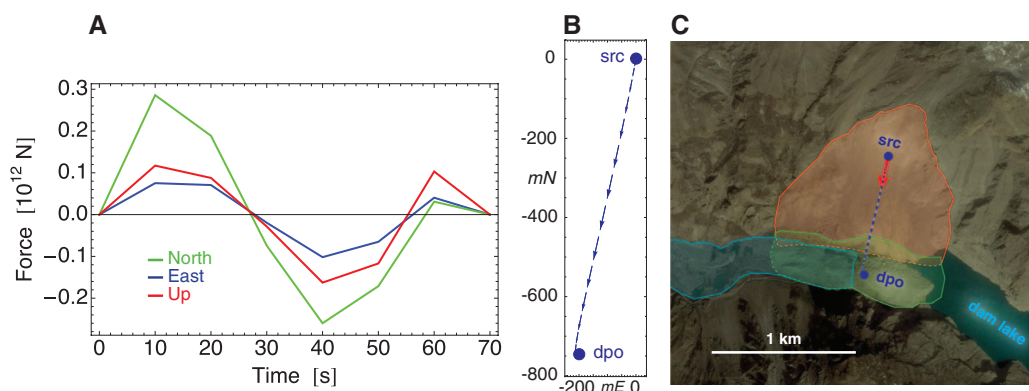
The event-detection algorithm locates events with an initial accuracy of 20 to 100 km (10). A terrestrial landslide source is established by combining this geographic location with satellite imagery, field photographs, news reports, local seismic recordings, and other sources. A comprehensive investigation of 195 unassociated detections for 2010 led to the identification of 11 major landslides (table S1, events 16 to 26). All of the seismically detected landslides generated long-period surface waves (SW) roughly equivalent to a magnitude  $M_{SW} \sim 5$  tectonic earthquake, and all were recorded at multiple seismographic stations. Tectonically generated surface-wave signals of this magnitude are routinely used to determine earthquake fault geometries and seismic moments (16), suggesting that similar methods could also be used to provide a quantitative characterization of the detected landslides. For example, Kanamori and co-workers (17, 18) measured a subhorizon-

tal force of  $\sim 150$  s duration and maximum amplitude  $\sim 10^{13}$  N associated with the massive debris avalanche after the 1980 eruption of Mount St. Helens volcano (table S1). Seismological analyses of long-period data have usually focused on single landslide events and typically have been limited to estimation of the average slide direction (often only in the horizontal), peak force, and duration of sliding (19–22). Field observations, by contrast, frequently suggest complex three-dimensional (3D) landslide trajectories, and numerical modeling has highlighted the effects of such complexity on the radiated seismic waves (7, 8).

We developed an inverse method (12) to infer the 3D force sequence generated by bulk landslide motion (23)—from which we can deduce the trajectory of slip and dynamic properties. The new algorithm builds on and extends established methods used in earthquake analysis (12, 16). When applied to one of the largest landslides of 2010, this approach results in a first-order characterization of the event (Fig. 1). On 4 January of that year, our algorithm (10, 11) automatically detected a seismic event of long-period magnitude  $M_{SW} \approx 5.3$  at 08:36 GMT and roughly located the source in northern Pakistan (table S1). None of the international earthquake-monitoring agencies ISC, IDC, or NEIC reported this event. After anecdotal reports that a major landslide had struck the village of Attabad that morning—blocking the Karakoram Highway, damming the Hunza River, and causing several fatalities (24)—we inspected long-period waveform data recorded on proximal stations and established that the seismic signal was likely caused by the Attabad slope failure. This association was confirmed by our inverse model, which provided a more accurate source location within 15 km of Attabad and which pointed to a direction of motion down to the south-southwest, consistent with local reports. These reports also indicated a time of failure consistent with the seismic detection.

The estimated time sequence of forces induced by acceleration of the Hunza-Attabad landslide indicates a roughly sinusoidal sequence lasting  $\Delta t \sim 60$  s (Fig. 1A). The 3D force vector components vary in a synchronous fashion, which suggests a consistent azimuth of acceleration and

**Fig. 1.** Landslide force history and trajectory for the Hunza-Attabad landslide. (A) Inversion of the landslide force history  $\mathbf{F}(t)$  (LFH) of this event, pinning the time of main failure at 08:37 UT (table S1). (B) The planform trajectory of landslide motion deduced by doubly integrating the LFH and scaling by the runout distance mapped in (C). (C) Satellite-image mapping of the landslide scar and runout. The estimated centers of the source (“src”) and deposits (“dpo”) are indicated; their spatial separation was used to estimate  $D_{hr}$ , determine the effective mass, and scale the displacement trajectory  $\mathbf{D}(t)$ .



Lamont-Doherty Earth Observatory of Columbia University, Palisades, NY 10964, USA.

\*Corresponding author. E-mail: ekstrom@ldeo.columbia.edu

deceleration and therefore a linear runout. During the first 25 s the force vector points consistently to the north-northeast with an upward vertical component, indicating reaction to acceleration of the slide mass downhill in the south-southwest direction. The subsequent time series reflects reversal of the force vector during deceleration, as the slide mass approached the bottom of the valley.

Because the negated force history is equivalent to the rate of change of bulk landslide momentum over time (23), its integration gives the

bulk momentum over time  $\mathbf{p}(t) = (m\mathbf{v})(t)$ . This time series is constrained to be stationary during inversion. Assuming a constant bulk mass  $m$  over time, further integration gives the mass-scaled, 3D vector trajectory of motion  $m\mathbf{D}(t)$ . If an independent measure of landslide volume or mass  $m$  is available, we can divide by  $m$  to obtain the 3D runout  $\mathbf{D}(t)$  and compare it against terrain data and postfailure imagery to test the validity of the inversion results and the assumption of constant mass. Alternative-

ly, we can estimate the bulk landslide mass by comparing the mass-scaled maximum horizontal displacement  $mD_h$  with a center-of-mass displacement estimated from terrain data and imagery. Using the second approach, illustrated in satellite imagery of Hunza-Attabad (Fig. 1C), we estimated a horizontal center-of-mass displacement of 940 m, which gave a mass of  $m \approx 1.4 \times 10^{11}$  kg and the runout path  $\mathbf{D}(t)$  shown in Fig. 1B. Evaluation in the field has estimated the deposited volume at  $\sim 45$  million  $\text{m}^3$  (24). Assuming a debris

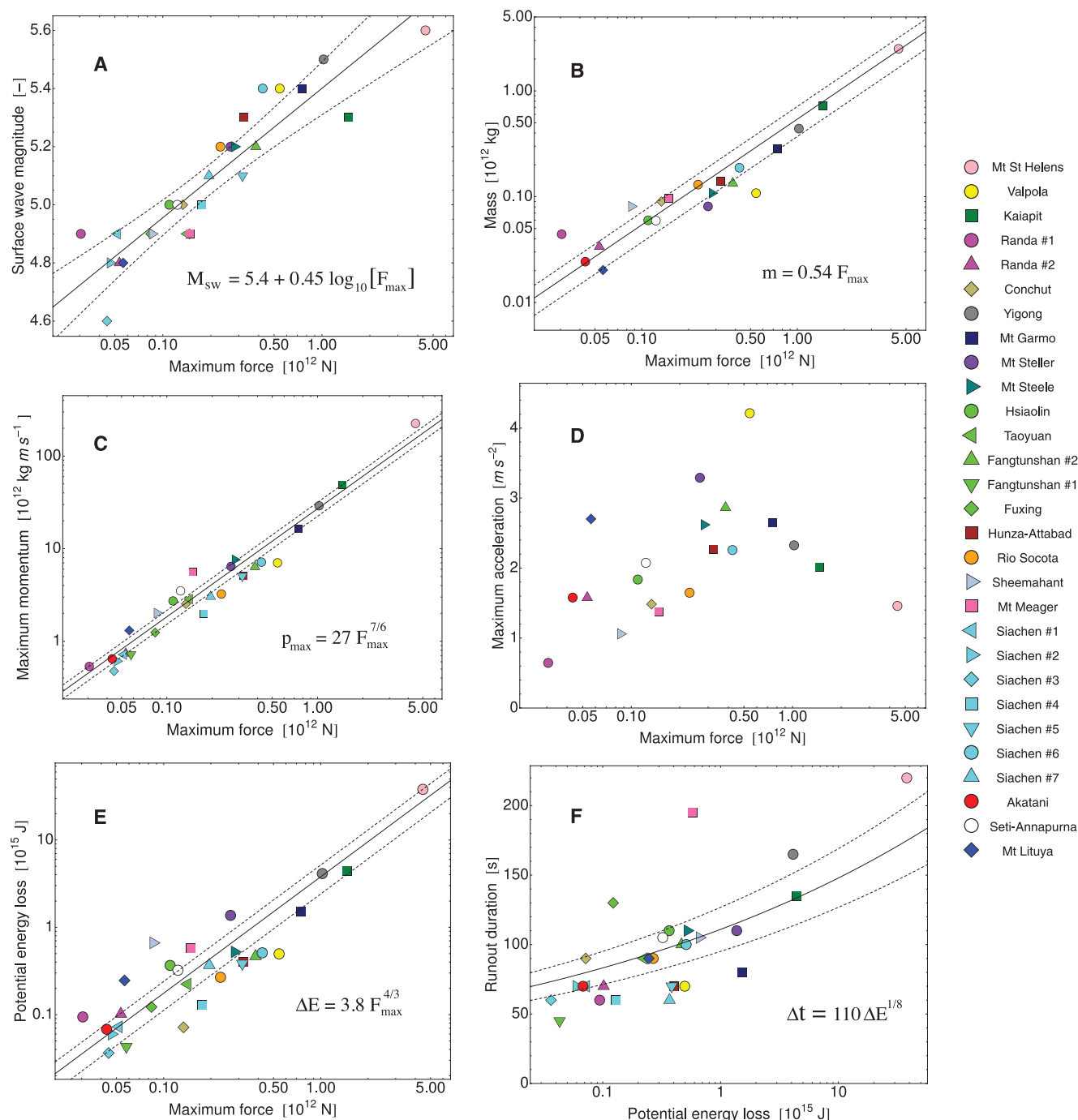


**Fig. 2.** Maximum force  $F_{\max}$  versus (A) long-period surface-wave magnitude  $M_{\text{sw}}$ , (B) mass  $m$ , (C) maximum momentum  $p_{\max}$ , (D) maximum acceleration  $a_{\max}$ , and (E) potential energy loss  $\Delta E$ . Runout duration  $\Delta t$  versus potential

energy loss  $\Delta E$  is shown in (F). In (A) to (C), (E), and (F), the solid lines show model fits and the dashed lines indicate model mean confidence intervals at the 99% level.



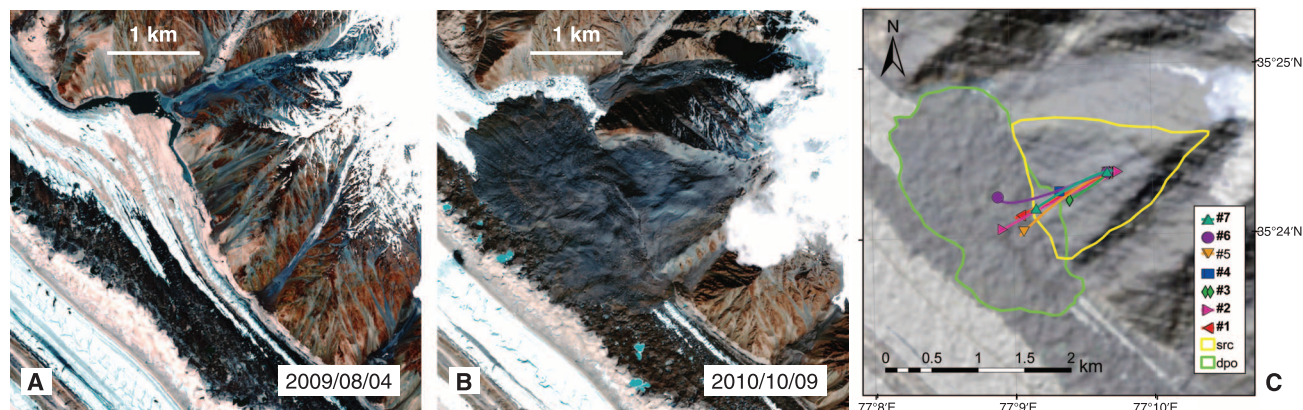


**Fig. 3.** Siachen landslides, September 2010. **(A)** Pre- and **(B)** postevent GeoEye 50-cm-resolution visible and near-infrared imagery of Siachen Glacier landslide complex. **(C)** Inferred trajectories for the seven Siachen landslides. The slide origins were

chosen to coincide, in order to illustrate the good agreement in average slide direction, with some variability in motion in the lower portions of the trajectories. Outlined in green and yellow are the approximate source and deposit areas, respectively.

density of  $2400 \text{ kg m}^{-3}$ , this suggests a source mass of  $\sim 1.1 \times 10^{11} \text{ kg}$ , broadly consistent with our estimate.

We applied the technique of landslide seismic detection and source inversion to a total of 29 events spanning 1980–2012 (table S1). This set includes the three largest landslides of the last 33 years: Mount St. Helens in 1980 (table S1), Kaiapit in 1988 (25), and Yigong in 2000 (26). Of these 29 events, 27 were recorded on global network stations and the two smallest—at Fāngtúnshān/Tāimā in Taiwan (27) in 2009 and Akatani in Japan (28) in 2011—were well recorded on regional networks. By analyzing all 29 landslides in a methodologically consistent fashion, we generated empirical constraints on catastrophic landslide dynamics spanning three orders of magnitude of failure mass that can be used with confidence in analyses of scaling (tables S1 and Fig. 2).

A practical result is the logarithmic relationship (Fig. 2A) that we see between the long-period magnitude  $M_{\text{SW}}$  and the maximum force  $F_{\text{max}}$ . The magnitude estimates span  $M_{\text{SW}} \approx 4.6$  to 5.6 and are available only for the 27 global detections. The maximum forces here span  $F_{\text{max}} \approx 4 \times 10^{10}$  to  $5 \times 10^{12} \text{ N}$  and are typically associated with the acceleration phase of the landslide. The correlation is strong, suggesting that the maximum force can be estimated from the long-period magnitude alone (to within a factor of 2) and prior to waveform modeling.

We find a consistent pattern of scaling (Fig. 2, B to F) among the inferred dynamic properties that can be explained with a very simple model of slope collapse and acceleration in which a single length scale  $L$  determines all the geometrical properties of the landslide source and its acceleration phase (12). The simple model and the inversion results indicate a linear dependence of landslide mass on maximum force  $m \approx 0.54 F_{\text{max}}$  (Fig. 2B). They indicate no scaling dependence, but much variability (Fig. 2D), for peak acceleration  $a \approx 2 \text{ m s}^{-2}$ . Observed scaling dependencies on maximum force match model deductions: Peak momentum is  $p_{\text{max}} \approx 27 F_{\text{max}}^{7/6}$  (Fig. 2C), potential energy loss is  $\Delta E \approx 3.8 F_{\text{max}}^{4/3}$

(Fig. 2E), and runout duration is  $\Delta t \approx 127 F_{\text{max}}^{1/6}$ . Similarly, we find dependencies on potential energy loss such as  $\Delta t \approx 110 \Delta E^{1/8}$  (Fig. 2F) and  $p_{\text{max}} \approx 10 \Delta E^{7/8}$  that accord with the model. Together our results indicate peak kinetic energy is on average about 24% of potential energy loss. A practical outcome is that the mass-force relation can be combined with the observed scaling between magnitude and force to provide an approximate means of estimating landslide mass (in  $10^{12} \text{ kg}$ ) from long-period magnitude alone as  $m \approx 0.54 \times 10^{2.2 M_{\text{SW}} - 12}$ .

Runout duration  $\Delta t$  and trajectory  $\mathbf{D}(t)$  inferred seismically reflect the phase of major height drop and thus large force. For some landslides, however, particularly for those running onto and down glaciers [such as Mount Garmo (29) in 2001 and Mount Lituya in 2012], a second, longer phase of low gradient, likely low-deceleration runout, was mapped on imagery, but not recorded in the long-period seismicity. Such long-runout events likely indicate unusually low rates of energy dissipation as a result of frictional melting of glacial ice.

The most notable, previously undocumented landslides we identified are the seven catastrophic ( $M_{\text{SW}}$  4.6 to 5.4; table S1) events detected over 4 days in September 2010 and located in the eastern Karakoram. All exhibited the seismic characteristics of landslides, and none were detected by earthquake monitoring agencies. Our inversions of these events indicate a common runout direction of west–west-southwest for all the failures, and analysis of multitemporal Landsat imagery (Fig. 3C) identified only one candidate slope failure, collapsing onto the Siachen Glacier, consistent with this time window and geographic location. Subsequent mapping using multitemporal GeoEye imagery (Fig. 3, A and B) confirmed multiple failures of the northern flank of the valley.

Unlike the Mount Garmo and Mount Lituya events, runout over the Siachen glacier surface was relatively short and comparable to the height drop. Using the GeoEye imagery, we estimated runout for the largest event at  $D_h \approx 1320 \text{ m}$  and

deduce the failure mass at around  $m \approx 1.9 \times 10^{11} \text{ kg}$  and maximum acceleration of  $2.2 \text{ m s}^{-2}$ . Because the other six events could not be tied to runout patterns in the imagery, we assumed the same maximum acceleration to calibrate their landslide force history (LFH) inversions, yielding estimates of failure masses ranging from  $m \approx 1.1 \times 10^{10} \text{ kg}$  to  $1.4 \times 10^{11} \text{ kg}$ .

This sequence of massive landsliding is an example of progressive slope failure involving multiple collapses of bedrock volumes each exceeding  $10^6$  to  $10^7 \text{ m}^3$ . Although it is recognized that episodes of massive mass-wasting often comprise a hierarchy of individual landslide events, repeated similar-scale failures of the same mountain slope over mere days are more difficult to explain. In our catalog of inversions, only the paired Randa events (30) in 1991 involve closely repeated failure of a similar scale at the same location. Were it not for the seismic detection, force inversion, and satellite-image mapping used here, the Siachen Glacier landslide deposit would likely be falsely interpreted as the composite of one or two extremely large failures. What is more, given its remote location, it would likely have gone undetected for some time.

## References and Notes

- D. Weichert, R. B. Horner, S. G. Evans, *Bull. Seismol. Soc. Am.* **84**, 1523 (1994).
- Y. Takei, M. Kumazawa, *Geophys. J. Int.* **118**, 20 (1994).
- Y. Fukao, *Geophys. J. Int.* **122**, 243 (1995).
- M. J. McSaveney, G. Downes, in *Landslides*, J. Rybar, J. Stemberk, P. Wagner, Eds. (Balkema, Lisse, Netherlands, 2002), pp. 649–654.
- G. B. Crosta, H. Chen, C. F. Lee, *Geomorphology* **60**, 127 (2004).
- S. N. Ward, S. Day, *Geophys. J. Int.* **167**, 991 (2006).
- L. Moretti et al., *Geophys. Res. Lett.* **39**, L16402 (2012).
- P. Favreau, A. Mangeney, A. Lucas, G. Crosta, F. Bouchut, *Geophys. Res. Lett.* **37**, L15305 (2010).
- E. A. Okal, *J. Phys. Earth* **38**, 445 (1990).
- G. Ekström, *Bull. Seismol. Soc. Am.* **96**, (4A), 1201 (2006).
- G. Ekström, M. Nettles, Global CMT catalog (2012); <http://globalcmt.org>.
- See supplementary materials on Science Online.
- G. Ekström, M. Nettles, G. A. Abers, *Science* **302**, 622 (2003).
- M. Nettles, G. Ekström, *Annu. Rev. Earth Planet. Sci.* **38**, 467 (2010).

15. A. Shuler, G. Ekström, *J. Volcanol. Geotherm. Res.* **181**, 219 (2009).
16. G. Ekström, M. Nettles, A. M. Dziewonski, *Phys. Earth Planet. Inter.* **200-201**, 1 (2012).
17. H. Kanamori, J. W. Given, *J. Geophys. Res.* **87**, 5422 (1982).
18. H. Kanamori, J. W. Given, T. Lay, *J. Geophys. Res.* **89**, 1856 (1984).
19. H. S. Hasegawa, H. Kanamori, *Bull. Seismol. Soc. Am.* **77**, 1984 (1987).
20. E. E. Brodsky, E. Gordeev, H. Kanamori, *Geophys. Res. Lett.* **30**, 2236 (2003).
21. M. La Rocca *et al.*, *Bull. Seismol. Soc. Am.* **94**, 1850 (2004).
22. N. A. Pino, M. Ripepe, G. B. Cimini, *Geophys. Res. Lett.* **31**, L02605 (2004).
23. W. G. Pariseau, *Eng. Geol.* **16**, 111 (1980).
24. D. Petley, *Int. Water Power Dam Constr.* **63**, 27 (2011).
25. M. Peart, *Q. J. Eng. Geol.* **24**, 399 (1991).
26. Y.-J. Shang *et al.*, *Geomorphology* **54**, 225 (2003).
27. C.-H. Lin, H. Kumagai, M. Ando, T.-C. Shin, *Geophys. Res. Lett.* **37**, L22309 (2010).
28. M. Yamada, Y. Matsushi, M. Chigira, J. Mori, *Geophys. Res. Lett.* **39**, L13301 (2012).
29. V. M. Kotlyakov *et al.*, *Mater. Gliatsiologicheskikh Issledovaniy* **95**, 221 (2003).
30. E. Eberhardt, D. Stead, J. S. Coggan, *Int. J. Rock Mech. Min. Sci.* **41**, 69 (2004).

**Acknowledgments:** We are grateful to C.-W. Lin, R.-J. Rau, S.-P. Lee, Hongey Chen, S.-H. Liu, and Y.-C. Tsang for help with analysis of landslides triggered by Typhoon Morakot; to

E. Choi and M. Reitz for discussions on landslide mechanics; and to D. Petley for help and information on several of the landslide events reported here. Data are available in the supplementary materials. This research was supported by NSF Awards EAR-0824694, EAR-1150072, and EAR-1227083.

#### Supplementary Materials

[www.sciencemag.org/cgi/content/full/339/6126/1416/DC1](http://www.sciencemag.org/cgi/content/full/339/6126/1416/DC1)

Materials and Methods

Supplementary Text

Fig. S1

Table S1

References (31–50)

19 November 2012; accepted 30 January 2013

10.1126/science.1232887

# Two Modes of Change in Southern Ocean Productivity Over the Past Million Years

S. L. Jaccard,<sup>1</sup> C. T. Hayes,<sup>2,5</sup> A. Martínez-García,<sup>1</sup> D. A. Hodell,<sup>3</sup> R. F. Anderson,<sup>2,5</sup> D. M. Sigman,<sup>4</sup> G. H. Haug<sup>1</sup>

Export of organic carbon from surface waters of the Antarctic Zone of the Southern Ocean decreased during the last ice age, coinciding with declining atmospheric carbon dioxide (CO<sub>2</sub>) concentrations, signaling reduced exchange of CO<sub>2</sub> between the ocean interior and the atmosphere. In contrast, in the Subantarctic Zone, export production increased into ice ages coinciding with rising dust fluxes, thus suggesting iron fertilization of subantarctic phytoplankton. Here, a new high-resolution productivity record from the Antarctic Zone is compiled with parallel subantarctic data over the past million years. Together, they fit the view that the combination of these two modes of Southern Ocean change determines the temporal structure of the glacial-interglacial atmospheric CO<sub>2</sub> record, including during the interval of “lukewarm” interglacials between 450 and 800 thousand years ago.

Antarctic ice core measurements reveal that regional air temperatures and atmospheric CO<sub>2</sub> concentration (*p*CO<sub>2</sub>) were tightly correlated over glacial-interglacial cycles of the past 800 thousand years (ky) (1). Many studies have inferred a dominant role for the Southern Ocean in modulating glacial-interglacial variability of atmospheric *p*CO<sub>2</sub> (2). The central role of the Southern Ocean is thought to reflect its leverage on the global efficiency of the biological pump, in which the production, sinking, and deep remineralization of organic matter sequesters carbon in the ocean interior, lowering atmospheric CO<sub>2</sub>. Dense subsurface water masses outcrop in the Southern Ocean, providing exchange pathways between the deep ocean and the atmosphere. Vertical exchange of water causes deeply sequestered CO<sub>2</sub> and nutrients to be mixed to the surface, fueling high rates of phytoplank-

ton productivity. Today, the Southern Ocean is the principal leak in the biological pump, because export production is inadequate to prevent the evasion of deeply sequestered carbon when waters are exposed to the atmosphere. The polar CO<sub>2</sub> leak can be directly inhibited during glacial stages by factors such as increased sea-ice

cover (3) and/or changes in buoyancy forcing and convection (4, 5). In addition, the glacial CO<sub>2</sub> reduction associated with these mechanisms would have been amplified by iron fertilization of the Subantarctic Zone (SAZ) of the Southern Ocean (6, 7) and associated alkalinity feedbacks (8).

Export production records from the Antarctic Zone (AZ) have been used to trace changes in the rate of Southern Ocean overturning through time (9, 10). However, these records only cover the last glacial cycle, restricting our understanding of the evolution of the Antarctic component of this two-mode system by which the Southern Ocean regulates the transfer of carbon between the ocean interior and the atmosphere over previous climatic cycles. Here, we report a high-resolution relative elemental concentration record from Ocean Drilling Program (ODP) site 1094 (53.2°S, 05.1°E; water depth 2850 m) (Fig. 1), which traces changes in AZ export production over the past million years (figs. S1 and S2). The time resolution achieved here rivals the measurement density typical for Antarctic ice-core records. These observations are complemented with reconstruction of <sup>230</sup>Th-normalized biogenic particle flux to the seafloor covering the last two glacial terminations (Fig. 2).

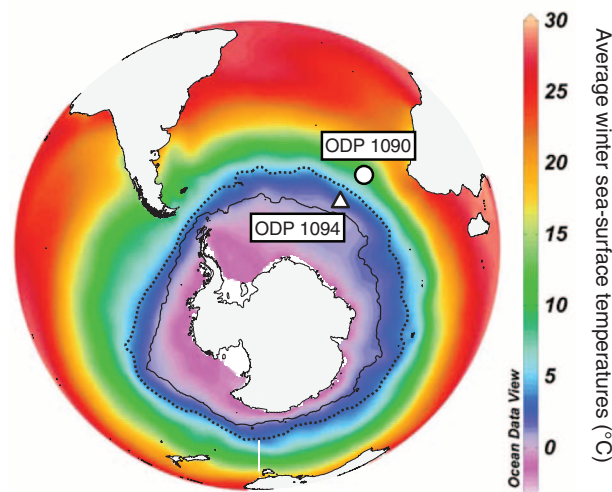


**Fig. 1.** Core locations shown on the January to March SST field. The black line delineates maximum winter sea-ice extent (using the 90% winter sea-ice concentration line) based on the Hadley Center sea-ice concentration data for 1978 to 2010 (34).

<sup>1</sup>Geological Institute, Department of Earth Sciences, ETH Zurich, Zurich, Switzerland. <sup>2</sup>Lamont-Doherty Earth Observatory, Columbia University, Palisades, NY, USA. <sup>3</sup>Godwin Laboratory for Paleoclimate Research, Department of Earth Sciences, University of Cambridge, Cambridge, UK. <sup>4</sup>Department of Geosciences, Princeton University, Princeton, NJ, USA. <sup>5</sup>Department of Earth and Environmental Sciences, Columbia University, New York, NY, USA.

\*Corresponding author. E-mail: samuel.jaccard@erdw.ethz.ch



The pelagic sediment analyzed in this study is dominantly composed of diatomaceous opal and terrigenous detritus, the latter of which is mostly ice-rafted, with a minor contribution from aeolian material (11). Assuming that sedimentary iron (Fe) is of detrital origin, barium (Ba) abundance normalized to Fe yields an estimate of the sedimentary concentration of biogenic (or excess) Ba (bioBa), which serves as a tool to reconstruct changes in the integrated flux of organic matter to the sediment (12). Normalization by Fe assumes that the detrital fraction has not varied substantially in space and time, supported by provenance studies, indicating that the tephra-rich terrigenous material at this site is consistently derived from the South Sandwich volcanic arc, with negligible contribution from Bouvet Island and possibly the Antarctic Peninsula (11). Calcium (Ca) normalized to Fe indicates the sedimentary concentration of biogenic carbonate ( $\text{CaCO}_3$ ). The records of Fe and Ti show almost identical trends in amplitude, but x-ray fluorescence signals are better for Fe, which is thus used for normalization. In these opal-rich sediments, elemental spectrum processing does not allow proper quantification of Al because of the overlapping Si peaks, precluding the use of Al as a normalizing agent.

The Ba/Fe record shows a strong climate-related signal (Fig. 3C), with high values during interglacials and lower values during cold stages. The Ba/Fe record is in good agreement with the  $^{230}\text{Th}$ -normalized flux of bioBa (Fig. 2C), supporting the use of Ba/Fe to infer bioBa throughout the record. The large-scale Ba variations cannot be explained as the result of bacterially mediated sulfate reduction and associated diagenetic barite ( $\text{BaSO}_4$ ) dissolution because no substantial sulfate reduction is observed in the interstitial water of the Pleistocene sediments of ODP site 1094 (13). Indeed, the  $^{230}\text{Th}$ -normalized flux of bioBa is similar to that of opal and chlorophyll transformation products (chlorins) measured in the same sediment core (Fig. 2). Preservation of these independent paleo-productivity proxies is favored in different sedimentary environments. Whereas the preservation of bioBa can be compromised by reducing conditions, the preservation of organic matter in general, and chlorins in particular, is enhanced when oxygen content is low (14). The preservation of opal is unrelated to the redox state of sediments but is primarily driven by the total sedimentation rate (15). The correlation between opal fluxes and excess  $^{231}\text{Pa}/^{230}\text{Th}$  at the same core site during the past 25 ky (9) and the correlation between opal fluxes and bioBa over the past 150 ky reported here indicate that the reconstructed opal fluxes most likely represent variable production by diatoms.

Consequently, the sedimentary Ba/Fe is interpreted to indicate lower bioBa accumulation and thus less export of organic matter from the surface ocean during cold periods, with the lowest bioBa concentrations coinciding almost

exclusively with the glacial maxima, consistent with measurements elsewhere in the Southern Ocean, south of the polar frontal zone (16) (fig. S3). Sea ice has the potential to directly alter export production by blocking sunlight vital for phytoplankton to undertake photosynthesis; however, sea ice was only present at this site during the winters of glacial periods (17), not during the summer growing season. Rather, changes in export imply a reduced supply of nutrients to the surface ocean. Phytoplankton growth is inhibited by the lack of bioavailable Fe in most parts of the Southern Ocean. Vertical mixing and upwelling (rather than atmospheric fluxes) appear to dominate the supply of Fe to the Antarctic surface ocean at present (18). Thus, the glacial decrease in productivity may have been driven by a reduction in this deep-water-derived iron supply.

Although various physical mechanisms have been proposed for a reduction in this deep-water exposure, they all involve reduction of wind-driven upwelling, wintertime vertical mixing, or both (4, 5, 19). Upwelling could be lowered by weaker westerlies and/or by a more northerly position for them, whereas wintertime vertical mixing is sensitive to upper ocean density stratification. Various processes can affect this stratification, including upwelling, which strips away the freshwater cap (halocline) that maintains vertical stability.

Of the nitrate imported into the Antarctic surface today, only a portion derives from Ekman upwelling, with the remaining deriving from wintertime vertical mixing (20). Given that the data suggest many-fold lower export production during peak ice ages, we infer that these changes in productivity likely require both a reduction

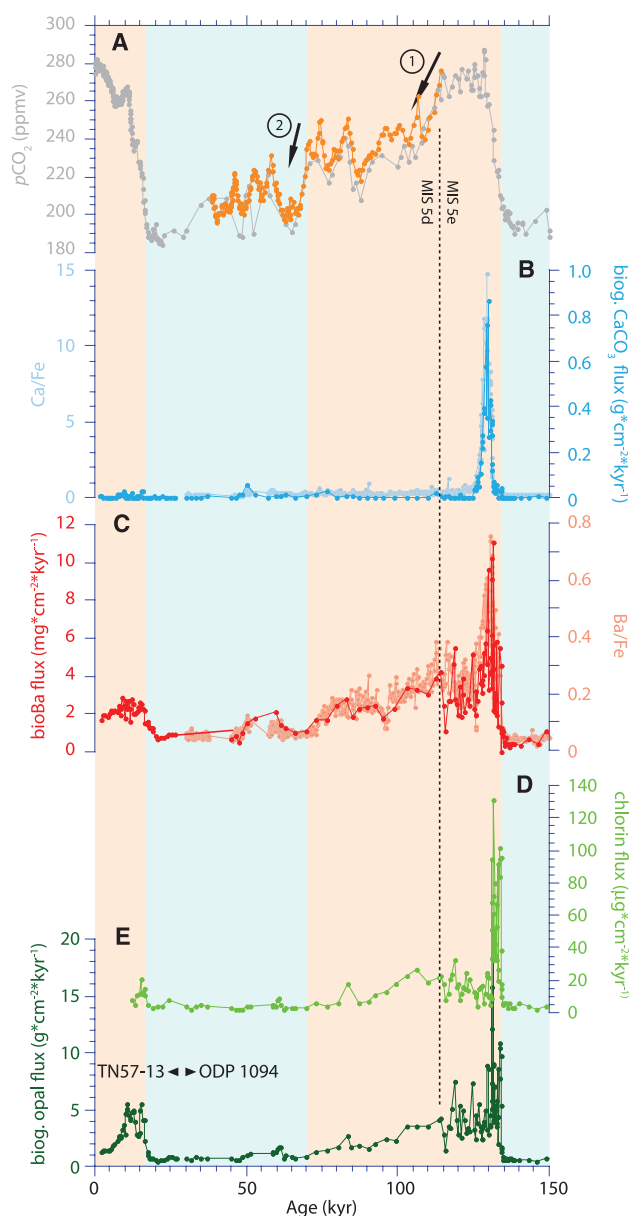


**Fig. 2.** Biogenic particle flux reconstructed by  $^{230}\text{Th}$  normalization for four independent proxies covering the last two glacial terminations. Discrete measurements for the last 25 ky were performed on core TN-57-13PC. (A) Atmospheric  $p\text{CO}_2$  (1, 35). (B) Comparison between  $\text{CaCO}_3$  flux and Ca/Fe. (C) Comparison between bioBa flux and Ba/Fe. (D) Chlorin flux. (E) Biogenic opal flux. Blue shadings highlight ice ages, whereas red shadings indicate interglacials. The two arrows highlight the two-step transition into ice ages.

in wind-driven upwelling and an increase in density stratification. This is important in that the latter change would affect deep-water formation, through which the Antarctic has its greatest direct leverage on atmospheric  $\text{CO}_2$  (21, 22).

Upon glacial terminations, large pulses of export production coincide with prominent increases in atmospheric  $\text{CO}_2$  concentrations reconstructed from Antarctic ice cores (Figs. 2 and 3). Flux determinations of three independent export production proxies suggest that the export of organic matter increased by more than an order of magnitude across the two last climate transitions (Fig. 2). Reconstruction of past silicon and nitrogen dynamics suggests that relative nutrient utilization did not rise sharply at the last glacial termination (23), such that the rise in bioBa and opal fluxes was a response to a large increase in the nutrient supply to the euphotic zone. These increases in export were accompanied by summer sea surface temperature (SST) overshoots and abrupt disappearances of winter sea ice (17). Summer SSTs increased by more than  $4^\circ\text{C}$  in less than 5 ky for the last five glacial terminations (17). Although the sequence of deglacial events remains to be resolved (9), the sys-

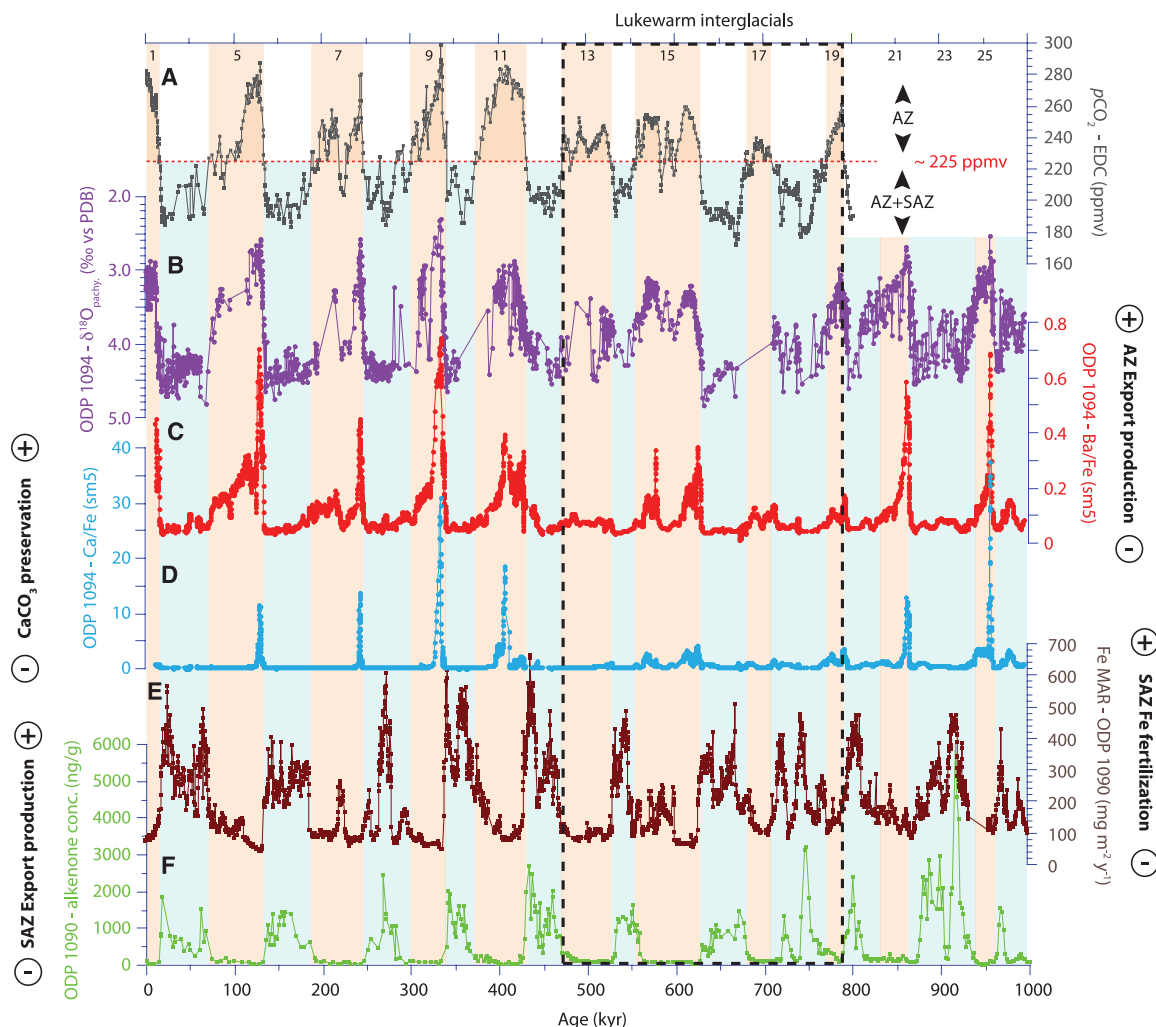
tematic and repeated glacial-to-interglacial rises in biogenic flux (Fig. 3) point to a robust pattern of enhanced Southern Ocean overturning during interglacials.

Moreover, we show that these glacial-to-interglacial export production increases were accompanied by short-lived  $\text{CaCO}_3$  spikes in these otherwise carbonate-poor sediments (Fig. 3D). We note that the preservation spike observed for the last glacial termination is muted at this site, for reasons that remain unclear. The near absence of  $\text{CaCO}_3$  in most of the record suggests that seafloor preservation of the  $\text{CaCO}_3$  rain regulated the bimodal character of the record. Although intervals with higher sedimentary  $\text{CaCO}_3$  concentrations could in principle reflect increased local  $\text{CaCO}_3$  export, the abrupt increases and the transient nature of the  $\text{CaCO}_3$  spikes compared with export production proxies argue instead for a transient deepening of the lysocline, as expected if  $\text{CO}_2$  was lost from deep waters at this time.

The decrease in deep-water exposure after peak interglacial conditions, indicated by declining export production, leads to  $p\text{CO}_2$  reduction, and this mechanism appears to apply in partic-

ular to the early stages of glaciation. As a general rule, elevated Antarctic export occurs during the peak interglacials, giving way to a major decline in the early stages of glaciation (Fig. 3 C), coinciding with the first half of the  $\text{CO}_2$  decline into each glacial period, 40 to 50 parts per million (ppm) (Fig. 3A, reaching  $\sim 225$  ppm). Remarkably, this is a similar, if slightly greater, reduction than is estimated by numerical models for the  $\text{CO}_2$  decline that should result from a strong reduction in Antarctic overturning (21, 24). Although further declines in Antarctic export production occur later in the glacial progression (Fig. 3C), the associated  $\text{CO}_2$  reduction associated with this mechanism should have nearly saturated (2). However, based on data from ODP Site 1090 in the SAZ to the north of ODP Site 1094, it appears that the later stages of glaciation and climate cross a threshold at which the SAZ undergoes a dramatic rise in productivity (Fig. 3F) (6, 25) coincident with increased dust-borne iron supply to the SAZ from continental regions upstream in the westerly wind field (Fig. 3E) (7). Iron fertilization in the SAZ would have permitted biological productivity in this region to sequester additional regenerated

**Fig. 3.** Records of (A) atmospheric  $p\text{CO}_2$  (1), (B) ODP 1094 planktic foraminifera  $\delta^{18}\text{O}$  (36, 37), (C) ODP 1094 Ba/Fe (data smoothed by a five-point running mean), (D) ODP 1094 Ca/Fe (data smoothed by a five-point running mean), (E) Fe flux to subantarctic core ODP 1090 (7), and (F) ODP 1090 sedimentary alkenone concentration (25) covering the past 1 million years. Red and blue shadings highlight intervals where AZ/SAZ processes, respectively, are dominantly controlling the partitioning of  $\text{CO}_2$  between the ocean interior and the atmosphere. During glacial inception, the first half of the  $p\text{CO}_2$  reduction is essentially accomplished by decreasing vertical mixing and upwelling in the AZ (red shading). The second portion of the  $p\text{CO}_2$  reduction (blue shadings), initiated around 225 parts per million by volume (ppmv), is achieved by enhancing carbon sequestration resulting from increased Fe fertilization in the SAZ, thereby leading the climate system to reach full glacial conditions.





carbon in the abyssal ocean, which would have further lowered atmospheric  $\text{CO}_2$  (16, 26). It is again notable that numerical model simulations of subantarctic iron fertilization predict roughly the observed  $\text{CO}_2$  declines of  $\sim 40$  ppm that occur later in the glacial progressions (21, 24, 26). In the modern ocean, there is upper ocean mixing across the fronts separating the AZ and the SAZ (27). Thus, during peak ice conditions, iron fertilization in the SAZ may have further depleted the AZ of surface nutrients, contributing to the continued decline of AZ export production to its glacial minimum. In any case, it is a remarkable characteristic of the two records that the SAZ biological response begins when AZ productivity has reached the lower half of its range (Fig. 3, C and F), with relatively little correlated variation between the AZ and SAZ (Fig. 4), and that the major changes in each correspond to roughly half of the observed  $\text{CO}_2$  variation (Fig. 4). In summary, the paleoceanographic records from both the AZ and SAZ merge with the numerical model estimates of the Southern Ocean to provide a coherent two-part Southern Ocean mechanism for the amplitude and timing of glacial interglacial  $\text{CO}_2$  change.

The potential for these two modes of the Southern Ocean to have different roles in glacial-interglacial  $\text{CO}_2$  change, first recognized in the context of the last glacial cycle (2, 16), is bolstered by the data reported here for the period of the “lukewarm” interglacials [marine isotope stage (MIS) 13 to 19]. The lukewarm interglacials are characterized by reduced amplitude of the

ice-core  $\delta\text{D}$  and  $\text{CO}_2$  records (Fig. 3) and a general decrease in global interglacial temperatures that appears to be more pronounced in Southern Ocean SST records (28). Given the potential dependencies of westerly wind position (29) and polar ocean water-column stability (30) on global temperature, the muting of the  $p\text{CO}_2$  increase during the lukewarm interglacials might have been linked to a reduced dynamic range of Antarctic overturning, with the abyssal ocean thereby maintaining a larger reservoir of regenerated carbon than in more recent interglacials (31). This hypothesis is supported by the Antarctic Ba/Fe record (Fig. 3C), which shows markedly reduced amplitude for the Ba/Fe maxima associated with the lukewarm interglacials (Fig. 4, squares with open circles along the x axis). Furthermore, this interval also generally has reduced deglacial  $\text{CaCO}_3$  peaks (Fig. 3D), which would suggest that proportionally less  $\text{CO}_2$  was released from the deep ocean. The expression of interglacials in the SAZ record is indistinguishable between the period containing the lukewarm interglacials and the rest of the record (Figs. 3 and 4) (7, 25), suggesting that the cessation of SAZ iron fertilization occurred during the lukewarms as in other interglacials.

In contrast to the lukewarm interglacials, MIS 21 and 25 were characterized by full-amplitude export production peaks in the AZ accompanied by large  $\text{CaCO}_3$  preservation events, suggesting an increase in upwelling and deep-ocean  $\text{CO}_2$  release during glacial terminations X and XI (Fig. 3), consistent with planktic foraminiferal pH estimates that suggest that both interglacials

had  $p\text{CO}_2$  values as high as recent interglacials (32). This observation further argues that the subsequent lukewarm interglacials represented a distinct period. Our observations thus indicate a strong coupling between Antarctic deep-to-surface exchange and the magnitude of the  $\text{CO}_2$  release from the ocean interior, which is consistent with observed changes in atmospheric  $p\text{CO}_2$  even beyond the interval covered by the Antarctic ice-core records.

There is much uncertainty and debate regarding the response of Southern Ocean overturning to ongoing global warming, as well to its impact on the oceanic uptake of anthropogenic  $\text{CO}_2$  (33). The paleoclimate data reported here argue strongly for a robust sensitivity of Antarctic overturning to global climate, in which overturning increases under warmer conditions. As the physical mechanism of this coupling is not yet clear, one cannot be confident that it will apply on the decadal to centennial scale and under the specific conditions of anthropogenic global warming. Nonetheless, the finding of stronger overturning under warmer climates, taken at face value, suggests a similar sense of change for the warmer future ocean.

## References

1. D. Lüthi et al., *Nature* **453**, 379 (2008).
2. D. M. Sigman, M. P. Hain, G. H. Haug, *Nature* **466**, 47 (2010).
3. R. F. Keeling, B. B. Stephens, *Paleoceanography* **16**, 112 (2001).
4. J. J. R. Todd, J. L. Russell, S. Carson, *Paleoceanography* **21**, PA2005 (2006).
5. A. J. Watson, A. C. Naveira Garabato, *Tellus* **58B**, 73 (2006).
6. N. Kumar et al., *Nature* **378**, 675 (1995).
7. A. Martinez-Garcia et al., *Nature* **476**, 312 (2011).
8. R. Keir, *Paleoceanography* **3**, 413 (1988).
9. R. F. Anderson et al., *Science* **323**, 1443 (2009).
10. R. François et al., *Nature* **389**, 929 (1997).
11. S. H. Nielsen, D. A. Hodell, G. Kamenov, T. Guilderson, M. R. Perfit, *Geochim. Geophys. Geosyst.* **8**, Q12005 (2007).
12. J. Dymond, E. Suess, M. Lyle, *Paleoceanography* **7**, 163 (1992).
13. R. Gersonde, D. A. Hodell, P. Blum, Eds., *Proceedings of the Ocean Drilling Program, Initial Results, Leg 177* (Ocean Drilling Program, College Station, TX, 1999), chap. 9.
14. K. A. F. Zonneveld et al., *Biogeosciences* **7**, 483 (2010).
15. F. L. Sayles, W. R. Martin, Z. Chase, R. F. Anderson, *Deep Sea Res. Part II Top. Stud. Oceanogr.* **48**, 4323 (2001).
16. K. E. Kohfeld, C. Le Quéré, S. P. Harrison, R. F. Anderson, *Science* **308**, 74 (2005).
17. A. Schneider-Mor et al., *Geophys. Res. Lett.* **32**, L10704 (2005).
18. N. Lefèvre, A. J. Watson, *Global Biogeochem. Cycles* **13**, 727 (1999).
19. A. E. S. Kemp, I. Grigorov, R. B. Pearce, A. C. Naveira Garabato, *Quat. Sci. Rev.* **29**, 1993 (2010).
20. M. J. Lourey, T. W. Trull, *J. Geophys. Res.* **106**, 31463 (2001).
21. M. P. Hain, D. M. Sigman, G. H. Haug, *Global Biogeochem. Cycles* **24**, GB4023 (2010).
22. I. Marinov et al., *Global Biogeochem. Cycles* **22**, GB3007 (2008).
23. M. G. Horn, C. P. Beucher, R. S. Robinson, M. A. Brzezinski, *Earth Planet. Sci. Lett.* **310**, 334 (2011).
24. V. Brovkin, A. Ganopolski, D. Archer, S. Rahmstorf, *Paleoceanography* **22**, PA4202 (2007).
25. A. Martinez-Garcia et al., *Paleoceanography* **24**, PA1207 (2009).
26. A. J. Watson, D. C. E. Bakker, A. J. Ridgwell, P. W. Boyd, C. S. Law, *Nature* **407**, 730 (2000).

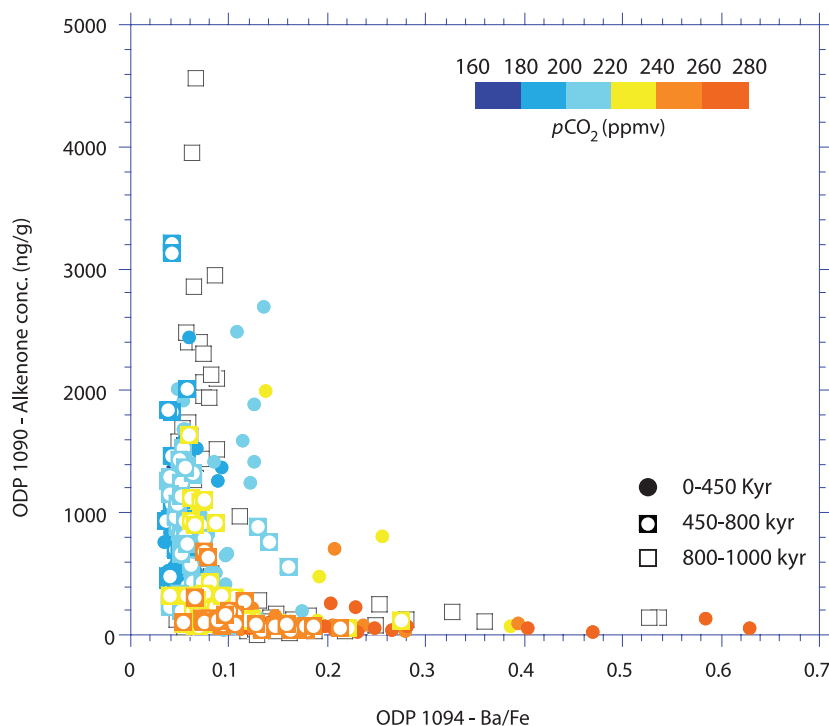


**Fig. 4.** Comparison between ODP 1094 Ba/Fe and ODP 1090 sedimentary alkenone concentration (25). Symbol color indicates  $p\text{CO}_2$ . Filled circles illustrate the period 0 to 450 ky, filled squares the lukewarm interval (450 to 800 ky), and the open squares the interval 800 to 1000 ky, for which ice core  $p\text{CO}_2$  data do not yet exist.

27. P. J. DiFiore *et al.*, *J. Geophys. Res.* **111**, C08016 (2006).
28. N. Lang, E. W. Wolff, *Clim. Past* **7**, 361 (2011).
29. J. Russell, K. W. Dixon, A. Gnanadesikan, R. J. Stouffer, J. R. Toggweiler, *J. Clim.* **19**, 6382 (2006).
30. A. M. de Boer, D. M. Sigman, J. R. Toggweiler, J. L. Russell, *Paleoceanography* **22**, PA2210 (2007).
31. S. L. Jaccard, E. D. Galbraith, D. M. Sigman, G. H. Haug, *Quat. Sci. Rev.* **29**, 206 (2010).
32. B. Hönisch, N. G. Hemming, D. Archer, M. Siddall, J. F. McManus, *Science* **324**, 1551 (2009).
33. C. Le Quéré *et al.*, *Nat. Geosci.* **2**, 831 (2009).
34. N. A. Rayner *et al.*, *J. Geophys. Res.* **108**, (D14), 4407 (2003).
35. B. Bereiter *et al.*, *Proc. Natl. Acad. Sci. U.S.A.* **109**, 9755 (2012).
36. D. A. Hodell *et al.*, in *Proceedings of the Ocean Drilling Program, Scientific Results*, R. Gersonde, D. A. Hodell, P. Blum, Eds. (Ocean Drilling Program, College Station, TX, 2003), vol. 177, chap. 9.
37. H. F. Kleiven, E. Jansen, in *Proceedings of the Ocean Drilling Program, Scientific Results*, R. Gersonde, D. A. Hodell, P. Blum, Eds. (Ocean Drilling Program, College Station, TX, 2003), vol. 177, chap. 12.

**Acknowledgments:** We thank S. Stefer for performing the XRF scanning measurements at the University of Bremen. We also acknowledge the Integrated Ocean Drilling Program for providing the samples used in this study and U. Röhl, A. Wülbbers and W. Hale for their support at the Bremen IODP core repository. This research used data acquired at the XRF Core Scanner Laboratory at the MARUM – Center for Marine

Environmental Sciences, University of Bremen. We further thank E. D. Galbraith as well as three anonymous reviewers, whose comments improved the manuscript. Financial support for this work was provided by the Swiss National Science Foundation (SNSF), the Deutsche Forschungsgemeinschaft (DFG), the U.S. National Science Foundation, and the Comer Science and Education Foundation.

#### Supplementary Materials

www.sciencemag.org/cgi/content/full/339/6126/1419/DC1  
Materials and Methods  
Figs. S1 to S3  
References

17 July 2012; accepted 16 January 2013  
10.1126/science.1227545

# Emergence and Diversification of Fly Pigmentation Through Evolution of a Gene Regulatory Module

Laurent Arnoult,\* Kathy F. Y. Su,\* Diogo Manoel,\* Caroline Minervino, Justine Magriña, Nicolas Gompel,† Benjamin Prud'homme†

The typical pattern of morphological evolution associated with the radiation of a group of related species is the emergence of a novel trait and its subsequent diversification. Yet the genetic mechanisms associated with these two evolutionary steps are poorly characterized. Here, we show that a spot of dark pigment on fly wings emerged from the assembly of a novel gene regulatory module in which a set of pigmentation genes evolved to respond to a common transcriptional regulator determining their spatial distribution. The primitive wing spot pattern subsequently diversified through changes in the expression pattern of this regulator. These results suggest that the genetic changes underlying the emergence and diversification of wing pigmentation patterns are partitioned within genetic networks.

Whether emergence and diversification of morphological traits both occur through changes at the same tier of a gene regulatory network is currently an open question in evolutionary biology. We addressed this question by studying a wing pigmentation pattern that evolved recently in the *Drosophila melanogaster* group. Although this male-specific wing spot assumes different shapes, colors, and intensities among species (Fig. 1 and fig. S1), phylogenetic reconstruction indicates that it emerged only once in this lineage and subsequently diversified (1).

We examined the expression pattern of *yellow* (*y*), a gene required for the production of black pigment patterns, including the wing spot (2). Yellow distribution in the wing of pupae or young adults precisely foreshadows the adult pigmentation pattern in the various species we studied (Fig. 1), suggesting that understanding the evolution of *y* expression patterns would illuminate how the wing spot appeared and diversified. The wing spot expression pattern of *y* in *D. biarmipes*,

a wing-spotted species, is encoded by an evolutionarily derived cis-regulatory element (CRE) of the *yellow* locus (2), the *spot* CRE [hereafter referred to as *y spot<sup>bia675</sup>* (3)]. Therefore, to decipher how the wing spot expression of *y* is spatially regulated, we sought to identify the transcription factors controlling the localized activity of the *y spot<sup>bia196</sup>* CRE, a minimal version of *y spot<sup>bia675</sup>* CRE with a similar activity (2).

The *y spot<sup>bia196</sup>* CRE is functional in *D. melanogaster* wing, and we used its transcriptional activity as a readout in an RNA interference (RNAi) screen targeting selected genes to identify its transcriptional activators. With this functional screen of the ~350 transcription factors expressed in a *D. melanogaster* late pupal wing (table S1), we identified a handful of candidates (fig. S2). Among five candidate activators, *Distal-less* (*Dll*) first caught our attention because of its well-defined role in wing patterning. When *Dll* is down-regulated, the activity of the *y spot<sup>bia196</sup>* CRE is severely affected (Fig. 2, A and B, and fig. S2C). Reciprocally, we overexpressed *Dll* throughout the wing, which resulted in an increase and an expansion of the *y spot<sup>bia196</sup>* activity (Fig. 2C). These genetic manipulations reveal that *Dll* is both necessary and sufficient to control the activity of the *y spot<sup>bia196</sup>* CRE in a *D. melanogaster* context.

By scanning the *spot<sup>bia196</sup>* CRE, we identified several putative *Dll* binding sites. We tested the ability of *Dll* to bind these sites in vitro (fig. S3, A and B) and, thus, discovered that *Dll* can physically interact with four of them. Mutations of these sites preventing *Dll* binding in vitro also impaired the activity of the *y spot<sup>bia196</sup>* CRE in vivo (Fig. 2D and fig. S3C). Of note, the same mutations also abolish the *y spot<sup>bia196</sup>* response to *Dll* overexpression (fig. S3D). Together, these results indicate that the *y spot<sup>bia196</sup>* CRE contains multiple binding sites for *Dll* and suggest that the evolution of a regulatory link between *Dll* and *yellow* was essential for the emergence of the wing spot.

The results obtained in *D. melanogaster* stimulated the investigation of the role of *Distal-less* in wing pigmentation pattern formation in *D. biarmipes*. We established a loss-of-function assay based on the expression of artificial short hairpin microRNA (shRNA) (4) and validated the system in *D. biarmipes* by silencing *yellow* in the pupal wing (fig. S5, A and C), which phenocopies a *y* mutant. The down-regulation of *Dll*, using the same shRNA approach, resulted in a dramatic reduction of the pigmentation spot (Fig. 3, A and B, and fig. S4, A to D); however, the uniform gray shading of the wing was not affected. Reciprocally, the overexpression of *Dll* throughout the wing yielded ectopic pigmentation across the wing (Fig. 3, A and C, and fig. S4, E to G and J). Together, these results establish that *Dll* plays an essential role in wing spot formation in *D. biarmipes*.

To test the specificity of the effect of *Dll* on wing spot pattern formation in *D. biarmipes*, we first examined the other transcription factors identified in our RNAi screen. Contrary to *Dll*, none of the candidates that we overexpressed across the wing were sufficient to induce ectopic pigmentation (fig. S4, H to M). These results highlight the specific role of *Dll* in the wing pigmentation spot formation. Second, we ectopically expressed *Dll* in the wing of the nonspotted species *D. ananassae*, a species with an ancestral pattern predating the wing spot evolution (Fig. 1) (1). In this species, *Dll* overexpression had no effect on wing pigmentation (fig. S6G), suggesting that the regulatory interactions between *Dll* and downstream pigmentation genes are absent. Consistent

Aix-Marseille Université, CNRS, UMR 7288, Institut de Biologie du Développement de Marseille-Luminy, 13288 Marseille cedex 9, France.

\*These authors contributed equally to this work.

†Corresponding author. E-mail: nicolas.gompel@univ-amu.fr (N.G.); benjamin.prudhomme@univ-amu.fr (B.P.)



with this, *y spot<sup>bia675</sup>* CRE activity (Fig. 3, D to F), *y* mRNA level (fig. S6), and Yellow distribution (fig. S5, B, E, and F) all respond to *Dll* expression changes in a *D. biarmipes* wing, whereas, in contrast, all remain unaffected when *Dll* is overexpressed in *D. ananassae* (fig. S6). Together, these results indicate that the regulatory link between *Dll* and *yellow* in the wing probably evolved in the common ancestor of wing-spotted species, after the divergence with the *D. ananassae* lineage.

The evolutionary co-option of *Dll* by *yellow* in the wing was presumably an essential step in the emergence of the wing spot, but it was certainly not solely sufficient for the pigmentation pattern to appear. The wing spot of the *D. biarmipes* *yellow* mutant shifts from black to light beige, but its shape remains unaffected (fig. S5C), indicating that at least one additional pigmentation gene is involved. This is consistent with the view that black pigment deposits result from multiple enzymatic activities (2, 5). We therefore hypothesized that during evolution, *Dll* became a key regulator controlling the shape of the wing pigmentation spot by coordinating the spatial deployment of several enzymatic activities. Overexpression of *Dll* throughout the wing of a *D. biarmipes* *yellow* mutant resulted in the expansion of the light beige color (fig. S5D), suggesting that *Dll* is governing the spatial distribution of multiple pigmentation genes. Hence, we tested whether *Dll* regulates *ebony*, a pigmentation gene whose expression pattern correlates with the wing spot shape in *D. biarmipes* (2). In wild-type (WT) males, *ebony* expression is repressed in the presumptive wing spot area (Fig. 3G). When *Dll* expression is down-regulated, *ebony* is no longer repressed in the spot area (Fig. 3H), whereas reciprocally, *Dll* overexpression reduces the *ebony* expression level across the wing (Fig. 3I). These results show that *Dll* controls the spatial distribution of *ebony* in the wing. More generally, our findings suggest that the wing spot emergence was brought on by the evolution of regulatory links between *Dll* and multiple pigmentation genes.

The wing spot diversified in shape and intensity among species of the *D. melanogaster* lineage (fig. S1), and *Yellow* distribution mirrors this diversification (Fig. 1). We therefore asked how *yellow* expression has changed among wing-spotted species. We noticed that the *y spot<sup>bia675</sup>* CRE precisely recapitulates the native *y* distribution in *D. biarmipes* (Fig. 3D), but not in *D. melanogaster* (Fig. 2A) (2). This difference indicates that some trans-acting factors have likely diverged between the two species. As *Dll* is an activator of the *y spot<sup>bia675</sup>* CRE, we compared its expression pattern between *D. melanogaster* and *D. biarmipes*. *Dll* is expressed in a gradient pattern in the wing blade around the margin during early pupal development in *D. biarmipes* (fig. S7, A and B), suggesting a conserved role in early wing development (6). However, ~30 hours after puparium formation, when the wing patterning is complete, *Dll* expression diverges between

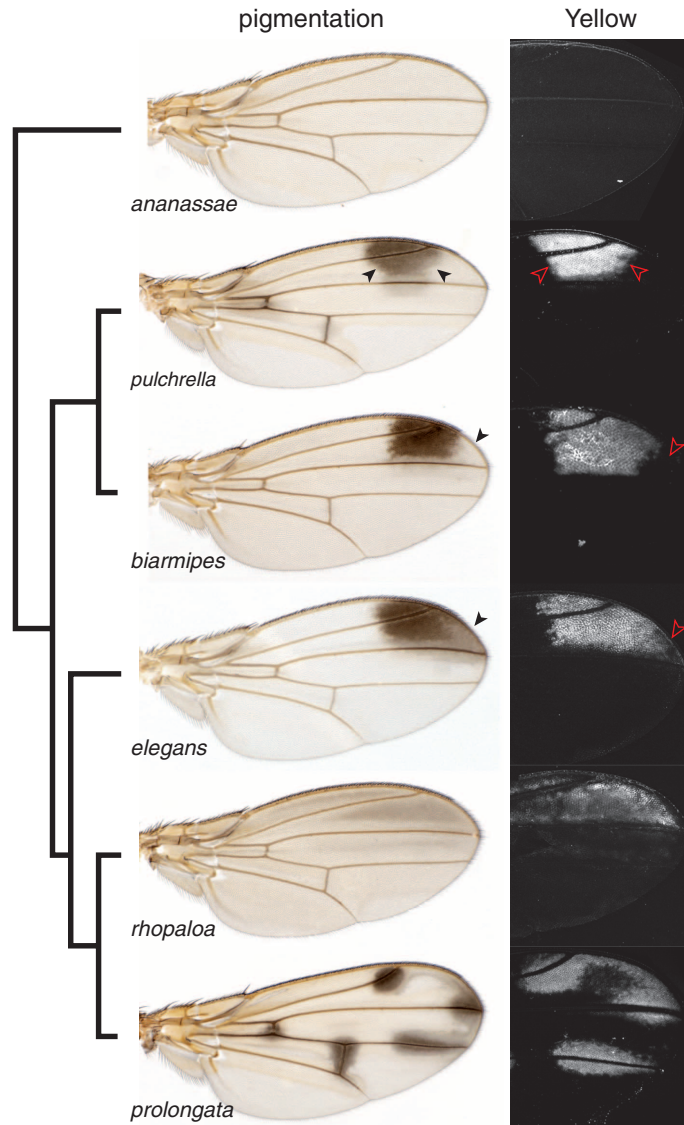


**Fig. 1.** A spot of black pigmentation (**left**) on male *Drosophila* wings assumes various shapes among species. These variations are precisely prefigured by the distribution of the *Yellow* protein (**right**) in the wing of young adults. The phylogenetic relationships of these species are indicated to the left. Arrowheads highlight subtle variations between closely related species.

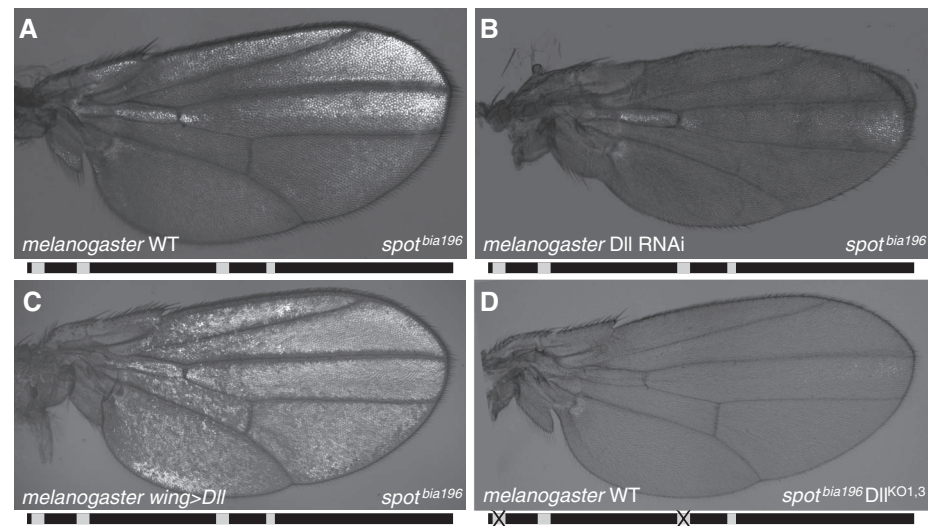


**Fig. 2.** In a *D. melanogaster* pupal wing, the activity of a *spot<sup>bia196</sup>*-reporter construct (**A**) is severely impaired when the transcription factor *Dll* is depleted (**B**) and enhanced when *Dll* is overexpressed (**C**). The effect mediated by *Dll* down-regulation (**B**) is mirrored by the mutation of *Dll* binding sites in the *spot<sup>bia196</sup>* CRE (**D**). The diagrams represent the *spot<sup>bia196</sup>* CRE and the localization of the *Dll* binding sites (gray boxes) and the mutated sites (crossed boxes).

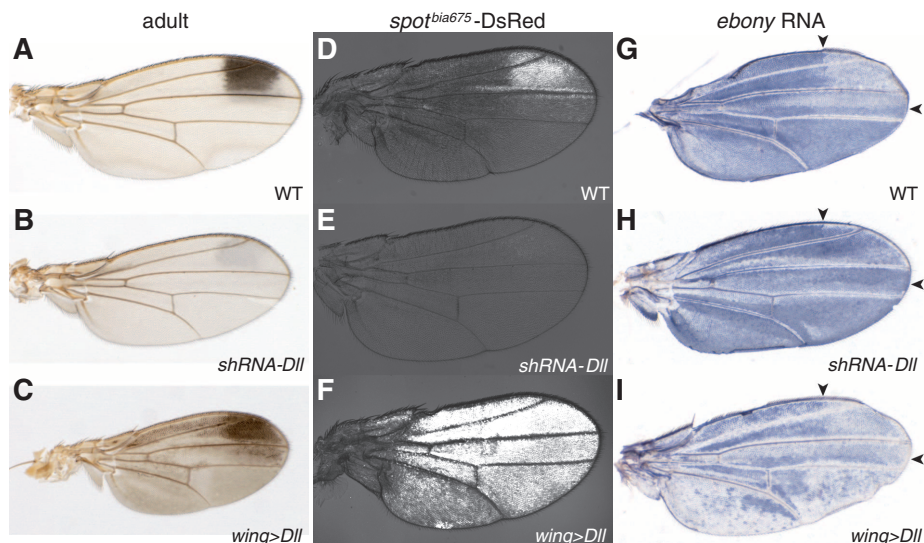


**Fig. 3.** Compared with the wild type (A), Dll down-regulation reduces the intensity of the pigmentation spot in *D. biarmipes* (B), whereas, conversely, the overexpression of Dll results in ectopic pigmentation across the wing (C). These effects are reflected in the activity of the yellow *spot<sup>bia675</sup>*-reporter construct (D to F), which is reduced when Dll is knocked down and expanded when Dll is overexpressed. They are also reflected in the expression of *ebony*, in a reciprocal manner (G to I). Note that the activity of *spot<sup>bia675</sup>* in a WT *D. biarmipes* context (D) precisely prefigures the native Yellow distribution and the shape of the pigmentation spot. Arrowheads in (G) to (I) indicate the boundaries of *ebony* distribution in the presumptive spot area in the wild type.

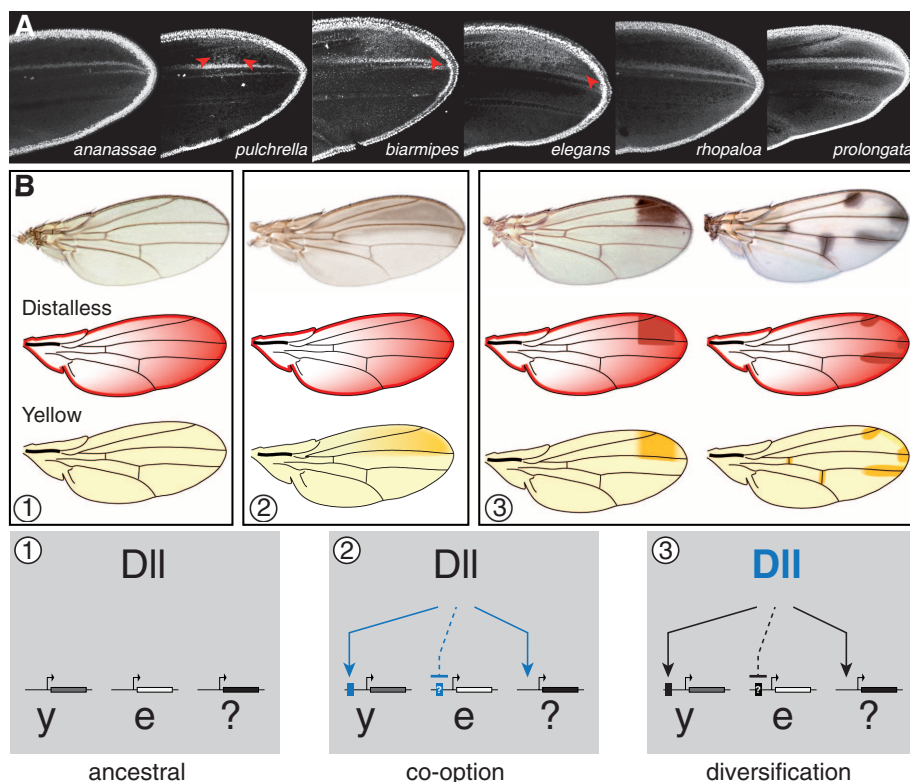


**Fig. 4.** (A) Differences in Dll distribution among species correlate with the shape of the spot (arrowheads indicate subtle spatial differences in the pigmentation patterns between *D. biarmipes*, *D. elegans*, and *D. pulchrella* prefigured by Dll distribution divergence). (B) A regulatory model of the emergence and diversification of the wing spot. The evolutionary transition from unspotted [(1), similar to *D. ananassae*] to spotted species [(2), similar to *D. rhopaloea*] required the assembly of a new genetic module. Subsequently, the spatial distribution of this module diversified through changes in Dll regulation, thereby creating different wing pigmentation patterns (3). The blue color indicates the evolution of new regulatory links in (2) and changes in Dll regulation in (3). Wings in (A) are at ~33% of pupal development. y, yellow; e, ebony.

the two species. Although in *D. melanogaster* Dll remains expressed in a gradient from the wing blade (fig. S7, K and L), in *D. biarmipes* a distinct expression pattern element prefiguring the shape of the pigmentation spot becomes visible (Fig. 4 and fig. S7, C to G). Therefore, *y spot<sup>bia675</sup>* CRE activity follows the spatial distribution of Dll in both *D. melanogaster* and *D. biarmipes*, reinforcing that Dll dictates the spatial distribution of yellow in the wing. Importantly, the spatially restricted expression pattern of Dll in *D. biarmipes* contrasts with the uniform distribution of other candidate transcription factors identified in our screen (fig. S7, I and J). These observations support the notion that Dll governs the spatial regulation of pigmentation genes involved in the wing spot formation.

As Dll pupal wing expression has changed between *D. melanogaster* and *D. biarmipes* and because Dll controls the spatial distribution of the pigmentation genes necessary to produce black pigment, we asked whether the diversification of Dll expression could account for the various wing pigmentation patterns among wing-spotted species in the *D. melanogaster* lineage. We found that, in all cases, the expression pattern of Dll predicts Yellow distribution and the adult pigmentation pattern at the wing tip (Fig. 4A and fig. S7H). These results suggest that the divergence of Dll wing expression pattern drives the diversification of wing pigmentation patterns in the *D. melanogaster* lineage.

On the basis of these results, we propose that the wing spot emerged through the independent and likely progressive recruitment by several pigmentation genes of multiple transcriptional regulators (2, 7), including Dll as a common spatial coordinator (Fig. 4B), probably through the evolution of binding sites for Dll in cis-regulatory sequences of these genes. These new regulatory links between Dll and the pigmentation genes created a novel genetic module sufficient for the formation of a primitive wing spot pattern. Subsequently, this module was deployed in various spatial patterns in the wings of different species through changes in Dll distribution, thereby creating diverse wing pigmentation patterns.

This work illustrates how a transcription factor governing several effector genes to form a morphological trait has become a privileged genetic target to modify the spatial pattern of this trait during evolution (8). A similar logic may apply generally to the numerous morphological patterns that vary spatially between related species (8–12): The emergence of these morphological novelties may result from the evolutionary modifications of effector genes, whereas their spatial diversification involves the redeployment of upstream patterning genes.

#### References and Notes

1. B. Prud'homme *et al.*, *Nature* **440**, 1050 (2006).
2. N. Gompel, B. Prud'homme, P. J. Wittkopp, V. A. Kassner, S. B. Carroll, *Nature* **433**, 481 (2005).
3. See the materials and methods and other supplementary materials on Science Online.



4. B. Haley, D. Hendrix, V. Trang, M. Levine, *Dev. Biol.* **321**, 482 (2008).
5. J. R. True, K. A. Edwards, D. Yamamoto, S. B. Carroll, *Curr. Biol.* **9**, 1382 (1999).
6. G. Campbell, A. Tomlinson, *Development* **125**, 4483 (1998).
7. B. Prud'homme, N. Gompel, S. B. Carroll, *Proc. Natl. Acad. Sci. U.S.A.* **104** (suppl. 1), 8605 (2007).
8. D. L. Stern, V. Orgogozo, *Science* **323**, 746 (2009).
9. A. Abzhanov, M. Protas, B. R. Grant, P. R. Grant, C. J. Tabin, *Science* **305**, 1462 (2004).
10. P. M. Brakefield *et al.*, *Nature* **384**, 236 (1996).
11. S. Marcellini, P. Simpson, *PLoS Biol.* **4**, e386 (2006).
12. R. D. Reed *et al.*, *Science* **333**, 1137 (2011).

**Acknowledgments:** We thank A. Kopp, S. B. Carroll, J. David, R. Mann, A. Mazo, M. Yamaguchi, and the Vienna *Drosophila* RNAi Center (VDRC, Vienna), Bloomington (Indiana), National Center of Genetics (Kyoto), and San Diego *Drosophila* Stock Centers for flies and antibodies; A. Polette and L. Mille for developing a custom quantification program for wing

pigmentation; J.-L. Mari for advice on programming; G. Storelli for help with cloning; A. Defaye for qPCR guidance; J.-Y. Sgro for microarray analysis; A. Kopp, F. Leulier, and J. Cande for helpful comments on the manuscript; Flybase for information support; and Le Calendal for logistical support. L.A. and K.F.Y.S. were supported by fellowships from the French government (Ministère de la Recherche de l'Enseignement Supérieur), D.M. by the Portuguese Foundation for Science and Technology (Fundação para a Ciência e a Tecnologia) and the GABBA graduate program, and K.F.Y.S. by the Fondation ARC pour la Recherche sur le Cancer. This work was funded by a EURYI award, a Human Frontier Science Program Career Development Award, the Agence Nationale de la Recherche, the France-Berkeley Fund, the Fondation Schlumberger pour l'Enseignement et la Recherche, and the CNRS. RNAi lines from the VDRC are covered by a Materials Transfer Agreement. The microarray data set is accessible in the National Center for Biotechnology Information Gene Expression Omnibus database (accession no. GSE43673). Author contributions: B.P. and N.G. conceived the project; all authors designed

the experiments; K.F.Y.S. and D.M. performed the RNAi screen; K.F.Y.S., D.M., and L.A. did the antibody stainings; K.F.Y.S., L.A., D.M., C.M., and B.P. cloned the molecular constructs; and D.M. and B.P. ran the biochemistry experiments. L.A. designed and carried out the shRNA experiments in *D. biarmipes*, did the qPCR analysis, optimized transgenesis, and developed the wing-peeling technique. L.A. and N.G. quantified the effects on pigmentation; K.F.Y.S., L.A., D.M., J.M., N.G., and B.P. made transgenic flies; L.A., N.G., and K.F.Y.S. took the images; all authors analyzed the data; and B.P. and N.G. wrote the paper, with feedback from L.A. and the other authors.

#### Supplementary Materials

www.sciencemag.org/cgi/content/full/339/6126/1423/DC1  
Materials and Methods  
Figs. S1 to S8  
Tables S1 and S2  
References (13–29)

6 December 2012; accepted 25 January 2013  
10.1126/science.1233749

# Structural Reorganization of the Toll-Like Receptor 8 Dimer Induced by Agonistic Ligands

Hiromi Tanji,<sup>1,3\*</sup> Umeharu Ohto,<sup>1,3\*</sup> Takuma Shibata,<sup>2</sup> Kensuke Miyake,<sup>2</sup> Toshiyuki Shimizu<sup>1,3,†</sup>

Toll-like receptor 7 (TLR7) and TLR8 recognize single-stranded RNA and initiate innate immune responses. Several synthetic agonists of TLR7-TLR8 display novel therapeutic potential; however, the molecular basis for ligand recognition and activation of signaling by TLR7 or TLR8 is largely unknown. In this study, the crystal structures of unliganded and ligand-induced activated human TLR8 dimers were elucidated. Ligand recognition was mediated by a dimerization interface formed by two protomers. Upon ligand stimulation, the TLR8 dimer was reorganized such that the two C termini were brought into proximity. The loop between leucine-rich repeat 14 (LRR14) and LRR15 was cleaved; however, the N- and C-terminal halves remained associated and contributed to ligand recognition and dimerization. Thus, ligand binding induces reorganization of the TLR8 dimer, which enables downstream signaling processes.

The Toll-like receptors (TLRs) are a family of pattern-recognition receptors that recognize microbial components and initiate subsequent immune responses (1). TLRs recognize multiple pathogen-associated molecular patterns and are expressed predominantly on cells of the immune system, such as macrophages, dendritic cells, neutrophils, and monocytes (2). Both TLR7 and TLR8 are involved in the recognition of single-stranded RNA (ssRNA) from various viruses (3–7), as well as small interfering RNAs (8–11). TLR7 and TLR8 also mediate the recognition of self RNA that is released from dead or dying cells and contribute to the pathogenesis

of autoimmune diseases, such as systemic lupus erythematosus (12).

Phylogenetic analysis has revealed that TLR7, TLR8, and TLR9 form a subfamily of proteins that each contain an extracellular domain of >800 residues and share functional and structural features (13, 14) (fig. S1). Before ligand recognition, both TLR8 and TLR9 exist as preformed dimers; ligand-induced conformational changes in the preformed dimer have been demonstrated for TLR9 (15). This preformed dimer contrasts with the ligand-induced dimerization mechanism of other TLRs (16–20).

Both TLR7 and TLR8 are believed to recognize uridine- and guanosine-rich ssRNA (3, 4). Moreover, several small-molecule compounds have been identified as TLR7 and TLR8 activators (21, 22). Some imidazoquinoline derivatives, such as resiquimod (R848), are recognized by both human TLR7 and TLR8 (21); whereas guanosine nucleotides analogs such as loxoribine, and other imidazoquinoline derivatives such as imiquimod (R837), selectively activate TLR7 but not TLR8 (22–24). With molecular masses of

200 to 300 daltons, these compounds are the smallest of the TLR ligands and are therefore attractive therapeutic targets for various infectious diseases. In fact, imiquimod is approved for treatment of external genital warts, actinic keratosis, and basal cell carcinoma. The lack of structural knowledge of TLR7 and 8 hinders understanding of the molecular mechanisms underlying activation of signaling and specific ligand recognition. In particular, an understanding of why and how TLR7 and TLR8 are activated by small ligands remains largely unknown.

We sought to determine the crystal structures of an unliganded preformed dimer and ligand-induced activated forms of human TLR8. The TLR8-R848 complex structure was initially determined using two heavy-atom derivatives (Pt and Cs) (fig. S2); the other structures were determined by the molecular replacement method, using the refined TLR8-R848 complex coordinates (table S1 and S2). TLR8 contains 26 leucine-rich repeats (LRRs), which is the largest number of LRRs among TLRs whose structures have been reported (Fig. 1A). Because TLR7, TLR8, and TLR9 are predicted to have a long insertion region (~40 amino acids) between LRR14 and LRR15, we chose to observe this insertion region (residues 442 to 481), hereafter referred to as the Z-loop.

Although purified TLR8 was found cleaved at the Z-loop, the N terminus (residues 31 to 432) and C terminus (residues 458 to 817) of the TLR8 monomer were directly associated with each other (Fig. 1B). The consensus  $\beta$  strands of LRR14 and LRR15 interacted to form a  $\beta$ -sheet structure (fig. S3A), which was positioned within the concave face of TLR8 (fig. S3B). At the convex face of the structure, LRR13 interacted with LRR15 directly (fig. S3A); as a result, the loop region of LRR14 located after the  $\beta$  strands was excluded from the main body of the LRR structure (fig. S3A). Although the loop region of LRR14 and the first half of the Z-loop (residues 433 to 457) were missing from the electron density maps, most likely because of the disorder of this portion, the latter half of the Z-loop (after Asp<sup>458</sup>) was well ordered in the concave face of the LRR structure

<sup>1</sup>Graduate School of Pharmaceutical Sciences, The University of Tokyo, Hongo, Bunkyo-ku, Tokyo 113-0033, Japan. <sup>2</sup>Division of Innate Immunity, Department of Microbiology and Immunology, Laboratory of Innate Immunity, Center for Experimental Medicine and Systems Biology, The Institute of Medical Science, The University of Tokyo, 4-6-1 Shirokanedai, Minato-ku, Tokyo 108-8639, Japan. <sup>3</sup>RIKEN Spring-8 Center, Kouto 1-1-1, Sayo, Hyogo 679-5148, Japan.

\*These authors contributed equally to this work.

†Corresponding author. E-mail: shimizu@molf.u-tokyo.ac.jp

and was stabilized by extensive contact with LRR3 to LRR18 (fig. S3B). At the end of the Z-loop, we observed a single turn of the  $\alpha$  helix, which was stabilized by a disulfide bridge between Cys<sup>479</sup> (within the Z-loop) and Cys<sup>509</sup> (within LRR16). These two Cys residues are highly conserved between the TLR7, 8, and 9 proteins (fig. S1).

Gel filtration analysis revealed that unliganded TLR8 was dimeric in solution (fig. S4), which suggested that the inactivated protein creates a preformed dimer. Consistent with the gel filtration results, the crystal structure of unliganded TLR8 exhibited a dimeric form (Fig. 1C). Throughout this Report, we indicate the second TLR8 and its residues in the dimeric TLR8 with asterisks. The two TLR8 monomers were separated at the C-terminal regions by  $\sim 53$  Å. The length of this separation likely precludes proper association of the cytoplasmic domain; therefore, this dimeric structure represents the inactivated form of TLR8.

We also determined the crystal structures of TLR8 in complex with three different agonistic chemical ligands, namely, CL097, CL075, and R848 crystal forms 1 to 3 (table S2). Despite TLR8's being in complex with different ligands and displaying differential molecular packing in the crystal structures, we observed essentially the same dimeric structures of TLR8 for each of the three ligands tested (fig. S5), which excludes the possibility of artificial dimer formation in the crystals. The crystallographic asymmetric unit of the TLR8-CL097 complex contained two copies of the TLR8 monomer, which were assigned as

components of the TLR8 dimer (Fig. 1D). Superposition of the two TLR8 molecules in the asymmetric unit yielded a small root mean square deviation (RMSD) value of 0.4 Å, which indicated that the two molecules are essentially identical. The two TLR8 monomers in the dimer, related by non-crystallographic (NCS) two-fold symmetry, were positioned in the lateral face of the LRR structure, in a manner similar to the positioning of other ligand-induced TLR structures (16–20). Upon ligand binding, the two C termini were brought into close proximity ( $\sim 30$  Å) (Fig. 1D and fig. S5), which would enable the subsequent dimerization of the intracellular Toll–interleukin-1 receptor (TIR) domain and downstream signaling, which, in turn, suggests that the ligand-bound dimer is a signaling complex.

The dimerization interfaces of the unliganded and the ligand-induced dimers bury  $\sim 1290$  Å<sup>2</sup> and  $\sim 2150$  Å<sup>2</sup> of the accessible surface area of the TLR8 structures, respectively (Fig. 2 and figs. S6A and S7). The unliganded form of TLR8 has a dimerization interface spanning from LRR8 to LRR18. In fact, the dimerization interface is formed by several hydrogen bonds (LRR8, LRR14–15, and LRR18) (table S3) and hydrophobic cores consisting of Tyr<sup>348</sup>, Phe<sup>261</sup>, Tyr<sup>567</sup>\*, and Phe<sup>568</sup>\*, and Phe<sup>405</sup>, Tyr<sup>353</sup>, Val<sup>378</sup>, Phe<sup>494</sup>\*, Phe<sup>495</sup>\*, and Pro<sup>432</sup>\*, which are spread around LRR8, LRR11–15, and LRR18 (fig. S6A). Ligand binding induced the local conformational changes of the loop structures of LRR5, LRR8, and LRR17–20, whereas the overall structures superpose well

with an RMSD value of 1.1 Å (fig. S6B). The dimerization interface of ligand-induced dimer is divided into two regions, the protein-protein interface and the ligand-mediated interface, which account for  $\sim 75\%$  and  $\sim 25\%$  of the buried surface area, respectively (Fig. 2 and fig. S7). The protein-protein interface involves both hydrogen bonds and hydrophobic interactions and is widely spread around LRR5, LRR8, and LRR14–20 (Fig. 2). Hydrogen-bonded pairs of Asn<sup>491</sup> O–Arg<sup>541</sup>\*, Ala<sup>514</sup> O–Arg<sup>541</sup>\*, and Glu<sup>427</sup>–His<sup>566</sup>\*, and van der Waals contact of Phe<sup>494</sup>–Phe<sup>494</sup>\* and Ser<sup>516</sup>–Ser<sup>516</sup>\* were observed near the two-fold NCS axis (Fig. 2, top panel, and table S3). At the peripheral region of the dimerization interface (Fig. 2, bottom panel), extensive van der Waals contacts and hydrogen bonds were observed. The ligand-mediated interface is composed of residues of LRR11–14 and LRR16–18 as described below.

Two clear electron densities corresponding to the ligand were observed in the crystals of TLR8 complexed with chemical ligands (fig. S8A). The two chemical ligands were located in the dimer interface of TLR8 and the two positions were related by the NCS two-fold axis, where the first is close to LRR11–14 and LRR16\*–18\*, and the second is close to LRR11\*–14\* and LRR16–18 (Figs. 2 and 3). These ligands were recognized by interactions with multiple amino acids from both TLR8 and TLR8\* and act as molecular glues bridging the two TLR8 molecules. All of the ligands tested occupied the same position

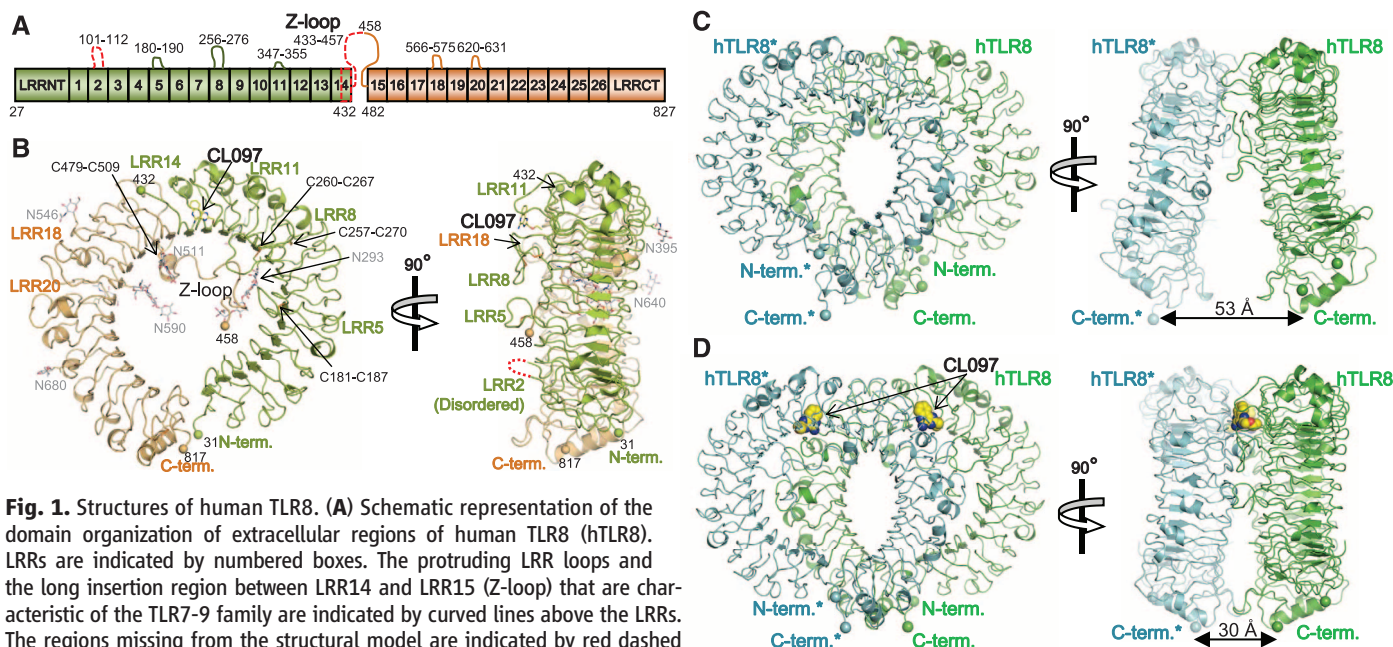


**Fig. 1.** Structures of human TLR8. (A) Schematic representation of the domain organization of extracellular regions of human TLR8 (hTLR8). LRRs are indicated by numbered boxes. The protruding LRR loops and the long insertion region between LRR14 and LRR15 (Z-loop) that are characteristic of the TLR7-9 family are indicated by curved lines above the LRRs. The regions missing from the structural model are indicated by red dashed lines. The N-terminal and C-terminal halves of TLR8 are shown in light green and light orange, respectively. (B) Monomer structure of the hTLR8-CL097 complex showing the lateral face (left) and the convex face from the N-terminal side (right). The bound CL097, N-glycan residues, and disulfide bonds are shown in stick representations. The O, N, and S atoms are colored red, blue, and orange, respectively. The C atoms of CL097 and N-glycans are shown in yellow and gray, respectively. The N and C termini of each

fragment are shown as spheres. (Left) Front and (right) side views of the preformed inactivated state (C) and ligand-induced activated state (D). TLR8 and its dimerization partner TLR8\* are green and cyan, respectively. The CL097 molecules in the activated dimerization interface are illustrated by space-filling representations. The distances between the two C $\alpha$  atoms of each C terminus are indicated.



**Fig. 2.** Dimerization interface of the ligand-induced TLR8 dimer. **(Left, middle)** A surface representation of the protein-protein interface (orange) and ligand-mediated interface (red). **(Right, middle)** Top view of the ligand-induced TLR8 dimer along the two-fold NCS axis. Magnified views of the central dimerization interface around the two-fold NCS axis (**top**) and the peripheral dimerization interface (**bottom**). Hydrogen bonds in the magnified views are indicated by dashed lines.

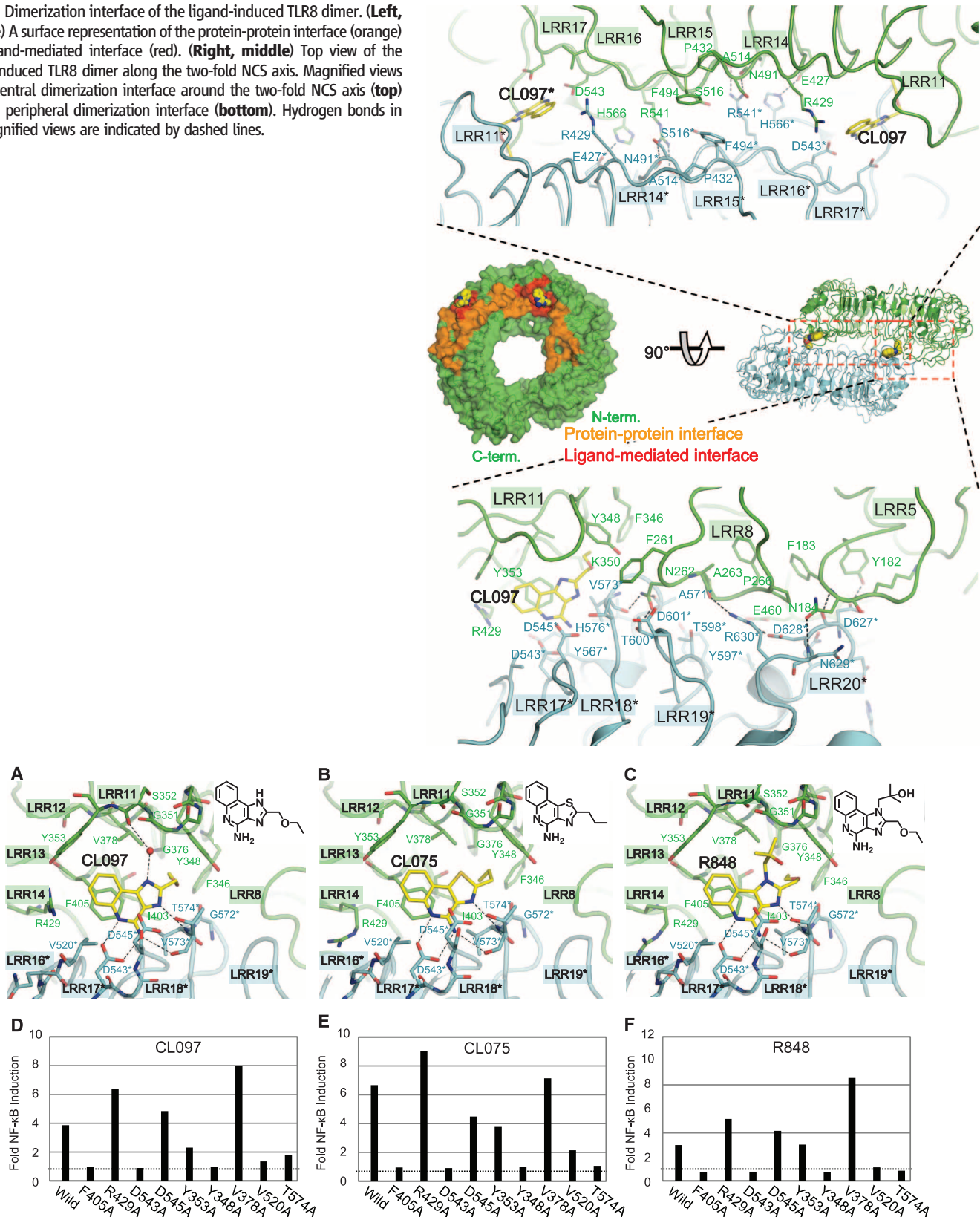


**Fig. 3.** Ligand recognition sites of TLR8. **(A), (B), and (C)** Residues involved in the interaction of TLR8 with CL097, CL075, and R848, respectively. The C atoms of the ligand molecules are yellow. Water molecules mediating the ligand recognition are indicated by red filled circles, and hydrogen bonds by dashed lines. The chemical structures of these ligands are shown at top right in each panel. **(D), (E), and (F)** NF-κB activity of human TLR8 mutants, stimulated by CL097,

CL075, and R848, respectively. The reactivity of wild type and various mutants of TLR8 were analyzed by an NF-κB-dependent green fluorescent protein reporter assay using Ba/F3 cells. Data represent the fold NF-κB induction, calculated as mean fluorescence intensity (MFI) of stimulated cells divided by MFI of nonstimulated cells. Dotted lines indicates the fold induction as 1. Data shown are representative of three independent experiments.

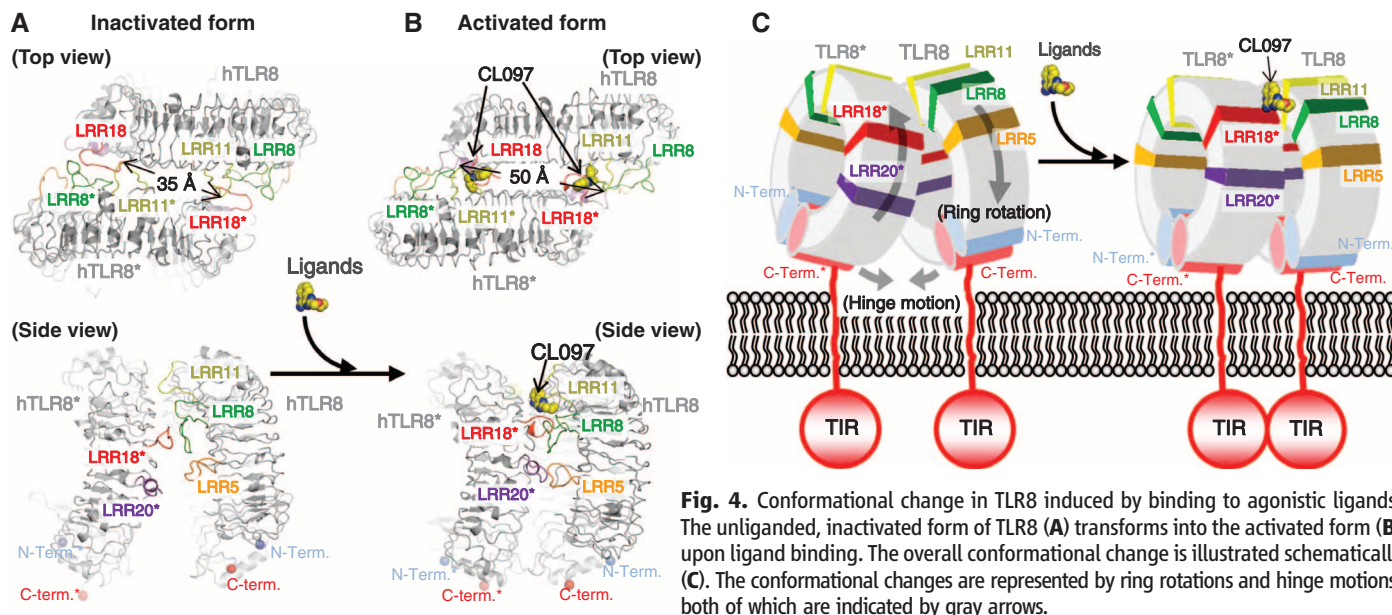


**Fig. 4.** Conformational change in TLR8 induced by binding to agonistic ligands. The unliganded, inactivated form of TLR8 (**A**) transforms into the activated form (**B**) upon ligand binding. The overall conformational change is illustrated schematically (**C**). The conformational changes are represented by ring rotations and hinge motions, both of which are indicated by gray arrows.

when the proteins were superposed (fig. S8B). The most noticeable interaction between TLR8 and these ligands was that of the benzene rings of imidazoquinoline (R848) or thiazoloquinolone (CL097, CL075) stacked on the side chain of Phe<sup>405</sup> (Fig. 3, A to C). The amidine group of the quinoline moiety formed hydrogen bonds with the side chain of Asp<sup>543</sup> with excellent geometry. The N atoms of the imidazole or thiazole moieties formed hydrogen bonds with Thr<sup>574</sup> N atoms. The 2-propyl (CL075) or 2-ethoxymethyl (CL097 and R848) substituent of these ligands protruded into the small hydrophobic pocket formed by Phe<sup>346</sup>, Tyr<sup>348</sup>, Gly<sup>376</sup>, Val<sup>378</sup>, Ile<sup>403</sup>, Phe<sup>405</sup>, Gly<sup>572</sup>, and Val<sup>573</sup>. These hydrophobic interactions may be important for the agonistic activity of chemical ligands targeting TLR8, because R837 (known as imiquimod) (fig. S9A), an imidazoquinoline compound similar to R848, specifically activates TLR7 but not TLR8 and lacks the 2-substituent in the imidazole ring. CL097 forms a water-mediated contact with the carbonyl oxygen of Ser<sup>352</sup>.

To determine the functional importance of the specific residues recognizing the chemical ligands, we mutated these residues to Ala and examined the ability of the mutant proteins to activate nuclear factor- $\kappa$ B (NF- $\kappa$ B) (Fig. 3, D to F). The Phe<sup>405</sup>, Asp<sup>543</sup>, Tyr<sup>348</sup>, Val<sup>520</sup>, and Thr<sup>574</sup> residues made contact with the ligand, and mutation of these residues to Ala either completely abolished or significantly weakened their ability to activate NF- $\kappa$ B. In contrast, mutation of other residues, including Arg<sup>429</sup>, Asp<sup>545</sup>, and Tyr<sup>553</sup>, resulted in either a retention or a slight reduction in NF- $\kappa$ B activity, which suggested that these residues are not essential for binding to the chemical ligands. NF- $\kappa$ B activity was notably up-regulated after mutation of Val<sup>378</sup> to Ala, particularly in response to R848; therefore, Val<sup>378</sup> may play a role in fine recognition or discrimination of nucleoside modifications.

Ligand binding opens up the TLR8 structure by 15 Å in the top lateral face of the LRRs, which enables the residues to recognize the ligand properly. Concomitantly, the dimerization interface is reorganized (Fig. 4). In the unliganded form, the interactions between LRR8 and LRR18\*, as well as LRR11–13 and LRR14\*–15\*, are the major contributors to formation of the dimerization interface. Upon ligand binding, the dimerization interface is rearranged; LRR8 changes its binding partner to LRR18\*–20\*, LRR18\* to LRR11, and LRR11–13 to LRR17\*–18\*. These rearranged interfaces include both the protein-protein and ligand-mediated interfaces. Concomitantly, Phe<sup>405</sup> (within LRR13), which makes a hydrophobic contact with Phe<sup>494</sup> (within LRR15\*) in the unliganded form, in turn, interacts with the ligand in the liganded form (fig. S10). In addition, the ligand-induced conformational change enables formation of new interactions between LRR5 and LRR20\*. As a result, the two C termini are brought into closer proximity, from 53 to 30 Å (CL097). The agonistic chemical ligand activates a preformed TLR8 dimer by inducing a conformational change in TLR8 ectodomains that, in turn, lead to an activated configuration of the cytoplasmic TIR signaling domains.

In conclusion, the TLR8 unliganded and liganded structures described in this study represent a milestone for understanding the signaling mechanism of the TLR7 to 9 family and will contribute to the development of therapeutic antiviral or modulating agents targeting the TLR7 to 9 subfamily.

#### References and Notes

1. C. A. Janeway Jr., R. Medzhitov, *Annu. Rev. Immunol.* **20**, 197 (2002).
2. V. Hornung et al., *J. Immunol.* **168**, 4531 (2002).
3. S. S. Diebold, T. Kaisho, H. Hemmi, S. Akira, C. Reis e Sousa, *Science* **303**, 1529 (2004).
4. F. Heil et al., *Science* **303**, 1526 (2004).
5. J. M. Lund et al., *Proc. Natl. Acad. Sci. U.S.A.* **101**, 5598 (2004).

6. J. Melchjorsen et al., *J. Virol.* **79**, 12944 (2005).
7. K. Triantafyllou et al., *Cell. Microbiol.* **7**, 1117 (2005).
8. V. Hornung et al., *Nat. Med.* **11**, 263 (2005).
9. M. Sioud, *J. Mol. Biol.* **348**, 1079 (2005).
10. J. T. Marques, B. R. Williams, *Nat. Biotechnol.* **23**, 1399 (2005).
11. M. Sioud, *Eur. J. Immunol.* **36**, 1222 (2006).
12. F. J. Barrat et al., *J. Exp. Med.* **202**, 1131 (2005).
13. T. H. Chuang, R. J. Ulevitch, *Eur. Cytokine Netw.* **11**, 372 (2000).
14. J. C. Roach et al., *Proc. Natl. Acad. Sci. U.S.A.* **102**, 9577 (2005).
15. E. Latz et al., *Nat. Immunol.* **8**, 772 (2007).
16. M. S. Jin et al., *Cell* **130**, 1071 (2007).
17. L. Liu et al., *Science* **320**, 379 (2008).
18. B. S. Park et al., *Nature* **458**, 1191 (2009).
19. J. Y. Kang et al., *Immunity* **31**, 873 (2009).
20. S. I. Yoon et al., *Science* **335**, 859 (2012).
21. M. Jurk et al., *Nat. Immunol.* **3**, 499 (2002).
22. H. Hemmi et al., *Nat. Immunol.* **3**, 196 (2002).
23. J. Lee et al., *Proc. Natl. Acad. Sci. U.S.A.* **100**, 6646 (2003).
24. F. Heil et al., *Eur. J. Immunol.* **33**, 2987 (2003).

**Acknowledgments:** The NF- $\kappa$ B luciferase reporter plasmid, pELAM1-luc, containing the human E-selectin promoter region was kindly provided by T. Muta. We thank the beamline staffs at Photon Factory and SPring-8 for their assistance with data collection. This work was supported by funding from a Japanese Ministry of Education, Culture, Sports, Science and Technology Grant-in-Aid (U.O., K.M., and T.S.), Takeda Science Foundation, and Mochida Memorial Foundation for Medical and Pharmaceutical Research (U.O.). The data presented in this manuscript are tabulated in the main paper and the supplementary materials. The coordinate and structure factor data of human TLR8 (unliganded form), TLR8-CL097, TLR8-CL075, TLR8-R848 (form1), TLR8-R848 (form2), and TLR8-R848 (form3) have been deposited to the Protein Data Bank (PDB) under the PDB IDs 3W3G, 3W3J, 3W3K, 3W3L, 3W3M, and 3W3N, respectively. We all declare that none of the authors have a financial interest related to this work.

#### Supplementary Materials

www.sciencemag.org/cgi/content/full/339/6126/1426/DC1  
Materials and Methods  
Supplementary Text  
Figs. S1 to S13  
Tables S1 to S3  
References (25–42)

22 August 2012; accepted 28 January 2013  
10.1126/science.1229159



# Export of Algal Biomass from the Melting Arctic Sea Ice

Antje Boetius,<sup>1,2,3,\*†</sup> Sebastian Albrecht,<sup>4†</sup> Karel Bakker,<sup>5†</sup> Christina Bienhold,<sup>1,2†</sup> Janine Felden,<sup>3†</sup> Mar Fernández-Méndez,<sup>1,2†</sup> Stefan Hendricks,<sup>1†</sup> Christian Katlein,<sup>1†</sup> Catherine Lalande,<sup>1†</sup> Thomas Krumpen,<sup>1†</sup> Marcel Nicolaus,<sup>1†</sup> Ilka Peeken,<sup>1,3†</sup> Benjamin Rabe,<sup>1†</sup> Antonina Rogacheva,<sup>6†</sup> Elena Rybakova,<sup>6†</sup> Raquel Somavilla,<sup>1†</sup> Frank Wenzhöfer,<sup>1†</sup> RV Polarstern ARK27-3-Shipboard Science Party†

In the Arctic, under-ice primary production is limited to summer months and is restricted not only by ice thickness and snow cover but also by the stratification of the water column, which constrains nutrient supply for algal growth. Research Vessel Polarstern visited the ice-covered eastern-central basins between 82° to 89°N and 30° to 130°E in summer 2012, when Arctic sea ice declined to a record minimum. During this cruise, we observed a widespread deposition of ice algal biomass of on average 9 grams of carbon per square meter to the deep-sea floor of the central Arctic basins. Data from this cruise will contribute to assessing the effect of current climate change on Arctic productivity, biodiversity, and ecological function.

Primary productivity in the central Arctic is limited by light and nutrients. Photosynthetically active radiation (PAR) for under-ice primary production is only available from May to August but is locally restricted by ice thickness and snow cover (1–4). Owing to stratification (5, 6), the mixed layer depth is limited to 10 to 30 m in summer (Table 1), which constrains the nutrient supply for algal growth (7). Hence, average estimates for primary production (PP) in the ice-covered central Arctic are low, on the order of 1 to 25 g C m<sup>-2</sup> year<sup>-1</sup> (8, 9). The contribution of ice algae is not well constrained, ranging from 0 to 80% (10–13). However, as a consequence of Arctic warming, primary productivity in and under the ice may be boosted by higher light transmission through thinning sea ice (3, 14, 15) and the increase in melt-pond coverage during summer (4, 16).

Assessing the consequences of current climate change in the central Arctic regions remains difficult because reliable baselines for Arctic productivity, biodiversity, and ecological function are lacking [reviewed in (17)]. During the 2012 sea-ice minimum, research vessel (RV) Polarstern visited the ice-covered eastern-central basins between 82° to 89°N and 30° to 130°E (Fig. 1). In this area, thick multiyear sea ice has been largely lost as a result of melt by atmospheric heat (18). Our airborne electromagnetic measurements confirmed that first-year ice dominated (>95%), with

an average modal thickness of less than a meter and a melt-pond cover of 30 to 40%.

Previous investigations of the underside of Arctic sea ice found that the diatom *Melosira arctica* grows meter-long filaments, anchoring in troughs and depressions under ice floes and covering up to 40 to 80% of the underside of undisturbed ice floes (12, 19–24) (Fig. 2). Warming and melting leads to their rapid sedimentation (20–23). Deposition of *Melosira* strands had been observed on the sea floor of Arctic shelves (12, 21), but their contribution to carbon export in the ice-covered basins remains unknown (25, 26). Particulate organic carbon flux to the deep sea, measured by sea-floor carbon demand (25) and

by sediment traps moored in the Amundsen Basin (27), was around 1 g C m<sup>-2</sup> year<sup>-1</sup> (>1500 m) in the 1990s, with a peak contribution of sub-ice algae of up to 28% in August (27). Repeated measurements during the first Arctic-wide sea-ice minimum in 2005–2007 showed an increased carbon flux of 6.5 g C m<sup>-2</sup> year<sup>-1</sup> (850 m), peaking in July (28).

During the expedition IceArc in summer 2012, we observed in seven out of eight regions sea-floor deposits of fresh *M. arctica* strands and other sub-ice algae at 3500- to 4400-m water depth (Fig. 1, fig. S1, and movies). Patches of algae of 1 to 50 cm in diameter covered up to 10% of the sea floor. This attracted opportunistic megafauna—such as the deep-sea holothurians *Kolga hyalina* (29) and *Elpidia heckeri* and the ophiurid *Ophiostriatus striatus*—which were observed to feed on the *Melosira* strands. Based on their color, chlorophyll *a* content, and chloroplast morphology, the freshest algal deposits were observed at the northernmost stations, 7 and 8 (>87°N). Stations 4 to 6 (82° to 85°N), north of the Laptev Sea margin, showed degraded algal deposits. In this area, megafauna biomass was substantially elevated, as was the pigment concentration of holothurian gut content (Table 1). The larger body sizes (>6 cm) and apparent fecundity of the *Kolga* population (based on gonad sizes) in this area suggested that sources of food had been available for at least 2 months and that the main algal flux had occurred before June. This matches observations of rapid melt and export of ice from the Laptev Sea as early as May 2012. By July, large open water areas had appeared within the ice zone up to 85°N (Fig. 1),

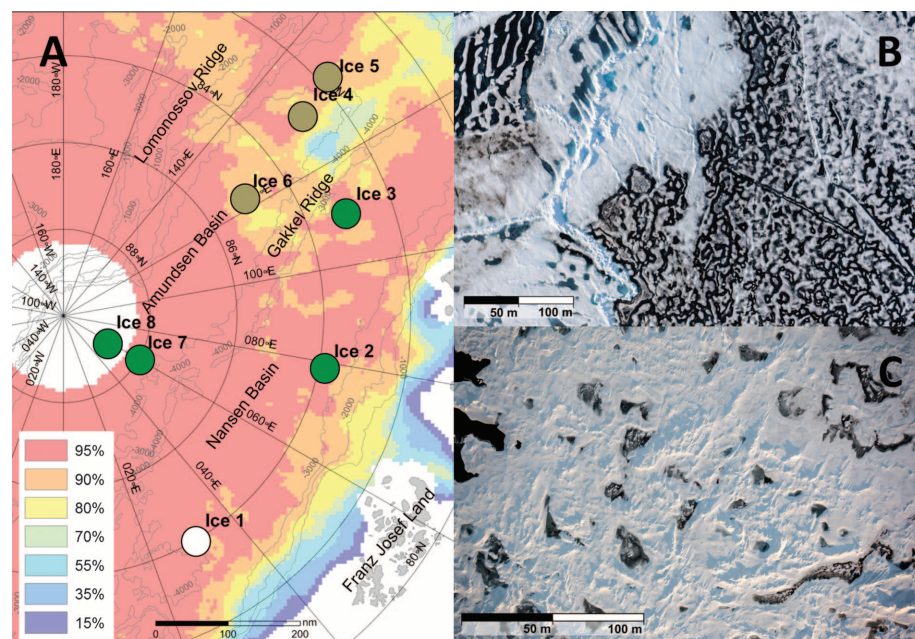


**Fig. 1.** Ice conditions during RV Polarstern Expedition IceArc (ARK27-3, 2 August to 8 October 2012). (A) Ice cover in July 2012 in percentages. Ice stations with fresh and degraded algal deposits are marked by green and brown circles, respectively. White indicates no deposits. (B) Aerial image of station 3 in mid-August. (C) Aerial image of station 6 in mid-September.

<sup>1</sup>Alfred Wegener Institute, Helmholtz Center for Polar and Marine Research, 27515 Bremerhaven, Germany. <sup>2</sup>Max Planck Institute for Marine Microbiology, 28359 Bremen, Germany. <sup>3</sup>MARUM, Center for Marine Environmental Sciences, University Bremen, 28334 Bremen, Germany. <sup>4</sup>FIELAX Gesellschaft für wissenschaftliche Datenverarbeitung mbH, 27568 Bremerhaven, Germany. <sup>5</sup>NIOZ Royal Netherlands Institute for Sea Research, 1790 AB Den Burg, Netherlands. <sup>6</sup>P. P. Shirshov Institute of Oceanology, Russian Academy of Sciences, 117997 Moscow, Russia.

\*Corresponding author. E-mail: antje.boetius@awi.de

†All authors with their contributions and affiliations appear at the end of this paper, and all other contributors are listed in the supplementary materials.

causing a rapid decline of the sea-ice cover, reflected in 1 to 2 m of melt-water content above the winter thermocline (Table 1).

Our surveys showed shreds of *M. arctica* (Table 1), indicating their melt-out earlier in the season (23). At 3500- to 4400-m depth, deposits of coiled *Melosira* strands (diameters of 5 to 12 cm) covered 0.1 to 10% of the sea floor. The carbon deposition by sub-ice algae was estimated to be equivalent to 1 to 156 g C m<sup>-2</sup> (median 9 g C m<sup>-2</sup>) (Table 1). For comparison, the 2012 pelagic new production in the same regions was estimated to be 7 to 16 g C m<sup>-2</sup> (median 11 g C m<sup>-2</sup>) (Table 1), with a contribution by diatoms of 36% based on silicate inventories (Table 1). *Melosira* strands are not used as food in the pelagial and sink rapidly to the sea floor (23). This results in a contribution of at least 45% of total primary production and >85% of carbon export in 2012.

The algal deposits at the sea floor and extracts of *Kolga* gut at stations 3, 4, 7, and 8 contained

living *Melosira* cells with green chloroplasts and lipid vesicles (Fig. 2). The algal deposits had variable high concentrations of chloroplast pigment equivalents (CPE) ( $27 \pm 21 \mu\text{g cm}^{-3}$ ;  $n = 18$  aggregate samples) and a high chlorophyll *a* to total pigment ratio ( $51 \pm 18\%$ ). In comparison, pigment contents of bare sediments next to the patches were low at  $0.8 \pm 0.3 \mu\text{g cm}^{-3}$ , matching concentrations found in the 1990s (25). The gut contents of *Kolga* specimens showed even higher pigment concentrations of, on average,  $51 \pm 47 \mu\text{g cm}^{-3}$  (Chl*a*/CPE ratio of  $41 \pm 14\%$ ;  $n = 15$  gut samples), and algae recovered from guts were still photosynthesizing when exposed to light (30).

Previous investigations focusing on oligotrophic deep-sea sediments have found a direct relationship between carbon flux, benthic biomass, and remineralization rates (31–35). However, despite the widespread deposition of algae observed in the eastern-central basins, apparently only sediment bacteria (as estimated from respi-

ration rates) (fig. S2) and large mobile megafauna had profited from the ice-algae deposition. Infauna burrows and tubes were rare, indicating an absence of the sediment-dwelling macrofauna characteristic of other deep-sea basins with seasonally sedimenting phytoplankton blooms [reviewed in (36)]. Furthermore, the bare sediments next to the algal deposits maintained oxygen fluxes of only 0.3 to 0.4 mmol O<sub>2</sub> m<sup>-2</sup> day<sup>-1</sup>, equivalent to a carbon demand of 1 to 2 g C m<sup>-2</sup> year<sup>-1</sup>. Such low rates are typical for oligotrophic deep-sea sediments (37, 38) and match carbon export fluxes measured in the 1990s in this area (25, 27). In contrast, in situ and ex situ microprofiling of diffusive oxygen fluxes into sediments covered by algal aggregates showed elevated rates of 5 to 6 mmol O<sub>2</sub> m<sup>-2</sup> day<sup>-1</sup>, equivalent to carbon fluxes of 25 g C m<sup>-2</sup> year<sup>-1</sup> (stations 7 and 8) (fig. S2). This suggests considerable microbial respiration (13 to 60%) of the algal carbon input. Accordingly, in cores covered by *Melosira* strands, oxygen penetration in the sediment was reduced to a few

**Table 1.** Distribution of algal aggregates and characteristics of sea-ice stations investigated. Methods are provided in the supplementary materials. Where available, averages and standard deviations are given. FYI, first-year ice; MYI, multiyear ice; n.d., not determined.

Ice station (no.)	1	2	3	4	5	6	7	8
Event*	PS80_224	PS80_237	PS80_255	PS80_277	PS80_323	PS80_335	PS80_349	PS80_360
Date	8/9/12	8/14/12	8/20/12	8/25/12	9/4/12	9/7/12	9/18/12	9/22/12
Latitude (N)	84°3.03'	83°59.19'	82°40.24'	82°52.95'	81°55.53'	85°06.11'	87°56.01'	88°49.66'
Longitude (E)	031°6.83'	078°6.20'	109°35.37'	130°7.77'	131° 7.72'	122°14.72'	61°13.04'	58°51.81'
Sea-ice cover (%)	80	80	70	80	60	50	100	100
Ice thickness (m)	1.0–1.2	1.2–2.0	0.7–1.2	0.7–0.9	1.2–1.7	0.9–1.7	1.2–1.8	1.1–1.8
First/multiyear ice	FYI	FYI	FYI	FYI	FYI	FYI/MYI	FYI/MYI	FYI/MYI
Melt-pond cover (%)	40	20	40	50	10	30	20	20
Drift (knots)	0.14 ± 0.1	0.35 ± 0.2	0.55 ± 0.2	0.24 ± 0.1	0.26 ± 0.1	0.29 ± 0.2	0.01 ± 0.0	0.17 ± 0.1
Surface radiation (W m <sup>-2</sup> )†	150 ± 93	97 ± 59	60 ± 38	56 ± 45	62 ± 76	26 ± 23	11 ± 6	5 ± 3
PAR under ice (W m <sup>-2</sup> )	33	5	9	n.d.	3	2	<1	<<1
Atmospheric temperature (°C)	–1.5	–1.2	0.3	–0.3	–3.3	–1.6	–3.9	–10.1
Seawater temperature (5 m, °C)	–1.5	–1.5	–1.6	–1.5	–1.5	–1.5	–1.8	–1.7
Salinity (5 m)	33.0	33.2	32.8	31.2	30.6	30.3	33.1	32.9
Mixed layer depth (m)	15	21	16	23	20	20	31	30
Melt water (m)‡	0.5	0.7	0.7	1.1	2.3	2.2	0.8	0.9
Nitrate concentration (μM, ‡0–2 m)	2.89	3.08	0.29	0.42	0.1	0.08	0.97	0.49
N:Si:N:P (‡0–2 m)	3/10	2/10	0.3/2	0.1/2	0.03/1	0.02/0.4	0.02/0.3	0.3/2
<sup>14</sup> C-PP (mg C m <sup>-2</sup> day <sup>-1</sup> )§	62	9	19	36	39	10	5	4
New PP (g C m <sup>-2</sup> year <sup>-1</sup> )‡	16	7	12	7	9	10	16	15
Diatom contribution (%)‡	40	28	32	24	n.a.	n.a.	41	40
Sub-ice algal cover (%)	0.04	0.19	<0.01	n.d.	0.04	0.03	0.55	0.13
Ice algae composition	dv. algaell	div. algaell	<i>Melosira</i>	n.d.	<i>Melosira</i>	<i>Melosira</i>	<i>Melosira</i>	<i>Melosira</i>
Sea-floor algal cover (%)	0	0.03 ± 0.04	1.3 ± 0.4	0.33 ± 0.4¶	0.5 ± 0.2¶	0.8 ± 0.6¶	2.2 ± 0.7	10.4 ± 0.5
Sediment CPE (μg cm <sup>-3</sup> )	0.7 ± 0.1	1.4 ± 0.3	1.0 ± 0.3	1.0 ± 0.4	0.7 ± 0.2	0.5 ± 0.1	0.6 ± 0.1	0.8 ± 0.5
Sediment Chl <i>a</i> /CPE ratio (%)	10	17	22	22	18	14	14	14
Megafauna biomass (g wet weight m <sup>-2</sup> )	0.42	1.01	3.36	1.07	3.19	5.49	3.46	0.33
Gut CPE (μg cm <sup>-3</sup> )	n.d.	n.d.	130 ± 20	41 ± 15	30 ± 2	3 ± 1	48 ± 12	n.d.
Gut Chl <i>a</i> /CPE ratio (%)	n.d.	n.d.	43	49	66	22	51	n.d.
Ice algae composition sediment/gut	n.d.	n.d.	<i>Melosira</i>	<i>Melosira</i>	<i>Melosira</i>	<i>Melosira</i>	<i>Melosira</i>	<i>Melosira</i>
				div. algaell	div. algaell	div. algaell		div. algaell
Ice algae C deposition (g C m <sup>-2</sup> )	0	0.5	20	5	7	11	32	156
Water depth (m)	4014	3485	3569	4161	4031	4355	4380	4374

\*Supplementary data available at <http://doi.pangaea.de/10.1594/PANGAEA.803293>.  
 †Refers to incoming global radiation at the surface.  
 ‡Estimates based on seasonal inventories of the mixed-layer depth of the previous freezing season (see supplementary materials).  
 §Depth-integrated rates for the water column euphotic zone (1% PAR under the ice).  
 ¶Diverse algae included in various ratios: *Porosira* sp., *Pleurosigma*, *Nitzschia* sp., *Fragilariopsis* sp., *Entomoneis* sp., *Chaetoceros* sp., *Navicula* sp., *Cylindrotheca*, and other chain-forming pennate diatoms.  
 ¶¶Estimates include discolored patches/degraded algal patches.



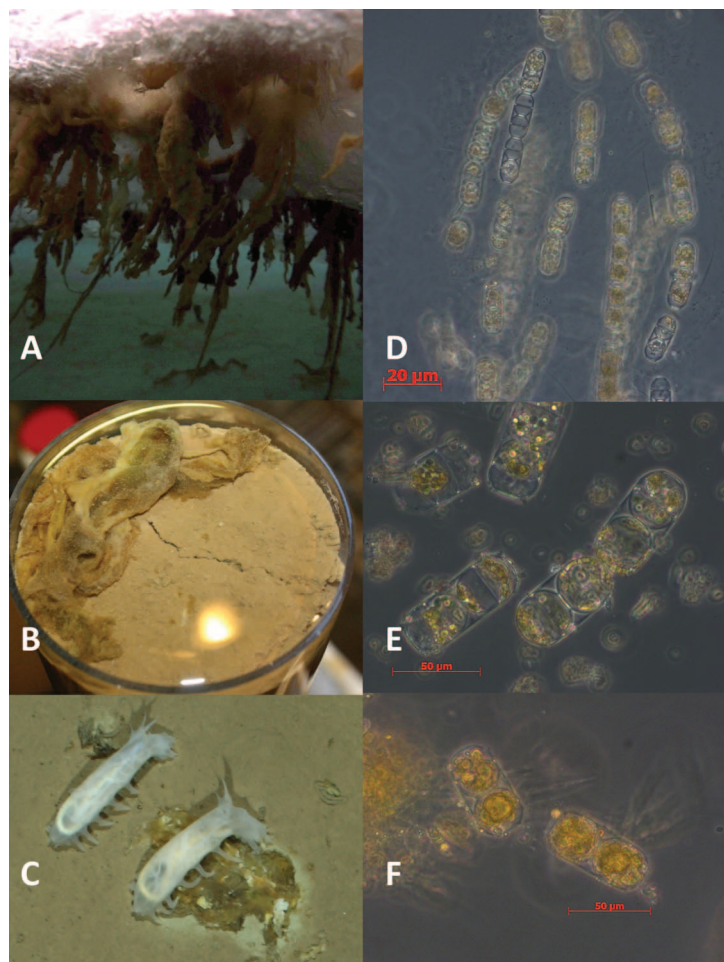


**Fig. 2.** *M. arctica* aggregations. Strands (~20 cm) of *Melosira* (A) under ice (station 7), (B) recovered from the sea floor (station 7), and (C) photographed in situ with *K. hyalina* grazing on deposits (station 3). (D to F) Microscopic images of *Melosira* cells from (A), (B), and (C) (extract of *Kolga* gut), respectively.

millimeters compared with the surrounding sediment, where oxygen penetrated >50 cm (fig. S1). Hence, if high exports of sea-ice algae had occurred regularly before 2012, oxygen penetration depth would have been less than observed, independent of the fresh *Melosira* deposits (30). Hence, we conclude that massive algal falls were rare.

Arctic climate models predict a further decline in the sea-ice cover, toward a largely ice-free summer in the Arctic in coming decades (39). Our observations support the hypothesis (14) that the current sea-ice thinning and increasing melt-pond cover may be enhancing under-ice productivity and ice-algae export, with ecological consequences from the surface ocean to the deep sea.

## References and Notes

- Cooperative Institute for Research in Environmental Sciences at the University of Colorado at Boulder, National Snow and Ice Data Center (NSIDC) Report (2012).
- S. Rysgaard, M. Kühl, R. N. Glud, J. Würdler Hansen, *Mar. Ecol. Prog. Ser.* **223**, 15 (2001).
- M. Nicolaus *et al.*, *J. Geophys. Res.* **115**, (C11), C11011 (2010).
- M. Nicolaus, C. Katlein, J. A. Maslanik, S. Hendricks, *Geophys. Res. Lett.* **39**, L24501 (2012).

- P. Bourgain, J. C. Gascard, *Deep Sea Res. Part I Oceanogr. Res. Pap.* **58**, 745 (2011).
- B. Rabe *et al.*, *Deep Sea Res. Part I Oceanogr. Res. Pap.* **58**, 173 (2011).
- J. E. Tremblay, J. Gagnon, in *Influence of Climate Change on the Arctic and Subarctic Conditions*, J. C. J. Nihoul, A. G. Kostianoy, Eds. (Springer Science Business Media B.V., Dordrecht, Netherlands, 2009), pp. 73–93.
- K. R. Arrigo, G. van Dijken, S. Pabi, *Geophys. Res. Lett.* **35**, L19603 (2008).
- P. Wassmann, D. Slagstad, I. Ellingsen, *Polar Biol.* **33**, 1641 (2010).
- E. N. Hegseth, *Polar Res.* **17**, 113 (1998).
- L. Legendre *et al.*, *Polar Biol.* **12**, 429 (1992).
- P. Wassmann *et al.*, *Prog. Oceanogr.* **71**, 232 (2006).
- M. Gosselin, M. Levasseur, P. A. Wheeler, R. A. Horner, B. C. Booth, *Deep Sea Res. Part II Top. Stud. Oceanogr.* **44**, 1623 (1997).
- K. R. Arrigo *et al.*, *Science* **336**, 1408 (2012).
- C. J. Mundy *et al.*, *Geophys. Res. Lett.* **36**, L17601 (2009).
- A. Rösel, L. Kaleschke, *J. Geophys. Res.* **117**, C05018 (2012).
- P. Wassmann, C. M. Duarte, S. A. Agustí, M. L. K. Sejor, *Glob. Change Biol.* **17**, 1235 (2011).
- J. Maslanik, J. Stroeve, C. Fowler, W. Emery, *Geophys. Res. Lett.* **38**, L13502 (2011).
- F. Nansen, *Northern Waters: Captain Roald Amundsen's Oceanographic Observations in the Arctic Seas in 1901* (Videnskabs-Selskabets Skrifter 1, Matematisk-Naturvidenskabelig Klasse 1, Kristiania, Norway, 1906).
- I. Melnikov, *The Arctic Sea Ice System* (Gordon and Breach Science Publishers, Amsterdam, 1997).
- W. G. Ambrose Jr., C. Quillfeldt, L. M. Clough, P. V. R. Tilney, T. Tucker, *Polar Biol.* **28**, 784 (2005).

- I. A. Melnikov, L. L. Bondarchuk, *Oceanology (Mosc.)* **27**, 233 (1987).
- E. E. Syvertsen, *Polar Res.* **10**, 277 (1991).
- J. Gutt, *Polar Biol.* **15**, 247 (1995).
- A. Boetius, E. Damm, *Deep Sea Res. Part I Oceanogr. Res. Pap.* **45**, 239 (1998).
- M. Klages *et al.*, in *The Arctic Organic Carbon Cycle*, R. Stein, R. W. Macdonald, Eds. (Springer, Heidelberg, 2003), pp. 139–167.
- K. Fahl, E. Nöthig, *Deep Sea Res. Part I Oceanogr. Res. Pap.* **54**, 1256 (2007).
- C. Lalonde, S. Belanger, L. Fortier, *Geophys. Res. Lett.* **36**, L21604 (2009).
- A. Rogacheva, *J. Mar. Biol. Assoc. U.K.* **92**, 1183 (2012).
- Materials and methods are available as supplementary materials on Science Online.
- B. D. Wigham, P. A. Tyler, D. S. M. Billett, *J. Mar. Biol. Assoc. U. K.* **83**, 175 (2003).
- J. W. Deming, P. L. Yager, in *Deep-Sea Food Chains and the Global Carbon Cycle*, G. T. Rowe, V. Pariente, Eds. (Kluwer Academic, Dordrecht, Netherlands, 1992), pp. 11–28.
- H. A. Ruhl, J. A. Ellena, K. L. Smith Jr., *Proc. Natl. Acad. Sci. U.S.A.* **105**, 17006 (2008).
- C.-L. Wei *et al.*, *PLoS ONE* **5**, e15323 (2010).
- U. Witte *et al.*, *Nature* **424**, 763 (2003).
- A. G. Glover *et al.*, *Adv. Mar. Biol.* **58**, 1 (2010).
- F. Wenzhöfer, R. N. Glud, *Deep Sea Res. Part I Oceanogr. Res. Pap.* **49**, 1255 (2002).
- J. P. Fischer, T. G. Ferdelman, S. D'Hondt, H. Roy, F. Wenzhöfer, *Biogeosciences* **6**, 1467 (2009).
- M. Y. Wang, J. E. Overland, *Geophys. Res. Lett.* **36**, L07502 (2009).

**Acknowledgments:** We thank the captain and crew of RV Polarstern expedition IceArc (ARK27-3) as well as our helicopter and meteorology teams for their excellent support with work at sea. This study was funded by the PACES (Polar Regions and Coasts in a Changing Earth System) program of the Helmholtz Association. Additional funds were made available to A.B. by the European Research Council Advanced Investigator grant 294757 and the Leibniz program of the Deutsche Forschungsgemeinschaft, and to B.R. for the Bundesministerium für Bildung, Wissenschaft, Forschung und Technologie project 03F0605E. Supplementary data are available at <http://doi.pangaea.de/10.1594/PANGAEA.803293>.

## Affiliations and contributions of the RV Polarstern ARK27-3-Shipboard Science Party

Writing team: Antje Boetius<sup>1,2,3</sup> with all coauthors. Ice physics and remotely operated vehicle (ROV) surveys: Stefan Hendricks,<sup>1</sup> Christian Katlein,<sup>1</sup> Thomas Krumpen,<sup>1</sup> Marcel Nicolaus<sup>1</sup>; Sea-ice biology: Mar Fernández-Méndez,<sup>1,2</sup> Ilka Peeken<sup>1,3</sup>; Oceanography and nutrients: Karel Bakker,<sup>5</sup> Catherine Lalonde,<sup>1</sup> Benjamin Rabe,<sup>1</sup> Raquel Somavilla<sup>1</sup>; Deep-sea surveys, sampling and measurements: Sebastian Albrecht,<sup>4</sup> Christina Bienhold,<sup>1</sup> Antje Boetius,<sup>1</sup> Janine Felden,<sup>1</sup> Antonina Rogacheva,<sup>6</sup> Elena Rybakova,<sup>6</sup> Frank Wenzhöfer

Fieldwork and scientific discussions: Shipboard Scientific Party, including other contributors listed in the supplementary materials. <sup>1</sup>Alfred Wegener Institute, Helmholtz Center for Polar and Marine Research, 27515 Bremerhaven, Germany. <sup>2</sup>Max Planck Institute for Marine Microbiology, 28359 Bremen, Germany. <sup>3</sup>MARUM, Center for Marine Environmental Sciences, University Bremen, 28334 Bremen, Germany. <sup>4</sup>FIELAX Gesellschaft für wissenschaftliche Datenverarbeitung mbH, 27568 Bremerhaven, Germany. <sup>5</sup>NIOZ Royal Netherlands Institute for Sea Research, 1790 AB Den Burg, Netherlands. <sup>6</sup>P. P. Shirshov Institute of Oceanology, Russian Academy of Sciences, 117997 Moscow, Russia.

## Supplementary Materials

[www.sciencemag.org/cgi/content/full/science.1231346/DC1](http://www.sciencemag.org/cgi/content/full/science.1231346/DC1)  
Materials and Methods  
Figs. S1 and S2  
Movies S1 and S2  
References (40–50)

10 October 2012; accepted 31 January 2013  
Published online 14 February 2013;  
10.1126/science.1231346

# Geometric Catalysis of Membrane Fission Driven by Flexible Dynamin Rings

Anna V. Shnyrova,<sup>1\*</sup> Pavel V. Bashkurov,<sup>2\*</sup> Sergey A. Akimov,<sup>2,3</sup> Thomas J. Pucadyil,<sup>4</sup> Joshua Zimmerberg,<sup>5</sup> Sandra L. Schmid,<sup>6</sup> Vadim A. Frolov<sup>1,7†</sup>

Biological membrane fission requires protein-driven stress. The guanosine triphosphatase (GTPase) dynamin builds up membrane stress by polymerizing into a helical collar that constricts the neck of budding vesicles. How this curvature stress mediates nonleaky membrane remodeling is actively debated. Using lipid nanotubes as substrates to directly measure geometric intermediates of the fission pathway, we found that GTP hydrolysis limits dynamin polymerization into short, metastable collars that are optimal for fission. Collars as short as two rungs translated radial constriction to reversible hemifission via membrane wedging of the pleckstrin homology domains (PHDs) of dynamin. Modeling revealed that tilting of the PHDs to conform with membrane deformations creates the low-energy pathway for hemifission. This local coordination of dynamin and lipids suggests how membranes can be remodeled in cells.

Cellular membranes can merge (fusion) or split apart (fission) without compromising their barrier function. This requires lipids to form localized, transient, nonbilayer structures to initiate topological transition (1–4), which in structurally stable lipid bilayers requires the application of membrane stresses (5, 6). Dynamin, the paradigmatic member of a superfamily of guanosine triphosphatases (GTPases) involved in membrane fusion and fission (7–9), produces curvature stress by radial constriction of the necks of endocytic vesicles (7). Fission follows constriction if the membrane curvature approaches a critical level sufficient to trigger spontaneous lipid rearrangements (3, 6, 7). Structural analyses of long dynamin helices suggest several possible conformational changes and/or remodeling modes capable of converting the GTP energy into strong membrane constriction (10–14). However, both in vivo and in vitro, dynamin operates in small and transient units (6, 15, 16). It remains uncertain whether plain radial constriction could support timely and nonleaky fission at these time and length scales. We hypothesized that tighter coordination between protein conformation and lipid rearrangements would be required to find an optimal trajectory of membrane remodeling.

To test this hypothesis, we analyzed the progression of membrane fission produced by dynamin-1

(hereafter, dynamin) on lipid nanotubes (NTs) pulled from lipid bilayers (17). On long 4- to 20- $\mu$ m fluorescently labeled NTs, dynamin [0.5 to 4  $\mu$ M (17)] polymerized into cylindrical scaffolds that expelled both membrane and luminal fluorescence, thus constricting the NTs (Fig. 1A, B). In the presence of 1 mM GTP, such constrictions were followed by fission (movies S1 and S2). Before fission, GTP promoted stochastic disassembly of the growing dynamin scaffolds (Fig. 1C and movies S1 to S3) (6, 16). However, in the assembled state, the average membrane constriction was similar with and without GTP (Fig. 1D and fig. S1). Thus, instead of increasing the average NT constriction (Fig. 1D and fig. S1) (6), GTP hydrolysis fueled dynamin reassembly cycles, seen as large oscillations of the length and position of individual dynamin scaffolds on NTs (Fig. 1, E and F, and fig. S2). These oscillations were also evident in fluctuations of the ionic permeability (conductance  $G_n$ , Fig. 2A) of the lumen of short 80- to 250-nm NTs (6). Although submicrometer scaffolds were sufficient to sever long NTs (movie S4), such small scaffolds underwent further disassembly to produce fission of short NTs (Fig. 2A), confirming that dynamin fission activity is localized to the nanoscale.

To quantify nanoscale fission events, we determined the radius ( $R_{NT}$ ), length ( $L_{NT}$ ), and elastic resistance of short cylindrical NTs (figs. S3 and S4) (17) and used these to calculate the NT constriction parameters from changes in  $G_n$ . Without GTP, dynamin produced stepwise decreases in  $G_n$  (Fig. 2B). This intermittent NT constriction implied either the formation of self-limited dynamin collars [e.g., rings (18)] and/or lipid resistance coming from swelling of the NT between dynamin scaffolds [figs. S2 and S5 (12–14, 19)]. However, the final steady-state conductance  $G_n^f$  (Fig. 2B) indicated a uniformly constricted cylindrical NT (6). Its luminal radius,  $R_{Dyn}$ , was calculated using Ohm's law:  $R_{Dyn} = R_{NT} \sqrt{G_n^f/k_D}$  [where  $k_D$  is the Debye correction (17)], yielding  $R_{Dyn} = 1.9 \pm 0.3$  nm ( $n = 13$  NTs).  $R_{Dyn}$  did not

depend on  $L_{NT}$  (fig. S6A), confirming uniform constriction. Considering dynamin scaffolds as cylinders creating similar membrane curvature with or without GTP (Fig. 1D), the length of elementary scaffolds ( $L_s$ ) producing conductance steps and oscillations could be calculated from  $\Delta G_n$  (Fig. 2, A and B) using the following equation (17)

$$\Delta(1/G_n) = L_s[(R_{NT}/R_{Dyn})^2/k_D - 1]/L_{NT} \quad (1)$$

Cumulative distribution of  $L_s$  (Fig. 2C) demonstrated that the scaffolds were substantially shorter in the presence of GTP than in its absence, and even shorter at the moment of fission ( $\Delta G_n^{fission}$ , Fig. 2A). Thus, GTP hydrolysis stimulated the optimization of the scaffold length for membrane fission.

All three distributions of scaffold lengths (Fig. 2C) showed a clear cutoff at  $L_s^{min} \approx 20$  nm [readily distinguishable from background noise (fig. S7)], implying a “minimal” dynamin unit capable of constricting NTs and causing their fission. Assuming that the smallest conductance jumps measured in the presence of GTP were made by this minimal scaffold, we applied linear regression of  $\Delta(1/G_n)$  on  $R_{NT}^2$  using Eq. 1 with  $L_s = L_s^{min}$ . Such a fit (Fig. 2D) recovered  $L_s^{min} = 25 \pm 7$  nm and  $R_{Dyn} = 1.9 \pm 0.4$  nm, confirming that the shortest scaffolds imposed the same local curvature with and without GTP. Because the pitch of a dynamin helix is  $\sim 10$  nm (7, 10, 14), fission required at least a two-rung dynamin scaffold, with two- to three-rung units mediating  $\sim 80\%$  of fission events (Fig. 2C).

In 10% of the fission events, the initial closure of the NT lumen was reversible. As the flickering fission pores in cellular systems (20, 21), the NTs switched between “open” and “closed” states (Fig. 3A). The latter apparently corresponded to hemifission, because GTP hydrolysis rendered dynamin scaffolds metastable and incapable of withstanding membrane tension so that, upon fission, the NT rapidly retracted into the lipid bilayer reservoir (Fig. 3B and movie S5) (6, 16, 22). In the absence of GTP, stable dynamin scaffolds inhibited NT retraction (Fig. 3B and movie S6). The observed flicker was much faster (tens of milliseconds, Fig. 3A) than both the GTP hydrolysis cycle [ $k_{cat} \sim 2$  s<sup>-1</sup> (23, 24)] and the reassembly of dynamin (seconds, Fig. 2A). Thus, flicker was not caused by cooperative transformations of dynamin helices associated with GTPase activity [such as constriction, extension, or twisting (11, 18, 22, 25)] or by the reassembly of dynamin scaffolds. Indeed, the open state was characterized by a preset conductance level (Fig. 3A), indicating that the flickering NT was constrained within a short dynamin scaffold of fixed geometry. Such two- to three-rung collars act as metastable catalytic centers mediating transitions between a constricted neck and hemifission, two main intermediates of fission.

We next explored the molecular basis for hemifission catalysis, focusing on the membrane-

<sup>1</sup>Biophysics Unit (CSIC, UPV/EHU) and Department of Biochemistry and Molecular Biology, University of the Basque Country, Leioa, Spain. <sup>2</sup>A. N. Frumkin Institute of Physical Chemistry and Electrochemistry, Russian Academy of Sciences, Moscow 119071, Russia. <sup>3</sup>National University of Science and Technology “MISIS”, Moscow 119049, Russia. <sup>4</sup>Indian Institute of Science Education and Research, Pune, India. <sup>5</sup>Program in Physical Biology, Eunice Kennedy Shriver National Institute of Child Health and Human Development, National Institutes of Health, Bethesda, MD 20892, USA. <sup>6</sup>Department of Cell Biology, University of Texas Southwestern Medical Center, Dallas, TX, USA. <sup>7</sup>IKERBASQUE, Basque Foundation for Science, Bilbao, Spain.

\*These authors contributed equally to this work.

†Corresponding author. E-mail: vadim.frolov@ehu.es



interacting interface of the dynamin collar formed by pleckstrin homology domains (PHDs) (7, 14). The Ile → Ala (I533A) mutation in the membrane-inserting variable loop 1 (VL1) of PHD suppresses fission without altering dynamin's polymerization or GTPase activity (26, 27). The mutant (I533A) and wild-type (WT) dynamins produced similar changes in  $G_n$ , both with and without GTP (Fig. 3C, D). Thus, I533A formed short metastable collars imposing the same curvature stress as the

WT. However, in the presence of GTP, I533A failed to produce hemifission or fission in seven out of eight trials, 150 s of observation each, whereas the WT severed 24 of 25 short NTs in  $33.6 \pm 4.6$  s after its addition to NTs. Thus, hemifission catalysis requires membrane wedging of PHDs in the metastable collar.

The hemifission intermediate has a distinct hourglass ("stalk") shape (3, 7), dramatically different from the cylindrical shape of constricted

NTs. On cylindrical NTs, PHD pairs in each rung of a dynamin collar form a long pedestal oriented along the NT axis [Fig. 4A and fig. S8 (7)]. For hemifission to occur, lipids must either detach from or move together with the PHDs. Simultaneous detachment from tens of PHDs in the rung is energetically improbable (17). Furthermore, the fission capability of I533A increased with phosphatidylinositol 4,5-phosphate [PI(4,5)P<sub>2</sub>] content, indicating that tighter adhesion

**Fig. 1.** GTP hydrolysis causes stochastic disassembly and softening of dynamin scaffolds. (A and B) In the absence of GTP, dynamin scaffolds (labeled with dynamin-Alexa488, green) constrict lipid nanotubes. The constriction causes a proportional decrease of membrane (labeled with Rh-PE, red) and luminal (labeled with 3-kD dextran-Alexa488, blue) fluorescence. Scale bars, 5  $\mu$ m. (C) Time sequence (0.5 s between frames, 2 s after dynamin addition) illustrating the development of membrane constriction (Rh-PE fluorescence decrease) with and without 1 mM GTP. Scale bars, 1  $\mu$ m. (D) Mean fluorescence intensities of Rh-PE of constricted parts of the NTs ( $F_{\text{NT}}^{\text{NT}}$ ), normalized to the initial fluorescence intensities of the NTs before dynamin application ( $F_{\text{NT}}^{\text{NT}_0}$ ) with and without GTP ( $n = 4$  scaffolds, error bars show standard deviation) (fig. S1). (E) Three-dimensional kymographs showing the steady-state behavior of dynamin scaffolds constricting NTs in the presence and absence of GTP. Rh-PE fluorescence is shown; the darker regions correspond to higher constriction (curvature). (F) Variations of the length of dynamin scaffolds ( $L_s$ ) in the steady state [as in (E)], normalized to the mean length for each scaffold ( $<L_s>$ ).

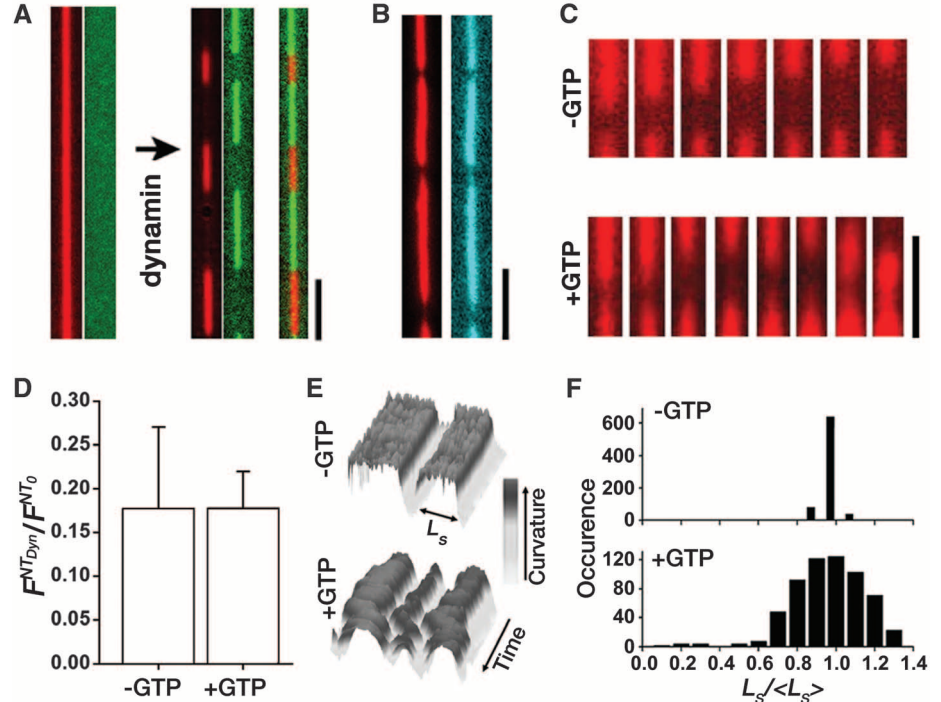
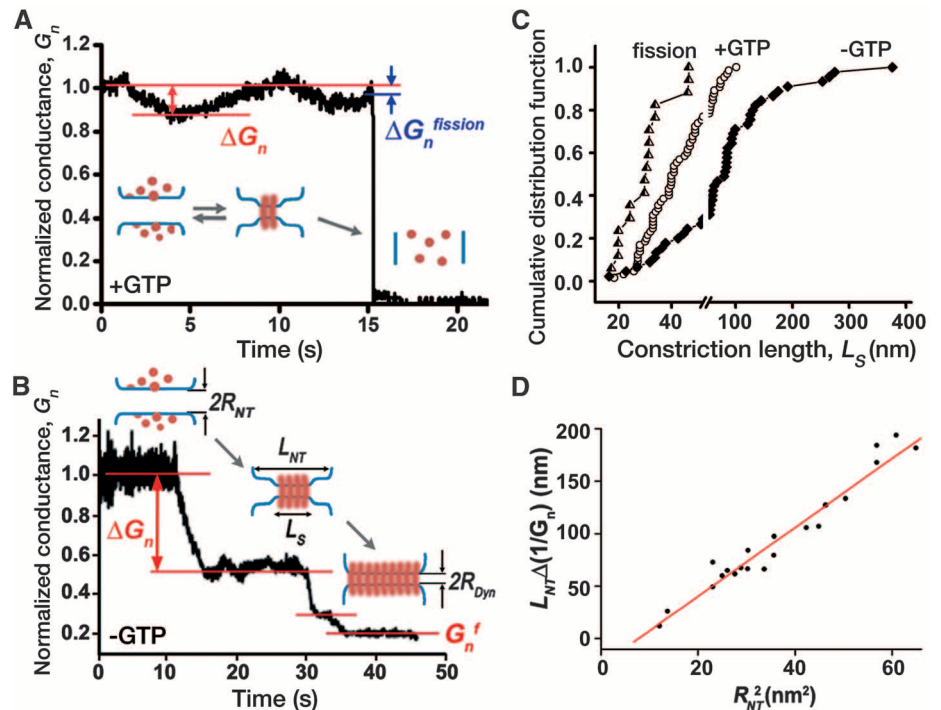


**Fig. 2.** A two-rung dynamin scaffold is the minimal fission unit. (A) Oscillations of the NT conductance [ $G_n$  normalized to the NT conductance before dynamin addition (17)] followed by fission (an acute decrease of  $G_n$ ) produced by dynamin applied at time ( $t = 0$ ) in the presence of 1 mM GTP. The cartoons illustrate reassembly of the dynamin scaffold during oscillations and NT fission. (B) Stepwise constriction of NT by dynamin applied at  $t = 0$  in the absence of GTP. The cartoons show the evolution of the dynamin scaffold during constriction. (C) Cumulative distribution functions of the length of the dynamin scaffold ( $L_s$ ) recalculated from the conductance steps ( $\Delta G_n$ ), measured as shown in (B) for "−GTP" ( $n = 13$  NTs) and (A) for "+GTP" ( $n = 22$  NTs) and "fission" ( $n = 17$  NTs). (D) Linear regression of  $\Delta(1/G_n)$  on  $(R_{\text{NT}})^2$ ,  $L_s^{\text{min}}$ , and  $R_{\text{DYN}}^2$  define the intercept and slope (Eq. 1),  $P < 0.001$ .



between PHDs and lipids promotes fission (fig. S9). Finally, flicker was much faster than dynamin detachment from the membrane [seconds (26)], indicating that PHDs can quickly adapt their position to lipids (Fig. 4A). Analyzing the possibility of PHD tilting theoretically, we found that the combination of tilting and membrane insertion promoted otherwise energetically unfavorable hemifission transformation (17). PHD pairs assembled into membrane-inserting ring(s) were

modeled, and the shallow insertion was parameterized by its width  $H_i$  in the axial direction (Fig. 4A) (17). Without tilt, the energy barrier for hemifission remained high even for large  $H_i$  (Fig. 4B). With tilt, the barrier decreased steeply with increasing  $H_i$  (Fig. 4B, C), explaining the impaired fission efficiency of I533A. For  $H_i = 1$  nm, the barrier became effectively zero for the two-ring system, revealing the soft deformation mode potentially responsible for fast flicker transitions

(Fig. 3A). Independent of  $H_i$ , the two-ring geometry remained optimal for fission, although PHD tilting significantly promoted fission mediated by a single ring or at the edge of a rigid dynamin scaffold (Fig. 4, A and C) (28). Thus, the kinetics of fission appear to be determined by the extent of membrane wedging by PHDs and the number of PHDs simultaneously available for tilting upon GTP hydrolysis, a stochastic function of the hydrolysis rate.

**Fig. 3.** Reversible hemifission is catalyzed by membrane wedging of PHDs. (A) Rapid switching (flicker) of the NT conductance between the open and closed states. The inset shows an example of a short-lived closed state. (B) In the presence of GTP (left), the multiple dynamin-Alexa488 scaffolds disassemble concomitant with NT retraction (movies S3 and S4). Without GTP (right), the scaffolds withstand membrane tension. Scale bars, 10  $\mu$ m. (C) Changes of  $G_n$  produced by I533A dynamin applied at  $t = 0$  in the presence (blue) and absence (red) of 1 mM GTP. (D) The mean luminal radius measured in the absence of GTP (open bars) and the mean length of protein scaffolds in the presence of 1 mM GTP (solid bars) for WT and I533A dynamins. Differences are statistically insignificant ( $P > 0.25$ ).

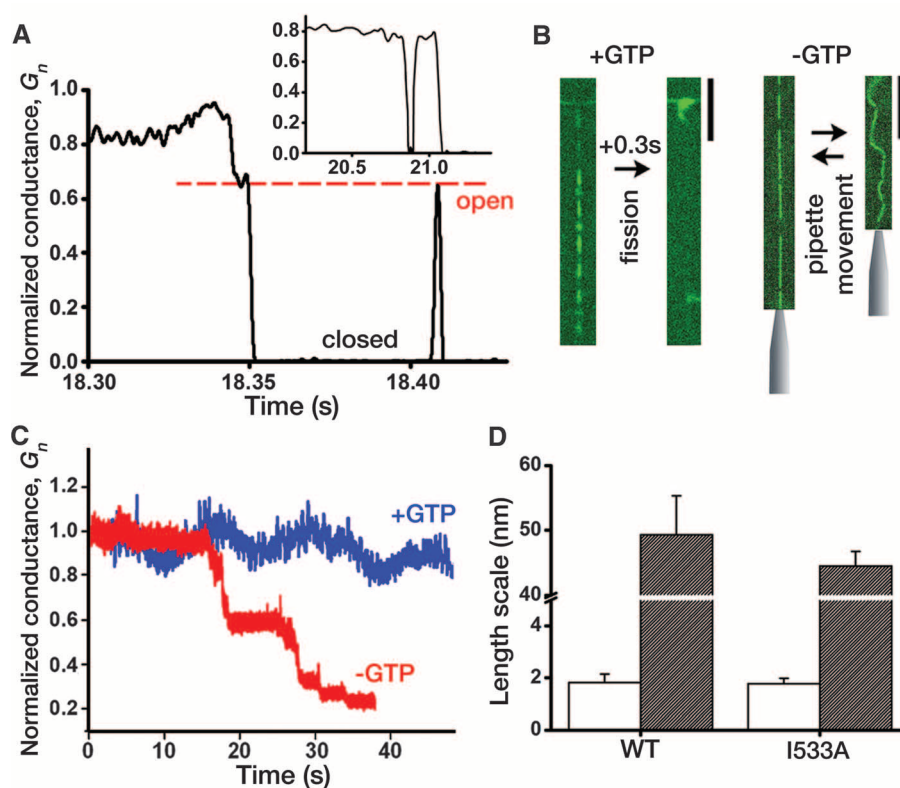
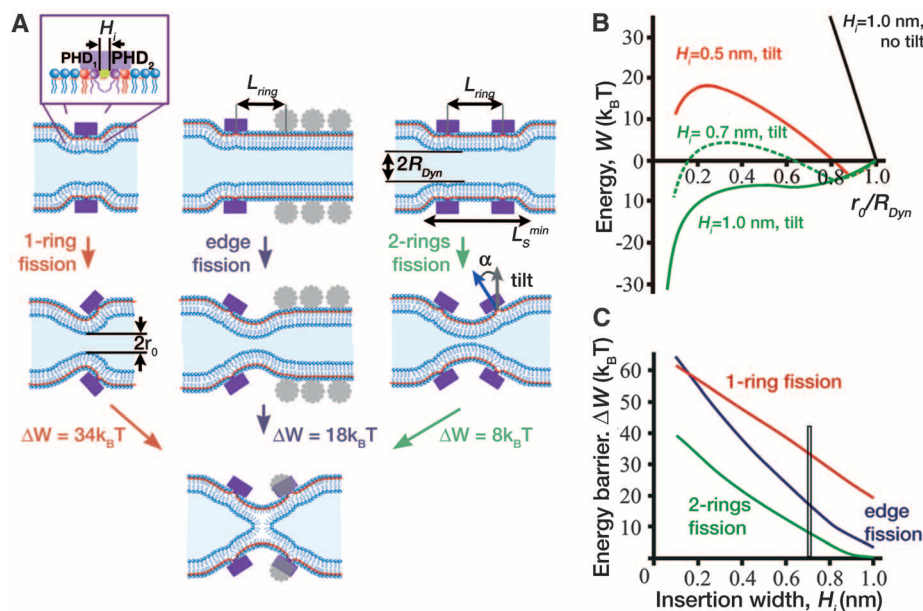


**Fig. 4.** Geometric catalysis of hemifission by dynamin rings. (A) Cartoon illustrating the coupling of PHD tilting (parameterized by the tilt angle  $\alpha$ ) with local narrowing of the NT (parameterized by the radius  $r_0$ ) during the transition from the cylindrical constricted state (parameterized by  $R_{dyn}$ ) to hemifission. The narrowing beneath a single flexible PHD ring (left) is further assisted by an adjacent rigid scaffold (middle) or a second flexible ring (right),  $L_{ring} = 12$  nm (the pitch of dynamin helix). The narrowing results in a significant decrease of the energy barrier ( $\Delta W$ ) to hemifission. The enlargement shows the two-PHD module (fig. S8) with shallow membrane insertion ( $H_i$ ) displacing the neighbor lipids.  $\Delta W$  values are for  $H_i = 0.7$  nm, corresponding to the rectangle in (C).  $k_B$  is the Boltzmann constant;  $T$  is absolute temperature. (B) Relative change of the NT elastic energy along the hemifission path (fig. S10), parameterized as  $r_0/R_{dyn}$  and calculated for different  $H_i$ . Zero energy corresponds to a narrowed cylindrical NT. When tilting is allowed for  $H_i = 0.7$  nm, it results in an initial spontaneous narrowing (fig. S10), followed by hemifission transition requiring additional energy  $\Delta W$ . For  $H_i = 1$  nm, hemifission becomes spontaneous. (C) Dependence of  $\Delta W$  on  $H_i$  for the geometries shown in (A).





Here we have shown that membrane fission can be driven by short and metastable dynamin collars formed during the transition state of the GTP hydrolysis cycle. These collars not only apply elastic stress (mechanochemical effects) but also, in a synergistic coordination with lipids, participate in the search for the optimal pathway of membrane rearrangements (catalytic effects) (7). This nanoscale coordination between the geometry of the protein scaffold, concerted membrane wedging, and membrane deformations define “geometric catalysis,” which yields a distinct low-energy pathway to hemifission (fig. S10). Without GTP, dynamin forms stable polymers that constrain highly curved membrane structures, thereby effectively inhibiting topological transitions (29), just as tighter substrate binding inhibits enzymatic catalysis. Hence our finding revises the general role of proteins as force drivers in membrane fission: Besides applying energy and stress, they can dynamically adapt to membrane deformations, providing a structural rationale for protein regulatory and catalytic function in membrane remodeling.

# References and Notes

1. V. A. Frolov, A. V. Shnyrova, J. Zimmerberg, *Cold Spring Harb. Perspect. Biol.* **3**, a004747 (2011).
2. V. A. Frolov, J. Zimmerberg, *FEBS Lett.* **584**, 1824 (2010).

3. M. M. Kozlov, H. T. McMahon, L. V. Chernomordik, *Trends Biochem. Sci.* **35**, 699 (2010).
4. S. L. Leikin, M. M. Kozlov, L. V. Chernomordik, V. S. Markin, Y. A. Chizmadzhev, *J. Theor. Biol.* **129**, 411 (1987).
5. L. Yang, H. W. Huang, *Science* **297**, 1877 (2002).
6. P. V. Bashkurov *et al.*, *Cell* **135**, 1276 (2008).
7. S. L. Schmid, V. A. Frolov, *Annu. Rev. Cell Dev. Biol.* **27**, 79 (2011).
8. G. J. Praefcke, H. T. McMahon, *Nat. Rev. Mol. Cell Biol.* **5**, 133 (2004).
9. S. M. Ferguson, P. De Camilli, *Nat. Rev. Mol. Cell Biol.* **13**, 75 (2012).
10. Y. J. Chen, P. Zhang, E. H. Egelman, J. E. Hinshaw, *Nat. Struct. Mol. Biol.* **11**, 574 (2004).
11. M. H. Stowell, B. Marks, P. Wigge, H. T. McMahon, *Nat. Cell Biol.* **1**, 27 (1999).
12. K. Faelber *et al.*, *Nature* **477**, 556 (2011).
13. M. G. Ford, S. Jenni, J. Nunnari, *Nature* **477**, 561 (2011).
14. J. S. Chappie *et al.*, *Cell* **147**, 209 (2011).
15. A. L. Mattheyses, C. E. Atkinson, S. M. Simon, *Traffic* **12**, 1394 (2011).
16. T. J. Pucadyil, S. L. Schmid, *Cell* **135**, 1263 (2008).
17. Materials and methods are available as supplementary materials on Science Online
18. J. E. Hinshaw, S. L. Schmid, *Nature* **374**, 190 (1995).
19. R. Shlomovitz, N. Gov, A. Roux, *New J. Phys.* **13**, 065008 (2011).
20. V. A. Frolov, V. A. Lizunov, A. Y. Dunina-Barkovskaya, A. V. Samsonov, J. Zimmerberg, *Proc. Natl. Acad. Sci. U.S.A.* **100**, 8698 (2003).
21. E. Suss-Toby, J. Zimmerberg, G. E. Ward, *Proc. Natl. Acad. Sci. U.S.A.* **93**, 8413 (1996).

22. A. Roux, K. Uyhazi, A. Frost, P. De Camilli, *Nature* **441**, 528 (2006).
23. B. D. Song, S. L. Schmid, *Biochemistry* **42**, 1369 (2003).
24. T. J. Pucadyil, *Curr. Top. Membr.* **68**, 33 (2011).
25. D. Danino, K. H. Moon, J. E. Hinshaw, *J. Struct. Biol.* **147**, 259 (2004).
26. R. Ramachandran, S. L. Schmid, *EMBO J.* **27**, 27 (2008).
27. R. Ramachandran *et al.*, *Mol. Biol. Cell* **20**, 4630 (2009).
28. S. Morlot *et al.*, *Cell* **151**, 619 (2012).
29. E. Boucrot *et al.*, *Cell* **149**, 124 (2012).

**Acknowledgments:** We are grateful to J. Rizo-Rey and P. Kuzmin for critical reading of the manuscript. This work was in part supported by Spanish Ministry of Economy and Competitiveness grant BFU2012-34885 (V.A.F.); the Basque Government Program Etorrek, grant IE12-332 (V.A.F.); Russian Foundation for Basic Research grant 11-04-02087 (P.V.B.); the Russian Academy of Science program “Molecular and Cell Biology” (P.V.B. and S.A.A.); the Ministry of Education and Science of the Russian Federation, grant 14.740.11.1409 (P.V.B.); the Intramural Program of the National Institute of Child Health and Human Development (J.Z.); and NIH grant GM42455 (S.L.S.). Additional data are presented in the supplementary materials.

# Supplementary Materials

www.sciencemag.org/cgi/content/full/339/6126/1433/DC1

Materials and Methods

Supplementary Text

Figs. S1 to S10

Movies S1 to S6

References (30–39)

11 December 2012; accepted 28 January 2013

10.1126/science.1233920

# RNA Helicase DDX3 Is a Regulatory Subunit of Casein Kinase 1 in Wnt-β-Catenin Signaling

Cristina-Maria Cruciat,<sup>1\*</sup> Christine Dolde,<sup>1\*</sup> Reinoud E. A. de Groot,<sup>2</sup> Bisei Ohkawara,<sup>1†</sup> Carmen Reinhard,<sup>1</sup> Hendrik C. Korswagen,<sup>2</sup> Christof Niehrs<sup>1,3‡</sup>

Casein kinase 1 (CK1) members play key roles in numerous biological processes. They are considered “rogue” kinases, because their enzymatic activity appears unregulated. Contrary to this notion, we have identified the DEAD-box RNA helicase DDX3 as a regulator of the Wnt-β-catenin network, where it acts as a regulatory subunit of CK1ε. In a Wnt-dependent manner, DDX3 binds CK1ε and directly stimulates its kinase activity, and promotes phosphorylation of the scaffold protein dishevelled. DDX3 is required for Wnt-β-catenin signaling in mammalian cells and during *Xenopus* and *Caenorhabditis elegans* development. The results also suggest that the kinase-stimulatory function extends to other DDX and CK1 members, opening fresh perspectives for one of the longest-studied protein kinase families.

Wnt-β-catenin signaling plays a pivotal role in the development of multicellular organisms and in disease, notably

cancer (1, 2). One important question in Wnt-β-catenin signaling concerns the casein kinase 1 (CK1) family, members of which have both negative and positive functions in Wnt signaling (3). CK1 kinases play diverse cellular roles from yeast to human—e.g., in membrane transport, cell division, DNA repair, circadian rhythms, and nuclear localization, as well as Wnt and Hedgehog signaling. Yet, despite their importance, whether and how these serine-threonine kinases are regulated is poorly understood, and the prevailing view is that CK1 family members are constitutively active (3–5). Among CK1 isoforms, CK1ε

plays a critical and evolutionarily conserved role in Wnt-β-catenin signaling (6–8). As a primary target, CK1ε phosphorylates and activates the scaffold protein dishevelled (Dvl) (9, 10), which binds components at the interface of Wnt receptors and the β-catenin destruction complex (11, 12). Dvl phosphorylation by CK1ε promotes binding of the coeffector Frat, dissociation of PP2A from the β-catenin degradation complex, and stabilization of β-catenin (13, 14).

We identified DDX3 in a genome-wide small interfering RNA (siRNA) screen for previously undescribed Wnt-β-catenin regulators in human embryonic kidney 293T (HEK293T) cells (15, 16) (information on materials and methods is available on Science online). DDX3 belongs to the family of adenosine 5′-triphosphate (ATP)-dependent DEAD-box RNA helicases, for which cellular functions and biological roles remain incompletely understood (17). DDX3 is a multifunctional protein involved in mRNA biogenesis processes and is implicated in cell cycle control, apoptosis, tumorigenesis, and viral infection (18). Knockdown of DDX3 by four independent siRNAs inhibited signaling in TOPFLASH reporter assays stimulated by Wnt3a but not by β-catenin (fig. S1, A and B). Cotransfection of *Xenopus* DDX3 rescued siDDX3 in a dose-dependent manner (fig. S1C), excluding siRNA off-target effects. Wnt1, Wnt3a, and Dvl1 signaling were inhibited by siDDX3, whereas constitutively active LRP6 (LRP6ΔE1–4) and β-catenin were unaffected (Fig. 1A). This epistasis is consistent with DDX3 acting at the level of Dvl, which is required for LRP6 activation.

<sup>1</sup>Division of Molecular Embryology, DKFZ-ZMBH Alliance, Deutsches Krebsforschungszentrum, Im Neuenheimer Feld 280, D-69120 Heidelberg, Germany. <sup>2</sup>Hubrecht Institute, Royal Netherlands Academy of Arts and Sciences and University Medical Center Utrecht, Netherlands. <sup>3</sup>Institute of Molecular Biology, D-55128 Mainz, Germany.

\*These authors contributed equally to this work.

†Present address: Division of Neurogenetics, Center for Neurological Diseases and Cancer, Nagoya University Graduate School of Medicine, Japan.

‡Corresponding author. E-mail: niehrs@dkfz-heidelberg.de

Knockdown of *DDX3* and of all three *Dvls* by siRNA did not reduce cytoplasmic  $\beta$ -catenin abundance, but inhibited nuclear  $\beta$ -catenin accumulation (Fig. 1B), indicating that loss of *DDX3* phenocopies loss of *Dvl* in Wnt signaling. Overexpressed *DDX3* synergized with *Wnt3a* in *Xenopus* embryonic axis duplication assays (Fig. 1C), as well as in *siamois* induction (Fig. 1D). These results suggest that *DDX3* functions in Wnt- $\beta$ -catenin signaling also in *Xenopus*.

*DDX3* was ubiquitously expressed throughout *Xenopus* embryogenesis (fig. S2). Injection of *DDX3* antisense morpholino (Mo) oligonucleotides elicited anteriorized embryos with enlarged heads and eyes, shortened tails, and defective melanocyte and eye pigmentation (Fig. 1E). This is the characteristic phenotype caused by inhibition of zygotic Wnt signaling (19, 20). In-

deed, knockdown of the Wnt co-receptor LRP6 with established morpholinos (21) phenocopied *DDX3* morphants (Fig. 1E). The *DDX3* Mo phenotype was specific because it was very efficiently rescued by coinjection of human *DDX3* mRNA (Fig. 1E).

Anteriorization of *DDX3* morphants was confirmed by expansion of the forebrain markers *bf1* and *otx2*, as well as down-regulation of the mid-hindbrain boundary marker *en2* and the hind-brain marker *krox20*, whereas the pan-neural marker *sox3* was unaffected (Fig. 1F and fig. S4A). This expression pattern was similar to that observed in LRP6 morphants (Fig. 1F). Moreover, *DDX3* morphants showed no apoptosis or changes in cell proliferation in the central nervous system (CNS) (fig. S3), indicating that the altered neural marker gene expression represents a defect of antero-

posterior (a-p) neural patterning, wherein Wnt- $\beta$ -catenin signaling acts as a morphogen (22). This conclusion was corroborated by gain-of-function experiments. When injected as plasmid DNA in *Xenopus* embryos, overexpressed *XWnt8* induces posteriorized embryos, which lack anterior neural structures. *DDX3* phenocopied this defect, because embryos injected with either *DDX3* or *XWnt8* DNA showed reduced expression of *otx2*, *en2*, and *sox3* and moderately increased expression of *krox20* (fig. S4B).

In *Xenopus* animal cap assays, *DDX3* Mo inhibited *Wnt3a*-stimulated induction of the direct Wnt targets *siamois*, *xnr3*, and *myoD*, as did LRP6 Mo (fig. S4C). Expression of *siamois* was rescued by coinjection of human *DDX3* as well as of  $\beta$ -catenin mRNA (fig. S4D), indicating that *DDX3* is specifically required for Wnt signaling

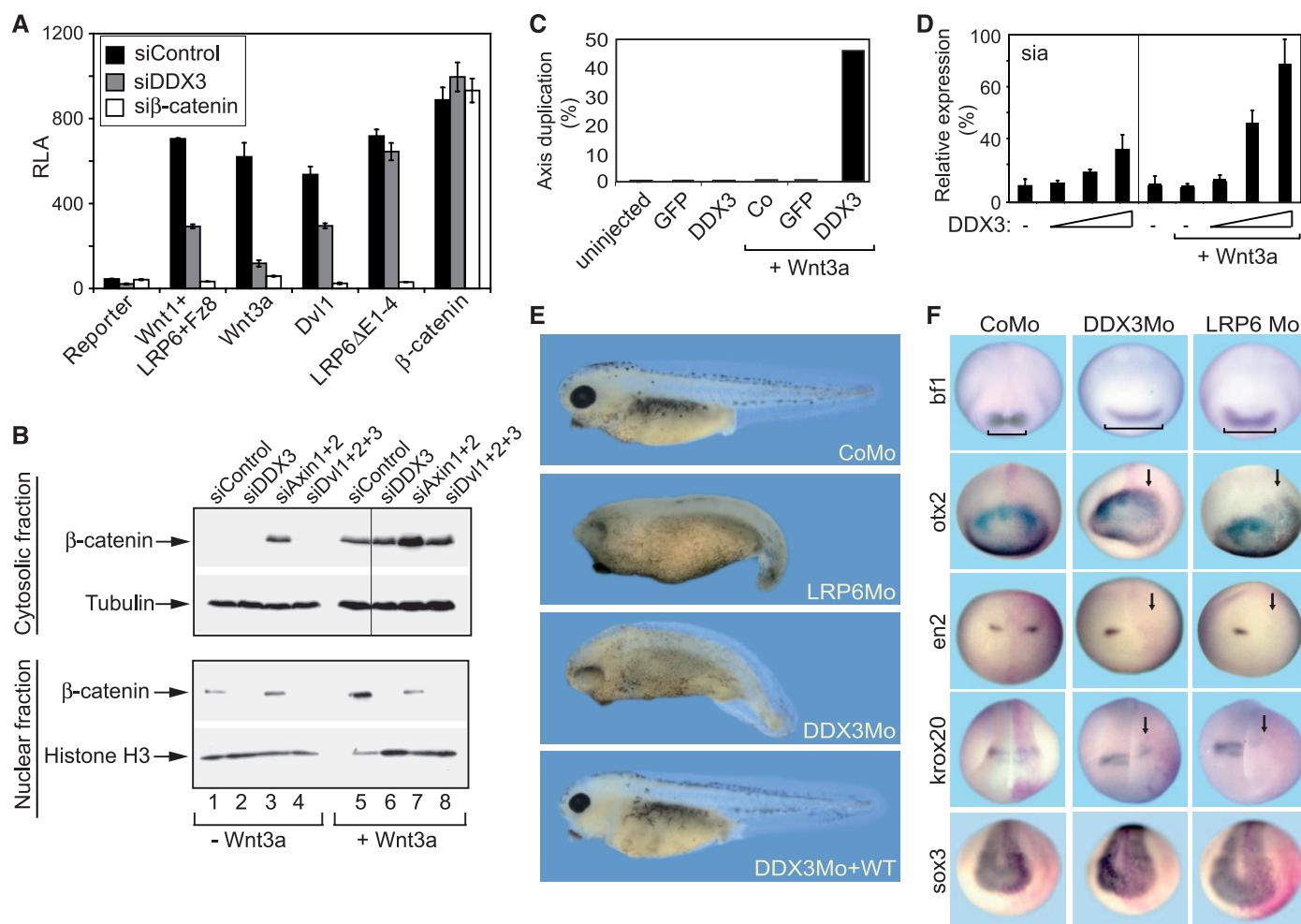


**Fig. 1.** *DDX3* is required for Wnt- $\beta$ -catenin signaling in mammalian cells and during a-p neural patterning in *Xenopus*. **(A)** Wnt luciferase reporter assay in HEK293T cells stimulated with *Wnt3a*-conditioned medium or by transfection with the indicated constructs, in the presence of the indicated siRNAs. RLA, relative luciferase activity. Error bars indicate SDs;  $n = 3$ , biological triplicates of one representative assay. **(B)** Western blot analysis of endogenous  $\beta$ -catenin from cytosolic and nuclear fractions of HEK293T cells stimulated with control or *Wnt3a*-conditioned medium in the presence of the indicated siRNAs. **(C)** *Xenopus* axis duplication assay by injection of the indicated mRNAs into the ventral blastomeres of four-cell-stage embryos. **(D)** Quantitative polymerase

chain reaction (QPCR) analysis of *siamois* using VMZ explants from *Xenopus* embryos injected with the indicated mRNAs. Explants were excised and analyzed from gastrula-stage embryos. Error bars indicate SDs;  $n = 2$  assays. VMZ, ventral marginal zone; *sia*, *siamois*. **(E)** Tadpole-stage *Xenopus* embryos that were injected at the two-cell stage in the animal hemisphere with *DDX3* or LRP6 antisense Mo oligonucleotides in the absence or presence of human *DDX3* mRNA (WT, wild type) as indicated. **(F)** Whole-mount in situ hybridization of neurula-stage embryos injected at four-cell stage in animal blastomeres with the indicated Mo plus  $\beta$ -galactosidase mRNA lineage tracer (red; arrow marks injected side).



and that it acts upstream of  $\beta$ -catenin. Moreover, in *Xenopus* Wnt-reporter assays, DDX3 Mo inhibited both endogenous and Wnt3a-stimulated luciferase expression (fig. S4E). The requirement of DDX3 was specific for Wnt, because signaling by various other growth factors (bone morphogenetic protein, nodal, transforming growth factor- $\beta$ , and fibroblast growth factor) was unaffected by DDX3 depletion in *Xenopus* (fig. S5, A to E) and HEK293T cells (fig. S5, F to I). We conclude that DDX3 regulates a-p CNS patterning in *Xenopus* embryos through Wnt- $\beta$ -catenin signaling.

To investigate whether the function of DDX3 in canonical Wnt- $\beta$ -catenin signaling is evolutionarily conserved beyond vertebrates, we knocked down *F58E10.3*, a DDX3 homolog in *Caenorhabditis elegans*. We assayed migration of Q neuroblast descendants, which depends on canonical EGL-20-Wnt signaling (fig. S6, A to D) (23). To sensitize the assay, we included a mutation in the Wnt secretion factor *vps-29* to reduce EGL-20-Wnt ligand concentration (24). Ubiquitous

knockdown of *F58E10.3* resulted in a twofold enhancement of the Wnt loss-of-function phenotype in *vps-29* mutants [QL migration: 35% Co RNA interference (RNAi);  $n = 187$ ; 70% *F58E10.3* RNAi;  $n = 60$ ; data not shown]. This suggests that *F58E10.3* is required for EGL-20-Wnt signaling. Next, we used the *egl-17* promoter to specifically express *F58E10.3* double-stranded RNA in the QL neuroblasts (25). This also resulted in an increased Wnt signaling defect (fig. S6B), demonstrating that *F58E10.3* functions cell autonomously. To position *F58E10.3* in the canonical EGL-20-Wnt pathway, we performed epistasis experiments with transgenic lines that overexpress EGL-20-Wnt (26) or a constitutively active, N-terminally truncated version of BAR-1- $\beta$ -catenin ( $\Delta$ N-BAR-1) (27). Overexpression of EGL-20-Wnt induces posterior migration of QR descendants (fig. S6A bottom) (26), and we found that this response was reduced in animals treated with *F58E10.3* RNAi (fig. S6C). By contrast, the response to  $\Delta$ N-BAR-1 overexpression

was similar in control and *F58E10.3* RNAi-treated animals (fig. S6D), indicating that *F58E10.3* acts downstream of EGL-20-Wnt but upstream of BAR-1- $\beta$ -catenin. In support of this, we found that *F58E10.3* RNAi enhances the Wnt signaling defect of *mig-5-Dvl* RNAi (fig. S6B'). The results show that a DDX3-related helicase is required for Wnt signaling in *C. elegans*, supporting its evolutionarily conserved function.

Because Dvl is positively regulated by DDX3 and CK1 $\epsilon$  phosphorylation (9, 10), we analyzed whether DDX3 may affect phosphorylation of Dvl2. Phospho-Dvl2 is typically monitored by its lower electrophoretic mobility, and both *siDDX3* and *siCK1 $\epsilon$*  inhibited Dvl2 phosphorylation (Fig. 2A). Conversely, DDX3 cotransfected with a limiting dose of CK1 $\epsilon$  induced Dvl2 phosphorylation (Fig. 2B). Moreover, in *Xenopus* animal cap assays, DDX3 synergized in a dose-dependent manner with limiting doses of Dvl2 and CK1 $\epsilon$ , but not with  $\beta$ -catenin, to increase expression of *siamois* (Fig. 2C). Thus, DDX3 is necessary and sufficient for Dvl2

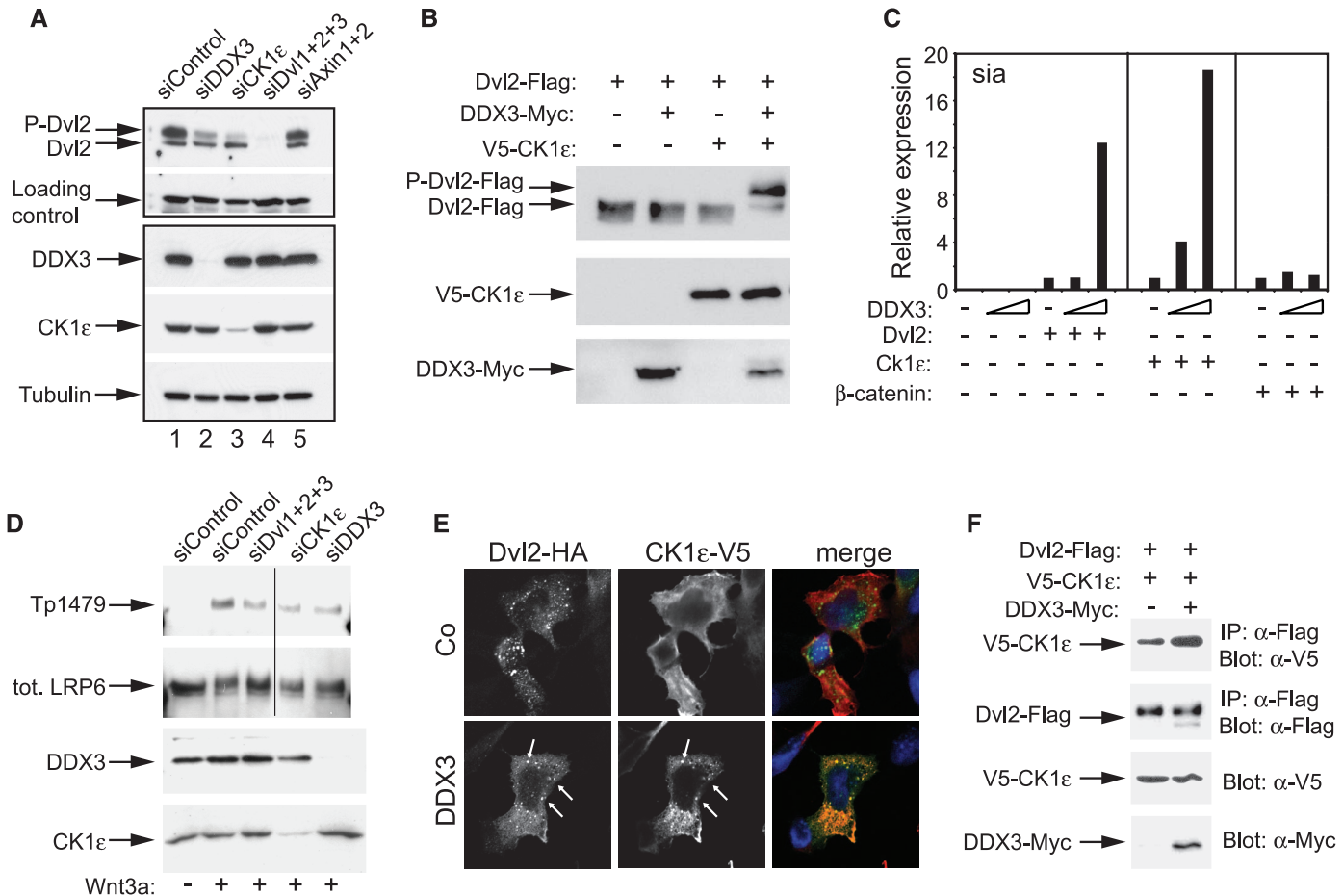


**Fig. 2.** DDX3 is required for Dvl2 phosphorylation and signalosome formation. (A) Western blot of endogenous Dvl2, DDX3, and CK1 $\epsilon$  from lysates of HEK293T cells treated with the indicated siRNAs. (B) Western blot analysis of Dvl2 phosphorylation status in lysates from HEK293T cells transfected as indicated. (C) QPCR analysis of *siamois* (sia) in animal cap explants from *Xenopus* embryos. Injected mRNA: *hDDX3* (0.5 and 1 ng). Ornithine decarboxylase was used for normalization. *Dvl2*, *CK1 $\epsilon$* , and  $\beta$ -catenin injected samples are set to 1. (D) Western blot of the indicated endogenous

proteins from membrane lysates of NTERA2 cells treated with the indicated siRNAs and stimulated for 1 hour with Wnt3a-conditioned medium or control medium. tot. LRP6, total LRP6. (E) Confocal microscopy of HeLa cells transfected with *Dvl2*-HA or *V5*-CK1 $\epsilon$  in the absence or presence of *DDX3*-Myc. A low dose of CK1 $\epsilon$  was used, as high CK1 $\epsilon$  leads to nonvesicular Dvl due to decreased polymerization (41). (F) CoIP of *V5*-CK1 $\epsilon$  with *Dvl2*-Flag from lysates of transfected HEK293T cells in the presence or absence of *DDX3*-Myc.

phosphorylation by CK1 $\epsilon$  and functionally interacts with both in Wnt signaling.

Wnt signal transduction involves LRP6 receptor clustering in signalosomes and phosphorylation at Thr<sup>1479</sup> (T1479), a process that depends on Dvl (28). Thus, LRP6 T1479 phosphorylation is also a proxy for Dvl activation. Indeed, Wnt-induced LRP6 T1479 phosphorylation was inhibited not only by CK1 $\epsilon$  and Dvl $\epsilon$  siRNAs, but also by depletion of DDX3 (Fig. 2D), showing its requirement for signalosome formation.

Dvl localizes in characteristic cytoplasmic punctae, which reflect its property to oligomerize (28, 29). By immunofluorescence microscopy of cells transfected with Dvl2 and a low dose of CK1 $\epsilon$ , we observed the typical Dvl2 punctae, whereas CK1 $\epsilon$  showed diffuse staining. Cotransfection of DDX3 induced recruitment of CK1 $\epsilon$  in Dvl2 punctae (Fig. 2E). Likewise, in coimmunoprecipitation (CoIP) experiments, transfected DDX3 enhanced recruitment of CK1 $\epsilon$  to Dvl2 (Fig. 2F). Dvl2-CK1 $\epsilon$ -DDX3 punctae were positive for the multivesicular body (MVB) marker TSG101, and transfected Dvl2 alone also partially localized in MVBs (fig. S7, A and B). MVBs represent a late-stage compartment

of endocytic Wnt signalosomes and they sequester glycogen synthase kinase GSK3 $\beta$  from the cytoplasm, thereby protecting  $\beta$ -catenin from degradation (30). These gain- and loss-of-function experiments suggest that DDX3 induces Dvl phosphorylation via CK1 $\epsilon$  and thereby stimulates signalosome formation.

In CoIP experiments with overexpressed proteins, Dvl2 and CK1 $\epsilon$  bound to DDX3 (fig. S7C). However, in *in vitro* binding assays only CK1 $\epsilon$  bound to DDX3, but not Dvl2 (Fig. 3A), suggesting that the interaction with CK1 $\epsilon$  is direct, whereas Dvl2 interaction with DDX3 may be indirect and, e.g., via CK1 $\epsilon$ . The interaction of DDX3 with CK1 $\epsilon$  was also confirmed by CoIP of endogenous proteins (Fig. 3B and fig. S8A), and this binding was insensitive to ribonuclease treatment (fig. S8, B and C). We examined whether the DDX3-CK1 $\epsilon$  interaction is regulated by Wnt, because CK1 $\epsilon$  activity is Wnt inducible (31). In CoIPs with endogenous proteins, Wnt3a stimulation enhanced binding of CK1 $\epsilon$  to DDX3 (Fig. 3C). Wnt3a stimulation also promoted recruitment of DDX3 to the plasma membrane (fig. S7D). The results indicate that DDX3 binds directly to CK1 $\epsilon$  in a Wnt-dependent manner.

DDX3 consists of an N- and a C-terminal region, which form independently folding subdomains (32). Both domains contribute to two enzymatic activities of DDX3, ATP hydrolysis and RNA unwinding (Fig. 3D). Structure-function analysis revealed that for DDX3 binding to CK1 $\epsilon$  (Fig. 3E) and for Wnt signaling (figs. S9, A to D, and S10), neither of these enzymatic activities is essential and that most of the C-terminal subdomain of DDX3 is required, whereas the N-terminal subdomain is dispensable. Deletion of the N terminus up to amino acid residue 456, including domains essential for ATP binding and hydrolysis and RNA helicase, had little effect on CK1 $\epsilon$  binding (Fig. 3E, lanes 3 and 4) or on the ability of the protein to rescue Wnt signaling in siDDX3-treated cells (fig. S9, A to C). By contrast, DDX3<sup>508-662</sup> failed in both binding to CK1 $\epsilon$  (Fig. 3E, lane 5) and Wnt signaling (fig. S9D). Failure in Wnt signaling was also observed for C-terminal deletions DDX3<sup>456-608</sup>, DDX3<sup>456-573</sup>, and DDX3<sup>1-573</sup> (fig. S10). In addition, we analyzed two mutants with impaired enzymatic activities: an RNA helicase-deficient mutant (AAA) and a mutant in which both helicase and ATPase activity are inhibited (DQAD) (33).

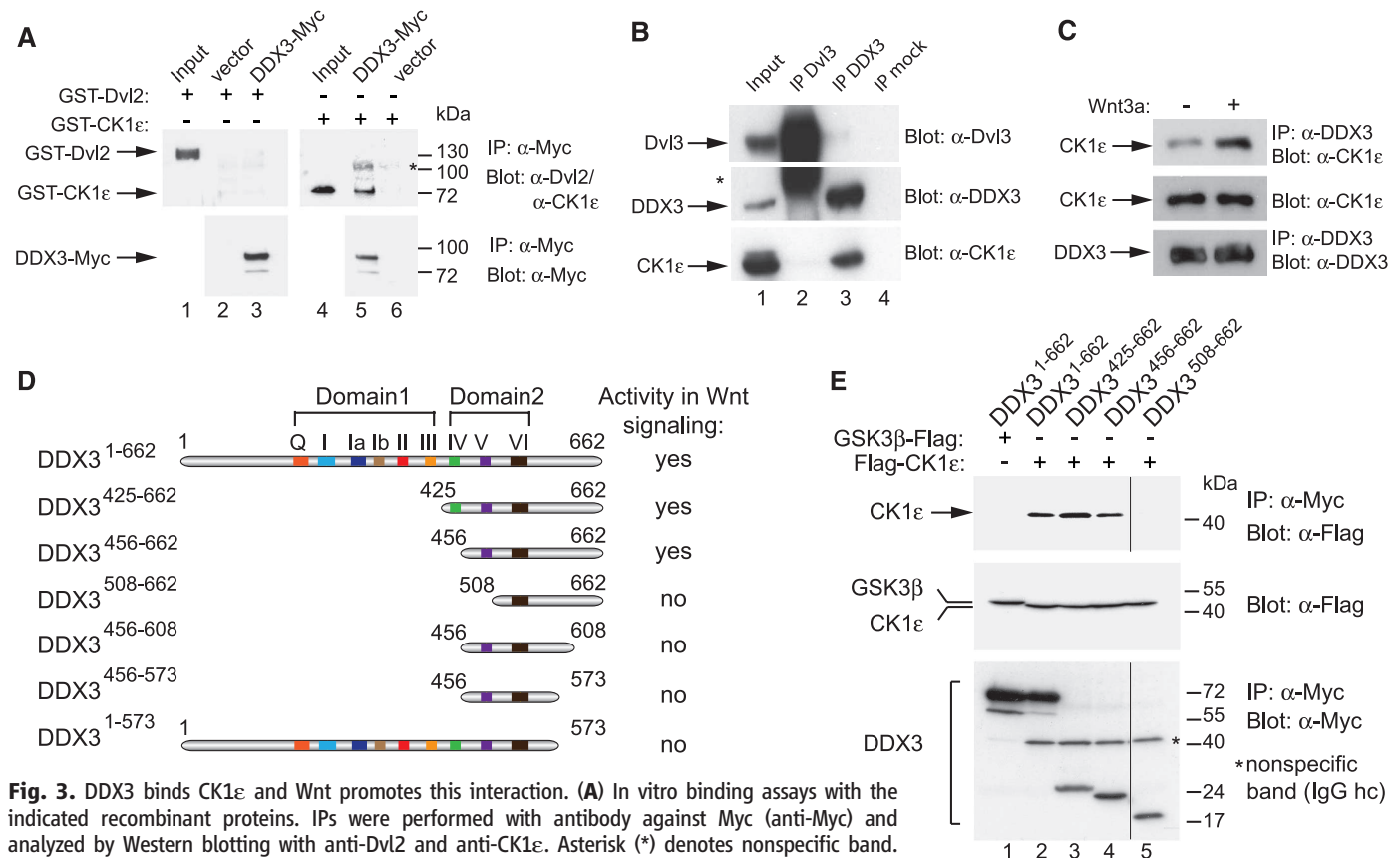


**Fig. 3.** DDX3 binds CK1 $\epsilon$  and Wnt promotes this interaction. **(A)** *In vitro* binding assays with the indicated recombinant proteins. IPs were performed with antibody against Myc (anti-Myc) and analyzed by Western blotting with anti-Dvl2 and anti-CK1 $\epsilon$ . Asterisk (\*) denotes nonspecific band. **(B)** CoIPs of endogenous proteins from lysates of HEK293T cells. Anti-Dvl3 serves as negative control. (\*) Nonspecific band. **(C)** CoIPs of endogenous proteins from lysates of HEK293T cells stimulated with control or Wnt3a-conditioned medium. **(D)** Schematic representation of C-terminally Myc-tagged DDX3 constructs used. Q and I to VI represent the conserved motifs of DEAD-box helicases, which are organized in domain 1 and 2 (17). Motifs Q, I, II, and VI bind ATP and are required for ATP hydrolysis. Motifs Ia, Ib, IV, and V are involved in RNA binding. Motif III is responsible for the communication between ATP-binding and RNA-binding sites. The Wnt signaling ability of DDX3 deletion mutants (from figs. S9 and S10) is summarized on the right. **(E)** CoIPs from lysates of HEK293T cells transfected with the indicated tagged constructs. DDX3 constructs as in (D).



When injected in *Xenopus* animal caps as mRNA, both mutants cooperated with Wnt3a in *siamois* induction (fig. S8, D and E), again demonstrating that DDX3 enzymatic activity is dispensable for Wnt- $\beta$ -catenin signaling. These mutations also had no effect on the ability of the protein to colocalize with Dvl2 in transfected cells (fig. S8, F and G).

Because the data indicated that DDX3 promotes phosphorylation of Dvl2 by CK1 $\epsilon$ , we asked if this effect is direct. In *in vitro* kinase assays with recombinant proteins, DDX3 greatly stimulated CK1 $\epsilon$  phosphorylation of Dvl2, and DDX3 itself also became phosphorylated (Fig. 4A). Moreover, DDX3 strongly enhanced CK1 $\epsilon$  activity toward a generic CK1-specific peptide substrate (Fig. 4B).

CK1 $\epsilon$  is an autorepressed enzyme because its autophosphorylated C-terminal domain interacts with and inhibits the kinase (34, 35). This autoinhibition can be relieved *in vitro* by protein phosphatases (36). However, the phosphatase inhibitor okadaic acid did not change the stimulatory effect of DDX3 on CK1 $\epsilon$  (fig. S11A). Moreover, a CK1 $\epsilon$  deletion mutant lacking the autoinhibitory tail (Flag-CK1 $\epsilon$  $\Delta$ C) had increased kinase activity, as expected, but was even more stimulated by DDX3 (Fig. 4C) and still bound to DDX3 (fig. S11B). In addition, DDX3 had no influence on the autophosphorylation of full-length or mutant CK1 $\epsilon$  (fig. S11, C and D). Moreover, other CK1 isoforms, which are not autorepressed, were also stimulated by DDX3 (see below). Hence, DDX3 activates CK1 $\epsilon$  independent of its C-terminal autophosphorylation.

Instead, kinetic analysis revealed a novel mechanism of CK1 activation: Although DDX3 had little effect on the  $K_m$  (apparent Michaelis constant) of CK1 $\epsilon$  toward its peptide substrate, it greatly improved the  $K_m$  of the kinase toward ATP, from 108 to 24  $\mu$ M (fig. S12). This was accompanied by a ~15-fold increased  $V_{max}$ . Thus, DDX3 acts as a V-type allosteric activator of CK1 $\epsilon$ , a regulatory mode typically found in protein kinases and small GTPases involved in signal transduction (37).

To delineate the domains required for CK1 $\epsilon$  stimulation, we tested immunopurified DDX3 deletion mutants in kinase assays. Whereas DDX3<sup>425-662</sup> and DDX3<sup>456-662</sup> stimulated CK1 $\epsilon$  activity, DDX3<sup>508-662</sup> showed no activity (fig. S9E), reflecting their CK1 $\epsilon$  binding and Wnt signaling activities.

Because CK1 family members share a highly conserved kinase domain, we examined whether DDX3 activates other CK1 isoforms as well. Indeed, DDX3 stimulated not only CK1 $\epsilon$  but also the three CK1 isoforms  $\alpha$ ,  $\delta$ , and  $\gamma$ 2, whereas GSK3 $\beta$  activity was unaffected (Fig. 4D). To corroborate that DDX3 regulates CK1 activity *in vivo*, we carried out kinase assays with CK1 $\epsilon$ , CK1 $\alpha$ , and CK1 $\gamma$  immunoprecipitated from cells after DDX3 siRNA knockdown. Wnt treatment was reported to stimulate CK1 $\epsilon$  kinase activity (31), and we could confirm this (Fig. 4E). No-

tably, siDDX3 reduced CK1 $\epsilon$  kinase activity in unstimulated as well as in Wnt3a-stimulated cells, indicating that DDX3 regulates CK1 $\epsilon$  activity *in vivo*. siDDX3 also reduced activity of CK1 $\alpha$ , which negatively acts in Wnt signaling (3), but upon Wnt stimulation, siDDX3 ceased to reduce CK1 $\alpha$  activity (Fig. 4F), suggesting that Wnt signaling uncouples CK1 $\alpha$  regulation by DDX3. Unlike CK1 $\epsilon$  and CK1 $\alpha$ , CK1 $\gamma$  activity was not inhibited by siDDX3 (fig. S13A). To corroborate that DDX3 promotes Wnt signaling primarily by activation of CK1 $\epsilon$  instead of CK1 $\gamma$ , we an-

alyzed constitutively active LRP6 $\Delta$ E1-4, for which T1479 phosphorylation bypasses the need for Wnt and Dvl (28). Although LRP6 $\Delta$ E1-4 T1479 phosphorylation was, as expected, reduced by dominant negative CK1 $\gamma$ , it remained unaffected by siDDX3, siDvl, or siCK1 $\epsilon$  (fig. S13B).

Finally, we tested other DDX family members in CK1 $\epsilon$  kinase assays (Fig. 4G). Notably, DDX4 and DDX56 also potently stimulated CK1 $\epsilon$  kinase, whereas other DDX proteins had little or no effect. No stimulation was observed also with DHX58 and -32 RNA helicases, DNA

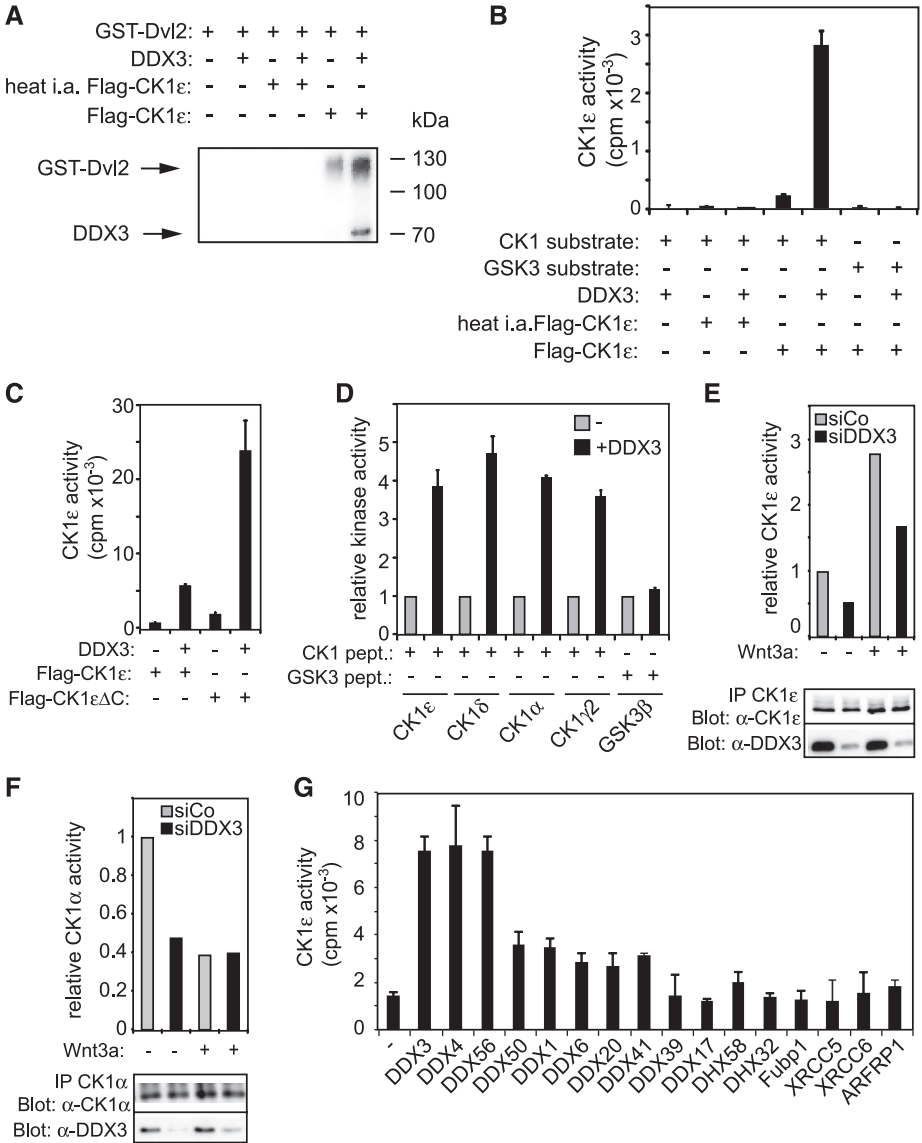


**Fig. 4.** DDX3 and other DEAD-box RNA helicases directly activate CK1 family members. (A) CK1 $\epsilon$  *in vitro* kinase assay with recombinant Dvl2 as substrate in the absence or presence of recombinant DDX3. Autoradiography after SDS–page polyacrylamide gel electrophoresis showing <sup>32</sup>P incorporation. (B to D) *In vitro* kinase assays with the indicated recombinant kinases and CK1- or GSK3-specific peptide substrate in the absence or presence of DDX3. (E and F) *In vitro* kinase assays of endogenous CK1 $\epsilon$  (E) and CK1 $\alpha$  (F) coimmunoprecipitated from lysates of HEK293T that were treated with the indicated siRNAs and stimulated with control or Wnt3a-conditioned medium. Kinase activity was normalized to total kinase (Western blot, lower panel). The experiment was performed three times with similar results. (G) CK1 $\epsilon$  *in vitro* kinase assay with CK1 peptide substrate in the absence or presence of the indicated recombinant proteins. Error bars indicate SDs;  $n = 3$  assays. cpm, counts per minute.

helicases XRCC5 and 6 and Fubp1, as well as the GTP-ase ARFRP1. Together the results raise the possibility that other DDX members also function as regulatory subunits of the CK1 family.

Our study reveals an unexpected biological and cellular activity of the RNA helicase DDX3 in Wnt- $\beta$ -catenin signaling and shows that this multifunctional protein is a regulatory subunit of CK1 $\epsilon$ . We propose a model wherein Wnt activation promotes recruitment of DDX3 to CK1 $\epsilon$ , which stimulates the kinase to phosphorylate and regulate target proteins, including Dvl. This in turn promotes clustering of Wnt-receptor complexes on Dvl aggregates and formation of signalosomes. Intriguingly, DDX3 is recurrently mutated in medulloblastomas belonging to a “Wnt subgroup” (38–40), which may be rationalized by our findings. Although DDX3 regulates Wnt- $\beta$ -catenin signaling in *Xenopus* development, *C. elegans*, and mammalian cells, it may not universally activate CK1.

That DDX3 regulates CK1 $\epsilon$  is surprising given the long-held view that CK1 family members are constitutively active and that specificity is regulated by substrate priming and enzyme-substrate proximity. Our results indicate that the kinase-stimulatory function may well extend to other DDX members and likewise not be limited to CK1 $\epsilon$ , opening fresh perspectives for one of the longest-studied protein kinase families.

## References and Notes

1. T. Grigoryan, P. Wend, A. Klaus, W. Birchmeier, *Genes Dev.* **22**, 2308 (2008).
2. H. Clevers, R. Nusse, *Cell* **149**, 1192 (2012).
3. M. A. Price, *Genes Dev.* **20**, 399 (2006).
4. J. K. Cheong, D. M. Virshup, *Int. J. Biochem. Cell Biol.* **43**, 465 (2011).
5. U. Knippschild *et al.*, *Cell. Signal.* **17**, 675 (2005).
6. T. J. Klein, A. Jenny, A. Djiane, M. Mlodzik, *Curr. Biol.* **16**, 1337 (2006).
7. C. Sakanaka, P. Leong, L. Xu, S. D. Harrison, L. T. Williams, *Proc. Natl. Acad. Sci. U.S.A.* **96**, 12548 (1999).
8. J. M. Peters, R. M. McKay, J. P. McKay, J. M. Graff, *Nature* **401**, 345 (1999).
9. C. Gao, Y. G. Chen, *Cell. Signal.* **22**, 717 (2010).
10. J. B. Wallingford, R. Habas, *Development* **132**, 4421 (2005).
11. C. Metcalfe, M. Bienz, *J. Cell Sci.* **124**, 3537 (2011).
12. K. A. Wharton Jr., *Dev. Biol.* **253**, 1 (2003).
13. S. Hino, T. Michiue, M. Asashima, A. Kikuchi, *J. Biol. Chem.* **278**, 14066 (2003).
14. Z. H. Gao, J. M. Seeling, V. Hill, A. Yochum, D. M. Virshup, *Proc. Natl. Acad. Sci. U.S.A.* **99**, 1182 (2002).
15. A. Glinka *et al.*, *EMBO Rep.* **12**, 1055 (2011).
16. C. M. Cruciat *et al.*, *Science* **327**, 459 (2010).
17. P. Linder, E. Jankowsky, *Nat. Rev. Mol. Cell Biol.* **12**, 505 (2011).
18. M. Schröder, *Biochem. Pharmacol.* **79**, 297 (2010).
19. S. Hoppler, J. D. Brown, R. T. Moon, *Genes Dev.* **10**, 2805 (1996).
20. A. Glinka *et al.*, *Nature* **391**, 357 (1998).
21. C. Hassler *et al.*, *Development* **134**, 4255 (2007).
22. C. Kiecker, C. Niehrs, *Development* **128**, 4189 (2001).
23. H. C. Korswagen, *Bioessays* **24**, 801 (2002).
24. M. Harterink *et al.*, *Nat. Cell Biol.* **13**, 914 (2011).
25. G. Ou, R. D. Vale, *J. Cell Biol.* **185**, 77 (2009).
26. J. Whangbo, C. Kenyon, *Mol. Cell* **4**, 851 (1999).
27. H. C. Korswagen *et al.*, *Genes Dev.* **16**, 1291 (2002).
28. J. Bilic *et al.*, *Science* **316**, 1619 (2007).
29. T. Schwarz-Romond, C. Merrifield, B. J. Nichols, M. Bienz, *J. Cell Sci.* **118**, 5269 (2005).
30. V. F. Taelman *et al.*, *Cell* **143**, 1136 (2010).
31. W. Swiatek *et al.*, *J. Biol. Chem.* **279**, 13011 (2004).
32. M. Högbom *et al.*, *J. Mol. Biol.* **372**, 150 (2007).
33. J. W. Shih, T. Y. Tsai, C. H. Chao, Y. H. Wu Lee, *Oncogene* **27**, 700 (2008).
34. K. F. Gietzen, D. M. Virshup, *J. Biol. Chem.* **274**, 32063 (1999).
35. G. Carmel *et al.*, *J. Biol. Chem.* **269**, 7304 (1994).
36. A. Cegielska, K. F. Gietzen, A. Rivers, D. M. Virshup, *J. Biol. Chem.* **273**, 1357 (1998).
37. T. Traut, *Regulatory Allosteric Enzymes* (Springer Science+Business Media, New York, 2008).
38. D. T. Jones *et al.*, *Nature* **488**, 100 (2012).
39. T. J. Pugh *et al.*, *Nature* **488**, 106 (2012).
40. G. Robinson *et al.*, *Nature* **488**, 43 (2012).
41. O. Bernatik *et al.*, *J. Biol. Chem.* **286**, 10396 (2011).

**Acknowledgments:** We thank M. Bienz, H. Clevers, X. He, R. Moon, R. Nusse, Y. H. Wu Lee, and D. Wu for reagents; D. Ingelfinger and M. Boutros for assistance with siRNA screening; and R. Voit for help with kinase assays. We thank G. Roth and Aska Pharmaceuticals Tokyo for generous supply of human chorionic gonadotropin. This work was supported by the Deutsche Forschungsgemeinschaft.

## Supplementary Materials

www.sciencemag.org/cgi/content/full/science.1231499/DC1  
Materials and Methods  
Figs. S1 to S13  
References

15 October 2012; accepted 18 January 2013  
Published online 14 February 2013;  
10.1126/science.1231499

# Phosphorylation of Dishevelled by Protein Kinase RIPK4 Regulates Wnt Signaling

XiaoDong Huang,<sup>1,2</sup> James C. McGann,<sup>3\*</sup> Bob Y. Liu,<sup>4\*</sup> Rami N. Hannoush,<sup>5\*</sup> Jennie R. Lill,<sup>6</sup> Victoria Pham,<sup>6</sup> Kim Newton,<sup>1</sup> Michael Kakunda,<sup>2</sup> Jinfeng Liu,<sup>7</sup> Christine Yu,<sup>8</sup> Sarah G. Hymowitz,<sup>8</sup> Jo-Anne Hongo,<sup>9</sup> Anthony Wynshaw-Boris,<sup>10</sup> Paul Polakis,<sup>4</sup> Richard M. Harland,<sup>3</sup> Vishva M. Dixit<sup>1†</sup>

Receptor-interacting protein kinase 4 (RIPK4) is required for epidermal differentiation and is mutated in Bartsocas-Papas syndrome. RIPK4 binds to protein kinase C, but its signaling mechanisms are largely unknown. Ectopic RIPK4, but not catalytically inactive or Bartsocas-Papas RIPK4 mutants, induced accumulation of cytosolic  $\beta$ -catenin and a transcriptional program similar to that caused by Wnt3a. In *Xenopus* embryos, *Ripk4* synergized with coexpressed *Xwnt8*, whereas *Ripk4* morpholinos or catalytically inactive *Ripk4* antagonized Wnt signaling. RIPK4 interacted constitutively with the adaptor protein DVL2 and, after Wnt3a stimulation, with the co-receptor LRP6. Phosphorylation of DVL2 by RIPK4 favored canonical Wnt signaling. Wnt-dependent growth of xenografted human tumor cells was suppressed by *RIPK4* knockdown, suggesting that *RIPK4* overexpression may contribute to the growth of certain tumor types.

**M**ice lacking receptor-interacting protein kinase 4 (RIPK4) die at birth with fused external orifices that result from defective epidermal differentiation (1). In humans, *RIPK4* mutations cause autosomal recessive Bartsocas-Papas syndrome, which is characterized by severe defects in face, skin, and limb development

(2, 3). To investigate RIPK4 signaling, we used a PathwayFinder (QIAGEN, Hilden, Germany) polymerase chain reaction (PCR) array to determine gene expression changes in human embryonic kidney 293T cells after transfection with RIPK4. Up-regulation of Wnt target genes such as *CCND1*, *LEF1*, *JUN*, *Myc*, and *TCF7* (fig. S1)

prompted us to compare RIPK4 transfection to Wnt3a treatment in human PA-I teratocarcinoma cells. RIPK4, but not the related kinases RIPK1, RIPK2, and RIPK3, caused transcriptional changes similar to those caused by Wnt3a (Fig. 1A), up-regulating *AXIN2*, *APCDD1*, *GAD1*, and *NKX1-2* (fig. S2). RIPK4 also activated a Wnt-dependent TOPbrite (4) luciferase reporter in 293 cells (Fig. 1B).

Wnt signaling stabilizes  $\beta$ -catenin in the cytosol, thereby facilitating its interaction with TCF transcription factors to drive Wnt-dependent gene expression (4). 293T cells overexpressing RIPK4 contained more cytosolic  $\beta$ -catenin than did cells

<sup>1</sup>Department of Physiological Chemistry, Genentech, 1 DNA Way, South San Francisco, CA 94080, USA. <sup>2</sup>Department of Molecular Diagnostics and Cancer Cell Biology, Genentech, South San Francisco, CA 94080, USA. <sup>3</sup>Department of Molecular and Cell Biology and Center for Integrative Genomics, University of California, Berkeley, CA 94720, USA. <sup>4</sup>Department of Cancer Targets, Genentech, South San Francisco, CA 94080, USA. <sup>5</sup>Department of Early Discovery Biochemistry, Genentech, South San Francisco, CA 94080, USA. <sup>6</sup>Department of Protein Chemistry, Genentech, South San Francisco, CA 94080, USA. <sup>7</sup>Department of Bioinformatics, Genentech, South San Francisco, CA 94080, USA. <sup>8</sup>Department of Structural Biology, Genentech, South San Francisco, CA 94080, USA. <sup>9</sup>Department of Antibody Engineering, Genentech, South San Francisco, CA 94080, USA. <sup>10</sup>Department of Pediatrics and Institute for Human Genetics, School of Medicine, University of California, San Francisco, CA 94143, USA.

\*These authors contributed equally to this work.  
†Corresponding author. E-mail: dixit@gene.com



transfected with empty vector, RIPK1, RIPK2, or RIPK3, but they did not contain more *CTNNB1* mRNA (Fig. 1C). Therefore, RIPK4 may inhibit  $\beta$ -catenin protein degradation in a similar manner to Wnt signaling. The kinase activity of RIPK4 appeared to be critical for its Wnt-like effects because catalytically inactive mutant RIPK4-K51R (K51R: Lys<sup>51</sup>→Arg<sup>51</sup>) neither activated the TOPbrite reporter nor altered cytosolic  $\beta$ -catenin levels (fig. S3). RIPK4 interaction with protein kinase C  $\delta$  (PKC- $\delta$ ) or PKC- $\beta$  was neither sufficient nor required for increased cytosolic  $\beta$ -catenin because the K51R mutation did not prevent PKC binding (fig. S4A), and knockdown of both PKC isoforms had no effect on  $\beta$ -catenin accumulation by wild-type (WT) RIPK4 (fig. S4B). Bartsocas-Papas syndrome RIPK4 point mutants (I81N and I121N; I, Ile; N, Asn) and a truncation mutant (S376X; S, Ser; X, stop codon.) did not alter the amount of cytosolic  $\beta$ -catenin (Fig. 1D), implying that RIPK4 signaling to  $\beta$ -catenin may be relevant to mammalian development.

We investigated whether RIPK4 was required for Wnt signaling in various cell lines. *RIPK4* knockdown in 293T, ovarian A2780, and ovarian COV434 cells reduced Wnt3a-induced accumulation of  $\beta$ -catenin, TOPbrite luciferase activation, and transcription of *AXIN2* and *APCDD1* (Fig. 1E and fig. S5), whereas Wnt3a signaling in pancreatic PANC-1, kidney 786-O, and breast Hs578T cells was not compromised by *RIPK4*

knockdown (fig. S6). Therefore, the contribution of RIPK4 to Wnt signaling appears to be context-dependent.

To explore a role for RIPK4 during development, we overexpressed *Xenopus laevis Ripk4* in the ventral-vegetal cells of *Xenopus* embryos, where ectopic expression of Wnt pathway agonists causes axis duplication (5). *Ripk4* alone did not produce a secondary axis, but it synergized with subthreshold amounts of *Xenopus Wnt8* (*Xwnt8*), such that a full secondary axis developed in ~25% of embryos (Fig. 2A). *Ripk4* overexpression in dorsal-marginal cells, like expression of Wnt agonists (6), broadened the region expressing the dorsal organizer gene *Chordin* (Fig. 2B). Catalytically inactive *Ripk4-K52R* had no effect (Fig. 2B). To test whether *Ripk4* was necessary for Wnt signaling in vivo, we suppressed *Ripk4* expression in *Xenopus* embryos with translation-blocking morpholinos and measured expression of Wnt target gene *Xnr3* in animal cap cells (7). *Xnr3* induction by *Xwnt8* was reduced (Fig. 2C and fig. S7), suggesting that RIPK4 is necessary for optimal Wnt pathway activation in this region. Absence of *Xbra* expression in the animal cap samples excluded the possibility that *Xnr3* derived from contaminating mesodermal tissue. *Ripk4* morpholinos also anteriorized the neural tube and caused a posterior shift in the hindbrain marker gene *Engrailed2* (Fig. 2D), a phenotype linked to reduced Wnt signaling (8). Two different *Ripk4*

morpholinos caused this phenotype, which was reversed by injection of human *RIPK4* (Fig. 2D, column 3), ruling out nonspecific, off-target effects of the morpholinos. *Ripk4-K52R* overexpression in dorsal-anterior cells elicited similar changes to those caused by *Ripk4* morpholinos (Fig. 2D, column 4), consistent with the kinase inactive mutant interfering with signaling by endogenous *Ripk4*. Finally, *Ripk4* or *Xwnt8* overexpression had the opposite effect of *Ripk4* depletion, expanding and shifting *Engrailed2* expression anteriorly (Fig. 2D, columns 5 and 6). Collectively, these experiments indicate that *Ripk4* can regulate Wnt signaling in vivo.

To investigate how RIPK4 regulates Wnt signaling, we monitored RIPK4-induced accumulation of cytosolic  $\beta$ -catenin and activation of a TOPbrite reporter gene after small interfering RNA (siRNA)-mediated depletion of Wnt pathway components. Loss of either the Wnt co-receptor LRP6 or the Dishevelled adaptor proteins (DVL1 to 3) blocked the increase in cytoplasmic  $\beta$ -catenin (fig. S8A) and decreased TOPbrite luciferase activity (fig. S8B). Endogenous RIPK4 coimmunoprecipitated with endogenous DVL2 from 293T cells, irrespective of Wnt3a treatment (Fig. 3A). A direct interaction seems likely, as in vitro translated DVL2 and RIPK4 interacted as well (fig. S8C). Wnt3a treatment induced interaction of LRP6 with RIPK4, albeit not until 15 min after treatment (Fig. 3B). These findings are consistent

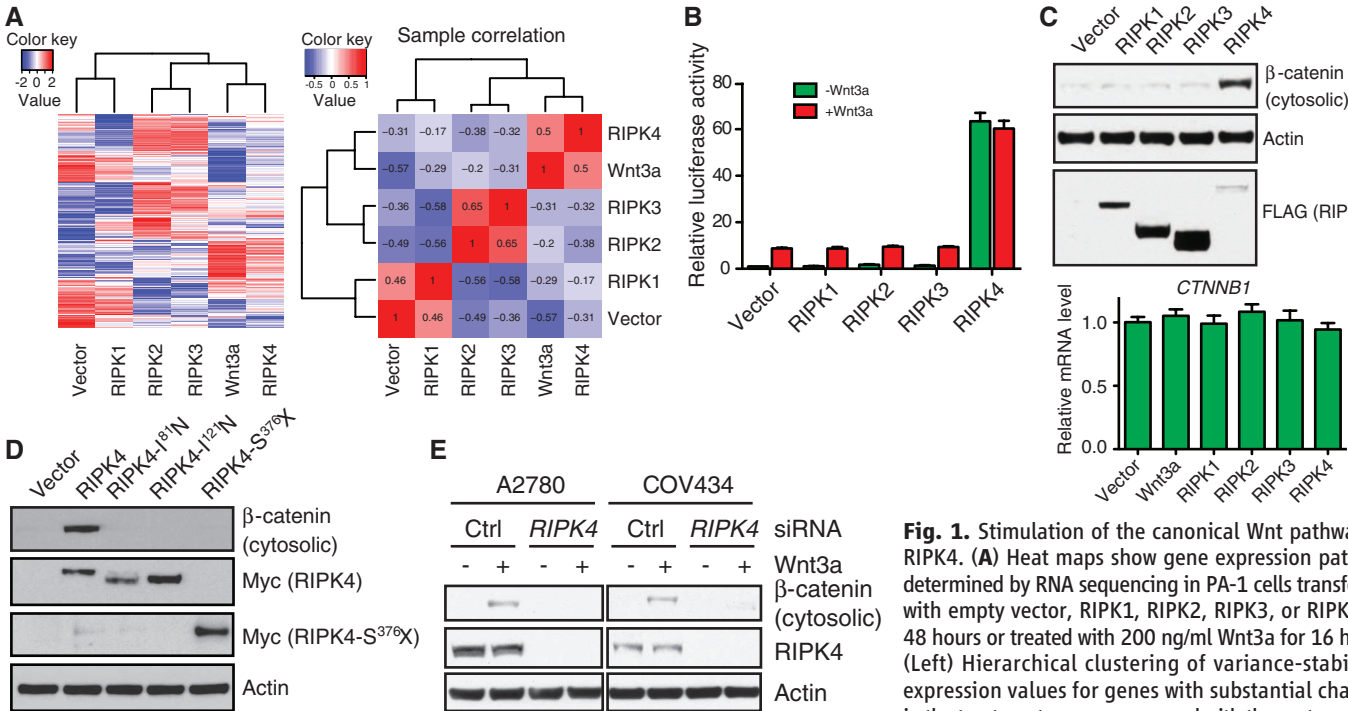


**Fig. 1.** Stimulation of the canonical Wnt pathway by RIPK4. (A) Heat maps show gene expression patterns determined by RNA sequencing in PA-1 cells transfected with empty vector, RIPK1, RIPK2, RIPK3, or RIPK4 for 48 hours or treated with 200 ng/ml Wnt3a for 16 hours. (Left) Hierarchical clustering of variance-stabilized expression values for genes with substantial changes in the treatment groups compared with the vector group.

(Right) Pearson's correlation coefficients between samples. (B) Expression of a TOPbrite luciferase reporter in 293 cells transfected with the constructs indicated and then cultured in the absence or presence of Wnt3a for 5 hours. Error bars represent the SEM of triplicate measurements. Results are representative of three independent experiments. (C) Cytosolic  $\beta$ -catenin protein abundance (top) and *CTNNB1* gene expression (bottom) in 293T cells transfected with RIPK4. Error bars represent the SEM of triplicate measurements. (D) Cytosolic  $\beta$ -catenin in 293T cells transfected with Bartsocas-Papas syndrome RIPK4 mutants. (E) Cytosolic  $\beta$ -catenin in A2780 or COV434 cells transfected with control (Ctrl) or *RIPK4* siRNAs for 60 hours and then treated with vehicle or Wnt3a for 2 hours.

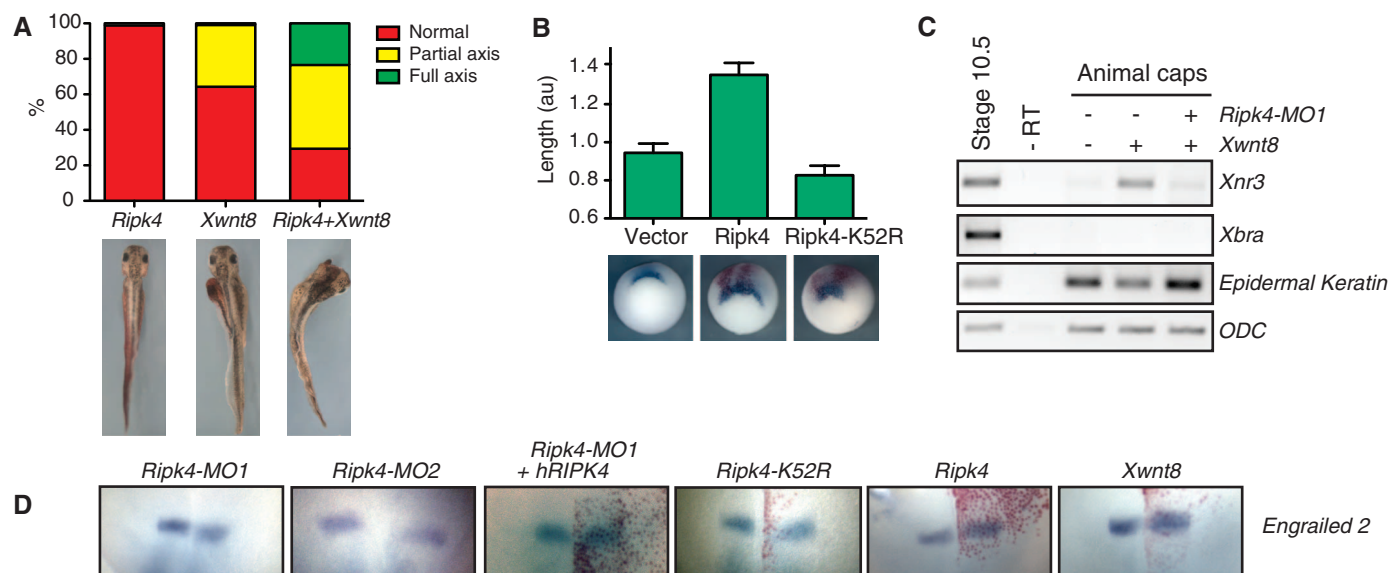


**Fig. 2.** Modulation of Wnt signaling in *Xenopus* by *Ripk4*. **(A)** Secondary axis formation in *Xenopus* embryos injected ventral vegetally with *Ripk4* (1 ng), *Xwnt8* (1 pg), or both. Two hundred sixty-nine embryos were examined in three independent experiments. Representative embryos are shown. **(B)** Length of *Chordin* expression along the blastopore lip of embryos injected at the four-cell stage with the RNAs indicated. Error bars represent the mean  $\pm$  SEM of 108 embryos. Vegetal views of representative embryos are shown. au, arbitrary units. **(C)** Reverse transcriptase (RT) PCR analyses show the effect of *Ripk4*

morpholinos on *Xwnt8*-induced expression of *Xnr3* in *Xenopus* animal cap cells. Control reactions contained RNA from stage 10.5 *Xenopus* embryos with or without RT. Amplification of *epidermal keratin* and *ornithine decarboxylase* (ODC) confirmed RNA integrity. **(D)** *Engrailed2* expression (blue) after blastomere injection at the two-cell stage (*Ripk4-MO1*, *Ripk4-MO2*, sorted by fluorescence of a coinjected fluorescein tracer) or the four-cell stage (all others). Right, injected side; top, anterior. Red staining is due to a nuclear  $\beta$ -galactosidase tracer.

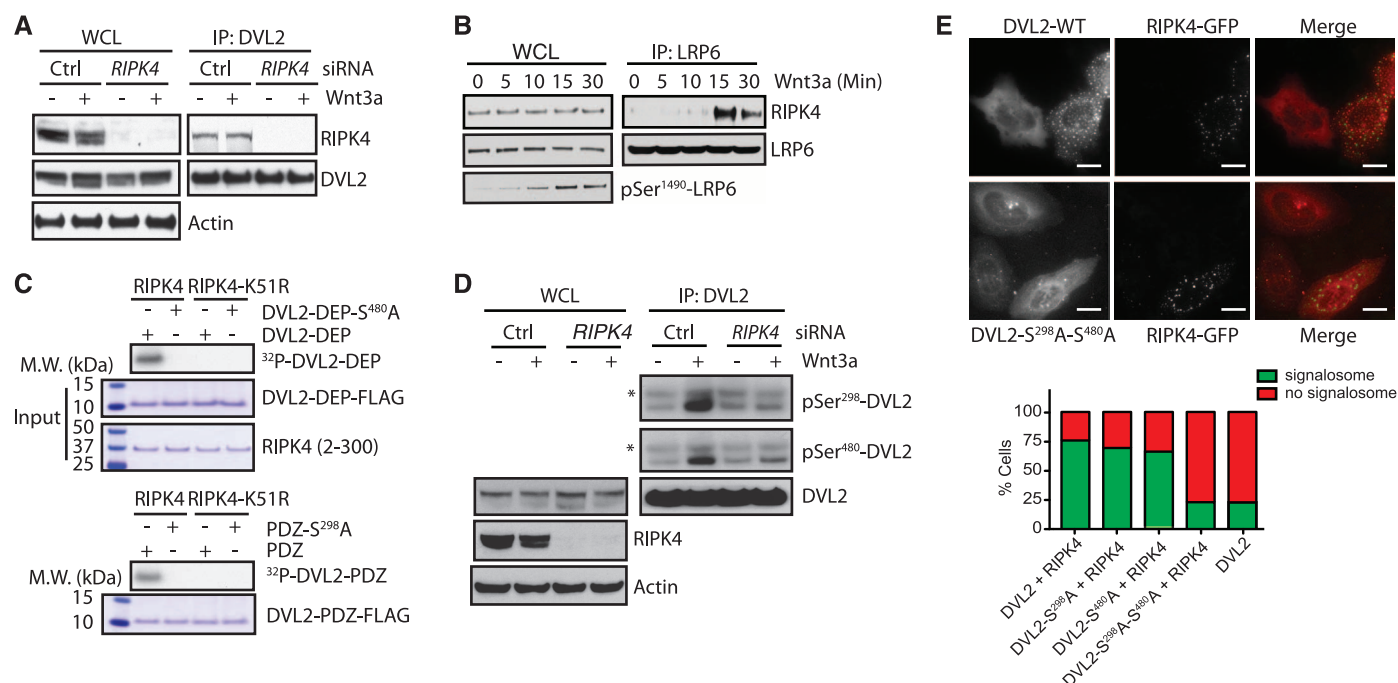


**Fig. 3.** Phosphorylation of DVL by RIPK4 promotes canonical Wnt signaling. **(A)** In 293T cells, endogenous RIPK4 coimmunoprecipitated with endogenous DVL2 in the presence or absence of 200 ng/ml Wnt3a for 30 min. Control (Ctrl) and *RIPK4* siRNAs confirmed RIPK4 antibody specificity. WCL, whole-cell lysates; IP, immunoprecipitation. **(B)** Endogenous RIPK4 coimmunoprecipitated with endogenous LRP6 in 293T cells treated with Wnt3a. **(C)** In vitro kinase

assays using the RIPK4 kinase domain and the DVL2 DEP (or PDZ) domain as a substrate. M.W., molecular weight. **(D)** RIPK4-dependent phosphorylation of endogenous DVL2 in 293T cells treated with Wnt3a for 10 min. Asterisks indicate nonspecific bands. **(E)** Effect of RIPK4-GFP on DVL2-FLAG cellular distribution in HeLa cells. Cells containing DVL2 puncta were enumerated by counting 250 cells per condition. Scale bars, 10  $\mu$ m.



with RIPK4 acting at the level of the Wnt receptor complex.

We explored whether RIPK4 phosphorylated LRP6, DVL, or their associated proteins. Finding no evidence of LRP6 phosphorylation, we focused on the DVL proteins as potential RIPK4 substrates. When DVL2 was coexpressed in 293T cells with RIPK4 or K51R catalytic inactive mutant RIPK4, two phosphopeptides, GDGGIYGS<sup>298</sup>IMK and KYAS<sup>480</sup>GLLK (G, Gly; D, Asp; Y, Tyr; M, Met; A, Ala; L, Leu), derived from the PDZ and DEP domains of DVL2, respectively, were enriched in cells expressing WT RIPK4 (fig. S9A). Both sites are conserved, being found in *Xenopus*, zebrafish, mouse, and human DVL isoforms (fig. S9B).

To determine if RIPK4 phosphorylated DVL2 directly, we purified the kinase domain of RIPK4 (amino acids 1 to 300) from Sf9 insect cells and tested its ability to phosphorylate the PDZ or DEP domains of DVL2 in vitro. The WT RIPK4 kinase domain, but not the K51R mutant, phosphorylated both domains, and mutation of DVL2 Ser<sup>298</sup> and Ser<sup>480</sup> prevented this phosphorylation (Fig. 3C). Antibodies recognizing each DVL2 phosphorylation site detected WT DVL2 overexpressed in 293T cells, but not DVL2 with the relevant serine residue mutated to alanine (fig. S9C). Further confirming the specificity of the antibodies, the WT DVL2 bands were not detected when the lysates were treated with calf intestinal alkaline phosphatase (fig. S9D). In keeping with DVL2 being a RIPK4 substrate, phosphorylation at Ser<sup>298</sup> and Ser<sup>480</sup> increased dramatically when DVL2 was cotransfected with RIPK4, but not RIPK4-K51R (fig. S9D).

When 293T cells were stimulated with Wnt3a, phosphorylation of DVL2 at Ser<sup>298</sup> and Ser<sup>480</sup>

increased transiently after 10 min (fig. S9E); this was attenuated by RIPK4 depletion (Fig. 3D and fig. S9E). To determine if DVL2 phosphorylation was necessary for Wnt3a signaling, we depleted *Dvl3* from *Dvl1*<sup>-/-</sup>*Dvl2*<sup>-/-</sup> mouse embryo fibroblasts to obtain DVL-null cells that were reconstituted with either WT or phospho-site mutant S298A/S480A DVL2. Cells expressing DVL2 S298A/S480A contained less cytosolic  $\beta$ -catenin after Wnt3a treatment than did cells expressing WT DVL2 (fig. S9F), suggesting that phosphorylation at one or both sites was necessary for maximal Wnt3a signaling.

Wnt3a treatment redistributes cytoplasmic DVL proteins into large signaling complexes detected as punctate structures by immunofluorescence microscopy (9). Approximately 20% of HeLa cells expressed DVL2-FLAG in puncta, whereas the rest contained cytoplasmic DVL2-FLAG (Fig. 3E). Cotransfection of RIPK4–green fluorescent protein (GFP) increased the percentage of cells with DVL2 puncta to more than 75% (Fig. 3E and fig. S10), suggesting that RIPK4 facilitates assembly of the DVL2 signalosome. DVL2 S298A/S480A did not form more puncta when coexpressed with RIPK4, whereas DVL2 containing a single Ser-to-Ala mutation behaved like WT DVL2 (Fig. 3E). These data indicate that RIPK4 phosphorylation at Ser<sup>298</sup> and Ser<sup>480</sup> promotes DVL2 signalosome assembly.

Mutations that enhance Wnt signaling are found in various human cancers (10), so we examined human tumors for overexpression of *RIPK4*. Microarray data revealed increased *RIPK4* mRNA in many ovarian, skin, and colorectal tumors (Fig. 4A). We detected RIPK4 protein and cytosolic  $\beta$ -catenin in several human ovarian adeno-

carcinomas; by contrast, RIPK4 was less abundant, and we did not detect cytosolic  $\beta$ -catenin in most noncancerous ovarian tissue samples (Fig. 4B and fig. S11A). To determine if RIPK4 contributes to tumor growth by enhancing Wnt signaling, we used a *RIPK4* short hairpin RNA (shRNA) to deplete RIPK4 from the Wnt-dependent human teratoma–derived NTERA-2 xenograft tumor model (11). We used colon HCT116 cells with an activating  $\beta$ -catenin mutation (12) as a control. Although RIPK4 depletion from the NTERA-2 and HCT116 cells was incomplete (fig. S11B), growth of the NTERA-2 cells in athymic nude mice was suppressed (Fig. 4, C and D). By contrast, RIPK4 depletion had no effect on HCT116 tumor growth. RIPK4 depletion from NTERA-2 tumors, but not HCT116 tumors, decreased expression of two Wnt-responsive genes, *GAD1* and *AXIN2* (fig. S11C), implying a critical role for RIPK4 in Wnt signaling upstream of  $\beta$ -catenin stabilization.

We have identified a RIPK4 signaling mechanism that might explain why its mutation in mammals causes severe developmental defects. RIPK4 appears to be recruited to the LRP6 co-receptor and phosphorylates DVL proteins after Wnt stimulation, leading to maximal stabilization of  $\beta$ -catenin and transcription of Wnt-responsive genes (fig. S12). Mutant forms of RIPK4 associated with human Bartsocas-Papas syndrome are compromised in this signaling ability. RIPK4 expression is restricted to vertebrates, indicating that phosphorylation of DVL proteins in lower organisms might require a different kinase. Finally, the finding that RIPK4-mediated Wnt signaling may promote human ovarian cancer suggests that small-molecule inhibitors of RIPK4 might hold therapeutic potential.

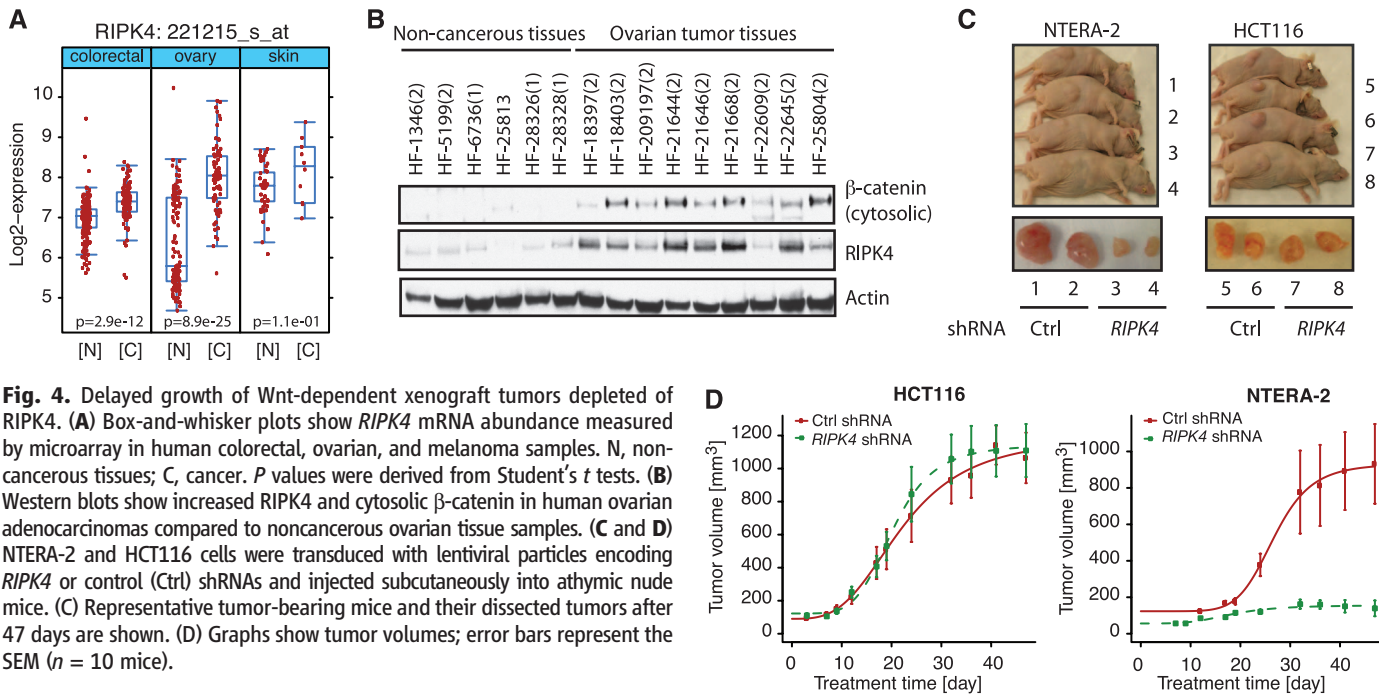


**Fig. 4.** Delayed growth of Wnt-dependent xenograft tumors depleted of RIPK4. **(A)** Box-and-whisker plots show *RIPK4* mRNA abundance measured by microarray in human colorectal, ovarian, and melanoma samples. N, non-cancerous tissues; C, cancer. *P* values were derived from Student's *t* tests. **(B)** Western blots show increased RIPK4 and cytosolic  $\beta$ -catenin in human ovarian adenocarcinomas compared to noncancerous ovarian tissue samples. **(C and D)** NTERA-2 and HCT116 cells were transduced with lentiviral particles encoding *RIPK4* or control (Ctrl) shRNAs and injected subcutaneously into athymic nude mice. **(C)** Representative tumor-bearing mice and their dissected tumors after 47 days are shown. **(D)** Graphs show tumor volumes; error bars represent the SEM (*n* = 10 mice).

## References and Notes

1. P. Holland *et al.*, *Curr. Biol.* **12**, 1424 (2002).
2. E. Kalay *et al.*, *Am. J. Hum. Genet.* **90**, 76 (2012).
3. K. Mitchell *et al.*, *Am. J. Hum. Genet.* **90**, 69 (2012).
4. Y. Zhang *et al.*, *Nat. Chem. Biol.* **5**, 217 (2009).
5. H. Clevers, R. Nusse, *Cell* **149**, 1192 (2012).
6. A. P. McMahon, R. T. Moon, *Cell* **58**, 1075 (1989).
7. W. T. Montross, H. Ji, P. D. McCrea, *J. Cell Sci.* **113**, 1759 (2000).
8. R. McKendry, S. C. Hsu, R. M. Harland, R. Grosschedl, *Dev. Biol.* **192**, 420 (1997).
9. K. Satoh *et al.*, *Proc. Natl. Acad. Sci. U.S.A.* **101**, 8017 (2004).
10. T. Schwarz-Romond, C. Merrifield, B. J. Nichols, M. Bienz, *J. Cell Sci.* **118**, 5269 (2005).
11. P. Polakis, *Genes Dev.* **14**, 1837 (2000).
12. V. I. DeAlmeida *et al.*, *Cancer Res.* **67**, 5371 (2007).
13. M. N. Kitaeva *et al.*, *Cancer Res.* **57**, 4478 (1997).

**Acknowledgments:** We thank K. O'Rourke, J. Huang, and the next-generation sequencing and baculovirus groups for technical assistance. The transcriptome sequencing data for PA1 cells have been submitted to the National Center for

Biotechnology Information, NIH, Gene Expression Omnibus ([www.ncbi.nlm.nih.gov/geo/](http://www.ncbi.nlm.nih.gov/geo/)) under accession no. GSE43362.

## Supplementary Materials

[www.sciencemag.org/cgi/content/full/science.1232253/DC1](http://www.sciencemag.org/cgi/content/full/science.1232253/DC1)  
Materials and Methods  
Figs. S1 to S12  
Table S1  
References (14–17)

1 November 2012; accepted 23 January 2013  
Published online 31 January 2013;  
10.1126/science.1232253

# A Localized Wnt Signal Orients Asymmetric Stem Cell Division in Vitro

Shukry J. Habib,<sup>1,2\*</sup> Bi-Chang Chen,<sup>2</sup> Feng-Chiao Tsai,<sup>3</sup> Konstantinos Anastassiadis,<sup>4</sup> Tobias Meyer,<sup>3</sup> Eric Betzig,<sup>2</sup> Roel Nusse<sup>1,3\*</sup>

Developmental signals such as Wnts are often presented to cells in an oriented manner. To examine the consequences of local Wnt signaling, we immobilized Wnt proteins on beads and introduced them to embryonic stem cells in culture. At the single-cell level, the Wnt-bead induced asymmetric distribution of Wnt- $\beta$ -catenin signaling components, oriented the plane of mitotic division, and directed asymmetric inheritance of centrosomes. Before cytokinesis was completed, the Wnt-proximal daughter cell expressed high levels of nuclear  $\beta$ -catenin and pluripotency genes, whereas the distal daughter cell acquired hallmarks of differentiation. We suggest that a spatially restricted Wnt signal induces an oriented cell division that generates distinct cell fates at predictable positions relative to the Wnt source.

Asymmetric cell division is a fundamental process involved in many aspects of stem cell biology and cancer (1), but insight into external cues that control asymmetric divisions is limited (2). Although much has been learned from examining asymmetric cell divisions in vivo (3–5), the complexity of tissues and the multiplicity of signals create challenges to understanding how localized growth factors affect cell behaviors at the single-cell level. Using in vitro studies, single cells and their divisions can be followed; however, growth factors that are added to the tissue medium present signals in a nonoriented way. To study how a given growth factor affects cell divisions or cell fates at the level of the individual cell, methods should be used to present purified signaling molecules in an oriented way.

Previously we found that Wnt3a protein maintains the self-renewal of several types of stem cells, including embryonic stem (ES) cells (6). Conversely, blocking endogenous Wnt signals made by ES cells leads to differentiation toward

Epiblast stem cells (EpiSCs) (6). ES cells are grown in media supporting pluripotency that include conditions that globally activate Wnt signaling (called 2i) (7, 8) and induce ES cells to divide in mainly symmetrical patterns (9). Hence, ES cells could provide a useful experimental model for assessing how a local rather than a global Wnt signal might direct stem cell fate choices.

To examine the effect of a spatially localized Wnt signal on ES cells, we immobilized Wnt signals to beads and observed single cells with live imaging. Although Wnt3a maintains ES cell pluripotency (6), the Wnt5a protein, which commonly operates through a non- $\beta$ -catenin-dependent pathway (10), did not (figs. S1 and S8F), allowing us to use Wnt5a as a control. We chemically immobilized purified Wnt3a or Wnt5a proteins to beads (figs. S2A and S3A) and confirmed their biological activity (figs. S2, B to D, and S3, B and C). ES cells were plated at low density in the presence of leukemia inhibitory factor (LIF), and individual cells with a bead attached were followed by live cell microscopy as they divided. We examined the location of Wnt signaling components by antibody staining. In the presence of Wnt3a beads (Fig. 1A), but rarely with Wnt5a beads (fig. S4), the Wnt receptor LRP6 became asymmetrically localized to the side of the ES cell contacting the bead. Moreover, a Frizzled1-GFP (green fluorescent protein) fusion protein (fig. S5) and the adenomatous polyposis coli (APC) protein, a component of the  $\beta$ -catenin destruc-

tion complex, were detected in close proximity to the Wnt3a beads (Fig. 1A and fig. S6).

In ES cells contacting Wnt3a beads before division,  $\beta$ -catenin was distributed asymmetrically close to the bead, overlapping with the location of APC (Fig. 1A and fig. S6). During division,  $\beta$ -catenin was retained at high abundance in the prospective proximal daughter cell, both at the cell membrane and in the nucleus (Fig. 1B). The asymmetric distribution of these Wnt components was maintained after the cells divided: The daughter cell in proximity to the Wnt3a bead preserved high amounts of LRP6 and APC, in contrast to the lower amounts in the distal cell (Fig. 1C and fig. S6).

Wnt pathway components can interact with astral microtubules and other components of the mitotic spindle, including centrosomes (11, 12). We investigated the effect of Wnt beads on the asymmetric inheritance of the centrosomes by expressing tagged Centrin1 (a component of the centriole) and the appendage component Ninein (13, 14). Ninein marks the centrosome with the older centriole (13–15), whereas the other centrosome receives new centrioles that initially lack these structures. By the end of division, centrosomes in 78% of the cells ( $n = 18$ ) that were attached to Wnt3a beads had a high abundance of Ninein (Fig. 2, A and B), whereas the segregation of Ninein was almost random in the presence of the Wnt5a beads (54%;  $n = 15$ ). Thus, the association with Wnt3a beads correlates with the asymmetric inheritance of centrosomes.

Because centrosomes orient the mitotic spindle, we investigated whether Wnt beads direct the orientation of cell division and partitioning of chromosomes during mitosis (16). ES cells expressing a histone 2B-Venus chimeric protein to mark chromosomes (Fig. 2, C and D) were incubated with Wnt beads and monitored during mitosis by rapid three-dimensional imaging of living cells (17). In 75% of the dividing cells ( $n = 16$ ), the axis of mitotic division was oriented in line with the Wnt3a bead (Fig. 2C and movie S1), whereas only 12% of divisions were oriented toward Wnt5a control beads ( $n = 12$ ; Fig. 2D and movie S2).

We investigated the effect of localized Wnt signals on pluripotency gene expression, by using various ES reporter cells including cells expressing a Nanog-Venus fusion protein and GFP-based reporters for Rex1, Sox2, and Stella (18–21). Pluripotency proteins were also followed by

<sup>1</sup>Department of Developmental Biology, Howard Hughes Medical Institute, Institute for Stem Cell Biology and Regenerative Medicine, Stanford University, 265 Campus Drive, Stanford, CA 94305, USA. <sup>2</sup>Janelia Farm Research Campus, 19700 Helix Drive, Ashburn, VA 20147, USA. <sup>3</sup>Department of Chemical and Systems Biology, Stanford University, Stanford, CA 94305, USA. <sup>4</sup>BIOTEC, Technische Universität Dresden Tatzberg 47-51, 01307 Dresden, Germany.

\*Corresponding author. E-mail: [rnusse@stanford.edu](mailto:rnusse@stanford.edu) (R.N.); [shabib@stanford.edu](mailto:shabib@stanford.edu) (S.J.H.)



antibody staining. The expression of Nanog, Rex1, and Stella has been shown to decline during ES cell differentiation (18–23). In dividing ES cells, we found that the transcriptional activities and protein abundance of the pluripotency markers were markedly higher in the Wnt3a-proximal daughter compared to the distal one (Fig. 3, A to C; fig. S7C; fig. S8, A to C; and fig. S9; and movies S3 to S6). Differences in gene expression levels were detectable before cytokinesis was complete (Fig. 3B, at 140 min; fig. S9A (a), at 120 min; and fig. S9B (a), at 200 min). By contrast, in the presence of Wnt5a beads, the two daughters had similar levels of marker expression (Fig. 3C; fig. S7, A to C, fig. S8, D to F; and fig. S9; and movies S7 to S10). As might be expected, cells exposed to two Wnt3a beads at opposing ends divided symmetrically (fig. S10). As additional controls, we generated attenuated forms of Wnt3a, using Wnt3a beads that were treated after coupling with a range of concentrations of the reducing agent dithiothreitol, lowering the signaling activity of the beads in a dose-dependent manner (fig. S3, B and C). The potency of these beads in inducing asymmetric gene expression of the reporter Rex1-GFP was reduced commensurate with the remaining level of Wnt signaling (fig. S6). We also tested the activity of another signal implicated in the Wnt pathway; an active form of R-Spondin bound to beads (fig. S11A). There was no significant effect on asymmetric gene expression (Fig. 3C), possibly related to the behavior of R-Spondin in vivo, where it acts as a systemic rather than a local Wnt activator (24).

Under “standard” conditions, including feeder cells that can be source of Wnts or the 2i conditions, ES cells divide mainly symmetrically (6–9). We asked whether a global Wnt environment would be required for the symmetrical divisions that ES cells undergo. As a test, we perturbed Wnt signaling locally by applying the Wnt inhibitor Dickkopf (DKK) on beads (fig. S11B). Under these conditions, we found a significant number of divisions giving rise to asymmetric gene expression in the daughter cells, but in a manner opposite to that induced by the Wnt beads. With DKK-beads, the distal cell had higher expression of the pluripotency gene Rex1 than the proximal cell (Fig. 3C). We could rescue the effect of a local Wnt or Wnt inhibition by incubating the cells at the same time under the 2i conditions (7, 8), indicating that the asymmetry induced by Wnt3a or DKK beads was not a nonspecific perturbation of the cells (Fig. 3C). We argue, based on the asymmetric Wnt inhibition experiments, that uniform Wnt signaling is required for symmetric daughter cell fate.

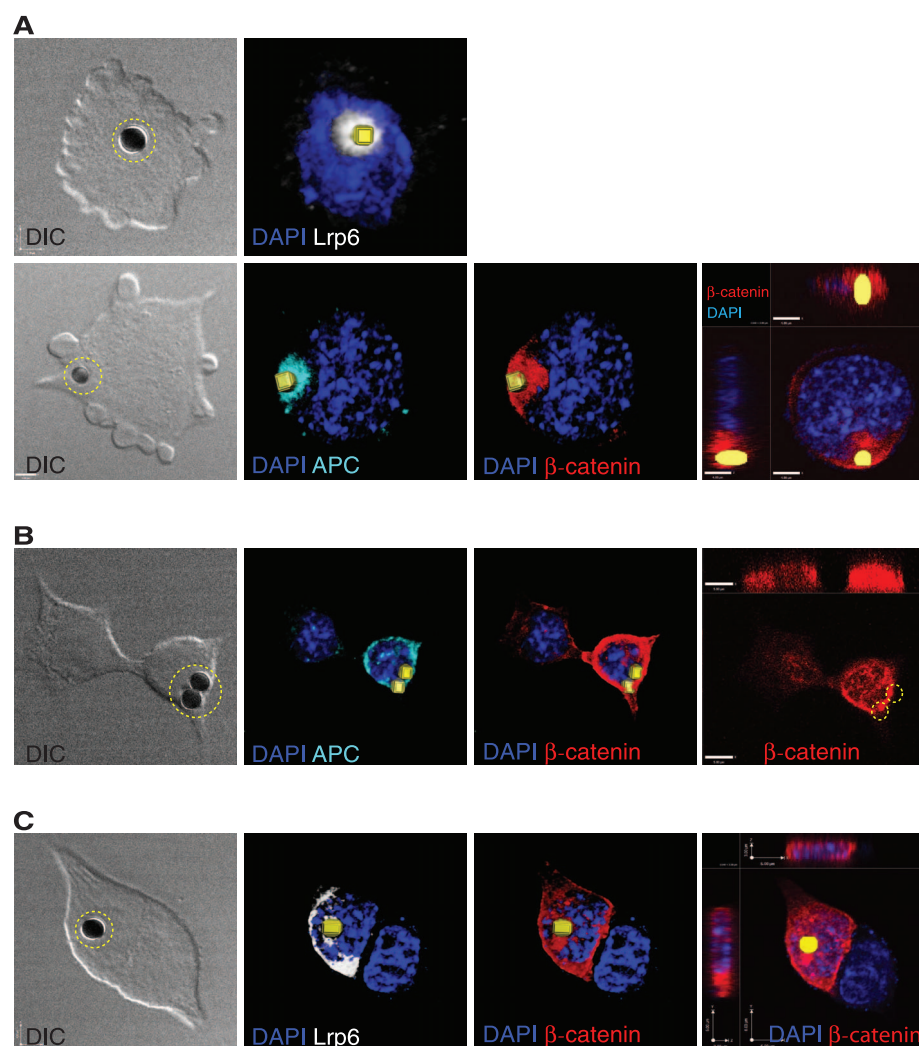
The lower levels of pluripotency markers in the Wnt3a-distal daughter cell suggested that distal cells enter a differentiation program with hallmarks of EpiSCs (22). The pluripotency gene *Oct4* is expressed at similar levels in ES cells and EpiSCs (6, 25, 26). We observed symmetrical distribution of Oct4-Venus after cell division,

either in the presence of Wnt3a or Wnt5a beads (Fig. 4, A and B). We assessed the expression of EpiSC markers, including Claudin6 (6, 25), which was higher in 60% of Wnt3a-distal cells (Fig. 4C) compared to Wnt5a distal cells (23% asymmetric expression; fig. S12). H3K27me3 focal staining, a hallmark of an inactivated X chromosome in female ES cells (27), was detected in 57% of Wnt3a bead–distal ES cells after division (Fig. 4D). Thus, localized Wnt3a signal specifies that the Wnt3a-distal cell enters a differentiation program with hallmarks of EpiSC fate.

The findings reported here suggest a mechanism for external control of asymmetric stem cell division and differentiation. Specifically, a spatially localized Wnt signal orients the mitotic division plane of stem cells. Then, in the dividing cell, the Wnt signal produces an asymmetric distribution of Wnt signaling components, generating a “Wnt-on” proximal cell that maintains

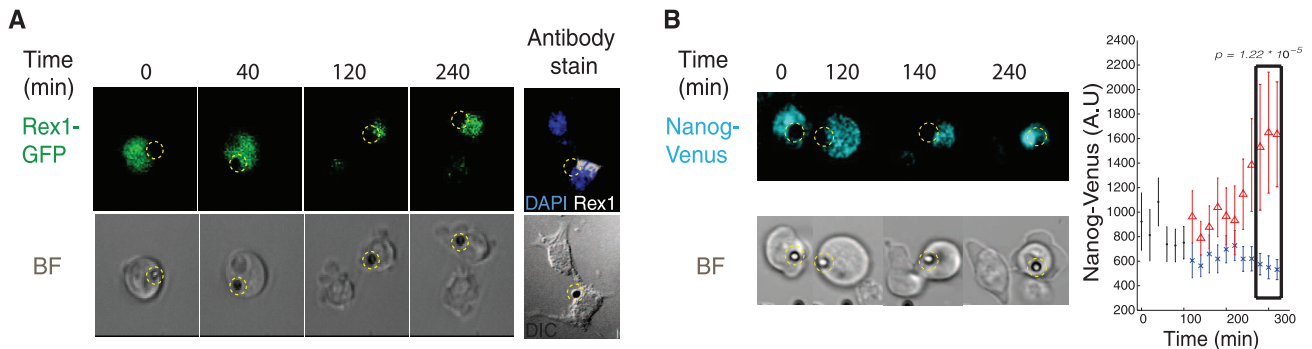
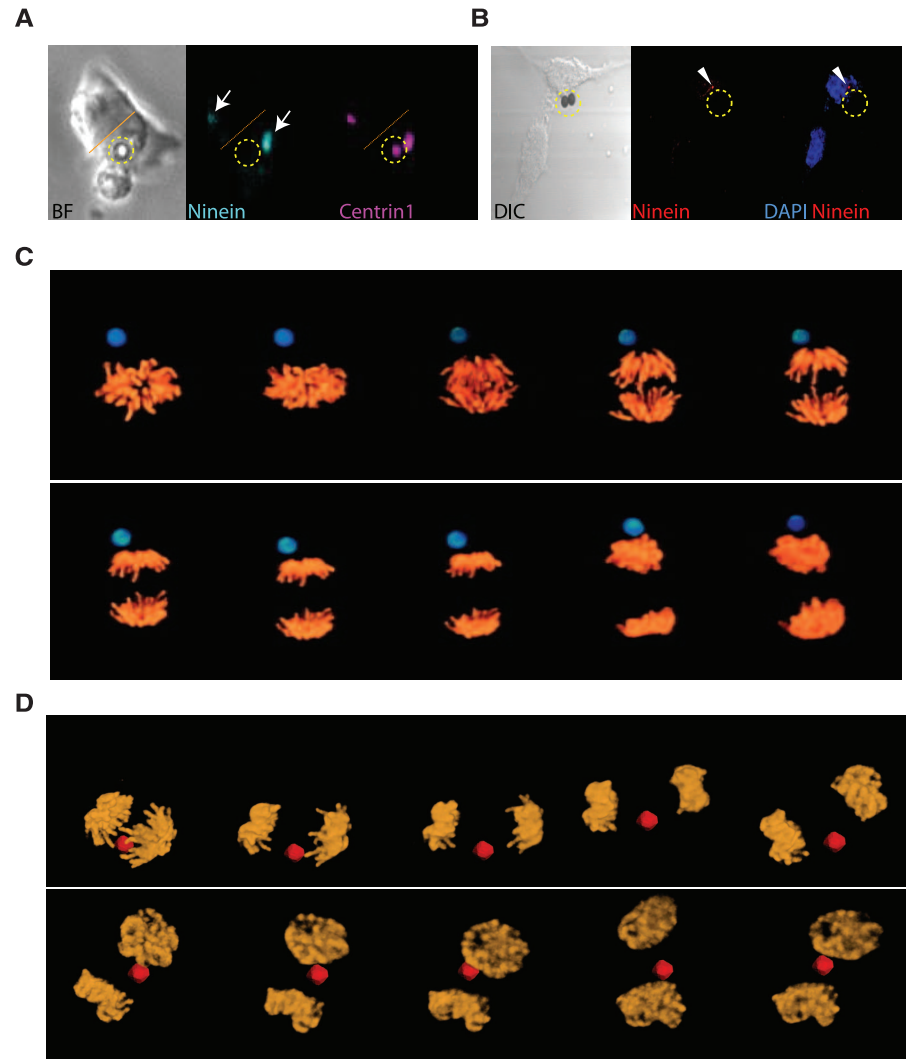
ES pluripotency and a “Wnt-off” distal cell that differentiates toward an EpiSC cell fate. Therefore, by orienting cell division, the Wnt signal positions the distal daughter cell out of its signaling range, leading to differentiation.

Although the protein distribution of Wnt signals in tissues is mostly unknown, a role for Wnts in setting up polarity is supported by findings made in vivo. Wnt signaling receptors in *Caenorhabditis elegans* and *Drosophila* distribute asymmetrically in cells that are exposed to local Wnt sources (28, 29). In *C. elegans*, the position of the P2 cell, which expresses Wnt, determines the polarity and divisional orientation of the neighboring EMS cell, leading to different fates of the EMS daughters (3–5). By growing single cells exposed to a symmetry-breaking signal, we have developed a system that allows for precise real-time examination of processes involved in asymmetric cell divisions.

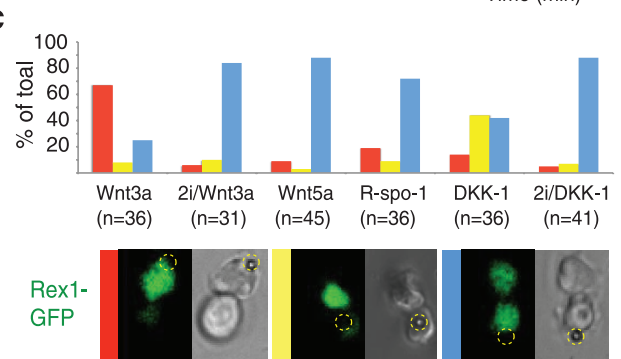


**Fig. 1.** Wnt3a beads induce asymmetric distribution of components of the Wnt/β-catenin pathway. Representative images of ES cells cocultured with Wnt3a beads (indicated by dashed yellow circle or reconstructed as a yellow square) and stained with antibodies to LRP6 (white), APC (cyan), and β-catenin (red). (A) Before division; (B) during division; (C) after division. The beads are 2.8 μm. The far right panels show optical sections through the nucleus. DAPI, 4',6-diamidino-2-phenylindole; DIC, differential interference contrast.

**Fig. 2.** Asymmetric inheritance of centrosomes and the orientation of the plane of mitotic division. Time-lapse imaging of dividing single ES cells cocultured with Wnt3a beads (indicated by a dashed yellow circle) and (A) expressing enhanced green fluorescent protein (EGFP)–Ninein (cyan; arrows) and DsRedex–Centrin1 (magenta). Dotted orange line indicates the boundary between two cells. (B) Immunostaining for endogenous Ninein (arrowheads). BF: bright-field image. (C and D) Representative images from three-dimensional time-lapse microscopy of segregating chromosomes in ES cells expressing H2B–Venus that were cocultured with Wnt3a beads (blue) or Wnt5a beads (red).



**Fig. 3.** Expression of the pluripotency genes Rex1 and Nanog during ES cell division. (A) Selected frames from time-lapse imaging of a dividing Rex-1 GFP reporter ES cell in the presence of a Wnt3a bead (indicated by a dashed yellow circle). The far right panel shows antibody staining for endogenous Rex-1 protein. (B) Selected frames from time-lapse imaging of a dividing Nanog-Venus reporter ES cell in the presence of a Wnt3a bead. Signal intensities of all frames were individually determined, and the mean  $\pm$  SD intensity values plotted. Red triangles represent signal intensities of the cell retaining contact with the bead after division. (C) Representative images of time-lapse microscopy of dividing Rex-1 GFP ES reporter cells cocultured in the presence of the indicated beads in 2i or 2i-free media. Cell divisions were classified based on the relative expression of GFP and plotted. Red bar: higher GFP amounts in the bead-proximal cell; yellow bar: higher amounts of GFP in the bead-distal cell; blue bar: similar amounts of GFP in either cell.





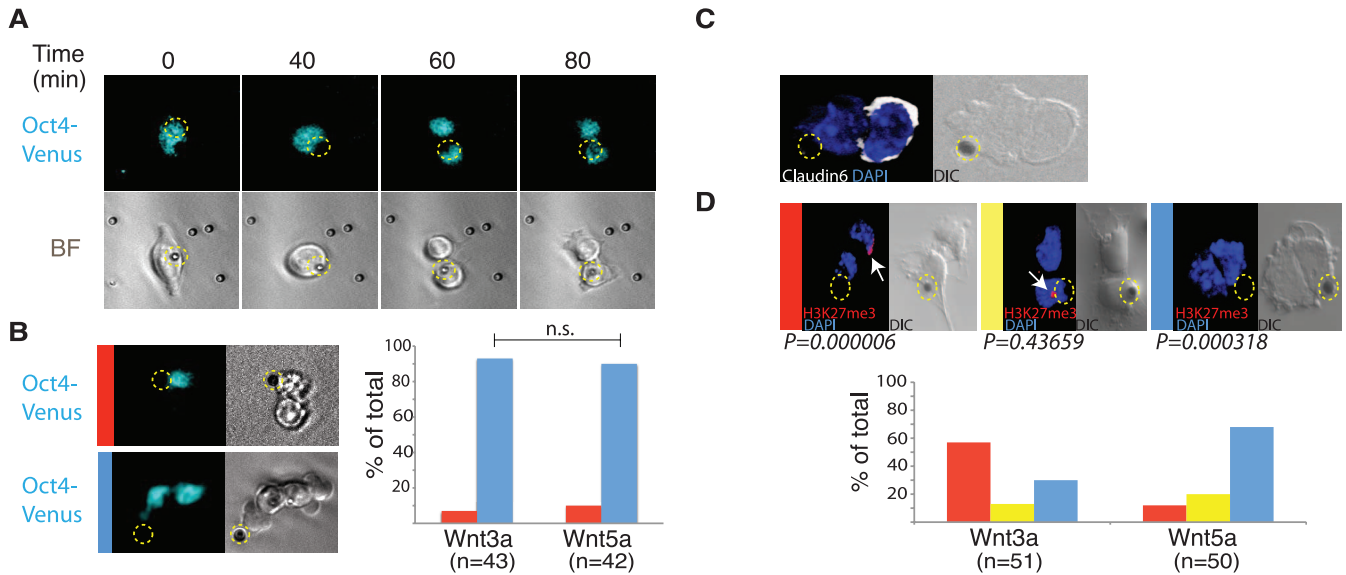


**Fig. 4.** Distal cells express markers of epiblast stem cell fate. **(A)** Selected frames from time-lapse imaging of a dividing Oct4-Venus reporter ES cell cocultured with a Wnt3a bead (indicated by a dashed yellow circle). **(B)** Divisions of Oct4-Venus ES cells cocultured with Wnt3a or Wnt5a beads were classified based on the relative expression of Venus, and plotted. Red bar: higher Venus abundance in the bead-proximal cell; blue bar: similar abundance of Venus in

both cells. **(C)** Antibody staining for Claudin6 in an ES cell cocultured with a Wnt3a bead. **(D)** Representative images of antibody staining for H3K27me3 (arrows) in LF2 female ES cells cocultured with Wnt3a or Wnt5a beads. Dividing cells were classified based on location of the H3K27me3 stain, and plotted. Red bar: H3K27me3 stain in the bead-proximal cell; yellow bar: H3K27me3 stain in the bead-distal cell; blue bar: no H3K27me3 stain in any cell.

#### References and Notes

1. R. A. Neumüller, J. A. Knoblich, *Genes Dev.* **23**, 2675 (2009).
2. A. D. Werts, B. Goldstein, *Semin. Cell Dev. Biol.* **22**, 842 (2011).
3. T. Walston *et al.*, *Dev. Cell* **7**, 831 (2004).
4. B. Goldstein, H. Takeshita, K. Mizumoto, H. Sawa, *Dev. Cell* **10**, 391 (2006).
5. K. Sugiyama, K. Mizumoto, H. Sawa, *Cell* **146**, 942 (2011).
6. D. ten Berge *et al.*, *Nat. Cell Biol.* **13**, 1070 (2011).
7. N. Sato, L. Meijer, L. Skaltsounis, P. Greengard, A. H. Brivanlou, *Nat. Med.* **10**, 55 (2004).
8. Q.-L. Ying *et al.*, *Nature* **453**, 519 (2008).
9. A. Surani, J. Tischler, *Nature* **487**, 43 (2012).
10. A. J. Mikels, R. Nusse, *PLoS Biol.* **4**, e115 (2006).
11. S. Bahmanyar *et al.*, *Genes Dev.* **22**, 91 (2008).
12. Y. M. Yamashita, D. L. Jones, M. T. Fuller, *Science* **301**, 1547 (2003).
13. M. M. Mogensén, A. Malik, M. Piel, V. Bouckson-Castaing, M. Bornens, *J. Cell Sci.* **113**, 3013 (2000).
14. X. Wang *et al.*, *Nature* **461**, 947 (2009).
15. M. Bornens, *Science* **335**, 422 (2012).
16. Y. M. Yamashita, M. T. Fuller, *J. Cell Biol.* **180**, 261 (2008).
17. T. A. Planchon *et al.*, *Nat. Methods* **8**, 417 (2011).
18. B. Payer *et al.*, *Genesis* **44**, 75 (2006).
19. Y. Toyooka, D. Shimosato, K. Murakami, K. Takahashi, H. Niwa, *Development* **135**, 909 (2008).
20. K. Hayashi, S. M. Lopes, F. Tang, M. A. Surani, *Cell Stem Cell* **3**, 391 (2008).
21. K. Arnold *et al.*, *Cell Stem Cell* **9**, 317 (2011).
22. A. M. Singh, T. Hamazaki, K. E. Hankowski, N. Terada, *Stem Cells* **25**, 2534 (2007).
23. I. Chambers *et al.*, *Nature* **450**, 1230 (2007).
24. K. A. Kim *et al.*, *Science* **309**, 1256 (2005).
25. P. J. Tesar *et al.*, *Nature* **448**, 196 (2007).
26. G. Guo *et al.*, *Development* **136**, 1063 (2009).
27. K. Plath *et al.*, *Science* **300**, 131 (2003).
28. M. A. Hilliard, C. I. Bargmann, *Dev. Cell* **10**, 379 (2006).
29. C. Korkut *et al.*, *Cell* **139**, 393 (2009).

**Acknowledgments:** These studies were supported by the Howard Hughes Medical Institute and by grants RC1-00133-1, RB4-05825, and TR1-02149 from the California Institute for Regenerative Medicine to R.N.; by NIH grant GM063702 to T.M.; and by the Center for Regenerative Therapies Dresden and grant DFG-SPP1356 to K.A. We thank the Stanford

Neuroscience Microscopy Service, supported by NIH NS069375. Patent applications are pending for the Bessel beam plane illumination microscopy (by E.B.) and for the Wnt, DKK, and R spondin1 immobilization technology and their applications (by S.J.H. and R.N.). We also thank M. Drukker, T. Schroeder, and T. Stearns for discussions. We appreciate discussions and comments on the manuscript by C. Logan and J. Nelson. S.J.H. was supported by a fellowship from the Deutsche Forschungsgemeinschaft (DFG) and a Siebel scholarship.

#### Supplementary Materials

www.sciencemag.org/cgi/content/full/339/6126/1445/DC1  
Materials and Methods  
Figs. S1 to S12  
Movies S1 to S10  
References (30–33)

3 October 2012; accepted 12 February 2013  
10.1126/science.1231077

## Type I Interferon Suppresses Type II Interferon–Triggered Human Anti-Mycobacterial Responses

Rosane M. B. Teles,<sup>1</sup> Thomas G. Graeber,<sup>4</sup> Stephan R. Krutzik,<sup>1</sup> Dennis Montoya,<sup>1</sup> Mirjam Schenk,<sup>1</sup> Delphine J. Lee,<sup>5</sup> Evangelia Komisopoulou,<sup>4</sup> Kindra Kelly-Scumpia,<sup>1</sup> Rene Chun,<sup>3</sup> Shankar S. Iyer,<sup>2</sup> Euzenir N. Sarno,<sup>6</sup> Thomas H. Rea,<sup>7</sup> Martin Hewison,<sup>3</sup> John S. Adams,<sup>3</sup> Stephen J. Popper,<sup>8</sup> David A. Relman,<sup>8,9</sup> Steffen Stenger,<sup>10</sup> Barry R. Bloom,<sup>11</sup> Genhong Cheng,<sup>2</sup> Robert L. Modlin<sup>1,2\*</sup>

Type I interferons (IFN- $\alpha$  and IFN- $\beta$ ) are important for protection against many viral infections, whereas type II interferon (IFN- $\gamma$ ) is essential for host defense against some bacterial and parasitic pathogens. Study of IFN responses in human leprosy revealed an inverse correlation between IFN- $\beta$  and IFN- $\gamma$  gene expression programs. IFN- $\gamma$  and its downstream vitamin D–dependent antimicrobial genes were preferentially expressed in self-healing tuberculoid lesions and mediated antimicrobial activity against the pathogen *Mycobacterium leprae* in vitro. In contrast, IFN- $\beta$  and its downstream genes, including interleukin-10 (IL-10), were induced in monocytes by *M. leprae* in vitro and preferentially expressed in disseminated and progressive lepromatous lesions. The IFN- $\gamma$ –induced macrophage vitamin D–dependent antimicrobial peptide response was inhibited by IFN- $\beta$  and by IL-10, suggesting that the differential production of IFNs contributes to protection versus pathogenesis in some human bacterial infections.

The identification of mechanisms of host resistance versus susceptibility is central to our ability to develop new approaches to

prevent and/or treat human infectious diseases. In most instances, the human immune response restricts the infection, preventing or limiting the

extent of disease. However, in some individuals the infection is not contained and instead progresses. Protective immunity against many intracellular bacteria depends on type 1 helper ( $T_H1$ ) T cell responses, in particular the production of the type II interferon (IFN), IFN- $\gamma$ , which can activate antimicrobial responses (1). However, the induction of type I IFNs, important for host defense against viral infections, is ineffective in the context of bacterial pathogens (2), such as

*Mycobacterium tuberculosis*, and is associated with a greater extent of disease (3). These clinical-immunological correlations suggest that type I IFNs can suppress IFN- $\gamma$ -induced antimicrobial responses in humans.

To explore the mechanisms by which type I IFNs may suppress IFN- $\gamma$ -induced host defense responses, we chose leprosy, a disease of skin and nerves caused by the intracellular pathogen *Mycobacterium leprae*, as a model for understanding the dynamics of immune responses in skin lesions. The clinical presentations of leprosy compose a spectrum that correlates with the type of immune response induced. In the self-healing tuberculoid (T-lep) form, the host immune response is able to effectively combat the pathogen, there are few skin lesions, and bacteria are rare. In the disseminated lepromatous (L-lep) form, the host immune response fails, resulting in numerous skin lesions characterized by abundant intracellular bacilli. T-lep lesions express  $T_H1$  cytokines including IFN- $\gamma$ , whereas L-lep lesions are characterized by  $T_H2$  cytokines as well as interleukin-10 (IL-10) (4). Reversal reactions (RRs) represent a shift from the L-lep toward the T-lep form, accompanied by a reduction of bacilli in lesions and enhanced  $T_H1$  cytokine responses (5).

The gene expression profiles of skin lesions from leprosy lesions were first evaluated by principal component analysis and hierarchical clus-

tering analysis (Fig. 1, A and B, and fig. S1), both revealing a distinct gene expression profile in L-lep lesions as compared with T-lep and RR lesions. Although the signal for all type I IFN mRNAs, including all 13 IFN- $\alpha$  genes and one IFN- $\beta$  gene, was within the microarray background noise resulting in absent calls, integration of the leprosy gene expression profiles with IFN-induced transcriptional profiles in healthy human peripheral blood mononuclear cells (PBMCs) (6) revealed that genes specifically induced by IFN- $\beta$ , including IL-10, were significantly enriched in the L-lep gene expression profile. In contrast, IFN- $\gamma$ -specific genes were significantly enriched in the T-lep (Fig. 1C and fig. S2) and RR lesions (fig. S3). The presence of a type I IFN gene expression signature in L-lep lesions was confirmed by analysis using the “interferome” database of IFN-regulated genes (7) (fig. S4).

An overall summation score of the IFN- $\beta$  and IFN- $\gamma$  profiles of each leprosy patient, calculated by using a gene voting approach (8), revealed a significant inverse correlation between the IFN-inducible programs; the IFN- $\beta$  profile greatest and the IFN- $\gamma$  profile lowest in L-lep lesions; and the IFN- $\gamma$  profile greatest and IFN- $\beta$  lowest in T-lep and RR lesions ( $r = -0.89$ , Fig. 1D). Further analysis revealed in L-lep lesions an IFN- $\beta$ →IL-10 pathway (9), previously shown to inhibit IFN- $\gamma$  activation of macrophages in a mouse model

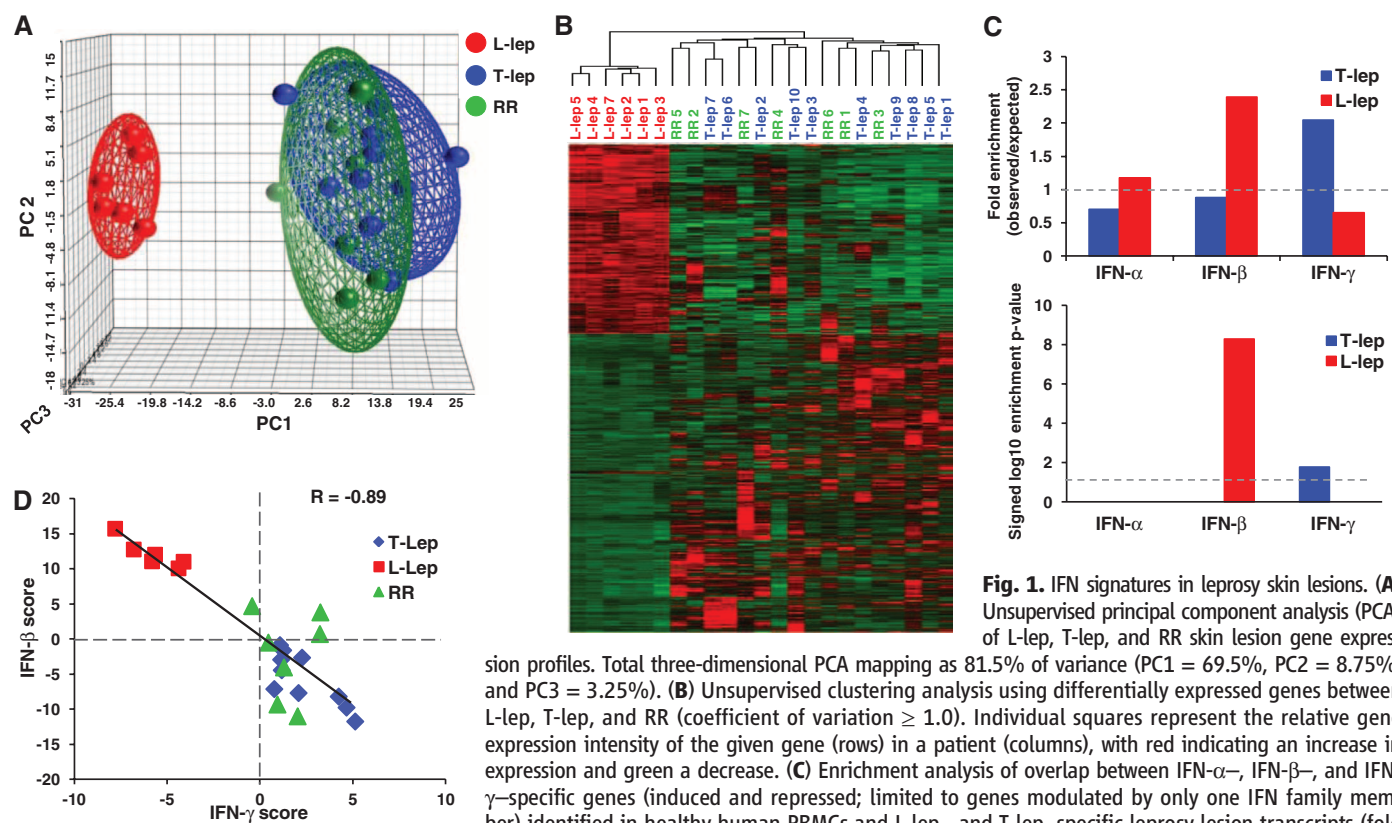


**Fig. 1.** IFN signatures in leprosy skin lesions. (A) Unsupervised principal component analysis (PCA) of L-lep, T-lep, and RR skin lesion gene expression profiles. Total three-dimensional PCA mapping as 81.5% of variance (PC1 = 69.5%, PC2 = 8.75%, and PC3 = 3.25%). (B) Unsupervised clustering analysis using differentially expressed genes between L-lep, T-lep, and RR (coefficient of variation  $\geq 1.0$ ). Individual squares represent the relative gene expression intensity of the given gene (rows) in a patient (columns), with red indicating an increase in expression and green a decrease. (C) Enrichment analysis of overlap between IFN- $\alpha$ -, IFN- $\beta$ -, and IFN- $\gamma$ -specific genes (induced and repressed; limited to genes modulated by only one IFN family member) identified in healthy human PBMCs and L-lep- and T-lep-specific leprosy lesion transcripts (fold change  $\geq 1.5$  and  $P \leq 0.05$ ). Dotted lines indicate either the expected fold enrichment of one (top) or the

hypergeometric enrichment  $P$  value of 0.05 ( $\log P = 1.3$ , bottom). Hypergeometric analyses were performed to determine fold enrichment (observed/expected) and signed log enrichment  $P$  value (negative for deenriched). The Bonferroni multiple hypothesis test correction was applied for each group ( $n = 6$ ). (D) IFN- $\beta$ - and IFN- $\gamma$ -specific gene voting summation scores were calculated for individual patient lesions in the leprosy subtypes of L-lep, T-lep, and RR.

<sup>1</sup>Division of Dermatology, David Geffen School of Medicine at University of California, Los Angeles, CA 90095, USA. <sup>2</sup>Department of Microbiology, Immunology and Molecular Genetics, David Geffen School of Medicine at University of California, Los Angeles, CA 90095, USA. <sup>3</sup>UCLA/Orthopedic Hospital Department of Orthopedic Surgery, David Geffen School of Medicine at University of California, Los Angeles, CA 90095, USA. <sup>4</sup>Crump Institute for Molecular Imaging, Institute for Molecular Medicine, Johnson Comprehensive Cancer Center, California NanoSystems Institute, Department of Molecular and Medical Pharmacology, University of California, Los Angeles, CA 90095, USA. <sup>5</sup>Department of Translational Immunology, John Wayne Cancer Institute, Santa Monica, CA, USA. <sup>6</sup>Department of Mycobacteriosis, Oswaldo Cruz Foundation, Rio de Janeiro, RJ, Brazil. <sup>7</sup>Department of Dermatology, University of Southern California School of Medicine, Los Angeles, CA 90033, USA. <sup>8</sup>Department of Microbiology and Immunology and Department of Medicine, Stanford University School of Medicine, Stanford, CA 94305, USA. <sup>9</sup>Veterans Affairs Palo Alto Health Care System, Palo Alto, CA 94304, USA. <sup>10</sup>Institute for Medical Microbiology and Hygiene, University Hospital of Ulm, Germany. <sup>11</sup>Harvard School of Public Health, Boston, MA 02115, USA.

\*Corresponding author. E-mail: rmodlin@mednet.ucla.edu



of infection (10). In contrast, an IFN- $\gamma$ -inducible vitamin D-dependent antimicrobial pathway (11) was found in the T-lep and RR lesions (fig. S5).

Analogous to leprosy, most individuals infected with *M. tuberculosis* localize and cure or contain the infection (latent tuberculosis); but in about 10% of patients the infection progresses to clinical disease, including pulmonary tuberculosis. A key study of gene expression profiles in peripheral blood from tuberculosis patients found a differential expression of an IFN-inducible gene profile in patients with active versus latent disease (3); the training cohort from this study is referred to here as TB1. Integration of the TB1 gene expression profiles with the PBMC-defined IFN-specific genes revealed an IFN- $\beta$ -induced gene program in active tuberculosis (figs. S6 and S7). Comparison of the IFN- $\beta$  signature in L-lep lesions versus TB1 as well as a second independent active tuberculosis cohort, TB2 (12), identified a common signature of 16 IFN- $\beta$ -induced genes (hypergeometric  $P$  value = 0.0007, fig. S7). Further integration with the gene expression profile of IL-10-treated monocytes revealed that 9 of 16 IFN- $\beta$ -induced genes in the leprosy and tuberculosis common signature are also downstream of IL-10 (hypergeometric  $P$  value = 0.02, fig. S7). The data indicate that a common IFN- $\beta$ -inducible gene program correlates with extent of disease in both leprosy and tuberculosis, suggesting that IFN- $\beta$  is a common factor contributing to pathogenesis in the two distinct mycobacterial diseases.

IFN- $\beta$  mRNA, detected by polymerase chain reaction (PCR), was more strongly expressed in L-lep versus T-lep lesions and L-lep versus RR lesions [analysis of variance (ANOVA),  $P < 0.05$ , Fig. 2A]. The mRNA expression for IFNAR1, encoding one of the type I IFN receptors, was more strongly expressed in L-lep versus either T-lep or RR lesions (Fig. 2A). In contrast, IFN- $\gamma$  mRNA was more highly expressed in both T-lep and RR versus L-lep lesions (Kruskal-Wallis,  $P < 0.05$ , Fig. 2A), consistent with previous findings by in situ hybridization (13) and PCR (4, 5). IFN- $\beta$  and IFNAR1 protein expression was also more evident in L-lep than T-lep or RR lesions, being present in cells throughout the granuloma (Fig. 2B and fig. S8). IFN- $\beta$  protein was found to localize in macrophages in L-lep lesions (figs. S9 to S11) colocalizing with CD14, CD209, and CD163 (14). The elevated expression of IL-10 transcripts in L-lep versus T-lep and RR in lesions, as well as other classic type I IFN-inducible genes, was also corroborated by PCR (Fig. 3A and fig. S12). IL-10 protein was also more highly expressed in L-lep lesions (Fig. 3B), in macrophages as well as T cells (figs. S13 and S14). Double immunofluorescence revealed that IFN- $\beta$  and IL-10 are coexpressed in L-lep lesions, with some cells expressing individual cytokines (Fig. 3C and fig. S15).

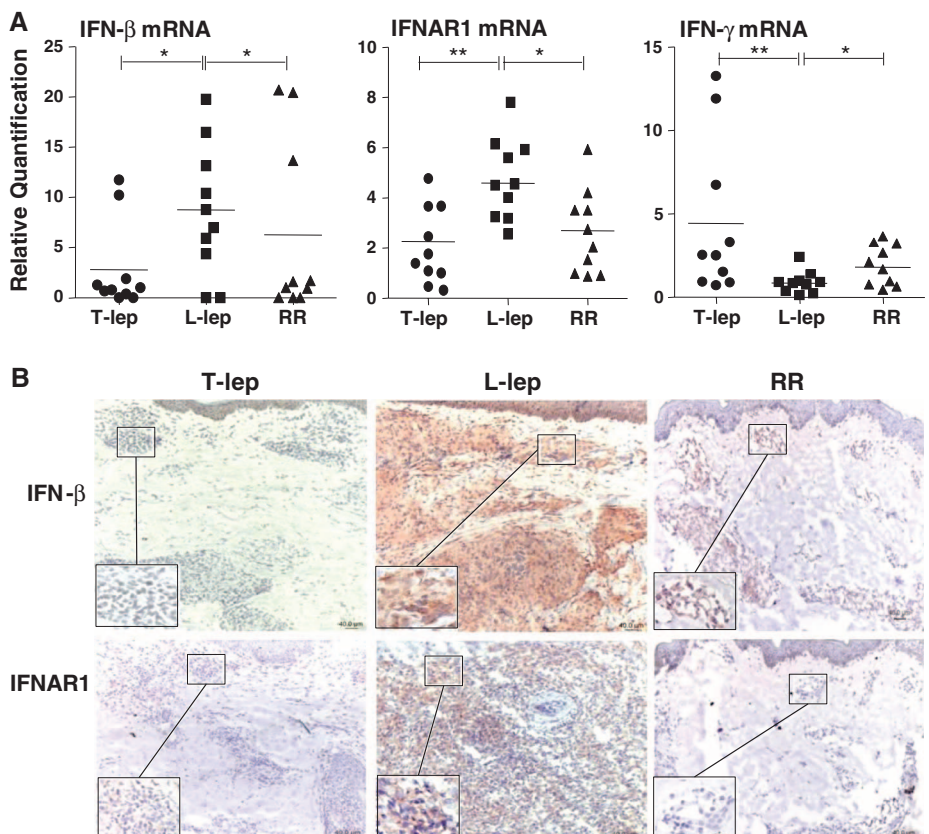
Both live and sonicated *M. leprae* induced IFN- $\beta$  mRNA and protein in vitro (Fig. 3D). Investigation of the relation between IFN- $\beta$  and IL-10 revealed that IFN- $\beta$  was sufficient to in-

duce IL-10 secretion (fig. S16) and that *M. leprae* induction of IL-10 (Fig. 3E) was partially dependent on type I IFN signaling, blocked by about 40% by monoclonal antibodies (mAbs) against IFNAR2 (anti-IFNAR2) (Fig. 3F and fig. S17) (9). Together, these data provide evidence for an *M. leprae*→IFN- $\beta$ →IL-10 pathway in L-lep lesions.

Analysis of the IFN- $\gamma$ -induced genes in T-lep lesions revealed several antimicrobial pathways, including activation of the vitamin D-dependent antimicrobial pathway, which leads to the induction of the antimicrobial peptides CAMP (cathelicidin) and DEF4 (beta-defensin 2), previously shown to be involved in antimicrobial activity in leprosy (14, 15) and tuberculosis (1, 11, 16, 17). The gene expression data confirmed the differential expression in T-lep and RR versus L-lep lesions of CYP27B1 mRNA, which encodes the vitamin D-1 $\alpha$ -hydroxylase that converts the prohormone 25-hydroxyvitamin D [25(OH)D] to the bioactive 1,25-dihydroxyvitamin D [1,25(OH) $_2$ D] form, as well as the mRNA for the vitamin D receptor (VDR), the transducer of 1,25(OH) $_2$ D-directed action in the nucleus of the cell (Fig. 4A). The expression of both CYP27B1 and the VDR were inversely correlated with IL-10 expression in the lesions (fig. S18).

On the basis of the differential expression of type I versus type II IFN-inducible pathways in leprosy, we hypothesized that IFN- $\beta$  and IL-10 inhibited the IFN- $\gamma$ -induced antimicrobial pathway. The ability of IFN- $\gamma$  to up-regulate CYP27B1

**Fig. 2.** IFN- $\beta$  is up-regulated in L-lep lesions. (A) Total mRNA was isolated from L-lep ( $n = 10$ ), T-lep ( $n = 10$ ), and RR ( $n = 10$ ) skin lesions; and the IFN- $\beta$ , IFNAR1, and IFN- $\gamma$  mRNA levels were analyzed by quantitative PCR (qPCR). The levels of IFN- $\beta$ , IFNAR1 and IFN- $\gamma$  were normalized to glyceraldehyde-3-phosphate dehydrogenase (GAPDH) levels in the same tissue. Statistical significance was calculated by one-way ANOVA followed by the posttest, Newman-Keuls multiple comparison test for IFN- $\beta$  and IFNAR1, and Kruskal-Wallis followed by Dunn's multiple comparison test for IFN- $\gamma$ . \*\* $P \leq 0.01$ ; \* $P \leq 0.05$ . (B) IFN- $\beta$  and IFNAR1 expression were detected in leprosy lesions (T-lep, L-lep, and RR); one representative labeled section is shown out of at least five; scale bars, 40  $\mu$ m. Original magnification, 100 $\times$ . (Insets) Higher magnification of inflammatory infiltrate areas. Original magnification, 400 $\times$ .



and VDR expression was completely blocked by the addition of IFN- $\beta$  or IL-10 (fig. S19). In addition, the ability of IFN- $\beta$  to inhibit IFN- $\gamma$  induction of CYP27B1 and VDR was reversed by the addition of neutralizing monoclonal anti-IL-10 (fig. S19). IL-10 also inhibited IFN- $\gamma$  induction of CYP27B1 activity in macrophages (18), blocking the metabolic conversion of 25(OH)D to bioactive 1,25(OH) $_2$ D (19) (Fig. 4B). Although IFN- $\gamma$  weakly inhibited the vitamin D-24-hydroxylase activity [catabolism of 25(OH)D to the inactive 24,25(OH) $_2$ D metabolite], this was also reversed by the addition of IL-10 (fig. S20). It should be noted that the T $_H$ 2 cytokine IL-4, also preferentially expressed in L-lep lesions (4, 20), enhances 24-hydroxylase activity, which

inactivates 1,25(OH) $_2$ D (19). Therefore, we conclude that IL-10 and IL-4 coordinate to regulate vitamin D metabolism and catabolism to inhibit IFN- $\gamma$ -induced antimicrobial responses.

The ability of IFN- $\gamma$  to up-regulate antimicrobial peptide gene expression, cathelicidin and DEF4, was completely blocked by addition of IFN- $\beta$  and IL-10 (Fig. 4C) and was reversed by the addition of anti-IL-10 (Fig. 4C). Thus, IFN- $\beta$  was shown to inhibit the expression of key genes involved in antimicrobial activity in human monocytes and macrophages. The effect of type I and II IFNs on the viability of intracellular *M. leprae* was subsequently investigated in vitro by using an infection model. Because *M. leprae* cannot be grown in vitro, we measured viability based on

the ratio of *M. leprae* 16S rRNA to the *M. leprae* repetitive element DNA (15, 21). IFN- $\gamma$  induced an antimicrobial activity against *M. leprae* in monocytes by ~35%, which was blocked ~70% by pharmacologic inhibition of the VDR (Fig. 4D) and completely abrogated by the addition of either IFN- $\beta$  or IL-10 (Fig. 4F and fig. S21). The ability of IFN- $\beta$  to inhibit the IFN- $\gamma$ -induced antimicrobial response against *M. leprae* was almost completely reversed by the addition of anti-IL-10. These studies indicate that the type I IFN program prominently expressed in L-lep lesions inhibits the IFN- $\gamma$ -induced antimicrobial response against *M. leprae*, primarily through the intermediation of IL-10 (fig. S22). Additionally, type I IFNs block the ability of inflammasome activators

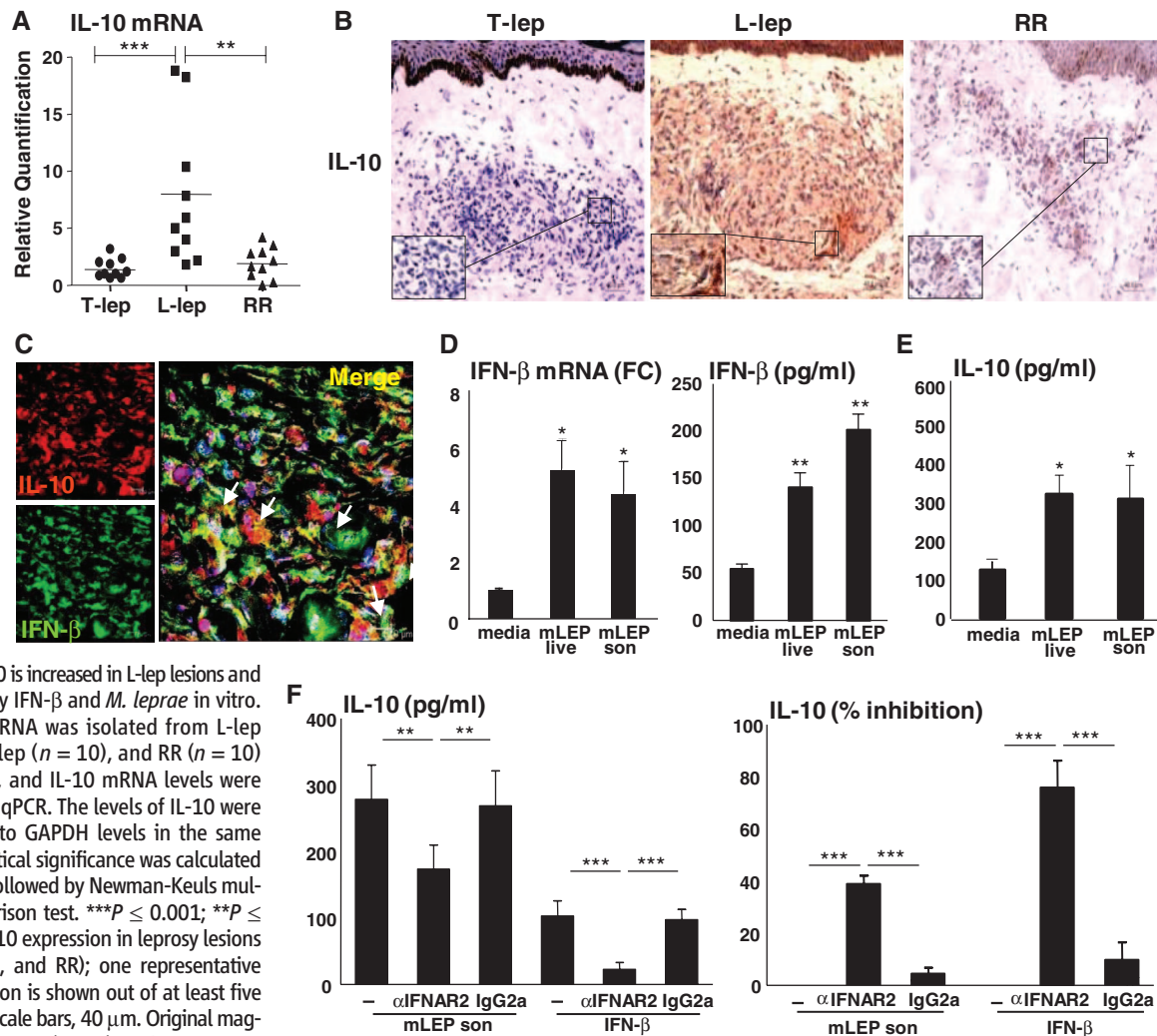


**Fig. 3.** IL-10 is increased in L-lep lesions and is induced by IFN- $\beta$  and *M. leprae* in vitro. (A) Total mRNA was isolated from L-lep ( $n = 10$ ), T-lep ( $n = 10$ ), and RR ( $n = 10$ ) skin lesions, and IL-10 mRNA levels were analyzed by qPCR. The levels of IL-10 were normalized to GAPDH levels in the same tissue. Statistical significance was calculated by ANOVA followed by Newman-Keuls multiple comparison test. \*\*\* $P \leq 0.001$ ; \*\* $P \leq 0.01$ . (B) IL-10 expression in leprosy lesions (T-lep, L-lep, and RR); one representative labeled section is shown out of at least five individuals; scale bars, 40  $\mu$ m. Original magnification, 200 $\times$ . (Insets) Higher magnification of inflammatory infiltrate area. Original magnification, 400 $\times$ . (C) Colocalization of IFN- $\beta$  (green) and IL-10 (red) in the inflammatory infiltrate of L-lep lesions. Data are representative of three individual L-lep samples; arrows indicate colocalization of the two cytokines. (D) Human monocytes were stimulated with live *M. leprae* (mLEP) or sonicated mLEP. After 6 hours, qPCR was performed for detection of IFN- $\beta$  (FC, fold change); supernatants were collected after 24 hours for detection of IFN- $\beta$  by enzyme-linked immunosorbent assay. Data are represented as mean  $\pm$  SEM,  $n = 7$ . Statistical significance was calculated by two-tailed Student's  $t$  test. \*\* $P \leq 0.01$ ; \* $P \leq 0.05$ . (E) Monocytes were stimulated with live mLEP or sonicated mLEP for 24 hours, and IL-10

protein levels were detected. Data are represented as mean  $\pm$  SEM,  $n = 7$ . Statistical significance was calculated by two-tailed Student's  $t$  test. \* $P \leq 0.05$ . (F) Human monocytes were stimulated with mLEP sonicated alone or in combination with either human IFNAR2 antibody or isotype control for 24 hours, and IL-10 protein levels were detected. Data are represented as mean  $\pm$  SEM,  $n = 4$ . Left graph shows the levels of IL-10 subtracted from media (average  $\pm$  64.5 pg/ml), and right graph shows the percentage of inhibition of IL-10 levels. Statistical significance was calculated by one-way ANOVA, and comparison between two groups was confirmed by the posttest and Newman-Keuls multiple comparison test. \*\*\* $P \leq 0.001$ ; \*\* $P \leq 0.01$ . IgG2a, immunoglobulin  $\gamma$ 2a.



(22) or *M. tuberculosis* infection (23, 24) to trigger production of IL-1, a cytokine also required for induction the vitamin D antimicrobial pathway (16). The inverse correlation between the expression of IFN- $\beta$  versus IFN- $\gamma$ , as well as their downstream target genes, suggests that the relative expression of IFNs at the site of infection is a key determinant of the outcome of the host response in leprosy. In studying a chronic human disease, it is difficult to separate initial cause from effect, but the data indicate that the IFN- $\beta$  in the fully developed disease is suppressing the development of a protective response. We also note that the relevance of the vitamin D pathway for host defense in leprosy is reflected in the genetic association of VDR single-nucleotide polymorphisms in L-lep patients (25) and the reported successful use of vitamin D as a therapeutic adjuvant in the treatment of leprosy (26).

We believe that these findings in the spectrum of leprosy may provide useful insights to mechanisms of resistance and pathogenesis in the related mycobacterial disease, human tuberculosis. Analogous to leprosy, in tuberculosis, IFN- $\gamma$  is critical for control of the infection. However, in some individuals, the infection with *M. tuberculosis* progresses to pulmonary and disseminated disease, analogous to the progressive form of leprosy. The most striking characteristic of the blood-based profiling “signature” for active tuberculosis was the increase in a set of genes regulated by IFN- $\beta$  (3, 12), with an overlap in IFN- $\beta$ - and IL-10-induced genes similar to progressive leprosy. The presence of the IL-10 signature profile in blood of tuberculosis patients and the finding of IL-10 mRNA and protein at the site of disease (27) suggest that there is likely to be a causal association between the IFN- $\beta$

and IL-10 profiles in active mycobacterial diseases and tissue damage. This raises the possibility that, in individuals who are able to maintain their *M. tuberculosis* in a latent or persistent state, a decrease in the type II IFN response or an increase in the type I response, perhaps induced by intercurrent viral infection, could shift the balance from latent to active disease.

We suggest that tuberculosis, like leprosy, comprises a spectrum of protective and pathogenic responses (28). From an evolutionary standpoint, if the immune response were fully effective in killing the pathogen, neither historically ancient disease would exist. When innate and acquired responses are compromised, as in HIV, tuberculosis, often seen as a chronic infectious disease, is transformed into a rapidly fatal disease, as in the case of extensively drug resistant (XDR) tuberculosis (29). Because *M. tuberculosis* exists

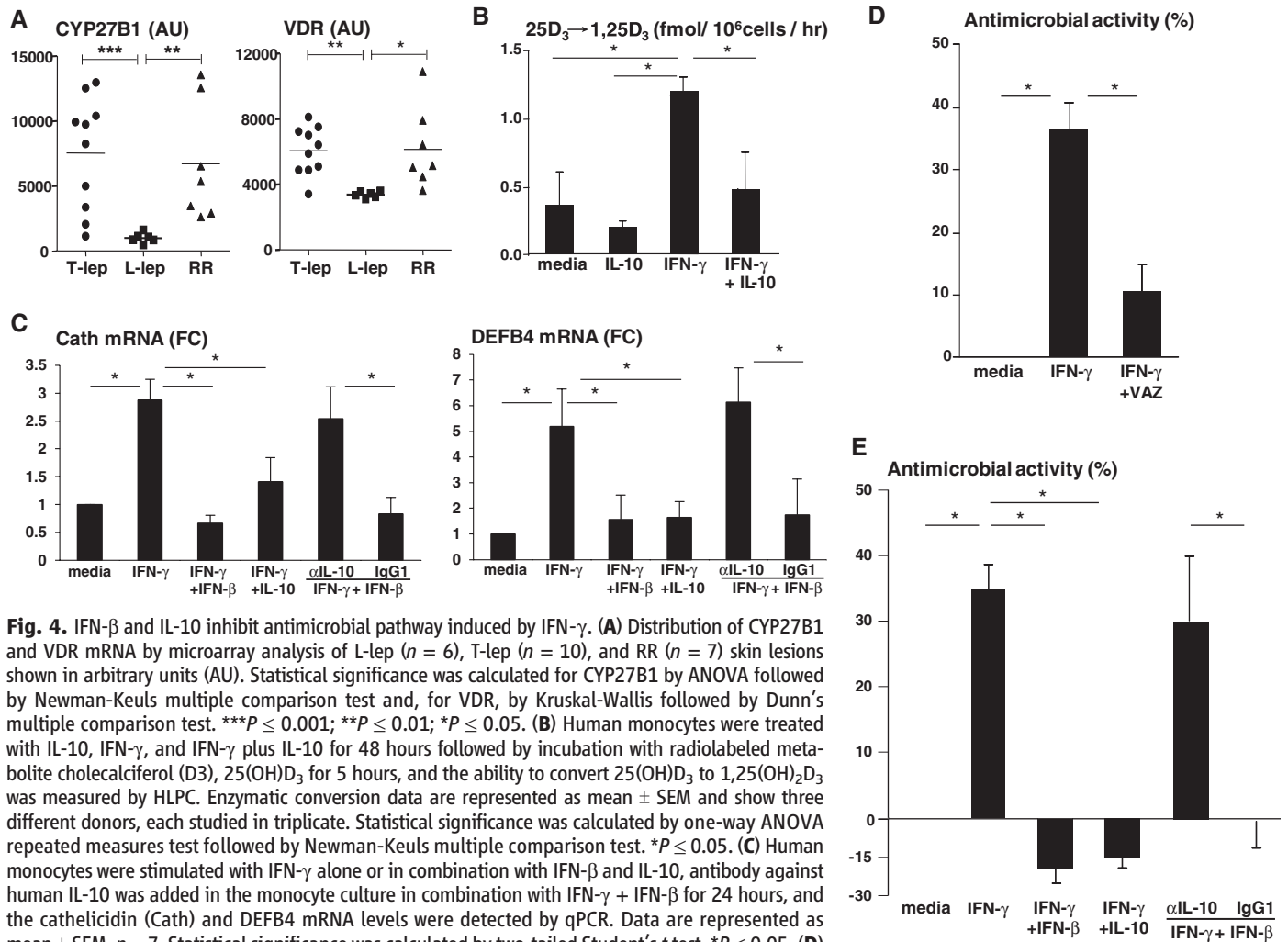


**Fig. 4.** IFN- $\beta$  and IL-10 inhibit antimicrobial pathway induced by IFN- $\gamma$ . (A) Distribution of CYP27B1 and VDR mRNA by microarray analysis of L-lep ( $n = 6$ ), T-lep ( $n = 10$ ), and RR ( $n = 7$ ) skin lesions shown in arbitrary units (AU). Statistical significance was calculated for CYP27B1 by ANOVA followed by Newman-Keuls multiple comparison test and, for VDR, by Kruskal-Wallis followed by Dunn's multiple comparison test. \*\*\* $P \leq 0.001$ ; \*\* $P \leq 0.01$ ; \* $P \leq 0.05$ . (B) Human monocytes were treated with IL-10, IFN- $\gamma$ , and IFN- $\gamma$  plus IL-10 for 48 hours followed by incubation with radiolabeled metabolite cholecalciferol (D<sub>3</sub>), 25(OH)D<sub>3</sub> for 5 hours, and the ability to convert 25(OH)D<sub>3</sub> to 1,25(OH)<sub>2</sub>D<sub>3</sub> was measured by HPLC. Enzymatic conversion data are represented as mean  $\pm$  SEM and show three different donors, each studied in triplicate. Statistical significance was calculated by one-way ANOVA repeated measures test followed by Newman-Keuls multiple comparison test. \* $P \leq 0.05$ . (C) Human monocytes were stimulated with IFN- $\gamma$  alone or in combination with IFN- $\beta$  and IL-10, antibody against human IL-10 was added in the monocyte culture in combination with IFN- $\gamma$  + IFN- $\beta$  for 24 hours, and the cathelicidin (Cath) and DEFB4 mRNA levels were detected by qPCR. Data are represented as mean  $\pm$  SEM,  $n = 7$ . Statistical significance was calculated by two-tailed Student's  $t$  test. \* $P \leq 0.05$ . (D) Human monocytes were pretreated with IFN- $\gamma$  and then infected with *M. leprae* at a multiplicity of infection of 10:1 overnight. After infection, cells were treated with IFN- $\gamma$  alone or in combination with VDR antagonist (VAZ). Viability of mLEP was calculated by the ratio of bacterial 16S RNA and DNA (RLEP) detected by qPCR, and percent increase or decrease relative to no treatment (media) was determined. Data are represented as mean  $\pm$  SEM,  $n = 5$ . Statistical significance was calculated by two-tailed Student's  $t$  test. \* $P \leq 0.05$ . (E) Human monocytes were pretreated and infected as described in (D). After infection, cells were treated with IFN- $\gamma$  alone or in combination with IFN- $\beta$  or IL-10; in some instances, human IL-10 antibody was added to the culture in combination with IFN- $\gamma$  plus IFN- $\beta$  for 4 days. Viability of *M. leprae* was calculated as described in (D). Data are represented as mean  $\pm$  SEM,  $n = 10$ . Statistical significance was calculated by two-tailed Student's  $t$  test. \* $P \leq 0.05$ .

essentially only in human species, it is likely to have evolved to persist in the human population, with a sufficient number of individuals developing pathology to assure transmission by aerosol and survival of the pathogen, the remainder containing the pathogen by protective host immune responses. Therapeutic interventions to block IFN- $\beta$ -induced pathologic responses as well as enhance in IFN- $\gamma$  responses may be an effective strategy to alter the balance to favor protection in mycobacterial and other infections.

## References and Notes

1. M. Fabri *et al.*, *Sci. Transl. Med.* **3**, 104ra102 (2011).
2. R. M. O'Connell *et al.*, *J. Exp. Med.* **200**, 437 (2004).
3. M. P. Berry *et al.*, *Nature* **466**, 973 (2010).
4. M. Yamamura *et al.*, *Science* **254**, 277 (1991).
5. M. Yamamura *et al.*, *J. Immunol.* **149**, 1470 (1992).
6. S. J. Waddell *et al.*, *PLoS ONE* **5**, e9753 (2010).
7. S. A. Samarajiva, S. Forster, K. Auchettl, P. J. Hertzog, *Nucleic Acids Res.* **37**, D852 (2009).
8. T. R. Golub *et al.*, *Science* **286**, 531 (1999).
9. S. S. Iyer, A. A. Ghaffari, G. Cheng, *J. Immunol.* **185**, 6599 (2010).
10. M. Rayamajhi, J. Humann, K. Penheiter, K. Andreasen, L. Lenz, *J. Exp. Med.* **207**, 327 (2010).
11. P. T. Liu *et al.*, *Science* **311**, 1770 (2006); 10.1126/science.1123933.
12. J. Maertzdorf *et al.*, *Proc. Natl. Acad. Sci. U.S.A.* **109**, 7853 (2012).
13. C. L. Cooper *et al.*, *J. Exp. Med.* **169**, 1565 (1989).
14. D. Montoya *et al.*, *Cell Host Microbe* **6**, 343 (2009).
15. P. T. Liu *et al.*, *Nat. Med.* **18**, 267 (2012).
16. P. T. Liu *et al.*, *PLoS ONE* **4**, e5810 (2009).
17. S. R. Krutzik *et al.*, *J. Immunol.* **181**, 7115 (2008).
18. J. S. Adams, M. A. Gacad, *J. Exp. Med.* **161**, 755 (1985).
19. K. Edfeldt *et al.*, *Proc. Natl. Acad. Sci. U.S.A.* **107**, 22593 (2010).
20. P. Salgame *et al.*, *Science* **254**, 279 (1991).
21. A. N. Martinez *et al.*, *J. Clin. Microbiol.* **47**, 2124 (2009).
22. G. Guarda *et al.*, *Immunity* **34**, 213 (2011).
23. A. Novikov *et al.*, *J. Immunol.* **187**, 2540 (2011).
24. K. D. Mayer-Barber *et al.*, *J. Immunol.* **184**, 3326 (2010).
25. S. Roy *et al.*, *J. Infect. Dis.* **179**, 187 (1999).
26. G. Herrera, *Int. J. Lepr.* **17**, 35 (1949).
27. P. F. Barnes *et al.*, *Infect. Immun.* **61**, 3482 (1993).
28. C. E. Barry 3rd *et al.*, *Nat. Rev. Microbiol.* **7**, 845 (2009).
29. N. R. Gandhi *et al.*, *Lancet* **368**, 1575 (2006).

**Acknowledgments:** We thank P. Liu for advice with the *M. leprae* viability assays and helpful discussion; M. So for help in the bioinformatic analysis; K. Zavala for help with the

high-performance liquid chromatography (HPLC) assays; A. Legaspi and A. DeLeon for help with the immunohistochemistry; M. Schibler and the University of California–Los Angeles, California NanoSystems Institute, Advanced Light Microscopy Core Facility for assistance with the confocal studies; D. Elashoff for help with the statistical analysis; and A. Steinmeyer, E. May, and U. Zügel from Bayer Pharma AG for the VDR antagonist ZK 159 222 (VAZ). The live *M. leprae* was provided by the U.S. National Hansen's Disease Programs through the generous support of the American Leprosy Missions and Society of St. Lazarus of Jerusalem. The data presented in this manuscript are tabulated in the main paper and supplementary materials. Gene expression files containing array data are available under the accession nos. GSE17763 and GSE43700 in the Gene Expression Omnibus (GEO) database. This work was supported in parts by NIH grants (P50 AR063020; R01s AI022553, AR040312, and AI047868; and Clinical and Translational Science Award grant UL1TR000124).

## Supplementary Materials

www.sciencemag.org/cgi/content/full/science.1233665/DC1  
Materials and Methods  
Figs. S1 to S22  
References (30–38)

5 December 2012; accepted 29 January 2013  
Published online 28 February 2013;  
10.1126/science.1233665

# Dual Origin of the Epithelium of the Mammalian Middle Ear

Hannah Thompson and Abigail S. Tucker\*

The air-filled cavity and ossicles of the mammalian middle ear conduct sound to the cochlea. Using transgenic mice, we show that the mammalian middle ear develops through cavitation of a neural crest mass. These cells, which previously underwent an epithelial-to-mesenchymal transformation upon leaving the neural tube, undergo a mesenchymal-to-epithelial transformation to form a lining continuous with the endodermally derived auditory tube. The epithelium derived from endodermal cells, which surrounds the auditory tube and eardrum, develops cilia, whereas the neural crest–derived epithelium does not. Thus, the cilia critical to clearing pathogenic infections from the middle ear are distributed according to developmental derivations. A different process of cavitation appears evident in birds and reptiles, indicating that this dual epithelium may be unique to mammals.

The mammalian middle ear is an air-filled cavity housed within the auditory bulla with three ossicles suspended within it, connecting the eardrum to the inner ear. The epithelial lining of the middle ear in the ventral region is continuous with the auditory (Eustachian) tube, which connects the middle ear to the pharynx. At embryonic day 12.5 (E12.5) in the mouse, the ossicles condense within the neural crest–derived first and second pharyngeal arches, adjacent to the developing inner ear and dorsal to the tip of the first pharyngeal pouch (1). In early postnatal mice, the future middle ear cavity is filled with neural crest cells surrounding the developing ossicles (2), which are positioned in the dorsal region of the future cavity (the attic), in addition to mesodermal cells that will mature to form the middle ear muscles. A process called

cavitation then occurs in which the neural crest cells are replaced by an air-filled cavity (2, 3), which surrounds the ossicles and muscles, allowing free movement in response to sound (fig. S1). The whole cavity is lined by an epithelium.

The current model of middle ear cavitation was proposed by Wittmaack (4) and suggests that the endoderm of the first pharyngeal pouch extends into the middle ear region, expanding and enveloping the middle ear structures, resulting in a cavity lined completely by endoderm. However, the middle ear cavity has suspended within it three ossicles in addition to muscles, blood vessels, and nerves that would prevent an epithelium expanding through as a continuous sheet. This prompted Schwarzbart to propose that during cavitation the endoderm ruptured and the neural crest formed the lining of the middle ear (5). To resolve these issues, we have made use of newly developed transgenic mouse lines *Sox17-2Acre* (6) and *Wnt1cre* (7) crossed with the reporter mouse line *R26R* (8). When stained

with X-Gal, this system permanently labels cells of endodermal or neural crest origin blue and therefore allows the embryonic origin of tissues within the developing middle ear to be determined.

*Sox17-2AcreR26R* mice trace cells that are currently expressing, or have previously expressed, *Sox17*. These include cells of endodermal origin and blood vessels. Contrary to previously published data that the epithelial lining of the middle ear is of endodermal origin (9, 10), the fully cavitated middle ear from P14 in *Sox17-2AcreR26R* mice was found to be labeled blue only in the epithelium around the opening to the auditory tube (Fig. 1B), with unstained epithelium around the attic region above the ossicles and along the cochlea (Fig. 1A). To determine the origin of the nonendodermal epithelial cells, *Wnt1creR26R* mice were stained with X-Gal. Around the auditory tube, the epithelium was LacZ-negative (Fig. 1D), whereas the epithelium lining the cavity around the ossicles and cochlea was LacZ-positive (Fig. 1C), in a complementary pattern to that observed in the *Sox17-cre* line. Careful mapping of the middle ear cavity with these reporter lines showed that the auditory tube and surrounding middle ear epithelium, extending up to and slightly beyond the eardrum on the lateral side, was endoderm-derived. In contrast, neural crest cells were found lining the middle ear cavity on the medial wall covering the otic capsule/cochlea and lining the attic region of the cavity in the vicinity of the ossicles (Fig. 1E) (number of samples analyzed = 15). In humans, the attic is connected to the mastoid air space, and these are therefore also likely to be lined with a neural crest–derived epithelium. The epithelium lining the middle ear cavity is therefore of dual origin, roughly half neural crest and half endodermal.

Department of Craniofacial Development and Stem Cell Biology, King's College London, Guy's Hospital, London, UK, SE1 9RT.

\*Corresponding author: abigail.tucker@kcl.ac.uk



If there are neural crest cells lining the middle ear cavity and it is assumed that the middle ear cavity is covered by an epithelium, it suggests that mesenchymal neural crest cells have undergone a mesenchyme-to-epithelium transformation (MET). This would mean that neural crest cells in this region of the ear start life in the neural tube as epithelial, transform to mesenchyme to migrate into the pharyngeal arches, and then transform back to an epithelium. A neural crest origin of the corneal endothelium has previously been shown in the eye (11). To confirm whether this was the case in the ear, markers

involved in epithelial-mesenchymal transformation (EMT) were investigated. Immunostaining for the epithelial-specific molecule E-cadherin was performed on X-Gal-stained *Wnt1creR26R* postnatal mice. The LacZ-positive blue cells lining the cavity of the middle ear expressed E-cadherin (Fig. 2, A and B). Cytokeratin14 (K14) is an epithelial-specific cytoskeletal protein. Using X-Gal staining on the *K14creR26R* mice (12), we observed that the epithelium of neural crest origin at postnatal day 14 (P14) did not express K14 (Fig. 2C); however, by P16 this gene was now expressed by all the epithelium

(Fig. 2D). Finally, to determine when the basal lamina of the epithelium was produced, we performed immunostaining against laminin and saw no expression at P14, just as cavitation is completing (Fig. 2E), but strong expression by P19 (Fig. 2F). This suggests that MET of neural crest cells occurs a few days after the cavitation of the ear is complete, resulting in the transformation of the neural crest cells at the retracting edge into an epithelium. A failure in the retraction of this mesenchyme, or a failure in the transformation of the mesenchyme to an epithelium, would result in retention of mesenchyme in the cavity

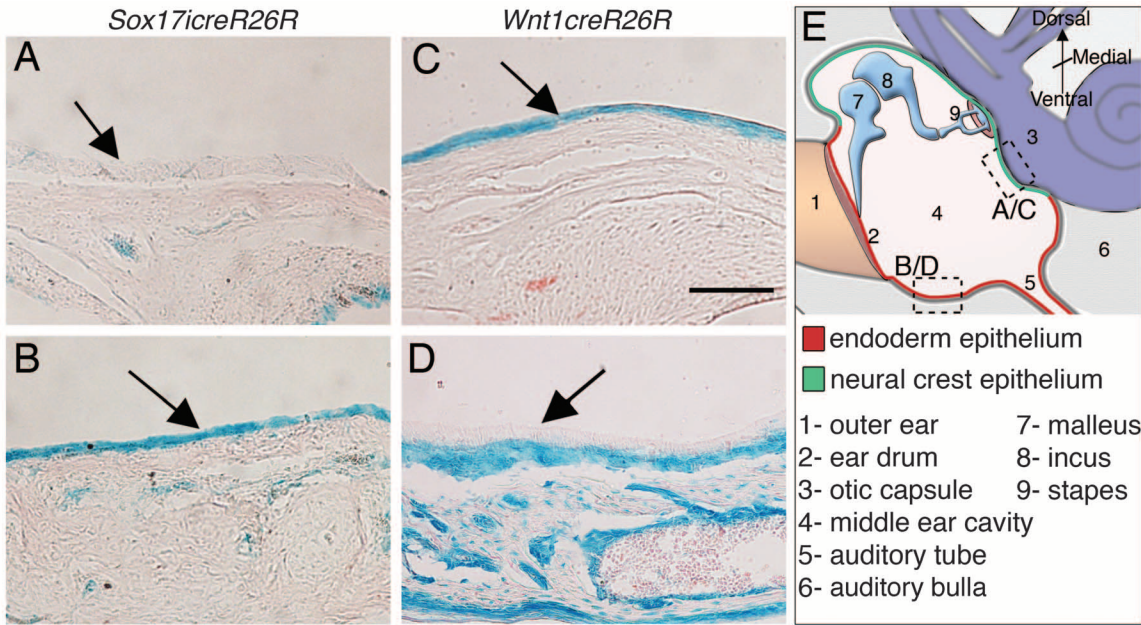


**Fig. 1.** The epithelial lining of the middle ear cavity is of dual origin. (A to D) X-Gal and eosin staining of postnatal mouse middle ears. LacZ-negative cells (A) and LacZ-positive cells of endoderm origin (B) are seen lining the middle ear cavity (arrows) in *Sox17-2AicreR26R* at P14. LacZ-positive

(C) and LacZ-negative (D) cells are observed (arrows) in *Wnt1creR26R* at P16. (E) Schematic representing the distribution of the endoderm and neural crest epithelium and indicating the positions of (A) to (D). Scale bar: 100  $\mu$ m.

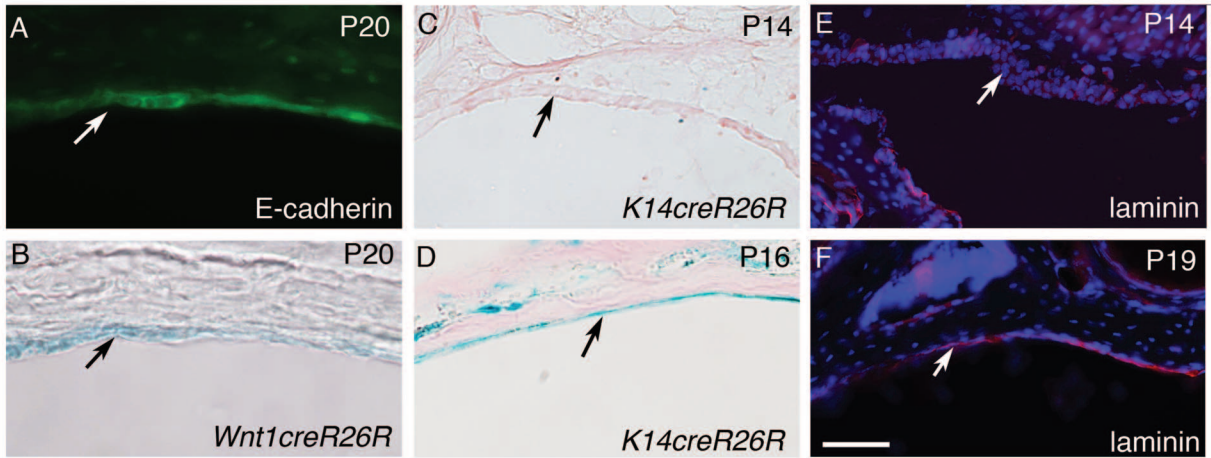


**Fig. 2.** Neural crest cells in the middle ear undergo a MET. (A) P20 *Wnt1creR26R* ear immunostained against E-cadherin (arrow). (B) LacZ staining of tissue in (A) shows neural crest origin of E-Cad positive tissue (arrow). (C and D) X-Gal- and eosin-stained *K14creR26R* neural crest-derived epithelium showing

LacZ-negative cells (C) at P14 and Keratin14 expressing blue cells at P16 [arrow in (D)]. (E and F) Immunostaining against laminin (red) and 4',6-diamidino-2-phenylindole (DAPI) (blue) showing neural crest epithelium without a basal lamina at P14 [arrow in (E)], but with a basal lamina by P19 [arrow in (F)]. Scale bar: 60  $\mu$ m.

and air spaces and may explain cases of residual mesenchyme observed in mutant mice and human patients (3, 13).

Previous studies in humans (14, 15), rats (9, 16), and guinea pigs (17, 18) have noted that the epithelium lining the middle ear cavity is of a different type in different regions of the cavity. The middle ear epithelium is known to be either pseudostratified; containing ciliated, goblet, and basal cells; or a simple epithelium without any cilia. We used scanning electron microscopy (SEM) to analyze the distribution of cilia within the mouse middle ear. We found that there were regions of densely ciliated epithelium (Fig. 3A), regions of epithelium with short cilia and long cilia interspersed with a few nonciliated cells (Fig. 3B), and regions of simple epithelium with no cilia (Fig. 3C). The epithelium dense with long cilia was found close to the auditory tube, in the ventral regions of the middle ear, and along the lateral edges of the cavity and was bordered with a region of mixed ciliated and nonciliated cells (Fig. 3D). A number of goblet cells, secreting mucus, were observed restricted to the area entering the auditory tube (Fig. 3A). Over the surface of the otic capsule and lining the attic, the epithelium was nonciliated and simple

(Fig. 3D). To compare the epithelial type with embryonic origin, we dissected *Sox17<sup>cre</sup>R26R* mice in the same way as for SEM and stained with X-Gal to visualize the endoderm-derived epithelium (Fig. 3E). Blue staining was seen in the ventral regions and along the edges of the cavity but not lining the attic in the vicinity of the ossicles or on the medial wall covering the otic capsule. The distribution of ciliated and nonciliated epithelium therefore appears to correspond to the embryonic origin of the cells lining the middle ear cavity. To confirm this, we costained *Wnt1<sup>cre</sup>R26R* middle ears with X-Gal and an antibody against acetylated  $\alpha$ -tubulin, which is a marker of cilia. We saw cilia on unstained epithelium of endodermal origin (Fig. 3, F and G) but not on X-Gal-positive epithelium of neural crest origin (Fig. 3, H and I, and fig.S2). In short, the neural crest-derived lining of the middle ear shows several epithelial markers but not the surface cilia typical of mucosal linings.

We have shown that the lining of the middle ear cavity is of both endoderm and neural crest origin and that neural crest cells undergo a mesenchymal-to-epithelial transformation. In this case, the continuity of the endoderm must be breached to allow the neural crest cells to line

the upper part of the middle ear cavity. Such a breach has been suggested from histology in the rat (19). To find out when and where this takes place, we looked at the embryonic development of the first pharyngeal pouch, as it becomes the future middle ear cavity. At E15.5, the first pharyngeal pouch appears as a continuous epithelium surrounding the future middle ear cavity (Fig. 4A), as shown by the continuous expression of the epithelial cell adhesion molecule E-cadherin (Fig. 4, B and C). By E17.5, the future middle ear cavity appears to be filling with mesenchyme (Fig. 4D) associated with a rupture of the first pharyngeal pouch (Fig. 4, E and F). This shows that during embryonic development in the mouse, the endoderm of the first pharyngeal pouch—after fully extending into the vicinity of the outer and inner ear—breaks down, allowing mesenchyme to fill the future middle ear cavity (Fig. 4G). The middle ear then remains filled with mesenchyme until about P6 (fig. S1A), when the cavitation process begins. Cavitation starts in the ventral region of the middle ear with a retraction of the middle ear mesenchyme away from the endoderm-derived epithelium, producing an air-filled cavity (fig. S1B). This retraction of mesenchyme continues in this way, pulling back past the

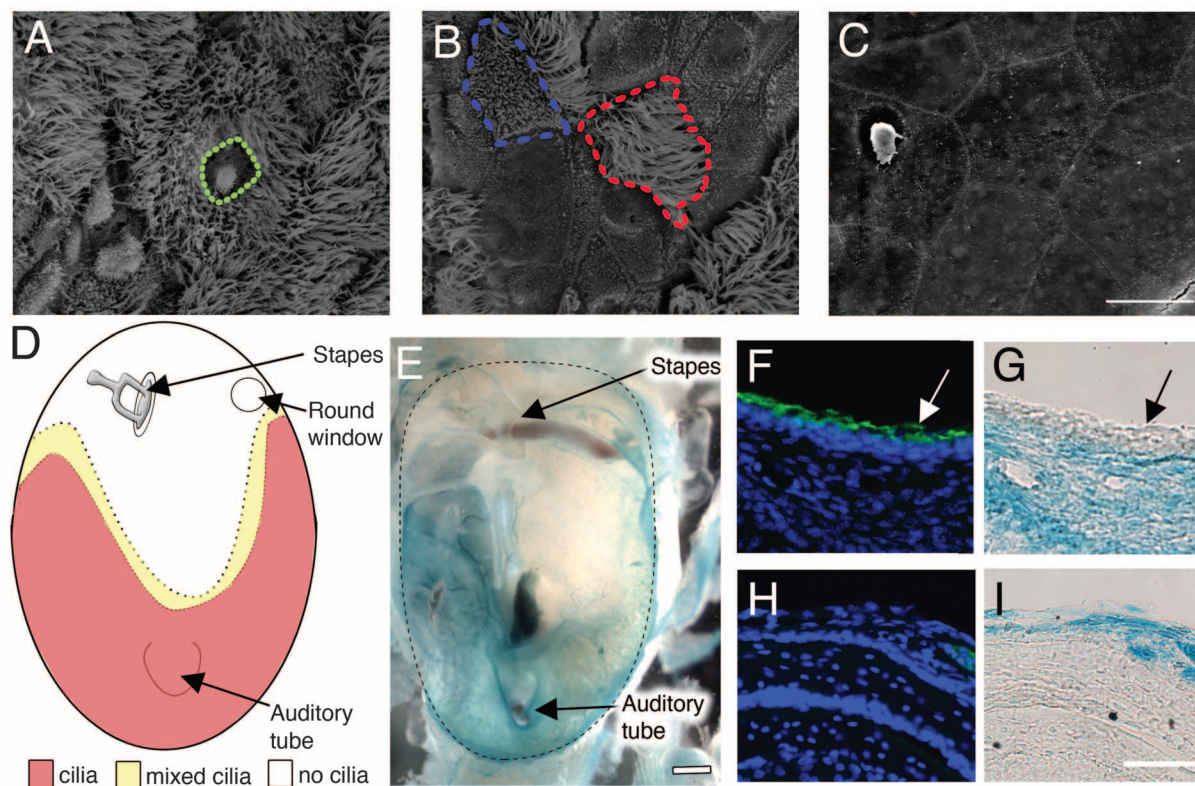


**Fig. 3.** Middle ear epithelium type is dependent on embryonic origin. (A to C) SEM imaging of the middle ear cavity surface epithelium, showing regions of densely ciliated cells and a goblet cell (green outline) (A), regions of mixed short-ciliated (blue outline), long-ciliated (red outline), and nonciliated cells (B), and regions of nonciliated epithelium (C). (D) Schematic representing the distribution of ciliated epithelium on the middle ear medial wall, with ciliated (red), mixed cilia (yellow), and simple nonciliated (white) regions. (E) Whole-mount X-Gal staining of P18 *Sox17-2AicreR26R* middle ear

(outlined) dissected by removal of the eardrum revealing the medial wall, showing endoderm (blue) near the auditory tube and along the cavity edges, but not in the center or near the ossicles. (F to I) *Wnt1creR26R* P12 mice immunostained with acetylated  $\alpha$ -tubulin (green), DAPI (blue) [(F) and (H)], and X-Gal stained (blue) [(G) and (I)], showing cilia on *Wnt1creR26R*-negative epithelium [arrows in (F) and (G)], but not on *Wnt1creR26R*-positive epithelium [(H) and (I)]. Scale bars: 10  $\mu$ m [(A) to (C)]; 500  $\mu$ m (E); 50  $\mu$ m [(F) to (I)].



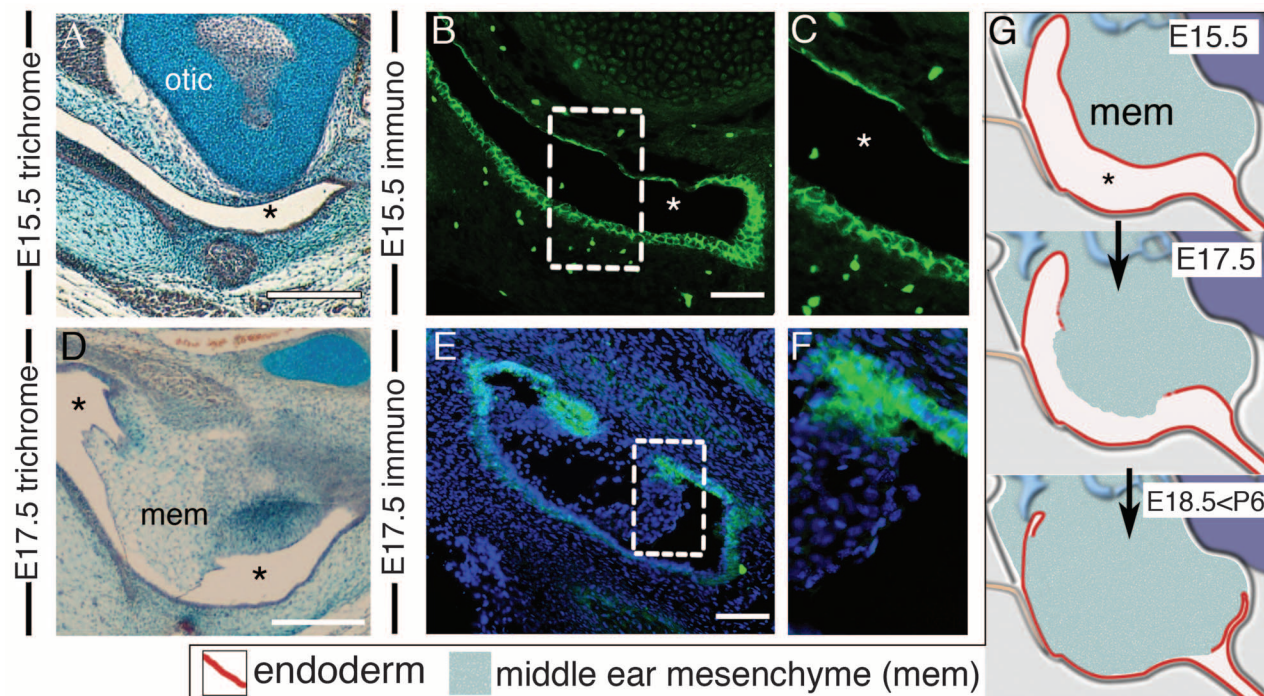


**Fig. 4.** The first pharyngeal pouch endoderm breaks and mesenchyme fills the middle ear cavity. Embryonic mice with Trichrome staining (**A** and **D**) or immunostained against E-cadherin (**B**, **C**, **E**, and **F**), showing intact epithelium lining the first pharyngeal pouch at E15.5 [**A** to **C**] and then broken at E17.5 [**D** to **F**]. (**G**) Schematic representing the endodermal first pharyngeal pouch during embryonic development; from the fully extended pouch with endodermal epithelial lining (red), to breakage of the epithelium, and finally the filling of the middle ear cavity with mesenchyme. Dorsal is top. Otic, otic capsule; \*, first pharyngeal pouch cavity. Scale bars: 75  $\mu$ m [**A** and **D**]; 50  $\mu$ m [**B** and **E**].

ossicles with the attic clearing last, eventually leaving a completely air-filled cavity (fig. S1C).

The three-ossicle mammalian middle ear is very different from that of other land tetrapods, which possess a single ossicle, the two additional ossicles having evolved by a transformation of the original jaw joint (20, 21). We therefore wanted to assess whether a similar break in the endoderm and influx of mesenchyme into the cavity occurred in nonmammals. In the chick and gecko, no rupture of the endoderm during middle ear development was observed using histology, and mesenchyme did not enter the cavity, which remained air-filled (fig. S3). In contrast, in another mammal, the shrew, a similar filling of the middle ear cavity to that in the mouse was observed during development. Further lineage analysis is necessary to assess whether the middle ear in nonmammals has a dual origin; however, it is interesting to note that a neural crest origin of the middle ear epithelium has not been reported after quail-chick neural crest grafts within this region (22, 23). In addition, unlike the heterogeneous mammalian middle ear epithelium, no regional differences were found in the avian middle ear epithelium, with a fairly simple epithelium being observed in all regions (24). It is therefore possible that nonmammals adopt the endodermal model, whereas the mesenchymal model is specific to mammals and may have evolved in connection with the incorporation of the jaw joint into the ear, which required cavitation of a previously solid area of mesenchyme.

We have shown that the highly versatile neural crest cells can undergo a mesenchyme-to-epithelium transformation, but they are unable to form the complex pseudostratified ciliated epithelium associated with the endodermally derived part of the middle ear. This implies that there may be constraints limiting the ability of the neural crest to form advanced epithelial cell types. As the neural crest-derived epithelium is simple and unciliated, its function to clear away mucus and debris efficiently would be limited, compared to the endodermally derived epithelium, which provides a logical explanation for why middle ear infections are more common and more severe in the neural crest-lined attic than in the ventral endoderm-lined region of the cavity (25). The origin of the middle ear epithelium therefore may have a direct consequence for health of the mammalian ear.

#### References and Notes

- M. H. Kaufmann, *The Atlas of Mouse Development* (Academic Press, London, 1992).
- K. Park, K. Ueno, D. J. Lim, *Am. J. Otolaryngol.* **13**, 93 (1992).
- C. A. Richter *et al.*, *Hum. Mol. Genet.* **19**, 1551 (2010).
- K. Wittmaack, *Über die Normale und die Pathologische Pneumatisation des Schläfenbeines* (Gustav Fischer, Jena, Germany, 1918).
- A. Schwarzbart, *J. Laryngol. Otol.* **73**, 45 (1959).
- S. Engert, W. P. Liao, I. Burtscher, H. Lickert, *Genesis* **47**, 603 (2009).
- Y. Chai *et al.*, *Development* **127**, 1671 (2000).
- P. Soriano, *Nat. Genet.* **21**, 70 (1999).
- D. A. Hilding, E. Szachowicz, S. A. Larsen, *Am. J. Otolaryngol.* **1**, 97 (1980).
- B. Proctor, *J. Laryngol. Otol.* **78**, 631 (1964).
- M. C. Johnston, D. M. Noden, R. D. Hazelton, J. L. Coulombre, A. J. Coulombre, *Exp. Eye Res.* **29**, 27 (1979).
- A. K. Indra *et al.*, *Horm. Res.* **54**, 296 (2000).
- V. J. Jaisinghani, M. M. Paparella, P. A. Schachern, D. S. Schneider, C. T. Le, *Am. J. Otolaryngol.* **20**, 363 (1999).
- J. Sade, *Arch. Otolaryngol.* **84**, 137 (1966).
- N. H. Buch, M. B. Jorgensen, *Arch. Otolaryngol.* **79**, 472 (1964).
- W. Kuijpers, J. M. van der Beek, P. H. Jap, E. L. Tonnaer, *Histochem. J.* **16**, 807 (1984).
- R. Haye, *Cell Tissue Res.* **148**, 431 (1974).
- D. J. Lim, M. M. Paparella, R. S. Kimura, *Acta Otolaryngol.* **63**, 425 (1967).
- W. F. Marovitz, E. S. Porubsky, *Ann. Otol. Rhinol. Laryngol.* **80**, 384 (1971).
- M. Takechi, S. Kuratani, *J. Exp. Zool. B Mol. Dev. Evol.* **314B**, 417 (2010).
- N. Anthwal, L. Joshi, A. S. Tucker, *J. Anat.* **222**, 147 (2013).
- G. Köntges, A. Lumsden, *Development* **122**, 3229 (1996).
- D. M. Noden, *Dev. Biol.* **96**, 144 (1983).
- F. Giannessi, R. Ruffoli, *J. Anat.* **183**, 103 (1993).
- S. Varshney *et al.*, *Indian J. Otolaryngol. Head Neck Surg.* **62**, 421 (2010).

- M. C. Johnston, D. M. Noden, R. D. Hazelton, J. L. Coulombre, A. J. Coulombre, *Exp. Eye Res.* **29**, 27 (1979).
- A. K. Indra *et al.*, *Horm. Res.* **54**, 296 (2000).
- V. J. Jaisinghani, M. M. Paparella, P. A. Schachern, D. S. Schneider, C. T. Le, *Am. J. Otolaryngol.* **20**, 363 (1999).
- J. Sade, *Arch. Otolaryngol.* **84**, 137 (1966).
- N. H. Buch, M. B. Jorgensen, *Arch. Otolaryngol.* **79**, 472 (1964).
- W. Kuijpers, J. M. van der Beek, P. H. Jap, E. L. Tonnaer, *Histochem. J.* **16**, 807 (1984).
- R. Haye, *Cell Tissue Res.* **148**, 431 (1974).
- D. J. Lim, M. M. Paparella, R. S. Kimura, *Acta Otolaryngol.* **63**, 425 (1967).
- W. F. Marovitz, E. S. Porubsky, *Ann. Otol. Rhinol. Laryngol.* **80**, 384 (1971).
- M. Takechi, S. Kuratani, *J. Exp. Zool. B Mol. Dev. Evol.* **314B**, 417 (2010).
- N. Anthwal, L. Joshi, A. S. Tucker, *J. Anat.* **222**, 147 (2013).
- G. Köntges, A. Lumsden, *Development* **122**, 3229 (1996).
- D. M. Noden, *Dev. Biol.* **96**, 144 (1983).
- F. Giannessi, R. Ruffoli, *J. Anat.* **183**, 103 (1993).
- S. Varshney *et al.*, *Indian J. Otolaryngol. Head Neck Surg.* **62**, 421 (2010).

**Acknowledgments:** The authors thank A. Warley and G. Vizcay in the Centre for Ultrastructural Imaging at King's College London for help with the SEM and J. Green for his helpful critique of the manuscript. We also thank H. Lickert and M. A. Basson for the Sox17-2Aicre line. This work was funded by a project grant from the Medical Research Council (G1001232). Sox17-2Aicre transgenic mice are available for noncommercial use subject to a material transfer agreement with Helmholtz Zentrum München, German Research Centre for Environmental Health (GmbH), through H. Lickert.

#### Supplementary Materials

www.sciencemag.org/cgi/content/full/339/6126/1453/DC1  
Materials and Methods  
Figs. S1 to S3

16 November 2012; accepted 11 February 2013  
10.1126/science.1232862

### MICROSCOPE CONTROLLER

The new DP26 standalone controller can be optimally positioned for user comfort and allows ultrafast imaging, without needing to boot up a computer or load dedicated software. This is especially useful for applications such as cell culture and pathology, as well as for microscopes shared by large groups. Using the controller, the camera can be linked directly to a monitor screen, while providing simple and intuitive control of digital zoom, image capture, and color balance. Image and video capture is fast and simple, all at the touch of a single button. With a USB connection, the standalone controller permits storage of videos and images, with exposure settings, magnifications, and other parameters stored for future reference. Images can also be saved to a shared folder on a networked drive via the Ethernet connection. Utilizing the progressive scan readout, the DP26 is capable of producing totally fluid imaging at up to 16 frames per second, while avoiding the occurrence of any distracting artifacts.

#### Olympus

For info: +49-40-23773-5913 | [www.microscopy.olympus.eu](http://www.microscopy.olympus.eu)



### MULTIPURPOSE VACUUM PUMP

The Vacuubrand MZ2C NT +AK+M+D is a dry diaphragm vacuum pump integrated with the essential accessories for basic rotary evaporation and other common laboratory tasks. The heart of the system is the powerful MZ2C NT chemistry-design oil-free pump with a 5 Torr ultimate vacuum, and 38 L per minute free air capacity—powerful enough for most laboratory-sized tasks, such as gel drying, rotary evaporators and smaller vacuum ovens. A flow control knob helps match pumping speed to vapor flow to quietly help prevent bumping and foaming, and an inlet catch pot helps keep condensate from compromising vacuum performance. A Bourdon dial vacuum gauge, and space-saving stand completes the package. Ultralow maintenance with no oil to monitor or change, and no cold trap is required to protect the pump. Typical service interval is well in excess of 10,000 operating hours.

#### BrandTech Scientific

For info: 860-767-2562 | [www.brandtech.com](http://www.brandtech.com)

### SUPERRESOLUTION MICROSCOPY SYSTEM

The MetaMorph Super-Resolution System, with synchronized image acquisition and processing, enables analysis of object details smaller than 250 nm in fixed- and live-cells. The new system features real-time image processing with its GPU-accelerated hardware, expanding the capabilities of optical microscopy in research and supports numerous scientific applications, from time-lapse studies to 3-D investigations. When using light microscopy alone, images of biological matter smaller than 250 nm appear blurred and, as a result, are virtually impossible to analyze. Superresolution microscopy can help to overcome the limits of light microscopy by reconstructing images at a resolution surpassing the diffraction limit of the objective lens. With patent-pending image processing techniques, the new MetaMorph Super-Resolution System is capable of 20 nm lateral resolution in real-time. The user-friendly software guides researchers through setup, acquisition, and analysis, with a dedicated workspace in the user interface ensuring that relevant configuration and display settings are readily accessible.

#### Molecular Devices

For info: 800-635-5577 | [www.moleculardevices.com](http://www.moleculardevices.com)

### SAMPLE STORAGE TUBES

The new 2 mL storage tube uniquely combines higher sample storage capacity and absolute sample traceability in an industry-standard 96-tube rack format. The new Micronic 2.00 mL storage tube uses a unique 2-D code laser encrypted on the tube bottom to enable easy identification and traceable storage of your samples. The unique 2-D code identifies the sample, its coordinates within a storage rack, the particular rack and the location of the rack in your freezer. Produced in a modern class 7 clean room production facility from ultrapure polypropylene, Micronic 2 mL tubes are certified RNase/DNase free and nontoxic making them the ideal secure medium for storage of liquid or solid samples. In addition to having the ideal shape for gripping with a robotic arm, Micronic 2 mL tubes have been designed to fit in the industry-standard format 96-tube Roborack, which enables loading with standard 8- or 12-channel pipettes and simple integration with automated liquid handling platforms.

#### Micronic

For info: +31-320-277070 | [www.micronic.com](http://www.micronic.com)

### SAMPLE MANAGEMENT SOFTWARE

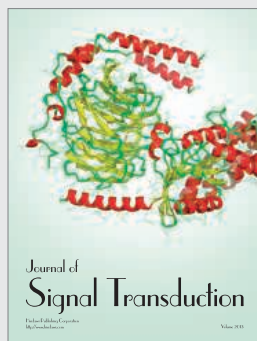
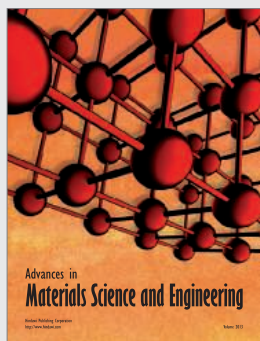
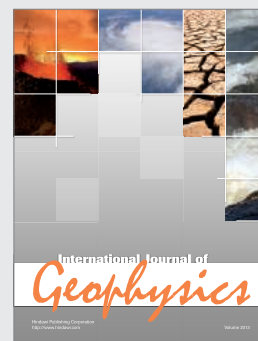
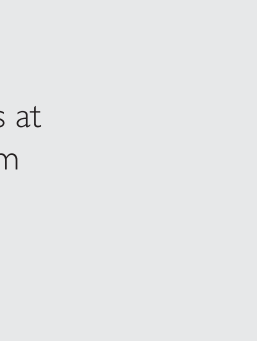
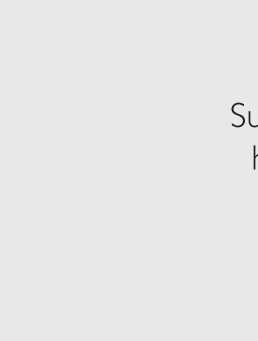
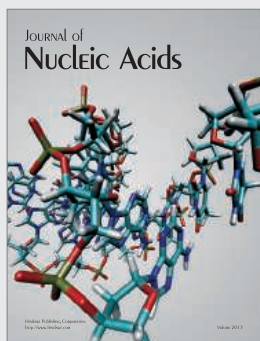
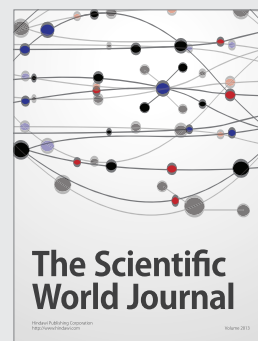
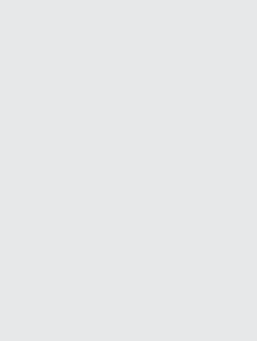
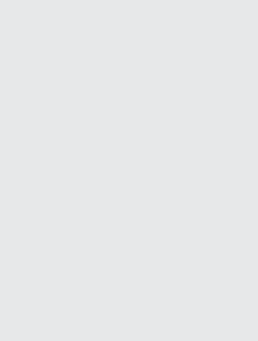
The Mosaic 5.0 is the latest development of the popular Mosaic software for the expert management of samples, including compounds, biological collections, reagents, and standards. Mosaic 5.0 provides comprehensive inventory management features, which include handling multiple substance types, managing storage locations, and supporting configurable sample-set management and usage restrictions. As well as a powerful interface for the simple ordering of stock samples, Mosaic also provides convenient interfaces to request the dispensing, customizable selection, reformatting, and dilution of samples into the desired format. Mosaic orders are processed using Mosaic's workflow management and fulfilment modules which can be integrated with a variety of manual and automated storage systems and instruments for maximum functionality. The Mosaic 5.0 software is available to new customers and to existing users via Titian's support and maintenance program.

#### Titian Software

For info: +44-(0)-2073-676869 | [www.titian.co.uk](http://www.titian.co.uk)

Electronically submit your new product description or product literature information! Go to [www.sciencemag.org/products/newproducts.dtl](http://www.sciencemag.org/products/newproducts.dtl) for more information. Newly offered instrumentation, apparatus, and laboratory materials of interest to researchers in all disciplines in academic, industrial, and governmental organizations are featured in this space. Emphasis is given to purpose, chief characteristics, and availability of products and materials. Endorsement by *Science* or AAAS of any products or materials mentioned is not implied. Additional information may be obtained from the manufacturer or supplier.





**Hindawi**

Submit your manuscripts at  
<http://www.hindawi.com>

## **CONGRATULATIONS TO THE 2013 CANADA GAIRDNER AWARD RECIPIENTS**



CANADA GAIRDNER  
INTERNATIONAL AWARD  
**HARVEY J. ALTER MD**

Distinguished NIH Investigator, Chief, Clinical Studies and Associate Director of Research, NIH, Bethesda, Maryland, USA

With **DR. MICHAEL HOUGHTON PhD**

University of Alberta, Edmonton, Canada (Declined the award)

**For critical contributions to the discovery and isolation of the hepatitis C virus, which has led to the development of new diagnostic and therapeutic agents**



CANADA GAIRDNER  
INTERNATIONAL AWARD  
**DANIEL W. BRADLEY MD PhD**

Centre for Disease Control (ret); Consultant in I.D., Atlanta, Georgia, USA



CANADA GAIRDNER  
INTERNATIONAL AWARD  
**STEPHEN JOSEPH ELLEDGE PhD**

Department of Genetics, Harvard Medical School, Cambridge, Massachusetts, USA

**For elucidation of the DNA damage response as a signaling network that controls DNA repair and genomic stability with profound implications for cancer and other diseases**



CANADA GAIRDNER  
INTERNATIONAL AWARD  
**SIR GREGORY WINTER CBE FRS**

Medical Research Council Laboratory of Molecular Biology, Cambridge, UK

**For the engineering of humanized monoclonal antibodies and their widespread use in medical therapy in cancer and infectious disease**



CANADA GAIRDNER  
GLOBAL HEALTH AWARD  
**KING K. HOLMES MD PhD**

University of Washington, Department of Global Health and Center for AIDS & STD, Seattle, Washington, USA

**For global scientific contributions to the field of sexually transmitted disease and their effective treatment and prevention**



CANADA GAIRDNER  
WIGHTMAN AWARD  
**JAMES C. HOGG MD PhD**

Professor Emeritus, Pathology and Laboratory Medicine, University of British Columbia, Vancouver, British Columbia, Canada

**For leadership in the understanding and treatment of chronic respiratory disease and for a visionary career as a national research builder**



# Explore the fascinating new world of QIAGEN®

Virtual showroom and application labs

Enjoy discovering innovative  
sample and assay technologies  
at new **QIAGEN.com**

- Experience new dimensions
- Discover fascinating innovations
- Relevant for your personal applications



Scan the code with your iPad,  
or go to [www.qiagen.com/qiagen-experience](http://www.qiagen.com/qiagen-experience).

# Experience



Sample & Assay Technologies



For more information, visit  
**www.Q5PCR.com**

# Fidelity at its finest.

## Q5<sup>®</sup> High-Fidelity DNA Polymerase

Q5 High-Fidelity DNA Polymerase sets a new standard for both fidelity and performance. With the highest fidelity amplification available (>100X higher than *Taq*), Q5 DNA Polymerase results in ultra-low error rates. Its unique buffer system provides superior performance for a broad range of amplicons, regardless of GC content. Available in master mix and hot start formulations, Q5 DNA Polymerase represents the finest in fidelity.

ALSO AVAILABLE: Optimized NEBNext<sup>®</sup> formulation for next generation sequencing library amplification

Mandarin Ducks (*Aix galericulata*) are frequently featured in Chinese art and are regarded as a symbol of fidelity.

### Robust amplification even with high GC amplicons



*Amplification of two human genomic amplicons of mid to high GC content. All reactions were conducted using 30 cycles of amplification and visualized by microfluidic LabChip<sup>®</sup> analysis. All polymerases were cycled according to manufacturer's recommendations. For the 78% GC amplicon, GC Buffers or enhancers were used when supplied with the polymerase.*

A = Q5<sup>®</sup> High-Fidelity DNA Polymerase (NEB)  
B = Phusion<sup>®</sup> High-Fidelity DNA Polymerase (NEB)  
C = KOD DNA Polymerase (EMD)  
D = PfuUltra<sup>™</sup> High-Fidelity DNA Polymerase (Agilent)

PHUSION<sup>®</sup> is a registered trademark and property of Thermo Fisher Scientific.  
Phusion<sup>®</sup> DNA Polymerase was developed by Finnzymes Oy, now a part of Thermo Fisher Scientific.  
PFUULTRA<sup>™</sup> is a trademark of Agilent Technologies, Inc.  
LABCHIP<sup>®</sup> is a registered trademark of Caliper Life Sciences, part of Perkin Elmer, Inc.  
NEBNext<sup>®</sup> and Q5<sup>®</sup> are registered trademarks of New England Biolabs, Inc.



Grete Lundbeck European Brain Research Foundation

# THE BRAIN PRIZE 2013

## 1 MILLION €

IS JOINTLY AWARDED TO

**ERNST BAMBERG**

MAX PLANCK INSTITUTE OF BIOPHYSICS, FRANKFURT AM MAIN, GERMANY

**ED BOYDEN**

MIT, CAMBRIDGE, MA, USA

**KARL DEISSEROTH**

STANFORD UNIVERSITY, CA, USA

**PETER HEGEMANN**

HUMBOLDT UNIVERSITY, BERLIN, GERMANY

**GERO MIESENBOCK**

UNIVERSITY OF OXFORD, UNITED KINGDOM

AND

**GEORG NAGEL**

UNIVERSITY OF WÜRZBURG, GERMANY

*'for their invention and refinement of optogenetics. This revolutionary technique allows genetically specified populations of neurons to be turned on or off with light, offering not only the ability to elucidate the characteristics of normal and abnormal neural circuitry but also new approaches to treatment of brain disorders.'*

THE AWARD CEREMONY WILL TAKE PLACE ON 2 MAY 2013 IN COPENHAGEN

ALL NOMINATIONS WERE REVIEWED BY THE DISTINGUISHED SELECTION COMMITTEE:

YVES AGID, FRANCE, HUDA AKIL, USA, COLIN BLAKEMORE, UNITED KINGDOM, CHAIRMAN, FRED H. GAGE, USA  
TOMAS HÖKFELT, SWEDEN, VICE-CHAIRMAN, FLORIAN HOLSBOER, GERMANY, RANGA R. KRISHNAN, SINGAPORE, JES OLESEN, DENMARK

GRETE LUNDBECK  
EUROPEAN  
BRAIN RESEARCH  
FOUNDATION

THE  
BRAIN  
PRIZE

*The Brain Prize recognizes and rewards outstanding contributions to European neuroscience, from basic to clinical*



# Support the sciences. **Get rewarded.**

Show your AAAS pride and reward yourself with the new AAAS Platinum Advantage Rewards Card from NASA Federal Credit Union.

Apply now and get  
**10,000 bonus points!**

Go to [nasafcu.com/AAASpromo](https://nasafcu.com/AAASpromo)



Get **10,000 bonus points** if you sign up for a card and spend \$3,000 within 90 days of account opening.

Learn more at  
[nasafcu.com/AAASpromo](https://nasafcu.com/AAASpromo).

Subject to credit approval.  
Membership in AAAS and NASA FCU is required.  
NASA FCU is federally insured by NCUA.



**eppendorf  
& Science**  
**PRIZE FOR  
NEURO  
BIOLOGY**



2012 Winner  
Dr. Marlene R. Cohen  
Assistant Professor  
University of Pittsburgh

## Call for Entries

**Application Deadline  
June 15, 2013**

### **Eppendorf & Science Prize for Neurobiology**

The annual Eppendorf & Science Prize for Neurobiology, an international award, honors young scientists for their outstanding contributions to neurobiological research. The winner and finalists are selected by a committee of independent scientists, chaired by Science's Senior Editor, Dr. Peter Stern. To be eligible, you must be 35 years of age or younger.

### **You could be next to win this prize and to receive**

- > Prize money of US\$25,000
- > Publication of your work in Science
- > Full support to attend the Prize Ceremony held in conjunction with the Annual Meeting of the Society for Neuroscience in the USA
- > An invitation to visit Eppendorf in Hamburg, Germany

It's easy to apply!

Learn more at: [www.eppendorf.com/prize](http://www.eppendorf.com/prize)

**eppendorf**







# STAY INFORMED! STAY CONNECTED!

Get more from your AAAS membership

Are you currently registered to receive e-mails from AAAS and *Science*?

E-mail is the primary way that AAAS communicates with our members about AAAS programs, new member benefits, invitations to special events, and, of course, the latest news and research being published in *Science*.

Sign up today to receive e-mails from AAAS and ensure that you are getting the most out of your membership and *Science* subscription.\*

To get started visit: [promo.aaas.org/stayconnected](http://promo.aaas.org/stayconnected)

You'll need your AAAS Member number. Find it above your name on your *Science* mailing label.

Don't miss a thing. Sign up for e-mail communications from AAAS today!





© 2013 Cell Signalling Technology, Inc. Cell Signalling Technology is a trademark of Cell Signalling Technology, Inc.



## There's only one Science



### Science Careers Advertising

For full advertising details, go to  
ScienceCareers.org and click  
For Employers, or call one of  
our representatives.

#### Tracy Holmes

Worldwide Associate Director  
Science Careers  
Phone: +44 (0) 1223 326525

#### THE AMERICAS

E-mail: [advertise@sciencecareers.org](mailto:advertise@sciencecareers.org)  
Fax: 202-289-6742

#### Tina Burks

United States/Canada/South America  
Phone: 202-326-6577

#### Marci Gallun

Sales Administrator  
Phone: 202-326-6582

#### Online Job Posting Questions

Phone: 202-312-6375

#### EUROPE / INDIA / AUSTRALIA / NEW ZEALAND / REST OF WORLD

E-mail: [ads@science-int.co.uk](mailto:ads@science-int.co.uk)  
Fax: +44 (0) 1223 326532

#### Lucy Nelson

Phone: +44 (0)1223 326527

#### Kelly Grace

Phone: +44 (0) 1223 326528

#### JAPAN

#### Yuri Kobayashi

Phone: +81-(0)90-9110-1719  
E-mail: [ykobayas@aaas.org](mailto:ykobayas@aaas.org)

#### CHINA / KOREA / SINGAPORE / TAIWAN / THAILAND

#### Ruolei Wu

Phone: +86-1367-1015-294  
E-mail: [rwu@aaas.org](mailto:rwu@aaas.org)

All ads submitted for publication must comply with applicable U.S. and non-U.S. laws. *Science* reserves the right to refuse any advertisement at its sole discretion for any reason, including without limitation for offensive language or inappropriate content, and all advertising is subject to publisher approval. *Science* encourages our readers to alert us to any ads that they feel may be discriminatory or offensive.

**Science Careers**

From the journal *Science*



ScienceCareers.org



Join Germany's  
international  
research  
community!



Our website offers a wide  
range of information:

- PhD programmes in Germany
- Career opportunities at German research institutes
- Research funding organisations
- Latest research news, events and much more

[www.research-in-germany.de](http://www.research-in-germany.de)



Find us on Facebook:  
[facebook.com/  
Research.in.Germany](https://facebook.com/Research.in.Germany)



Follow us on Twitter:  
[twitter.com/  
ResearchGermany](https://twitter.com/ResearchGermany)



AN INITIATIVE OF THE  
Federal Ministry  
of Education  
and Research

**Research in  
Germany**



**Land of Ideas**

For recruitment in science,  
there's only one  
**Science**  
Careers in  
Biotech/Pharma

**Career Feature:  
April 12, 2013**

Ads accepted  
until April 8 if  
space is still  
available.



Crossover between Industry and Academia isn't new but collaborations have become increasingly important for both work sectors. Academicians need to better understand how they can get involved with industry and what benefits can be gained from these arrangements. Use this opportunity to champion your company's partnership opportunities and reach scientists eager to learn more about industry.

Your job is seen by 700,000 readers around the globe from varied backgrounds and it sits on special bannered pages promoting careers in biotech/pharma.

Bonus distributions to:

- Experimental Biology, April 20–24, Boston, MA
- BIO International Convention, April 22–25, Chicago, IL
- BIO International Convention Career Fair, April 22, Chicago, IL

#### To book your ad:

E-mail: [advertise@sciencecareers.org](mailto:advertise@sciencecareers.org)  
Or telephone us:  
United States: 202-326-6582  
Europe/RoW: +44 (0) 1223 326500  
Japan: +81-(0)-90-9110-1719  
China/Korea/Singapore/Taiwan/Thailand: +86-1367-1015-294

**Science Careers**

From the journal *Science*



ScienceCareers.org

# In the Global Competition For Smart Minds, Germany Grows Its Catch

Ever since the European Council's decision in 2000 to transform the European Union into "a competitive and dynamic knowledge-based economy," Germany's federal government has been pumping money into research and development through various mechanisms. As a result, not only are German research institutions forging major changes in the way that researchers teach, collaborate, and advance in their careers, they are also creating more jobs. These jobs run the gamut from junior and senior researchers to support staff. With good long-term funding prospects and attractive salaries, Germany has become a major contender in the global competition among nations to draw in top talent. **By Gunjan Sinha**



Humboldt University, Berlin

In 2003, **Barbara Conradt** left the Max Planck Institute for Neurobiology in Martinsried, Germany to take a job in the United States—she thought it was for good. She had accepted a tenure-track position at the Geisel School of Medicine (formerly Dartmouth Medical School), in Hanover, New Hampshire. Not only did the position offer better long-term job prospects and a supportive research community, she much preferred the openness and diversity of the American academic environment.

"I was excited about the U.S. system," says Conradt, which she had experienced first-hand having finished both her Ph.D. and a postdoc in the United States. "I thought I would never move back to Germany," she recalls. So it was no wonder that when a recruiter approached her in 2010 with a job opportunity at the Center for Integrated Protein Science in Munich (CIPSM), Germany, she balked. But she soon reconsidered. If she were offered the job, she thought, she would merely use it as leverage to boost her standing at Dartmouth.

Things turned out quite differently, however. "I realized that a lot had happened in Munich," Conradt explains. The campus had grown, the university environment had become more diverse, and there were more women. "I really felt like this was a place I wanted to come back to and make a difference," she says. CIPSM offered her a full professorship and also offered to move her entire lab over. She accepted the offer with open arms.

## Upcoming Features

Cancer Research Careers:  
Academia vs. Industry—March 29

Biotech and Pharma:  
Forging Academic Collaborations—April 12

Regional Focus: Wales—April 26

CIPSM was established in 2006 through Germany's Excellence Initiative—a program that invites institutes of higher education to apply for federal grant money to fund growth in three areas: graduate programs, clusters of excellence that focus on and accelerate hot research topics, and institutional strategies (also called future concepts) that improve the institution's quality of research and teaching. Launched in 2005, the Excellence Initiative was a bold plan to push innovation at what was seen as Germany's inertial university system. In addition to receiving lump sum state funding, universities could now compete for additional federal funding by submitting ideas for new educational strategies, research initiatives, or collaborations that span multiple research institutes. By fostering innovation, the goal was to create "elite universities" that could compete with the world's best universities in drawing in top talent. The first and second rounds of the initiative doled out €1.9 billion to universities between 2007 and 2012. The third and final round will award €2.7 billion to universities through 2017—a total of €4.6 billion to a total of 39 universities across 13 states.

The Excellence Initiative isn't the only mechanism by which **continued**

By fostering innovation, the goal was to create "elite universities" that could compete with the world's best universities in drawing in top talent.

Otmar Wiestler





money is flowing into the sciences. Since the European Council's decision in 2000 to transform the European Union into "a competitive and dynamic knowledge-based economy" by 2010, Germany has increased spending on research and development dramatically—the results of which are already tangible. Between 2005 and 2010, the number of jobs in research and development grew by 15%.

Not only has industry contributed to this growth by increasing research and development expenditure by 21% during the same period, the federal government upped research and development investment from €9 billion in 2005 to approximately €13.8 billion in 2012—an increase of 53%, according to the Federal Ministry of Education and Research (Bundesministerium für Bildung und Forschung, or BMBF).

The result has been that regions around the country that have traditionally been hubs of research and development are expanding and innovating and in the process creating new job opportunities.

### The South: Bavaria

Not only can the state of Bavaria lay claim to hosting two elite universities, the Technische Universität München (TUM) and the Ludwig-Maximilians-Universität München (LMU), it can also boast winning the second highest share of award money through both Excellence Initiative rounds for a total of €370 million.

At the CIPSM—an excellence cluster set up by the TUM, the LMU, and the Max Planck Institutes of Neurobiology and Biochemistry—the focus is on protein science. The CIPSM includes three locations on the outskirts of the city of Munich—Großhadern/Martinsried, Garching, and Weihenstephan—and university physics and medicine departments in downtown Munich. The center enables scientists from LMU and TUM, as well as scientists from the neighboring Max Planck Institutes and the Helmholtz institutes, to come together and work on common research goals. Since 2007, CIPSM has received about €45 million from

○ **To the west, the state of Baden-Württemberg has been the most successful state in the Excellence Initiative competition. The state's universities garnered a total of €545 million—the most of any state.**



Baden-Baden

the Excellence Initiative and funding of the cluster has been renewed for 2012 through 2017, with a budget of approximately €7 million per year.

"I have not regretted [leaving Dartmouth] at all," says Conradt, who studies cell apoptosis and mitochondrial dynamics in *Caenorhabditis elegans*. Conradt moved to CIPSM at a time when NIH funding had "really dropped," she says. Meanwhile in Germany, the federal and state governments continue to prioritize funding of research and development over the long-term, which is vital for scientific progress, she adds. Just as appealing, the academic environment in and around Munich continues to change in ways that promote diversity. For example, like most excellence clusters, CIPSM's official language is English. Teaching of the sciences at the Master's level at CIPSM's host universities is also now conducted in English, which has really helped draw people from all over the world, she says.

### Baden-Württemberg

To the west, the state of Baden-Württemberg has been the most successful state in the Excellence Initiative competition. The state's universities garnered a total of €545 million—the most of any state.

In 2008, **Virginie Lecaudey** became the first junior professor at the Centre for Biological Signalling Studies (BIOSS)—a cluster of excellence at the University of Freiburg. At BIOSS the focus is on combining analytical methods with synthetic biology approaches to characterize complex signaling pathways—a field of study that is unique in Germany. In landing the job, Lecaudey feels "quite lucky," she says, because it is a tenure-track position. Once nonexistent in Germany, tenured-track positions are now being created by universities as part of the wave of on-going changes brought on by the Excellence Initiative.

Traditionally, universities have offered tenured professor positions only to academics outside of their institution; so junior researchers have had no path towards advancing their careers within the same institution. That's because to become a tenured professor an academic must also earn *Habilitation*—a second more rigorous dissertation that qualifies academics to supervise dissertations and teach junior scholars. (While *Habilitation* is no longer required, it is still considered important.) At the same time, the university rule of *Hausberufungsverbot* prohibits academics from becoming professors at the same university at which they have earned *Habilitation*. This restriction combined with the fact that job openings are rare because turnover can **continued**



Munich



150 Years  
Science For A Better Life

HealthCare

[www.career.bayer.de](http://www.career.bayer.de)

**Marion Hitchcock** wants to make the world a better place - for everyone. As a scientist at Bayer, Marion knows she is doing just that. Searching for solutions and never giving up. That is the passion that unites all of us at Bayer. We call it the Bayer Spirit. If you feel it, too, then it is high time we had a chance to talk about a career at Bayer.

## Postdoctoral Scientists

Bayer HealthCare is a leading pharmaceutical company. Its pharmaceutical business, Bayer Pharma AG, is headquartered in Berlin, Germany, where more than 500 scientists discover new medicines with the goal to improve the life of patients suffering from various types of cancers and benign gynecological diseases. To strengthen this research, we are offering 10 postdoctoral positions in several areas including survival signaling, tumor metabolism, cell cycle regulation, cancer immunotherapy, epigenetic regulation of transcription, inflammation and nociception in endometriosis.

**Job description** As a Postdoctoral fellow at Bayer Pharma AG your tasks will involve

- Evaluation of patho-mechanisms and identification of novel targets as starting points for new drug discovery programs
- Establishment and characterization of novel preclinical in vitro and in vivo model systems
- Scientific planning, evaluation, interpretation and presentation of experimental studies
- Collaboration in interdisciplinary project groups across various functions

This is a fixed-term contract for three years.

### Your qualifications

- MD or a university degree in Biology, Biochemistry, Pharmacy or Veterinary Medicine with a PhD in the field of Oncology, Veterinary Sciences or Pharmacology
- Creative and flexible thinking
- Ability to work in a team as well as independently
- Sense of responsibility and ability to adapt to a dynamic research environment
- Excellent organizational skills and the expertise to instruct and train staff
- Proficient verbal/written communication and presentation skills
- Fluent command of English, a basic knowledge of German is helpful but not required

**Your application** If your background fits this profile, please apply online at [www.career.bayer.de](http://www.career.bayer.de) (Reference Code 0000052222).

[www.career.bayer.de](http://www.career.bayer.de)

Fon +49 214 30 9 97 79



## Featured Participants

**Centre for Biological Signaling Studies (BIOSS)**  
**University of Freiburg**  
[www.bioss.uni-freiburg.de/cms/index.php](http://www.bioss.uni-freiburg.de/cms/index.php)

**Center for Integrated Protein Science in Munich (CIPSM)**  
[www.cipsm.de](http://www.cipsm.de)

**German Cancer Research Center**  
[www.dkfz.de/en/index.html](http://www.dkfz.de/en/index.html)

**German Federal Ministry of Research and Education**  
[www.bmbf.de](http://www.bmbf.de)

**Max Delbrück Center for Molecular Medicine (MDC)**  
**Berlin-Buch Member of the Helmholtz Association**  
[www.mdc-berlin.de/en](http://www.mdc-berlin.de/en)

**NeuroCure Excellence Cluster**  
[www.neurocure.de](http://www.neurocure.de)



Christian Rosenmund



Virginie Lecaudey

**Once nonexistent in Germany, tenured-track positions are now being created by universities as part of the wave of on-going changes brought on by the Excellence Initiative.**

be slow, have made it difficult for junior researchers to advance. Therefore, the creation of tenure-track positions reflect a major change in the system.

Last year, the TUM established the Faculty Tenure-Track System, for example, that aims to create the first 100 tenure-track professorships between now and the year 2020. The plan is to recruit young researchers who have international experience and have demonstrated recognition in their fields, such as by publishing in high-impact journals or winning early-career prizes. Researchers can be hired as assistant professors on a six-year contract that lead to a tenure evaluation.

While the Excellence Initiative has helped forge change at universities, the government's commitment to research and development in Germany isn't stopping there. Just north of Freiburg, in the city of Heidelberg, the German Cancer Research Center (Deutsches Krebsforschungszentrum or DKFZ) has been awarded government money to create additional comprehensive cancer care centers across Germany, says **Otmar Wiestler**, chairman and scientific director of the DKFZ. Last year, the DKFZ announced the launch of the German Consortium for Translational Cancer Research. DKFZ will partner with seven university hospitals to create translational centers at each university site. The consortium is a joint initiative of the Federal Ministry of Education and Research, German Cancer Aid (Deutsche Krebshilfe), and the DKFZ. The BMBF and the participating states provided approximately €12 million for the consortium last year. The annual budget will be gradually raised to reach about €28 million by 2014. German Cancer Aid will provide additional funding upon request for defined research projects and after an evaluation.

To get the project running, DKFZ will be recruiting 21 physician scientists for full professorship positions. This is no easy task, Wiestler says. "People with medical training have lots of job options," he says. "These people are precious. It is very important to provide attractive packages." To that end, DKFZ offers competitive salaries and long-term funding, Wiestler adds.

### The North: Berlin

While Baden-Württemberg is certainly the leader in terms of cash flowing into research, Berlin can now boast claim to being the only other German city, next to Munich, to host two "elite universities." Early in 2012, Humboldt University became the second university in Berlin (after Freie University) to claim the "elite university" title. In addition to winning funding for three of its graduate schools and a strategy to strengthen its overall standing, Humboldt University's NeuroCure Cluster of Excellence won follow-on funding.

NeuroCure's aim is to boost the prominence of neuroscience research in Berlin by forging collaboration among university scientists and researchers from the Max Delbrück Center for Molecular Medicine (MDC) in Berlin Buch, the Deutsche Rheuma-Forschungszentrum (German Rheumatic Disease Research Center), and the Leibniz-Institute for Molecular Pharmacology. The interdisciplinary research projects focus on the functions of the nervous system.

"What is special about NeuroCure isn't the direction of the research but rather what we are doing with the money," says **Christian Rosenmund**, coordinator of the cluster. Universities in Germany's poorer states, such as Berlin, have been suffering from budget cuts for years (universities receive the bulk of their funding from state governments), he explains. Many professorships in Berlin have simply been left vacant. Under the previous coordinator, Dietmar Schmitz, NeuroCure spent a majority of the €5.4 million annual Excellence Initiative funding to establish new professorships and provide them with appropriate equipment, says Rosenmund. Since 2006, NeuroCure has recruited 20 new researchers. "This is unheard of," says Rosenmund, "you're lucky if you get three or four into a single department."

With the additional funds, universities are also able to offer attractive financial packages, an important factor when recruiting scientists from the U.S. where salaries are typically higher. Schmitz recruited Rosenmund in 2009 from the Baylor College of Medicine in Houston, Texas, U.S. In taking the job, Rosenmund accepted a salary cut. But after seeing his budget remain flat for five years in the U.S. and having to face the constant threat of cuts, the opportunity to build something new from the ground up and better long-term funding **continued**



**Alexander von Humboldt**  
Stiftung/Foundation



## Shine your light in Germany

**Profit from excellent conditions for research**

**The Alexander von Humboldt Professorships are Germany's way of creating a beacon effect and energising its research landscape. Every year, the Alexander von Humboldt Foundation is offering ten of the world's leading researchers up to five million EUR each to create new or consolidate existing internationally visible research focus areas at German universities.**

Academics of all disciplines are eligible for an Alexander von Humboldt Professorship, provided that they are established abroad and recognised internationally as top-class researchers. They will be nominated by German universities – where appropriate in cooperation with non-university research institutions. Each Alexander von Humboldt Professorship will be sponsored for a period of five years on the premise that the university presents a convincing strategy to sustain the position once the funding period has come to an end.

This will allow new, long-term research groups to be established, conducting cutting-edge international research. The German Ministry of Education and Research is supporting this programme.

The Humboldt Foundation actively promotes equal opportunities and therefore particularly welcomes nominations on behalf of leading female academics.

More information: [www.humboldt-foundation.de/ahp-en](http://www.humboldt-foundation.de/ahp-en).

**Closing dates for applications: 15 April and 15 October.**

**Exzellenz verbindet –  
be part of a worldwide network.**



Alexander von Humboldt Foundation  
Jean-Paul-Str. 12  
53173 Bonn  
Germany  
[info@avh.de](mailto:info@avh.de)

**[www.humboldt-foundation.de](http://www.humboldt-foundation.de)**



prospects in Germany were enough compensation, he says.

Further north in the Berlin suburb of Buch, an even larger influx of new talent will soon be moving in. In November of last year, the federal and state government of Berlin announced support for a cooperative venture between MDC and the Charité University Hospital to establish the Berlin Institute of Health (BIH). The aim is to quickly translate basic research into clinical applications. The MDC is one of 18 research institutions of the Helmholtz Association, all of which are funded 90% by the federal government and 10% by the states.

A major emphasis at the MDC is on systems medicine whereby researchers focus on characterizing molecules and biochemical pathways that are similar among different diseases. For example, certain proteins, such as NF-kappaB, are highly active at sites of inflammation. Since inflammation is involved in many diseases, these proteins can serve as a common therapeutic target. The BIH will function as a place for physicians and researchers to come together to study and correlate the clinical aspects of diseases with the molecular aspects and vice versa, says **Walter Rosenthal**, scientific director of the MDC. Beginning in 2013, the federal and state government will provide €300 million to the BIH over the next five years. An additional €40 million over a period of 10 years will also be donated by a private foundation. The BIH will ultimately occupy its own physical space and is expected to be fully operational by 2018 with an annual budget of €80 million. New hires will have joint appointments at either the Charité or MDC and the BIH.

“Germany is very research friendly right now,” Rosenthal says. “We can offer very attractive packages.”

### Funding Isn't Everything

But while the money is certainly flowing, some scientists continue to be frustrated by obstacles that money alone can't overcome. Language, for example, can still be a barrier. While many institutions hold English as the official language, life outside of the academic environment can be challenging without basic German skills, says Lecaudey, a native of France. And while institutions have made huge strides in recruiting female scientists and in supporting families, the culture at large hasn't kept pace. It can be difficult to place children under three years of age in daycare in West Germany, for example, in part because it has

been culturally frowned upon for mothers to leave care of such young children to someone else. Schools have also traditionally only been open until early afternoon. However, these aspects are slowly changing. There are major government efforts towards keeping schools open for full days and towards building more day-care centers with guaranteed availability, regardless of a child's age.

More pressing is the question of whether the funding flood will last, particularly for those supported by the Excellence Initiative, which ends in 2017. State governments and universities are expected to pick up the tab, but in poorer states, such as Berlin, junior researchers may lose their jobs and support staff and core facilities may wither. For his part, Rosenmund encourages all researchers at NeuroCure to seek out as much third-party funding as possible; this sentiment was echoed by Conradt and Lecaudey.

There is one change that might help, however. Last year, Germany's constitutional law was amended to allow the federal government to help finance universities, not only on a project basis, but also over the long-term.

In the meantime, one thing is clear: the work environment for scientists in Germany has changed and is still changing. The last 10 years has seen a switching of the guard, says Conradt, as younger scientists with international experience come to occupy positions of power. They are bringing back ideas and making the system more open and diverse, she says. Indeed, between 2005 and 2009 alone the number of non-German scientists working in Germany increased by one-third, according to the BMBF. The increase in government spending on research and development which, at 2.88% of GDP, is the highest percentage of any EU member state, combined with the political push from the very top to move science forward promise to continue to make Germany an enticing place for scientists to work and live.

*Gunjan Sinha is a freelance writer living in Berlin, Germany.*

DOI: 10.1126/science.opms.r1300130

“Germany is very research friendly right now,” Rosenthal says. “We can offer very attractive packages.”

CREDIT: © ISTOCKPHOTO.COM/NIKADA

Berlin





# THE H.C. ØRSTED POSTDOC PROGRAM

## Technical University of Denmark (DTU)

DTU invites highly talented young researchers to apply for stipends under the H.C. Ørsted Postdoc Program. The program is named after the founder of the university, H.C. Ørsted, who discovered electromagnetism. We seek candidates who have obtained outstanding

results during their PhD studies and who have demonstrated excellence and potential in their field of study.

In order to be considered, applications must include a confirmation letter signed by the relevant DTU department head, stating

that the department and the candidate have agreed upon the research plan.

Applications must be based on the details of the full text announcement.

Application deadline: **10 May 2013**

DTU is a technical university providing internationally leading research, education, innovation and public service. Our staff of 5,000 advance science and technology to create innovative solutions that meet the demands of

society; and our 7,600 students are educated to address the technological challenges of the future. DTU is an independent academic university collaborating globally with business, industry, government, and public agencies.

**Further details: [dtu.dk/career](http://dtu.dk/career)**



## SCIENCE AND TECHNOLOGY AT A GLOBAL SCALE - SET THE STANDARDS FOR THE FUTURE

See our PhD-programmes at [dtu.dk/phd](http://dtu.dk/phd)

### FOCUS ON GERMANY



max-planck-institut für  
neurobiologie



The Max Planck Institute of Neurobiology in Martinsried, Germany, invites applications for

### Two Max Planck Research Group Positions in the field of Assembly and Function of Neural Circuits

We are looking for outstanding scientists with an original and exciting research program addressing fundamental questions in neuroscience, including how genetic programs prescribe the formation of neuronal circuits, how these circuits control and execute behavior, and to what extent developmental aberrations cause nervous system disorders later in life. We are envisioning a focus on well-established or novel vertebrate model systems, including but not limited to zebrafish and mouse. We expect the successful candidates to contribute actively to the institute's multi-disciplinary research on the basic function, structure and development of the nervous system ([www.neuro.mpg.de](http://www.neuro.mpg.de)).

The position holders will lead an independent research group, with generous funds for positions, start-up investments, and annual running costs. The position is considered equivalent to a W2 Professorship and will initially be for 5 years with the possibility of twice a 2-year extension. The group will have access to the institutional infrastructure including animal and transgenic facilities, microscopy, imaging and histology services. PhD students may be enrolled through the international PhD program IMPRS-LS ([www.imprs-ls.de](http://www.imprs-ls.de)) or the Graduate School in Systemic Neuroscience ([www.gsn.uni-muenchen.de](http://www.gsn.uni-muenchen.de)).

The MPI of Neurobiology is an international research institute with English as the working language. A childcare facility is located on campus. Women are especially encouraged to apply. Disabled applicants with equal qualifications will be given preferential treatment.

Applications (refer to our website for details) and inquiries should be sent until April 7th to Tobias Bonhoeffer, Managing Director, MPI of Neurobiology through Kristin Reuter ([reuter@neuro.mpg.de](mailto:reuter@neuro.mpg.de)).

## Ostrow School of Dentistry of USC

### ASSISTANT PROFESSOR (TENURE-TRACK) OR ASSOCIATE PROFESSOR

The Ostrow School of Dentistry of USC seeks outstanding candidates for a tenure-track position at the rank of assistant or associate professor in the Division of Biomedical Sciences to conduct cutting-edge research in the areas of cell and developmental biology, tissue regeneration, cell-signaling and/or gene regulation. The successful candidate will establish a research program with relevance to craniofacial and skeletal biology at the USC Center for Craniofacial Molecular Biology. Examples of appropriate research interests include molecular mechanisms of organogenesis, stem cell biology, and genetics of craniofacial malformations, and orofacial disease-related research.

Candidates must have a PhD in developmental biology, stem cell biology, or molecular biology, and should have a DDS/DMD or equivalent dental degree. Exceptional candidates without dental degree will be considered. Candidates with translational research interest are strongly encouraged to apply. The successful candidate is expected to develop independent extramurally funded research programs, which complement our interests as described at <http://www.usc.edu/hsc/dental/ccmb> and <http://pibbs.usc.edu>

Interested applicants should submit a cover letter, complete curriculum vitae, statement of current and future research plans, selected recent publications, and arrange to have three letters of reference sent to: **Dr. Yang Chai, Search Committee Chair, USC Center for Craniofacial Molecular Biology, Ostrow School of Dentistry of USC, c/o Ms. Patricia Thompson, 2250 Alcazar Street, CSA 103, Los Angeles, CA 90033; [patthomps@usc.edu](mailto:patthomps@usc.edu)**. Consideration of applicants will begin immediately and will continue until the position is filled.

*USC values diversity and is committed to Equal Opportunity in Employment. Women and men, and members of all racial and ethnic groups are encouraged to apply.*





Rat der  
Eidgenössischen  
Technischen  
Hochschulen  
ETH-Rat

Conseil des  
écoles  
polytechniques  
fédérales  
CEPF

Consiglio  
dei  
politecnici  
federali  
CPF

Cussegl da las  
scolas  
politecnicas  
federalas  
CSPF

Board of the  
Swiss Federal  
Institutes of  
Technology  
ETH Board

The Swiss Federal Institute of Technology Zurich (ETH Zurich) stands for excellent teaching, pioneering basic research and the application of the results for the benefit of society. Together with EPFL and the four federal research institutes PSI, WSL, Empa and Eawag, ETH Zurich is part of the ETH Domain, whose strategic management and supervisory body is the ETH Board. The ETH Board is advertising the position of

## President of the Swiss Federal Institute of Technology Zurich (ETH Zurich)

since the current holder will be retiring and the ETH Board will have to propose a successor to the Swiss government, the Federal Council.

ETH Zurich was established in 1855 and is one of the internationally leading universities in the field of technical and natural sciences, and as such provides researchers with an inspiring environment and their students with a thorough education. Currently, more than 20,000 people are studying, working and carrying out research at ETH Zurich. Outstanding research conditions, a state-of-the-art infrastructure and an attractive environment provide an ideal setting for creative personalities.

### Requirements

Your record in exact, natural or engineering sciences has been internationally recognised. You are able to identify and foster outstanding potentials and visionary ideas, specify strategic guidelines and raise issues in current scientific, technological and societal areas. As an experienced executive in a big organisation, preferably in the field of science or in trade and industry, you have provided evidence of your integrative leadership skills. You have good networks inside and outside the scientific community, and you are prepared to develop ETH Zurich's future and to lend an active hand in shaping the entire ETH Domain with great dedication.

Your personality is characterised by a high degree of social competence, assertiveness and the ability to deal with conflict, also in a participative management culture like that of ETH Zurich. You possess a high degree of communication competence, which you would use both inside and outside the university, and you understand Switzerland's political structures, legislative processes and cultural diversity. Finally, you have a good command of German and English, and preferably a knowledge of French. You are willing to hold office for at least two terms (i.e. eight years). Ideally the starting date would be at the beginning of 2015.

### Applications

Please send your complete application to the President of the ETH Board, Dr. iur. Fritz Schiesser, ETH-Rat, Haldeliweg 15, 8092 Zurich, Switzerland. He will also be available for further information (phone +41 44 632 20 01, schiesser@ethrat.ch). All applications received by 15 April 2013 will be considered for the selection process. Your application will be treated with strict confidentiality. Applications from women are particularly welcome.

## WOMEN IN SCIENCE

forging  
new pathways in  
green  
science



Read inspiring stories of women working in "Green Science" who are blending a unique combination of enthusiasm for science and concern for others to make the world a better place.

Download this  
free booklet  
[ScienceCareers.org/  
LorealWiS](http://ScienceCareers.org/LorealWiS)



This booklet is brought to you by the  
AAAS/Science Business Office  
in partnership with the  
L'Oréal Foundation

## Diabetes

CENTER OF EXCELLENCE



UMassMemorial  
Health Care



University of  
Massachusetts  
UMASS Medical School

### DIABETES CLINICAL/TRANSLATIONAL INVESTIGATOR

The Diabetes Center of Excellence at the University of Massachusetts Medical School invites applications for a SENIOR TENURED or JUNIOR TENURE-TRACK clinical or translational investigator faculty position. The Diabetes Center of Excellence currently consists of basic and physician scientists representing a broad range of disciplines in the biomedical and clinical sciences, with members from several Medical School Departments and Programs working together as central New England's leading center for diabetes clinical care, innovation, and discovery. The Center occupies state-of-the-art clinical and research space on an expanding Medical School campus. Clinical and community investigators benefit from infrastructure for recruitment and retention of research participants, resources for measurement, behavioral and nutritional interventions, top-notch facilities, academic-community research partnerships, and by basic research support from core facilities for deep sequencing, proteomics, genotyping, fluorescence-activated cell sorting, digital imaging/confocal microscopy, genomics/bioinformatics, transgenic/knockout mice, and mouse metabolic phenotyping. Adult and pediatric clinical efforts of the Diabetes Center are housed in a new Ambulatory Clinical Care building designed so that patients can receive appropriate retinal photos, foot care, diabetes education, and other routine medical care at one location. The position will be highly competitive with regard to start-up funds, and salary. The Center seeks an individual of outstanding clinical and/or translational research potential relating to diabetes pathophysiology or treatment.

Applicants should send curriculum vitae, statement of research interests, and names and addresses of three references to:

David M. Harlan, M.D.  
Co-Director, Diabetes Center of Excellence  
Search Committee Chair  
c/o Patricia Cannon  
55 Lake Avenue North  
Albert Sherman Center, Room AS7.2049  
Worcester, MA 01655  
Patricia.cannon@umassmed.edu  
508.856.3800

*As an Equal Opportunity and Affirmative Action Employer, UMMS recognizes the power of a diverse community and encourages applications from individuals with varied experiences, perspectives, and backgrounds.*



## WE'RE NOT INVESTING IN RESEARCH. WE'RE INVESTING IN RESEARCHERS.

History shows that great breakthroughs often come from unexpected places. The only constant is talent. Pathway to Stop Diabetes provides five- to seven-year grants of \$1.625 million to enlist a new generation of brilliant scientists, regardless of their current field of study, and provides freedom, autonomy, professional mentoring and opportunities for collaboration to drive new breakthroughs. It's a radical new road for diabetes research. And one that can accelerate your career.



### PATHWAY TO STOP DIABETES

American Diabetes Association  
RESEARCH FOUNDATION

APPLICATIONS BY  
NOMINATION ONLY.  
DEADLINE:  
AUGUST 16, 2013.  
FIND OUT MORE AT  
[DIABETES.ORG/  
PATHWAY](http://DIABETES.ORG/PATHWAY)



## INSPIRED BY PASTEUR SUPPORTED BY SANOFI

With the great success of the first Sanofi – Institut Pasteur Awards in 2012, Sanofi and the Institut Pasteur are pleased to announce the continuation of these Awards in 2013.

These Awards will honor and support four scientists, whose outstanding research shows real progress in the life sciences that contributes to global public health specifically in the five following fields:

- Tropical and neglected diseases
- Innovative approaches to disease prevention, including vaccines
- New approaches to drug resistance
- Therapeutic approaches to diseases and senescence: neurobiology and regenerative medicine
- Immunology, immunomodulation, immunogenetics, translational technologies

Nomination of mid-career\* as well as senior scientists from all over the world are encouraged.

A distinguished international Jury will choose the Awardees:

Prof. Peter C. Agre, Prof. Elizabeth H. Blackburn, Prof. Alice Dautry, Prof. Jörg Hacker, Prof. Ivan I. Dedov, Prof. Philippe Monteyne, Prof. Philippe Sansonetti, Dr Elias Zerhouni.

Scientific Coordinator of Awards: Prof. Paul Lazarow ([2013awards@pasteur.fr](mailto:2013awards@pasteur.fr))

\*The Awards are for scientists who have published outstanding research as principal investigators.

### AWARDS AND PROCEDURE:

The four winners will each receive an award of 100 000 euros.

More information and the nomination form are available on the website: [www.sanofi-institutpasteur-awards.com](http://www.sanofi-institutpasteur-awards.com)

### DEADLINE TO SUBMIT NOMINATIONS:

Friday, 3<sup>rd</sup> May, 2013.

### AWARDS CEREMONY:

Tuesday, 5<sup>th</sup> November, 2013 in Paris.



## ASSISTANT PROFESSOR/ASSOCIATE PROFESSOR/ PROFESSOR

Department of Basic Science and Craniofacial Biology  
NYU COLLEGE OF DENTISTRY

The New York University College of Dentistry (NYUCD) is one of the largest academic dental institutions in the United States. NYUCD is a vital and growing research institution committed to education of the next generation of clinicians and scientists. Dr. Nicola C. Partridge was recruited as the Chair of Basic Science & Craniofacial Biology in 2009, and she has been actively recruiting faculty since. The Department of Basic Science and Craniofacial Biology is seeking three faculty candidates with expertise in Anatomy, Physiology, or Pharmacology. Appointment will be tenure track or non-tenure track at the Assistant/Associate Professor/Professor rank. NYU has excellent possibilities for collaboration with engineering and physical scientists at Polytechnic Institute of New York University and the new NYU Bioengineering Institute.

Candidates are required to have a doctoral degree and be prepared to undertake an independent research program. Prior teaching experience is strongly preferred. In addition, a documented history of academic accomplishments in the area of teaching, research and scholarly activity is desirable. Responsibilities include: teaching and engaging in basic and/or healthcare related research, which should complement established research programs in the college including Craniofacial and Bone Biology, Cancer, Tissue Engineering, and/or Infectious Diseases; team teach courses in the basic sciences to students from a range of healthcare related disciplines; and institutional commitment to the University, College, and Department.

NYU offers an excellent benefits package. Salary and academic rank will be commensurate with credentials and experience. An excellent start-up package and salary support will be available as well as renovated laboratory space. Applicant should send curriculum vitae, statement of proposed research and the names and addresses of three references to: **Dr. Nicola C. Partridge, Chair, Department of Basic Science & Craniofacial Biology, New York University College of Dentistry, 345 East 24th Street, Room 902A, New York, NY 10010.**



NEW YORK UNIVERSITY

NYU is an Equal Opportunity/Affirmative Action Employer.

### ANNOUNCEMENTS

## 2013 SUMMER INSTITUTES & CONFERENCES

at the University of Washington  
Seattle, Washington, USA

- ◆ **18th Summer Institute in Statistical Genetics**  
8-26 July 2013, <http://sisg.biostat.washington.edu>
- ◆ **5th Summer Institute in Statistics and Modeling in Infectious Diseases**  
8-24 July 2013, <http://depts.washington.edu/sismid/>
- ◆ **2nd Summer Institute in Biostatistics**  
12-16 August 2013, <http://sib.biostat.washington.edu>
- ◆ **SQG Conference: "Impact of Large-Scale Genomic Data on Statistical and Quantitative Genetics"**  
24-26 November 2013, <http://www.sqg13.org>



UNIVERSITY of WASHINGTON



UW Biostatistics  
[biostat.washington.edu](http://biostat.washington.edu)  
[biostat@u.washington.edu](mailto:biostat@u.washington.edu)



### Join the Conversation!

Twitter is a great way to  
connect with AAAS  
members and staff about  
the issues that matter  
to you most. Be a  
part of the discussion  
while staying up-to-date  
on the latest news  
and information about  
your personal  
member benefits.

**Follow us**  
**@AAASmember**  
**and join the**  
**conversation with**  
**#AAAS**



[MemberCentral.aaas.org](http://MemberCentral.aaas.org)

The University of Edinburgh is an exciting, vibrant, research led academic community offering opportunities to work with leading international academics whose visions are shaping tomorrow's world.



College of Humanities and Social Science

College of Medicine and Veterinary Medicine

College of Science and Engineering

### Chancellor's Fellowships

£37,382 - £44,607

The University of Edinburgh, a global top 20 University located in one of the world's finest cities, is making a further major investment in the future of its academic staff with the appointment of a second cohort of prestigious tenure-track Fellowships across all disciplines. These 5-year Fellowships are intended to support outstanding candidates at the start of their independent academic careers. Up to 100 positions are available.

A Chancellor's Fellow will already show the ability to conduct world-leading research and exhibit clear potential to become an international leader in their discipline. The Fellow will be able to concentrate on research in the first instance, progressively acquiring the full duties of University Lecturer across the period of the Fellowship. Subject to satisfactory review at the end of 3 years, the Fellow will move to an open contract on the University academic staff.

Committed to Equality and Diversity

The University of Edinburgh is a charitable body, registered in Scotland, with registration number SC005336.

Appointment will normally be made on the Grade 8 Academic scale (£37,382-£44,607), dependent on experience. In exceptional circumstances a more senior appointment may be made. Positions are available with immediate effect and it is expected that successful applicants will be in post by September 2013.

General advice may be obtained by emailing [chancellorsfellows@ed.ac.uk](mailto:chancellorsfellows@ed.ac.uk) or from the appropriate Head of School or Centre, details of which are available on our website.

**Applications containing a detailed CV and a 1-page outline of a proposed research programme should be made online at [www.ed.ac.uk/jobs](http://www.ed.ac.uk/jobs) by searching for Chancellors Fellowships.**

**Closing date: 18 April 2013 (5pm).**

[www.ed.ac.uk/jobs](http://www.ed.ac.uk/jobs)



### Plant Virologist Assistant or Associate Professor

The Institute of Agriculture and Natural Resources (IANR) at the University of Nebraska-Lincoln (UNL) is committed to world-class excellence in applications of agricultural and life sciences towards a sustained high quality of life for the citizens of Nebraska and a quickly growing global population. Reflecting this commitment, IANR has announced an immediate initiative to hire more than 30 new tenure-track faculty members to fill strategic needs in impact areas of Science Literacy, Stress Biology of Plants and Animals, Healthy Humans, Healthy Agro/Eco Systems, and Computational Sciences. To view a listing of all of these positions, and for details as positions are released, please see <http://ianrhome.unl.edu/web/ianr/growingianr>.

Within this growth initiative, IANR is seeking applicants for an academic year tenure-leading plant virology position (90% research/10% teaching) to develop a nationally and internationally recognized research program in the broad area of emerging viral diseases with a focus on economically important agricultural and bioenergy crops. The incumbent is expected to apply novel approaches to virus discovery as well as understand the impact of global climate change on the epidemiology of emerging plant diseases. The incumbent will also function as the State Virologist with responsibility for managing virus diseases of economically important crops. Expectations include the development of a strong extramurally funded research program, publication of research results in refereed scientific journals and presentations at professional meetings. Collaboration with other virology programs in the Nebraska Center for Virology and in stress biology is expected. The incumbent will be expected to teach courses in virology, plant pathology or microbiology and advise undergraduate and graduate students as well as serve on graduate committees and contribute to curriculum development in the Plant Sciences. The tenure-home for the position will be the Department of Plant Pathology with an appointment in the Nebraska Center for Virology. The person will be housed in a laboratory in the Morrison building, which is home to the Nebraska Center for Virology.

A Ph.D. in plant biology, biochemistry, plant pathology or a closely related field is required. For the Assistant Professor level, preference will be given to candidates with at least two years of experience. For the Associate Professor level, an externally supported, nationally recognized research program in the broad area of plant virology is required. The successful candidate will have a strong commitment to education and research, excellent communication skills, and the desire and ability to work cooperatively on multi-disciplinary projects.

To view the complete position details and make application for this position, go to the UNL Employment web site: <http://employment.unl.edu>. Search for requisition number **F\_130088**. Click on "**Apply to this Job**". Complete the application and attach a letter of interest, curriculum vitae, contact information for three professional references, a 2-3 page description of research interests, and a brief statement of teaching philosophy. Review of applications will begin on **May 1, 2013** and continue until the position is filled or the search is closed.

*The University of Nebraska has an active National Science Foundation ADVANCE gender equity program, and is committed to a pluralistic campus community through Affirmative Action, Equal Opportunity, work-life balance, and dual careers.*



## Science Careers is the forum that answers questions.



Science Careers is dedicated to opening new doors and answering questions on career topics that matter to you. With timely feedback and a community atmosphere, our careers forum allows you to connect with colleagues and experts to get the advice and guidance you seek as you pursue your career goals.

### Science Careers Forum:

- » Relevant Career Topics
- » Timely Advice and Answers
- » Community, Connections, and More!



Visit the forum and join  
the conversation today!

*Your Future Awaits.*



The University of Pennsylvania, School of Dental Medicine invites applications for tenured Professor and Chair of the Department of Anatomy and Cell Biology. Candidates are sought who have a strong record in research and extramural funding, particularly in the areas of cellular and stem cell biology related to tissue development, regeneration and repair. Commitment to teaching and service is an important consideration.

The Department Chair will have the opportunity to build new and existing research areas. The School of Dental Medicine is situated on a walkable campus that includes the Schools of Medicine, Veterinary Medicine, Nursing, Engineering, and the Children's Hospital of Philadelphia, and has a vibrant and interdisciplinary research program. The School is committed to education of dental health professionals in order to prepare graduates to become leaders in the delivery of dental care and in oral health research. The Department is responsible for teaching physiology, anatomy and histology to 1st year dental students and for the ongoing development of these courses to meet the educational needs of new generations of oral health professionals. Responsibilities of the Chair include: recruitment and retention of faculty, provision of leadership in the areas of faculty research, teaching and service and oversight of departmental activities such as budget development and administration.

Individuals with a PhD or dual degree including DMD/DDS, MD, DVM or equivalent are invited to submit a statement of research and teaching interests, curriculum vitae and a vision statement related to Departmental leadership. Review of applications will begin immediately and continue until the position is filled.

Applicants should apply online at:

<http://facultysearches.provost.upenn.edu/applicants/Central?quickFind=51163>

For further information regarding the above position, contact the Chair of the Search Committee: **Robert Ricciardi, PhD, Chair, Dept. of Microbiology, University of Pennsylvania, School of Dental Medicine, 240 S. 40th St, Philadelphia, PA 19104** or [ACBchair@dental.upenn.edu](mailto:ACBchair@dental.upenn.edu).

*The University of Pennsylvania is an Equal Opportunity Affirmative Action Employer; women and minority candidates are strongly encouraged to apply.*



UNIVERSITY of MARYLAND  
SCHOOL OF MEDICINE

### Neurobiology Faculty Position

The Department of Anatomy and Neurobiology (<http://neurobiology.umaryland.edu>) is recruiting for tenured/tenure-track faculty positions in Neuroscience. We are particularly interested in candidates whose research will complement existing strengths in the Department, including: chemical senses, peptidergic circuits, sensorimotor systems, neurodegeneration and neural circuits subserving motivated behaviors and cortical functions. Candidates should have a strong record of scholarly activity and an independent funded research program that can catalyze multi-PI initiatives within the department.

We offer an outstanding intellectual and collaborative environment with highly competitive salary and recruitment packages. All department faculty are members of the Graduate Program in Life Sciences and the interdisciplinary Program in Neuroscience (<http://neuroscience.umaryland.edu>).

Candidates should submit the following as one single PDF file to [facsearch@umaryland.edu](mailto:facsearch@umaryland.edu): detailed curriculum vitae, a brief statement of research interests and goals, and names/contact information for three references. For best consideration candidates should submit their application by June 1, 2013 and should be addressed to the attention of: **Dr. Joseph Cheer, Chair of Faculty Search Committee.**

*University of Maryland is an Equal Opportunity, Affirmative Action Employer. Minorities, women, veterans, and individuals with disabilities are encouraged to apply.*



## FOUNDING SCIENTIFIC DIRECTOR THE ERNEST J. DEL MONTE NEUROMEDICINE INSTITUTE Rochester, NY

The University of Rochester Medical Center (URMC) invites applications and nominations for the Founding Scientific Director of the Ernest J. Del Monte Neuromedicine Institute. The vision for the institute is that it will be an umbrella for neuromedicine at URMC and the university. The Scientific Director of the Del Monte Institute will provide the broad scientific and administrative leadership for the Neuromedicine Research programs and will report to the Dean of the Medical School. S/he will have the unique opportunity to define and shape a coherent identity and vision for neuromedicine research at URMC, lead in a collaborative effort to set priorities, and forge partnerships throughout the university. The institute will conduct cutting-edge basic and translational research primarily related to degenerative and developmental, disorders, sensory, motor, and cognitive function/dysfunction, and injuries to the nervous system including stroke, trauma, and inflammation.

URMC is uniquely positioned to make a major impact on neuromedicine, in multiple areas of basic neuroscience research and in connecting scientific discoveries to the clinic thus enabling URMC to serve as a hub of outstanding research and patient care. Currently URMC research into the nervous system and its disorders accounts for approximately \$30 million direct (\$40 million total) grant funding annually. The concept of an institute that coordinates and enhances the already excellent laboratories and departments is widely embraced by the URMC leadership, which is committed to its long-term focus of support for neuromedicine and has dedicated new research space for the Institute in excess of 25,000 square feet.

The founding director will seek to strengthen connections between the Medical Center, the College of Arts and Sciences and the Hajim School of Engineering, located in close proximity to URMC. In all activities the director is charged with fostering an inclusive environment that accelerates and deepens the collaborations to create a Neuromedicine enterprise whose whole is greater than the sum of its parts.

Candidates for this position must hold a Ph.D. in neuroscience or a related field and/or an M.D. and must qualify for the rank of full professor at the University of Rochester. Desirable candidates will have an accomplished academic career with a distinguished research record. S/he will have a demonstrated record of management, mentorship, and collaboration.

**TO APPLY:** Applications and nominations, including a resume and a substantive cover letter responding to the challenges outlined above, should be sent to: **Philip Jaeger, Vice President, Heather Brome, Senior Associate, Isaacson, Miller, E-mail: 4695@imsearch.com, Phone: 617.262.6500**

*The University of Rochester is an Equal Opportunity Employer and women and minorities are encouraged to apply.*



Founded in 1911, The University of Hong Kong is committed to the highest international standards of excellence in teaching and research, and has been at the international forefront of academic scholarship for many years. The University has a comprehensive range of study programmes and research disciplines spread across 10 faculties and about 100 sub-divisions of studies and learning. There are over 23,400 undergraduate and postgraduate students coming from 50 countries, and more than 1,800 members of academic and academic-related staff, many of whom are internationally renowned.

### Post-doctoral Fellowships and Research Assistant Professorships

Applications are invited for a number of positions as Post-doctoral Fellow (PDF) and Research Assistant Professor (RAP), at the University of Hong Kong, on or before February 28, 2014. Appointments will be made for a period of 2 to 3 years.

PDF and RAP posts are created specifically to bring new impetus and vigour to the University's research enterprise. Positions are available from time to time to meet the strategic research needs identified by the University. Positions are available in the following Faculties/Departments/Schools/Centres:

- Real Estate and Construction
- School of Humanities
- School of Modern Languages and Cultures
- Faculty of Dentistry
- Civil Engineering
- Electrical and Electronic Engineering
- Mechanical Engineering
- Community Medicine
- Medicine
- Psychiatry
- Centre for Cancer Research
- School of Chinese Medicine
- Research Centre of Heart, Brain, Hormone and Healthy Aging
- Research Centre of Infection and Immunology
- Public Health Research Centre
- Centre for Reproduction, Development and Growth
- School of Biological Sciences
- Chemistry
- Physics
- Geography
- Psychology
- The Hong Kong Institute for the Humanities and Social Sciences
- The State Key Laboratory for Liver Research
- The Hong Kong Jockey Club Centre for Suicide Research and Prevention

#### Post-doctoral Fellows

PDFs are expected to devote full-time to research. Applicants should be doctoral degree holders having undertaken original research that has contributed to the body of knowledge. A highly competitive salary commensurate with qualifications and experience will be offered. Annual leave and medical benefits will also be available.

#### Research Assistant Professors

The main focus of an RAP's duty is research. RAPs can however be assigned some teaching duties, up to 50% of the normal teaching load. Applicants should be research active and have a proven publication record. A highly competitive salary commensurate with qualifications and experience will be offered, with a contract-end gratuity and University contribution to a retirement benefits scheme (totalling up to 15% of basic salary). Annual leave and medical benefits will also be offered.

#### Procedures

Prospective applicants are invited to visit our webpage at <http://jobs.hku.hk> to view the list of the Faculties/Departments/Schools/Centres and their research areas for which PDF/RAP positions are currently available. Before preparing an application, they should contact the Head of the appropriate academic unit to ascertain that their research expertise matches the research area for which a vacant PDF/RAP post is available.

Applicants must submit a completed University application form, which should clearly state **which position they are applying for**; and in which academic discipline. They should also provide further information such as details of their research experience, publications, research proposals, etc.

Application forms (341/1111) can be obtained at <http://www.hku.hk/apptunit/form-ext.doc>. Further particulars can be obtained at <http://jobs.hku.hk/>. **Closes April 15, 2013.** The University thanks applicants for their interest, but advises that only shortlisted applicants will be notified of the application result.

The University is an equal opportunity employer and is committed to a No-Smoking Policy



# *There's only one* GALILEO GALILEI

Born in 1564, Galileo Galilei once contemplated a career in the priesthood. It's perhaps fortunate for science that upon the urging of his father, he instead decided to enroll at the University of Pisa. His career in science began with medicine and from there he subsequently went on to become a philosopher, physicist, mathematician, and astronomer, for which he is perhaps best known. His astronomical observations and subsequent improvements to telescopes built his reputation as a leading scientist of his time, but also led him to probe subject matter counter to prevailing dogma. His expressed views on the Earth's movement around the sun caused him to be declared suspect of heresy, which for some time led to a ban on the reprinting of his works.

Galileo's career changed science for all of us and he was without doubt a leading light in the scientific revolution, which is perhaps why Albert Einstein called him the father of modern science.

Want to challenge the status quo and make the Earth move? At *Science* we are here to help you in your own scientific career with expert career advice, forums, job postings, and more — all for free. For your career in science, there's only one *Science*. Visit [ScienceCareers.org](http://ScienceCareers.org) today.



For your career in science, there's only one **Science**



[ScienceCareers.org](http://ScienceCareers.org)



## AAAS is here – helping scientists achieve career success.

Every month, over 400,000 students and scientists visit ScienceCareers.org in search of the information, advice, and opportunities they need to take the next step in their careers.

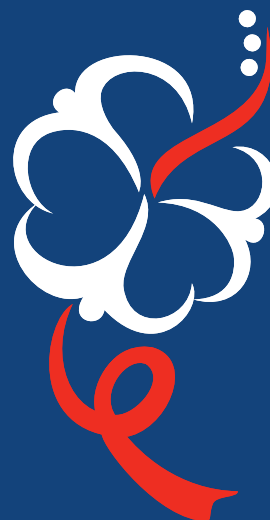
A complete career resource, free to the public, *Science Careers* offers a suite of tools and services developed specifically for scientists. With hundreds of career development articles, webinars and downloadable booklets filled with practical advice, a community forum providing answers to career questions, and thousands of job listings in academia, government, and industry, *Science Careers* has helped countless individuals prepare themselves for successful careers.

As a AAAS member, your dues help AAAS make this service freely available to the scientific community. If you're not a member, join us. Together we can make a difference.

To learn more, visit  
[aaas.org/plusyou/sciencecareers](http://aaas.org/plusyou/sciencecareers)



## CONFERENCE



## IAS 2013

The IAS Conference on HIV Pathogenesis, Treatment and Prevention is the world's largest scientific meeting focused on HIV and AIDS.

IAS 2013 is a crucial opportunity to examine the latest developments in HIV-related research, and to explore how scientific advances can be translated quickly into effective interventions to prevent and treat HIV.

### IAS 2013 KEY DATES:

**1 April 2013:**  
Volunteer applications open

**3 April 2013:**  
Late breaker submissions open

**18 April 2013 - 24:00 CET:**  
Registrations late fee deadline

**7 May 2013 - 24:00 CET:**  
Late breaker submissions close

For more information and to register:  
**[www.ias2013.org](http://www.ias2013.org)**





## POSITIONS OPEN

### CENTER FOR VIROLOGY AND VACCINE RESEARCH

Beth Israel Deaconess Medical Center  
Boston, Massachusetts

Beth Israel Deaconess Medical Center and Harvard Medical School are seeking faculty members at the **INSTRUCTOR, ASSISTANT PROFESSOR, or ASSOCIATE PROFESSOR** level to lead independent research programs in the Center for Virology and Vaccine Research, Department of Medicine. The successful candidate will be a recognized basic, translational, or clinical investigator with a Ph.D. and/or M.D. and a research focus in virology, immunology, microbiology, vaccinology, or infectious diseases. Academic rank at Harvard Medical School will be based on qualifications. Preference will be given to candidates with a track record of independent funding.

*Beth Israel Deaconess Medical Center and Harvard Medical School are Equal Opportunity Employers. Women and minorities are particularly encouraged to apply.* Please submit application letter and current curriculum vitae to:

Dan H. Barouch, M.D., Ph.D.  
Director, Center for Virology and  
Vaccine Research  
Beth Israel Deaconess Medical Center  
Attn: Kathryn Kelly  
E-mail: [kkelly7@bidmc.harvard.edu](mailto:kkelly7@bidmc.harvard.edu)  
Telephone: 617-735-4574

# Your career is our cause.

Get help  
from the  
experts.

**www.  
sciencecareers.org**

- Job Postings
- Job Alerts
- Resume/CV Database
- Career Advice
- Career Forum

**Science Careers**

From the journal *Science* AAAS

☒ More scientists agree — we  
are the most useful website.

**www.ScienceCareers.org**

# Download your free copy today.

**ScienceCareers.org/booklets**



From technology specialists to patent attorneys to policy advisers, learn more about the types of careers that scientists can pursue and the skills needed in order to succeed in nonresearch careers.

**Science Careers**

From the journal *Science* AAAS